ELECTRONIC STRUCTURE AND REACTION DYNAMICS OF MOLECULAR AND CLUSTER ANIONS VIA PHOTOELECTRON IMAGING

by

Kostyantyn Pichugin

A Dissertation Submitted to the Faculty of the

DEPARTMENT OF CHEMISTRY

In Partial Fulfillment of the Requirements
For the Degree of

DOCTOR OF PHILOSOPHY

In the Graduate College

THE UNIVERSITY OF ARIZONA

2010

THE UNIVERSITY OF ARIZONA
GRADUATE COLLEGE

As members of the Dissertation Committee, we certify that we have read the dissertation

prepared by Kostyantyn Pichugin

entitled Electronic Structure and Reaction Dynamics of Molecular and Cluster Anions via Photoelectron Imaging

and recommend that it be accepted as fulfilling the dissertation requirement for the

Degree of Doctor of Philosophy

____ Date: March 19, 2010
Dr. Andrei Sanov

____ Date: March 19, 2010
Dr. Mark Smith

____ Date: March 19, 2010
Dr. Bonner Denton

____ Date: March 19, 2010
Dr. Oliver Monti

____ Date:

Final approval and acceptance of this dissertation is contingent upon the candidate's submission of the final copies of the dissertation to the Graduate College.

I hereby certify that I have read this dissertation prepared under my direction and recommend that it be accepted as fulfilling the dissertation requirement.

____ Date: March 19, 2010
Dissertation Director: Andrei Sanov

STATEMENT BY AUTHOR

SIGNED: Kostyantyn Pichugin

ACKNOWLEDGEMENTS

Primarily, I would like to thank Prof. Andrei Sanov for being the best research advisor I ever had. This work would not be possible without his patience and persevering support through out my Ph.D. carrier at the University of Arizona.

I also need to thank the current and past members of the Sanov research group for their friendship, encouragement and help. In particular, I am indebted to our former postdoc Richard Mabbs, who is now an Assistant Professor at the Washington University in St. Louis. Richard, you were a true mentor to me in both life and science! I am deeply missing our “dark lab” conversations during data collection and your British humor. I am very grateful to Dr. Daniel Goebbert for being a great friend and for the fruitful research collaboration resulted in a number of publications. I also got fortunate to meet and work with Luis Velarde, Terefe Habteyes, Emily Grumbling, Dmitry Khuseynov, and Lori Culberson. These folks became my true friends and family for all the years I worked in Sanov group. I will never forget you guys!

I own many thanks to my dissertation committee for their time and contribution to improve this work. A special acknowledgment goes to Prof. Mark Smith for teaching me scientific writing skills and for detailed discussion of each dissertation chapter I gave him. I also thank to Prof. Oliver Monti for the discussion of quantum interference model for *para*-dinitrobenzene anion. Big thanks to Dr. Andrei Astachkine for his friendship and proofreading part of my dissertation.

A big thank you goes to the staff from our department electronic (Markus and Mike) and machine (Lee and Ed) shops, who were always there when I needed help fixing the apparatus. Also, without their support for developing in-vacuum heating system it would be impossible for me to complete the experiment on nitroaromatic anions.

Finally, I would like to express my appreciation to Graduate Fellowship, State of Arizona Prop. 301 Imaging Program for the financial support during 2006-2007 years.

DEDICATION

To my wife Tetyana and my children Oleksandra and Andrei – my love and my life.

To my parents Nadiya and Yuriy, who gave me their support and unconditional love over my entire life.

TABLE OF CONTENTS

TABLE OF CONTENTS ─ Continued

TABLE OF CONTENTS ─ Continued

LIST OF FIGURES

LIST OF FIGURES ─ Continued

LIST OF FIGURES ─ Continued

LIST OF FIGURES ─ Continued

LIST OF FIGURES ─ Continued

LIST OF FIGURES ─ Continued

LIST OF TABLES

ABSTRACT

The electronic structure and reaction dynamics of molecular and cluster anions in the gas phase has been investigated using negative ion velocity-map imaging photoelectron spectrometer. Photoelectron images provide important information about both energies and symmetries of the parent anion orbitals from which photoelectron originates. The symmetry and the ordering of several low-lying electronic states of neutral nitromethane ($X\,^1\mathrm{A}'$, $a\,^3\mathrm{A}''$, $b\,^3\mathrm{A}''$, and $A\,^1\mathrm{A}''$) are assigned based on a group theoretical analysis of the transitions angular distributions and the results of DFT calculations.

The through-bond electronic coherence in meta- and para-dinitrobenzene anions is explored by recording a series of photoelectron images in 532-266 nm wavelength range. Photoelectron angular distributions for both isomers exhibit oscillatory behavior characteristic of the quantum interference effect, suggesting that dinitrobenzene anions retain their high symmetry electronic structures in the gas phase.

Photoelectron imaging experiments on $[\mathrm{O(N_2O)}_n]^-$, n =0–9 at 266 and 355 nm provide clear evidence of a switch from the covalent $\mathrm{NNO_2}^-$ cluster core to the atomic O^- core occurring between n = 3 and 4. The experimental results and theoretical modeling indicate that despite the greater stability of $\mathrm{NNO_2}^-$ relative to the $\mathrm{O}^- + \mathrm{N_2O}^-$ dissociation limit, an O^- cluster core becomes energetically favored over $\mathrm{NNO_2}^-$ for $n > 3$, due to the more efficient solvation of the atomic anion.

The photodissociation dynamics of $\mathrm{I_2}^-$ and IBr^- anions on the respective A' excited-state anion potentials is effectively unraveled in 780 nm pump – 390 nm probe time-

resolve experiments. The time-dependent photoelectron spectra and classical trajectory calculations of the IBr^- dissociation provide the first rigorous dynamical test of the recently calculated A' potential for this system. The photoelectron anisotropy cyclic variation observed in photodissociation of I_2^- is interpreted in the context of dual-center quantum interference model.

The 390 nm pump – 390 nm probe experimental data reveal fast (≤100 fs) and delayed (~ 700 fs) appearance of the I^- channel in the photodissociation of I_2Cl^- and $BrICl^-$ anions respectively. The difference in the reaction time-scales is attributed to the distinct dissociation pathways available for the anions to form I^- product.

CHAPTER 1

INTRODUCTION

The primary objective of the work described in this dissertation is to outline the study of the electronic structure and reaction dynamics of isolated molecular and cluster anions in the gas phase at the most fundamental level. Our approach is to use photoelectron imaging as the direct means for probing electronic properties of negative ions. The power of this spectroscopic method is that it renders the information about both the energy eigenvalues and the symmetries of the electronic wavefunctions from which photoelectrons originate. Moreover, the combination of photoelectron imaging with ultrafast femtosecond pump-probe techniques reveals temporal transformations of molecular orbitals during chemical reactions. This chapter presents a general introduction to the field of negative ion photoelectron spectroscopy with a particular emphasis on the imaging approach, followed by a brief overview of the dissertation.

Negative ions are of great importance in diverse areas of chemistry, physics, astronomy, materials science, biology, medicine, and the chemical process industry.[1-8] Owing to the weakly bound nature of the excess electron, the fundamental physical and chemical properties of anions are qualitatively different from those pertinent to their cation and neutral analogs. In negative ions, the interaction between an outermost valence shell electron and the neutral core is primarily governed by the charge-dipole or charge-quadrupole interactions and therefore the long-range attractive potential for the electron falls off quickly as a higher power of 1/r. As a consequence, anions typically posses only a few bound excited electronic states and are more sensitive to the external perturbations.

Studying negatively charged ions is a challenging venture for both theoreticians and experimentalists. The experimental difficulties are primarily related to the production of anions in quantities sufficient for the spectroscopic observation. The lifetime is also an issue as many negative ions lose their excess electron through autodetachment process and/or dissociate before they can be probed in a spectrometer. From the theoretical perspective, the calculation of negative ions is also a complex task requiring the inclusion of large basis sets and the rigorous treatment of the electron correlation effect due to the highly diffuse nature of the highest occupied orbital accommodating the extra electron.

Photoelectron spectroscopy is a powerful tool ideally suited for probing the electronic structure and chemical reactivity of anions in the most direct way. On the other hand, negative ions are appealing as an experimental target because the removal of the weakly bound excess electron usually requires much smaller photon energies (1-4 eV) than for the neutrals and cations (~ 10 eV and higher). Hence, the research can be performed using commercially available tabletop ultrafast nanosecond and femtosecond lasers. In addition, anions as charged particles can be conveniently separated according to their charge, composition and size using mass spectrometric techniques, allowing selective photodetachment from the species of interest.

Anion photoelectron spectra contain important information about the ground and excited electronic states of the corresponding neutral accessed in the photodetachment process. The advantage of photoelectron spectroscopy is that it allows for the direct observation of the “dark” states which can not be detected by electronic absorption spectroscopy due to the spin selection rule. Extracted from photoelectron spectra, electron affinities and vertical detachment energies provide (at the Koopmans' approximation) the experimental estimate of the parent anion orbital energies and can be used in a thermochemical cycle to deduce bond dissociation energies and reaction enthalpies. Furthermore, the vibrational progressions in the photoelectron bands can be exploited to accurately determine vibrational frequencies for the observed electronic states of the neutral molecule.

Apart from isolated species, photoelectron spectroscopy is also invaluable to study the intermediate states of matter – cluster anions. Negative ions are very sensitive to the chemical environment due to the diffuse nature of valence electron densities. This makes cluster anions an ideal model for learning the details of microscopic solvation and elementary chemical processes in bulk systems.[7] Typically, the cluster anion $X^{-}(M)_n$ consists of the negatively charged core X^{-} and the solvent shell formed from the neutral molecules, M. Solvation usually stabilizes an anion as a result of the attractive ion-neutral interactions. This leads to larger vertical detachment energies as the number of solvent molecules increases. Therefore, it is possible to estimate the stepwise solvation energies from the shifts in the photoelectron band positions. Generally, the increase in vertical detachment energies is expected to be monotonic with the number of solvent molecules and thus the sharp discontinuities in this trend serve as an indicator of dramatic changes in the chemical structure of the anionic core.[9-12]

A particularly powerful incarnation of photoelectron spectroscopy is its combination with the ultrafast pump-probe techniques. Femtosecond time-resolved photoelectron spectroscopy (TRPES) reveals a variety of chemical processes, involving changes in the electronic structure, on the natural timescale of atomic motions. A typical time-resolved experiment can be broken down into three main stages: (1) a molecular anion of choice is brought to an excited electronic state by absorbing a pump photon, which serves as a trigger to initiate a reaction; (2) the reaction proceeds for some well-defined and controllable time; (3) the evolution of the system is observed by detaching the extra electron with the probe photon and recording the temporally resolved photoelectron signal. The pump and probe photons must satisfy certain requirements. The pump photon has to be in resonance with the target exited state and the energy of the probe photon must be sufficient to remove the electron from the excited anion. In the ideal situation, the pump photon should not detach the electron from the anion. Otherwise, the population of the parent anions is depleted, which results in the reduction of the pump-probe signal and its contamination with the photoelectrons generated solely by the pump photons. This problem can be partially circumvented by collecting a pump-only signal separately and then subtracting it from the pump+probe spectra (see Time-Resolved Measurements section of Chapter 2 for more details).

It should be emphasized that the absorption of the ultrafast femtosecond pump pulse creates a nonstationary state, i.e a coherent superposition of the excited state eigenstates (a wavepacket), on which the ground state of the anion is projected. The evolution of the wavepacket is determined by the topological character of the excited state potential energy surface. In the case of a bound excited state, the wavepacket is trapped between the inner and outer turning points of a potential well. A coherent vibrational wavepacket motion can be efficiently monitored by recording the time-dependent oscillations in the electron kinetic energy. These oscillations arise from the difference in energy between excited anionic and neutral potentials at the instantaneous position of the wavepacket pinned by a probe photon. In addition, the intensity of the photoelectron signal also changes in time reflecting periodical spreads and revivals of the wavepacket.

When a molecular anion is excited to a dissociative state, the wave packet accelerates by sliding down the repulsive part of the potential energy surface and then keeps going towards larger internuclear distances until the bond cleavage occurs. Unlike for a bound potential, there are no revivals and the wavepacket simply spreads out during its evolution on the excited state surface. Experiments which probe these processes are essential for exploring the shape of the excited state potentials and the reaction time scales. The occurrence of nonadiabatic transitions between excited states leads to more complex dynamics than in the previous scenarios. Nonadiabatic processes in polyatomic anions are responsible for charge transfer, internal conversion, autodetachment, nuclear rearrangements (isomerization), and change in the reaction pathways. Studying charge and energy flow within molecular systems during photoinduced nonadiabatic reactions is fundamental for understanding light harvesting, vision, and atmospheric processes.

Historically, negative ion photoelectron spectroscopy is a relatively young yet rapidly growing research field. The first photoelectron studies on negative ions in the gas phase are dated back to the pioneering work of Carl Lineberger[13-20] and John Brauman[21-24] in the beginning of 1970s. The advent of ultrafast pulsed lasers and advancements in the production of negative ions[25,26] led to a significant improvement and explosion of research activity in this area. A substantial breakthrough in the field of negative ions was accomplished by Daniel Neumark, whose group was the first to apply femtosecond time-resolved photoelectron spectroscopy to investigate the intricate details of the I_2^- photodissociation.[27] During the last decade, TRPES has matured into a comprehensive technique and was successfully employed to study the time evolution of the electronic structure for a variety of molecular and cluster anions.[28-30]

Another important milestone was the introduction of the imaging technique. Ion imaging was originally developed by Chandler and Houston[31,32] in 1987 for studying ionic photofragments. Later, the imaging technique was significantly improved and applied to photoelectrons with the addition of velocity mapping approach devised by Eppink and Parker.[33,34] Velocity mapping effectively reduces the spatial blurring of photoelectron images by projecting the resulting photoelectrons onto the imaging detector according to their velocity regardless of the initial position in the interaction volume defined by the overlap between the laser and ion beams.

The main advantages of photoelectron imaging over traditional photoelectron spectroscopy are the uniform detection sensitivity in the entire range of electron kinetic energies, 100% collection efficiency, and the capability of measuring photoelectron angular distributions (PADs) which are intimately related to the parent anion orbital symmetries.[35-39] In this regard, photoelectron imaging can be referred to as the "experimental quantum mechanics" because it provides an investigator with both the eigenvalues (binding energies) and the symmetries of the eigenfunctions (through photoelectron angular distributions) of bound electrons in atoms or molecules. The importance of the PADs can not be overemphasized. Photoelectron angular distributions are extremely helpful in assigning the symmetry of the transition terms, learning about the transformation of the molecular orbitals during dissociation, quantum interference effects and scattering processes.[30,37,40-45] Traditionally, the photoelectron spectroscopy community has focused on the transition energies often disregarding the information provided by the angular distributions. In this dissertation, both the energy and the anisotropy dimensions are exploited at the same degree to get an in-depth look at the electronic structure and reaction dynamics of molecular and cluster anions.

The rest of this dissertation is organized as follows. The negative ion photoelectron imaging spectrometer, laser sources as well as acquisition and analysis of photoelectron images are described in detail in Chapter 2. In Chapter 3, photoelectron imaging of nitromethane anion is used to study several exited electronic states of the neutral. The symmetries of the observed electronic states are assigned based on the DFT calculations and a group theoretical analysis (s&p model) of the corresponding photoelectron angular distributions. Chapter 4 is devoted to the photoelectron imaging of nitroaromatic anions. The quantum interference effect revealed in the photodetachment from meta- and para-dinitrobenzene anions is explained in the context of the two-center molecular interferometer. Chapter 5 presents an investigation of solvation induced switching from the covalent NNO_2^- cluster core to O^- core observed in the photoelectron imaging experiments on $[O(N_2O)_n]^-$ cluster anions. Chapter 6 describes time-resolved photoelectron imaging experiments on diatomic halogen anions I_2^- and IBr^-. This chapter is divided into three parts. The first portion of the chapter addresses the bond breaking process from the energetic perspectives. The second part focuses on evolution of the photoelectron angular distribution during photo-induced dissociation of the anions, with a particular emphasis on the observed dual-center quantum interference effect for the symmetric I_2^-. The rest of the chapter is devoted to a complimentary time-resolved study on I_2^- using a different pump-probe energy scheme. Chapter 7 extends the studies on halogen molecular anions to mixed trihalides. In this chapter, the photodissociation dynamics of I_2Cl^- and $BrICl^-$ anions is explored via time-resolved photoelectron imaging of the I^- product. Chapter 8 describes future possible experiments and is intended to motivate a forthcoming research based on the proposed ideas.

CHAPTER 2

EXPERIMENTAL SETUP AND DATA ANALYSIS

2.1 Overview of Negative Ion Photoelectron Imaging Spectrometer

All experiments described in this dissertation were carried out on the negative-ion photoelectron imaging spectrometer described previously.[46,47] The experimental apparatus employs pulsed negative-ion generation and mass-analysis techniques pioneered by Lineberger and co-workers,[48,49] combined with a velocity-mapped[33,34] imaging[31,32] (VMI) scheme for the detection of photoelectrons. A general overview of the apparatus is given below. While some minor additions are thoroughly described in this chapter, the reader is referred to the original work[1] for the detailed technical specifications and drawings of the instrument.

A schematic diagram of the experimental apparatus is shown in Figure 2.1. The apparatus consists of three differentially pumped regions: *ion source chamber*, *time-of-flight tube*, and *detection chamber*. The ion source chamber is pumped by a 10″ diffusion pump (Varian VHS 10); the time-of-flight region is pumped by a 6″ (Varian VHS 6) diffusion pump and turbo pump (Leybold TMP 361); the detection region separated from the time-of-flight region by a pneumatic gate valve is pumped by another turbo pump (Leybold TMP 361). The diffusion and turbo pumps are water-cooled using a liquid-to-liquid heat exchanger (Coolflow System II, Neslab Inc.), and each of the vacuum pumps

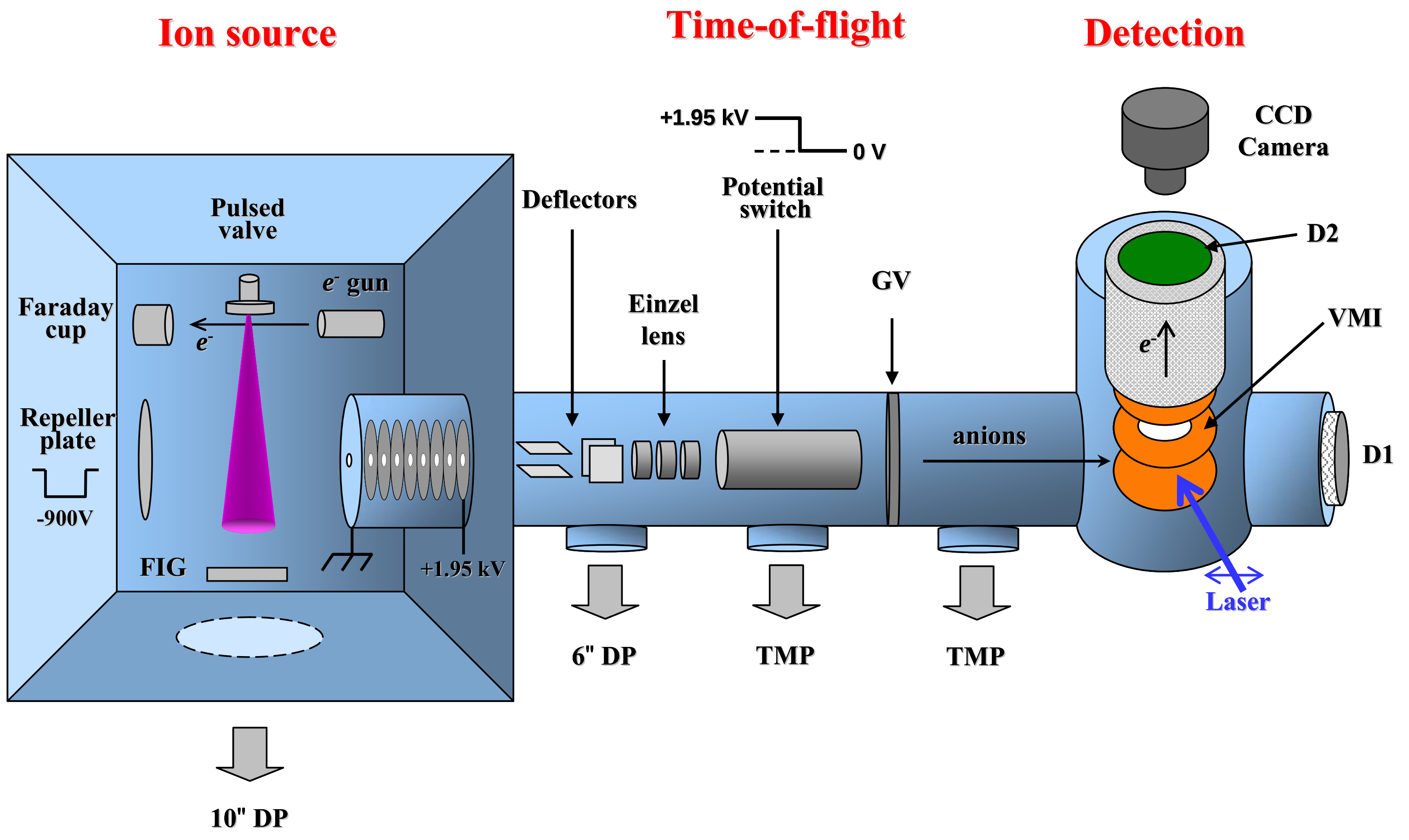

Figure 2.1 Schematic diagram of the Negative Ion Photoelectron Imaging Spectrometer. In the figure, FIG – Fast Ionization Gauge, DP – Diffusion Pump, TMP – Turbo-Molecular Pump, GV – Gate Valve, D1 – inline ion/neutral Detector, D2 – position sensitive imaging Detector, VMI – Velocity-Map Imaging lens. The laser radiation is polarized linearly, parallel to the plane of the imaging detector as indicated by the double-sided arrow on the laser beam.

is backed up by a separate rotary pump. The base pressures achieved for the ion source chamber, time-of-flight region, and detection chamber are $(3–5)\times10^{-6}$, $(2–4)\times10^{-8}$, and $(1–2)\times10^{-9}$ Torr. When the instrument is operated, the pressure inside the differentially pumped regions typically rises up to $(3\text{-}5)\times10^{-5}$, $(5\text{-}8)\times10^{-8}$, and $(2\text{-}4)\times10^{-9}$ Torr respectively.

Anions are formed in the source chamber by expansion of a sample gas through a pulsed nozzle into high vacuum. The supersonic expansion is continuously bombarded with high energy (about 1 keV) electrons from an electron gun. The resulting anions are pulse extracted into a time-of-flight mass spectrometer where they get accelerated up to about 2.7 keV, guided by a set of electrostatic horizontal and vertical deflectors, and spatially focused using the Einzel lens. After leaving the Einzel lens, anions fly into potential switch which references the anions back to the ground potential without affecting their kinetic energy. The ions are detected with mass-resolution at the end of the flight tube using an in-line dual-microchannel-plate (MCP) detector (labeled as D1 in Figure 2.1). Photoelectrons are produced in the center of extraction region of VMI electrostatic lens by intersecting the mass-selected anions of interest with a linearly polarized laser beam. The imaging lens projects the photodetached electron cloud onto a position sensitive MCP detector with a phosphor screen (D2) mounted at the end of an internally μ-metal-shielded electron flight tube. Images are recorded from the phosphor screen using a charge-coupled device (CCD) thermoelectrically cooled camera (Roper Scientific Inc.) which ultimately transfers the signal to a computer for data analysis.

The subsequent sections in this chapter provide additional experimental details on the major components and operation of the instrument, laser systems, time-resolved measurements, and data analysis.

2.2 The Ion Source Chamber: Formation of Negative Ions

The Ion Source chamber contains an electron gun, nozzle, Faraday cup, repeller plate, and fast ionization gauge. A sample gas, typically at a total stagnation pressure of 20-40 psi, is expanded into the source chamber through a pulsed nozzle (General valve series 9 or 99 with Kel-F poppet). The nozzle is fired by the General Valve IOTA ONE pulse driver with the repetition rate of 50 or 70 Hz depending on which laser system (see Light Sources and Instrument Operation sections for more details) is used to trigger the instrument.

The electron gun can be positioned either perpendicular to (as shown in Figure 2.1) or along the axis of the supersonic expansion. In the perpendicular arrangement the outgoing beam of electrons crosses the expansion just a few millimeters downstream from the nozzle orifice and ends in a Faraday cup. The Faraday cup is a metallic cylinder serving two purposes: (1) it prevents a charge buildup on various components inside the source chamber by capturing high energy electrons from the electron gun; (2) an operator can monitor the direction of the electron beam by reading a current from the Faraday cup through an ampmeter. When the electron gun is placed inline of the supersonic expansion, the electron beam propagates straight up into the nozzle throat. In this case the nozzle also functions as a Faraday cup and it is possible to learn about the direction of electron beam by measuring current from the nozzle. The inline arrangement is preferred for the production of larger anionic clusters as has been shown by the Johnson group,[50] however the life time of the filament in the electron gun is significantly reduced compared to the perpendicular setup.

High energy electrons emitted from the electron gun penetrate through the supersonic jet creating a number of slow secondary electrons by ionizing the neutral atoms and/or molecules of the sample (S):

$$S + e^{-}(\sim 1\text{ keV}) \rightarrow S^{+} + e^{-}(\text{slow}) + e^{-}(\text{fast}, \sim 990\text{ eV}) \qquad (2.1)$$

The negative ions are produced by secondary electron attachment to the neutral species:

$$S + e^{-}(\text{slow}) \rightarrow S^{-*} \qquad (2.2)$$

A “newly born” negative ion has to give up the excess energy in order to stabilize. This can be achieved in several ways: (i) by transferring the energy to a third body

$$S + e^{-}(\text{slow}) + M \rightarrow S^{-} + M^{*} \qquad \text{(three-body stabilization)} \qquad (2.3)$$

(ii) by breaking apart and channeling the extra energy to translational and internal degrees of freedom of the neutral fragment(s)

$$S + e^{-}(\text{slow}) \rightarrow A^{-} + B^{*} \qquad \text{(dissociative attachment)} \qquad (2.4)$$

(iii) by evaporating solvent atom(s)/molecule(s), which is only possible for cluster anions

$$S_{n} + e^{-}(\text{slow}) \rightarrow S_{m}^{-} + (n\text{-}m)S \qquad \text{(evaporative cooling}^{51}\text{)} \qquad (2.5)$$

If none of the stabilization pathways is available then anion will lose the extra electron

$$S^{-*} \rightarrow S(v>0) + e^{-} \qquad \text{(thermionic emission)} \qquad (2.6)$$

Generating negative ions with the electron gun positioned perpendicularly to the gas expansion can be more problematic. The formation process is very sensitive to the geometry and direction of the electron beam. In general, a set of the optimal conditions is a point on the multidimensional surface of adjustable settings such as the sample gas stagnation pressure, voltages on the Anode plate, Einzel lens, and deflectors in the electron gun, etc... Although an experienced operator might have a good feeling of what those settings should to be, it is not uncommon to spend days or even weeks looking for ions.

The signal from the fast ionization gauge (FIG) can be used to efficiently find the optimal set of parameters to generate anions. The FIG (Model FIG-1, Beam Dynamics Inc.) used in our laboratory is a modified version of a standard Bayard-Alpert gauge optimized for very rapid response to changes in pressure (response time is < 5 μs). The FIG head contains a hot cathode (heated filament) and a grid collector. A hot cathode produces a beam of electrons that passes through the gauge and ionizes gas atoms and/or molecules. The resulting ions travel to the collector which is at zero volts. The current depends on the number of ions, which depends on the pressure in the gauge. Figure 2.2 shows the FIG output recorded with a digital oscilloscope. When no or very little negative ions are generated (Figure 2.2.a) the FIG signal contains only base line and dip features. The base line of the signal is due to the background pressure in the source chamber while the dip corresponds to the temporal profile of a gas pulse from the nozzle. The author of this dissertation has noticed that a sharp spike (circled in Figure 2.2.b) appears in the FIG signal at the optimal conditions for anion production. A possible explanation for this effect is that the overall current (generated by cations) from the FIG collector is reduced due to the presence of negatively charged species in the jet.

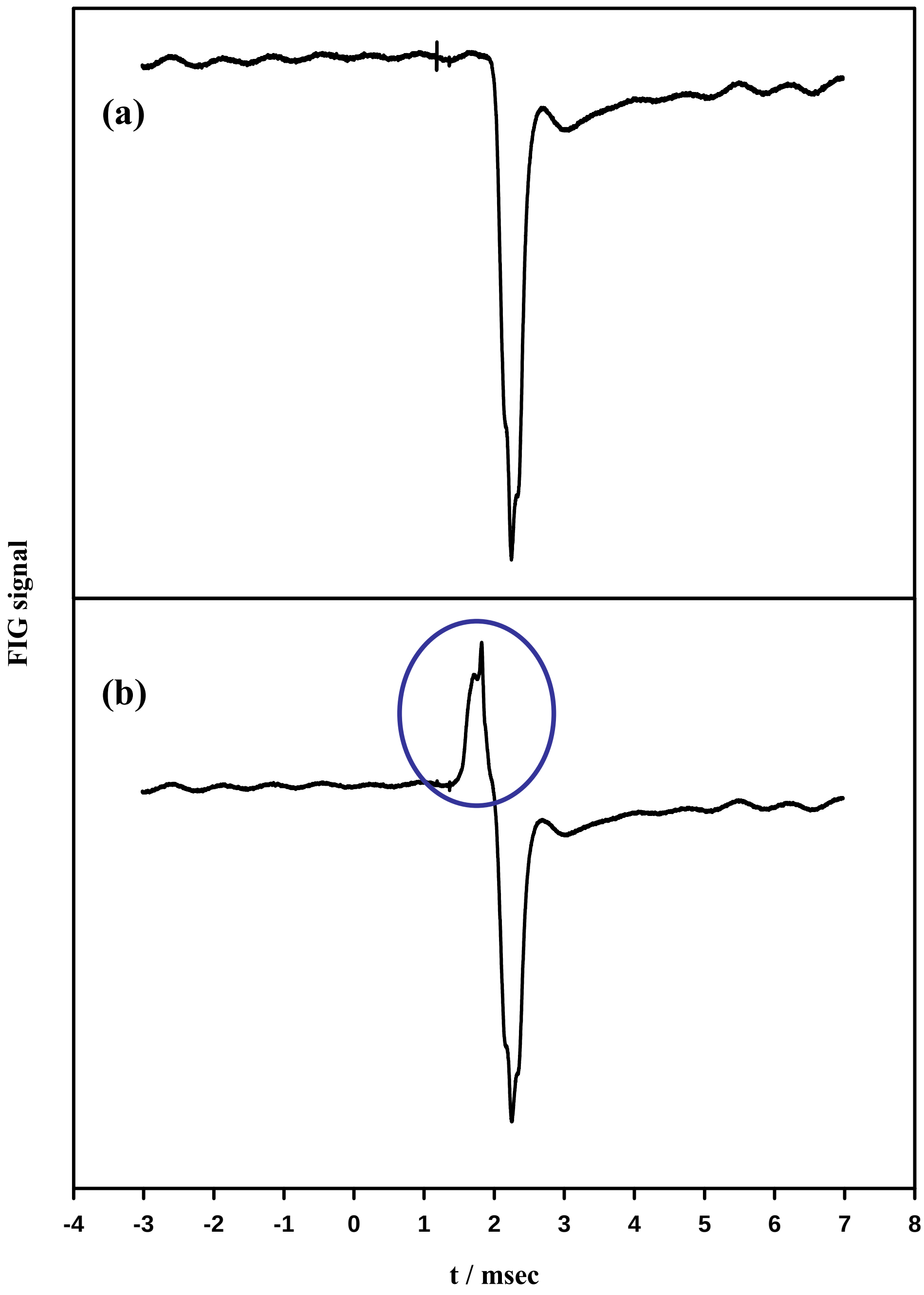

Figure 2.2 A guideline for negative ion generation using a signal from the fast ionization gauge (FIG). The origin of the abscissa corresponds to the time when the nozzle is fired. (a) corresponds to a set of experimental settings at which very little or no anions being formed. (b) optimal conditions for the anion formation; the encircled sharp spike indicates that negatively charged species are present in the supersonic jet.

After the interaction with the high energy electrons, the expanding supersonic jet is essentially a cold electrically neutral plasma containing positive, negative and remaining neutral species. Further downstream from the nozzle, the expansion passes between two parallel plates. One of which is a repeller plate and the other is time-of-flight entrance plate with the small (4 mm) opening in the center. The entrance plate is always set at the ground potential while the repeller plate is pulsed up to -950 V by a 10 ns rise/fall time high voltage pulse generator module (model PVM 4210, Directed Energy Inc.). The output voltage from the pulse generator can be adjusted by a voltage controller.

The entrance hole to the time-of-flight region is located about 18 cm from the nozzle. Anions are extracted perpendicularly, with respect to the direction of the supersonic expansion, into the time-of-flight tube by applying a negative high voltage pulse to the repeller plate. Only a small fraction of negative ions contained in a cylindrical volume with a diameter of the entrance aperture (4 mm) is ejected into the time-of-flight region.

2.3 Time-of-Flight Mass Spectrometer

The linear time-of-flight (TOF) mass spectrometer used in our instrument is similar to that originally developed by Wiley and McLaren,[52] which consists of two acceleration stages and a field free drift region. The first region is pulsed until all the ions are pushed into the second region with a constant in time uniform electric field supplying the ions with more kinetic energy. After acceleration, the ions enter a field free drift region providing them with the necessary time to separate in bunches according to their mass-to-charge ratio. The important feature of the Wiley-McLaren TOF mass spectrometer is that the identical ions with different velocities in the direction of the time-of-flight axis will eventually pass each other. The distance at which this happens is called the spatial focus of the mass spectrometer. The position of the spatial focus is independent of the ion mass and can be adjusted by tuning the electric field in either of the two accelerating regions.

At the point the supersonic jet from the nozzle passes the repeller plate, it spreads up to 5-7 cm in diameter.[53] The spatial distribution of ions in the supersonic expansion leads to an energy spread since the identically charged particles experience different electric potentials during the extraction process. The energy spread is estimated to be about 400 eV for a typical 800 V/cm extraction field used in our instrument. Therefore, the spatial focusing of the ions afforded by the Wiley-McLaren conditions is very important since it provides us with improved mass resolution. In addition, the photoelectron signal is also enhanced due to better spatial overlap of the anion packets with the laser beam.

The TOF region of the mass spectrometer includes the acceleration stack, ion optics (ion deflectors and Einzel lens), and potential switch. The pulse extracted anions from the source chamber enter the acceleration stack made of ten identical circular electrodes. Each plate is 1/32″ thick, 3″ in diameter and has a 1″ hole in the center for the ions to pass through. The entrance plate is at the ground potential while the last plate is floated at +1.95 kV. The plates in the stack are separated from each other by 0.16″ Teflon spacers and are electrically connected using 1 MΩ vacuum-grade resistors. After passing the acceleration stack, the ions with a total kinetic energy of 2,350 ± 200 eV (assuming -800 V potential on the repeller plate) fly through the set of ion optics and potential switch.

Two pairs of ion deflectors (horizontal and vertical) are set at the same potential as the acceleration stack (+1.95 kV) with the additional 0 to ±100 V provided by the floated power supplies. The ion deflectors are used to adjust the trajectory of the ion beam compensating for the transverse velocity component acquired by the ions during supersonic expansion. The Einzel lens consists of three stainless steel cylindrical electrodes separated from each other by 0.16″ Teflon spacers. Each of the cylinders is 1.5″ long and 1.5″ in diameter. The terminal electrodes are floated at +1.95 kV, while the voltage on the middle electrode can be varied from 0 to +1 kV. The Einzel lens operates similar to the positive optical lens by converging ion trajectories to a single spot on the time-of-flight axis. The focal length of the Einzel lens is determined by the voltage settings on the middle electrode.

The potential switch is a 24″ long and 3″ OD stainless steel tube. When the ions enter potential switch it is initially set at the beam potential provided by a high voltage pulse generator (model PVX-4140, Directed Energy Inc.). At a selected time the potential is rapidly switched to ground, and therefore only ions inside the tube will pass to the field free drift region of the mass spectrometer. In this regard the potential switch works as a simple mass gate by selecting a “mass window” of interest from the entire set of ions entered mass spectrometer. The advantage of this approach is that the ion detector will not be saturated by the presence of unwanted species.

The ions are detected at the end of the TOF tube by a Chevron-type dual microchannel plate detector (Burle, Inc.) which is powered through the voltage divider by a high voltage power supply (model 205B-05R, Bertan Associates Inc.). The input voltage (+V_0) from the power supply is distributed to the MCP detector in the following way: the front MCP, rear MCP, and the anode plate receive $V_0 \times 0.66$, V_0-200, and V_0 volts respectively. The negative ions are post-accelerated by about +1 kV bias on the front MCP before impacting the detector. A strong electric field from the microchannel plates is isolated from the rest of the instrument by the 70 wires-per-inch nickel mesh maintained at ground potential.

The digital oscilloscope (model TDS3032, Tektronix Inc.) records an amplified signal (model 6931, Philips Scientific amplifier) from the detector anode plate. After averaging for 512 experimental cycles, the TOF signal is transferred from the oscilloscope to a computer for further analysis. The mass assignment is accomplished by calibrating the spectra using the following empirical equation

$$t = a\sqrt{\frac{m}{q}} + t_0 \tag{2.7}$$

where t is the time-of-flight, a is a proportionality constant, and m/q is a particle mass-to-charge ratio. The a and t_0 parameters are found by solving the system of two equations for the selected peaks with known masses. The identity of the chosen species can be readily confirmed by recording their photoelectron spectra.

2.4 Detection: Velocity-Map Photoelectron Imaging

Photoelectrons are produced in the detection region by interrogating the negatively charged species of interest with a linearly polarized laser beam. The detection region contains velocity map[33,34] imaging[31,32] (VMI) lens, field free electron flight tube, and position sensitive MCP detector with P43 phosphor screen coupled to a fiber optic vacuum window (Burle, Inc.).

The VMI lens consists of three parallel oxygen-free high conductivity copper plates spaced by 1″ intervals. Each plate is 1/32″ thick and 4″ in diameter. The top and middle plates also have a 1″ opening in the center while the bottom plate is blind. Both anion and laser beams propagate right in between the bottom and middle plates and intersect perpendicularly at the point laying on the VMI lens axis. The bottom plate is set at a repulsive negative potential. Resulting photoelectrons are pushed up through the middle and upper plates, which are kept at the ground and positive potentials respectively.

Due to the finite size of anion and laser beams, the photoelectrons are born at different spatial positions in the interaction volume. In general, the spatial distribution of photoelectrons leads to image blurring, which was the major drawback in the original imaging approach introduced by Chandler and Houston.[31,32] The velocity mapping technique developed by Eppink and Parker[33,34] overcomes this deficiency by projecting photoelectrons with identical velocities onto the same position on the imaging detector regardless of their origin. For the imaging lens to operate in the velocity mapping regime, a certain ratio has to be established between the voltages on the top (V_{top}) and bottom (V_{bottom}) plates. By tuning the voltages for the best image resolution, this empirical ratio is found to be $\left|\frac{V_{top}}{V_{bottom}}\right| \approx 3$ for our instrument. The image size depends on the photoelectron kinetic energy and the time-of-flight to the imaging detector. Therefore, it is possible to zoom in/out photoelectron image on the detector by changing VMI voltages on the top and bottom plates while keeping their ratio constant.

After traveling through the μ-metal shielded field-free flight tube, photoelectrons hit the imaging detector. To reduce the amount of background signal, the potential difference between the two imaging MCPs is normally maintained at 1.0-1.2 kV. During detection time (about 200 ns), the bias across MCPs is pulsed (model PVM-4150, Directed Energy Inc.) up to 1.8 kV. A fine nickel mesh of 333 wires-per-inch maintained at the ground potential isolates the field free region from the detector electric field. The signal from the phosphor screen is recorded with a CCD camera (CoolSnap, Roper Scientific, Inc.). The home written data acquisition software, CoolImage, transfers acquired image from the CCD chip to a computer interfaced with the camera through the capture board. The final photoelectron image is typically accumulated for $1\text{-}5\times10^5$ experimental cycles.

2.5 Triggering

Any photoelectron imaging experiment, no matter how long or complex, is built upon a series of discreet units, experimental cycles. In the present setup, each experimental cycle is initiated by an external trigger pulse from a laser. The logical sequence of events during the cycle is controlled by a digital delay generator (model DG535, Stanford Research Systems), which is timed by another delay generator (model 555, BNC Inc) receiving the external trigger. The marginal delay generator provides an extra flexibility to manipulate the incoming signal. This way, it is possible to synchronize the arrival of laser beam with anions of interest by postponing the startup of apparatus experimental cycle. In addition, when the instrument is triggered by the femtosecond laser system, DG555 reduces the frequency of external trigger from 1 kHz to 70 Hz, the maximum repetition rate afforded by the nozzle (9 or 99 Series, General Valve).

The four delay channels available in DG535 are linked to the cycle start time, T_0, in the following way:

$$C = T_0 + T_c \text{ (1700 – 2100 μs)} \tag{2.8}$$

$$D = C + T_d \text{ (5 – 90 μs)} \tag{2.9}$$

$$A = C + T_a \text{ (6 – 95 μs)} \tag{2.10}$$

$$B = A + T_b \text{ (200 – 300 ns)} \tag{2.11}$$

It should be emphasized that the time intervals given in parentheses are representative of the delays used in a “typical experiment” and may significantly vary depending on experimental conditions, e.g., nature of the chemical sample, backing pressure, potential on the repeller plate, etc.

The apparatus experimental cycle begins by firing the nozzle at T_0 time. The nozzle is opened for about 180 – 300 μs. The duration of the nozzle pulse is controlled by the settings on the General Valve IOTA ONE pulse driver. The CD output of the DG535 provides a pulse which is the intersection of the C and D delays, i.e., it starts at the time C and ends at the beginning of D. During the CD pulse the repeller plate and potential switch are energized up to ~ -800V and +1.95 kV respectively. Once the pulse is over, the potentials are dropped back to 0 V. Since the potential switch operates as a simple mass gate (see Time-of-Flight Mass Spectrometer section for more details), changing C and D delays allows scroll the entire mass spectra in the “mass window” of interest.

The AB pulse provides the "imaging window" time when the microchannel plates on the imaging detector receive the extra +1 kV bias to detect photoelectrons. The A delay strongly depends on the anion time-of-flight. The right value can be found by running a CCD camera in the focusing regime (capturing one snapshot after another with the exposure time of about 3 seconds) and adjusting A for the best possible photoelectron signal. The above procedure takes time, and it is easy to miss a weak photoelectron signal. The following empirical equation has been established by fitting a large set of experimentally found A values for the chosen anion time-of-flights:

$$A = 0.925 \times t + 0.144 \tag{2.12}$$

where t is the time-of-flight in microseconds. Using the estimated value, an operator can quickly find the photoelectron signal from selected anion of interest and then improve it by fine tuning the A delay.

2.6 Light Sources

All experiments described in this dissertation were performed using either femtosecond or nanosecond tabletop laser systems currently available in our laboratory. Both systems were purchased from Spectra-Physics Lasers, Inc.

The ultrafast femtosecond laser system consists of Spitfire, Ti:sapphire regenerative amplifier, pumped by Evolution-X, nanosecond Nd:YLF laser supplying 527 nm light, 10 W at 1 kHz. A seed beam (790nm, <80 fs pulse width, 1 W at 82 MHz) for the amplifier is provided by Tsunami, mode-locked Ti:sapphire laser, which is pumped by a continues-wave Nd:YVO_4 solid-state laser, Millennia Vs, with 532 nm, 26 W output. The regeneratively amplified Ti:sapphire laser system produces 800 nm, 1 mJ, 90 – 120 fs pulses at 1 kHz repetition rate. The fundamental temporal pulse width is measured using a single-shot autocorrelator (Positive Light SSA). When necessary, the fundamental frequency can be doubled (400 nm, 30 μJ/pulse) or tripled (267nm, 20 μJ/pulse) using a Super Tripler femtosecond harmonic generator (Super Optronics, Inc.). The second harmonic is produced by passing 800 nm radiation through 100-μm-thick beta barium borate (BBO) crystal. To triple the frequency, the second harmonic is combined with the fundamental in another BBO crystal. The radiation wavelength is monitored using a fiberoptics spectrometer (Ocean Optics, Inc.).

A Q-switched Nd:YAG laser (Quanta-Ray Lab 130-50, Spectra Physics) provides <10 ns pulses at 50 Hz repetition rate. The laser outputs the fundamental at 1064 nm with 200 mJ/pulse. The second (532 nm, 70 mJ/pulse), third (355 nm, 30 mJ/pulse), and forth (266 nm, 15 mJ/pulse) harmonics are generated using Potassium Titanyl Phosphate ($KTiOPO_4$, KTP) crystals mounted in the Harmonic Generator compartment of the laser head. Typically 10-70% of the maximum available laser power is used in the experiment. In order to enhance photoelectron signal, the laser beam can be mildly focused with a 2.0 m focal length lens, positioned 1.3m before the laser and ion beam crossing.

2.7 Time-Resolved Measurements

Femtosecond time-resolved photoelectron spectroscopy is a powerful tool for investigating the excited state dynamics in isolated molecular anions. Time-resolved measurements are performed using pump-probe technique: a molecular anion is brought into the excited anionic state by absorbing a pump photon and after a well-defined, although variable, time the evolution is probed with the second photon, which leaves the system in a neutral state by removing the extra electron.

Figure 2.3 shows pump-probe optical line setup for single-color 400 + 400 nm (a) and two-color 800 + 400 nm (b) time-resolved experiments. In the single-color arrangement, the fundamental ~ 800 nm light from the ultrafast femtosecond Ti:sapphire laser system (see Light Sources section for the detailed description of the femtosecond laser system) is frequency-doubled in Super Tripler femtosecond harmonic generator (Super Optronics, Inc.). The resulting 400 nm radiation is separated into two beams using a 50% beam splitter (BS_1). One of the beams travels a fixed optical path length, while the other is directed through a motorized translation stage (Newport ESP300 Universal Motion Controller) to enable controlled temporal separation of the pump and probe pulses. Finally, the beams are recombined before entering the detection chamber using a second 50% beam splitter (BS_2), which inevitably leads to a 50% loss in the power of each beam. The polarization vectors of the two beams are parallel to each other and to the ion beam axis. The zero pump-probe delay is found by scanning thorough the motorized delay stage until a pattern of interference fringes shows up, indicating that two coherent beams are overlapped both in time and space. The temporal overlap (cross correlation) of the pump and probe pulses is determined by locating two end points where the interference pattern disappears. Measured this way pump-probe cross-correlation width is about 250 fs, which defines approximate time resolution for 400 + 400 nm time-resolved experiment.

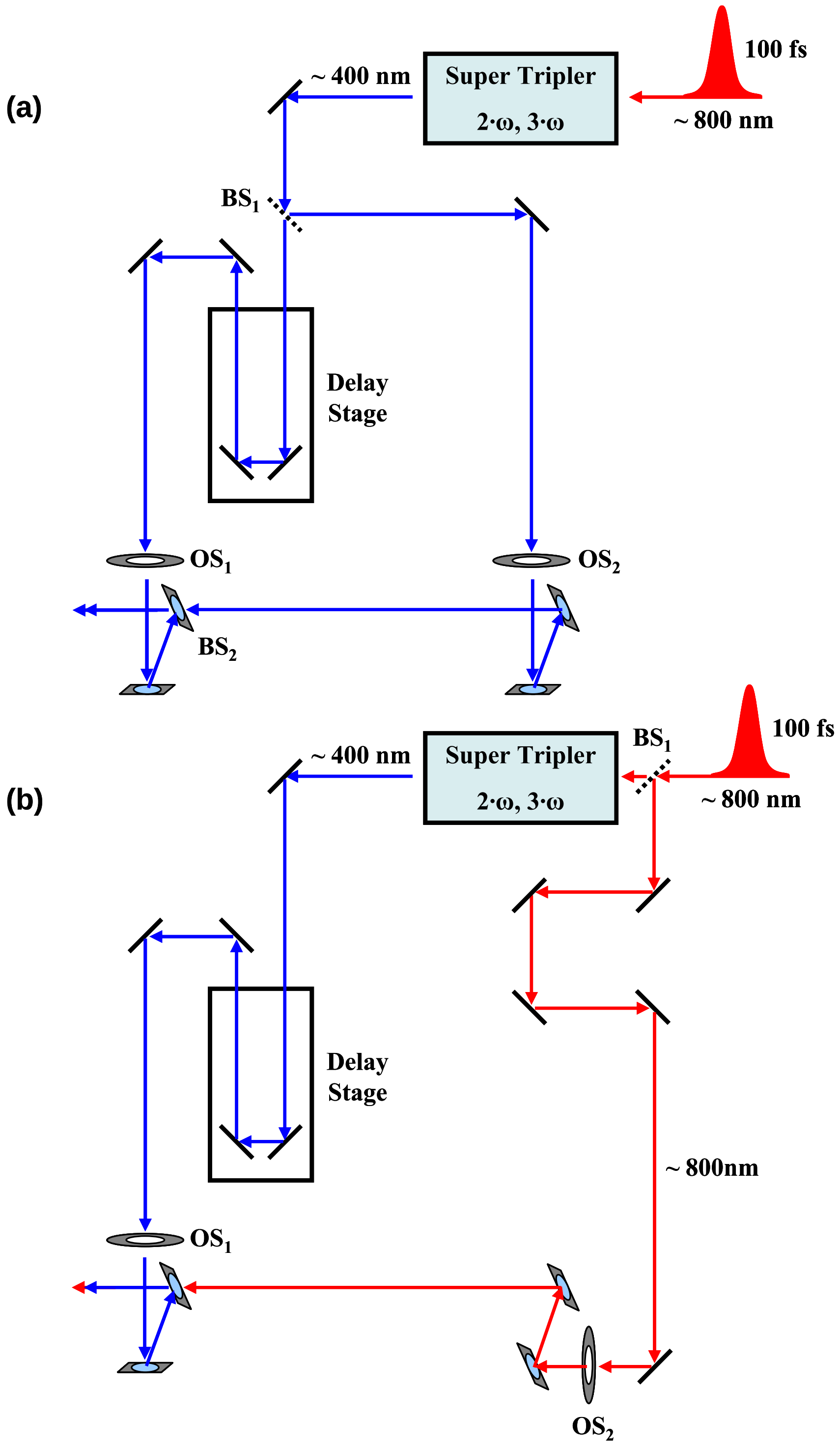

Figure 2.3 Pump-probe optical line arrangement for (a) single-color 400 + 400 nm and (b) two-color 800 + 400 nm time-resolved experiments. In figure, BS is a 50% beam splitter, and OS stands for optical shutter.

In the two-color experiment, only half of the fundamental output is used to generate a second harmonic. The remaining 800 nm light goes through the optical line of a fixed path length, while the frequency doubled, 400 nm, radiation is directed through the delay stage. The two beams are merged into a single beam using a dichroic mirror. The position of zero delay and the cross-correlation (~ 300 fs) are determined by passing combined beams through the BBO crystal and monitoring the sum-frequency signal. Unlike in the single-color experiment, the determined zero-delay has to be corrected for the dispersion-induced pump-probe delay due to the laser beams of different frequency passing through the entrance window in the detection region. This additional delay of 650 fs (the 800 nm pulse comes first) is estimated as an average of the zero-delay positions measured before and after a pair of fused silica windows in the detection region.

Time-resolved data acquisition procedure described below is the same for both single- and two-color experiments. Computer-controlled optical shutters (Uniblitz, Vincent Associates, Inc.) are placed in the path of each separated laser beam. A photoelectron image obtained with both shutters opened contains not only pump-probe signal but also the signals coming from individual pump and probe laser beams. The pump-only and probe-only images are collected with one corresponding shutter opened and the other closed. After the pump-only and probe-only signals are subtracted away from pump + probe image, it is necessary to add a background image, collected with both shutters closed, to compensate for the initial double background subtraction. Thus a single data acquisition cycle equation is “pump-probe” = “pump + probe” – “pump-only” – “probe-only” + “extra background”. Each image in this cycle is accumulated for 10 seconds. A typical pump-probe image is a collection of 60 acquisition cycles, which totals to 42,000 experimental cycles. The final image for each time delay is obtained by combining several of such 10 min pump-probe images, representing the result of ~ 5×10^6 experimental cycles.

2.8 Analysis of Photoelectron Images

In general, a photoelectron image represents a two-dimensional (2-D) projection of the original three-dimensional (3-D) probability density distribution of the photodetached electron. Due to cylindrical symmetry imposed by the linear laser polarization (parallel to the imaging detector surface), the nascent 3-D distribution can be uniquely reconstructed via inverse Abel transformation.[32] All images in this dissertation are analyzed using the BAsis Set EXpansion (BASEX) program developed in Hanna Reisler group by Dribinski and co-workers.[54] The program fits a raw 2-D image using a basis set of analytical Abel-transformed functions and then reconstructs the original 3-D distribution from the expansion coefficients.

The radial distribution is obtained from the Abel inverted image, a slice along the laser polarization axis through the center of reconstructed 3-D sphere, by integrating signal intensity over the polar angle θ at each r. The distance from the center of Abel-inverted image is directly proportional to the velocity of photoelectrons, $v \propto r$, and therefore $eKE \propto r^2$, where eKE is the electron kinetic energy. The energy spectra $P(eKE)$ is calculated from the radial distribution $P(r)$ using

$$eKE = eKE_{calibr}\frac{V}{V_{calibr}}\left(\frac{r}{r_{calibr}}\right)^2 \tag{2.13}$$

$$P(eKE) = P(r)\frac{dr}{d(eKE)} \propto P(r)\frac{1}{\sqrt{eKE}} \tag{2.14}$$

In Equation 2.13, eKE_{calibr}, r_{calibr}, V_{calibr} are the calibration values of the electron kinetic energy, the radial maximum of the corresponding peak in the spectra, and the focusing potential on the upper VMI plate. The calibration is done by recording the photoelectron spectra of the anion with well-known electron affinity (EA), e.g. I^-, O^-, NO^-, and calculating the eKE_{calibr} using the energy conservation law:

$$eKE = hv - EA \tag{2.15}$$

where hv is the photon energy. The Equation 2.14 transforms the spectra from the coordinate to the energy space by multiplying the photoelectron signal intensities with $\frac{dr}{d(eKE)}$ Jacobean.

In addition to the photoelectron spectrum, a photoelectron image provides another important quantity – the photoelectron angular distribution (PAD), which contains the information about the symmetry properties of the parent anion electron orbitals. The PAD is computed by integrating the reconstructed image intensities over the radial range for each value of the polar angle θ measured with respect to the laser polarization axis. The integration limits are typically set to the FWHM of the selected peak in the photoelectron spectrum. Within the electric dipole approximation, the general PAD expression for the photodetachment from anions with linearly polarized light is given by [36,55,56]

$$\frac{d\sigma}{d\Omega}=\frac{\sigma}{4\pi}\sum_{n=0}^{2N}\beta_n P_n\left(\cos(\theta)\right) \qquad (2.16)$$

where $\frac{d\sigma}{d\Omega}$ and σ are the differential and total photodetachment cross-sections, β_n are the anisotropy parameters, and P_n are the nth-degree Legendre polynomials. The polar angle θ defines the electron emission direction with respect to the laboratory-frame laser polarization axis. In Equation 2.16, the summation includes only $\beta_n P_n$ terms of even degrees, i.e. $n = 0, 2, 4, .., 2 \cdot N$, where N is the number of photons involved in the detachment process. The anisotropy parameters are obtained by fitting Equation 2.16 to the experimental PADs.

The relation between the anisotropy parameters and the character of the PADs is particularly straightforward for a single photon detachment data. In this case, the expression for the differential cross-section simplifies to

$$\frac{d\sigma}{d\Omega}=\frac{\sigma}{4\pi}\left[1+\beta_2 P_2\left(\cos(\theta)\right)\right]=\frac{\sigma}{4\pi}\left[1+\frac{\beta_2}{2}\left(3\cos^2(\theta)-1\right)\right] \qquad (2.17)$$

and the only remaining anisotropy parameter ($-1 \leq \beta_2 \leq 2$) becomes correspondingly negative, positive, and zero for the perpendicular $\frac{d\sigma}{d\Omega}\propto\sin^2(\theta)$, parallel $\frac{d\sigma}{d\Omega}\propto\cos^2(\theta)$, and isotropic $\frac{d\sigma}{d\Omega}=const$ angular distributions.

As an illustrative example, Figure 2.4 shows the photoelectron imaging of the halogen atomic anions I^-, Br^-, and Cl^- at 266 nm. For all of the chosen negative ions, the photoelectron images exhibit two transition rings corresponding to the detachment from

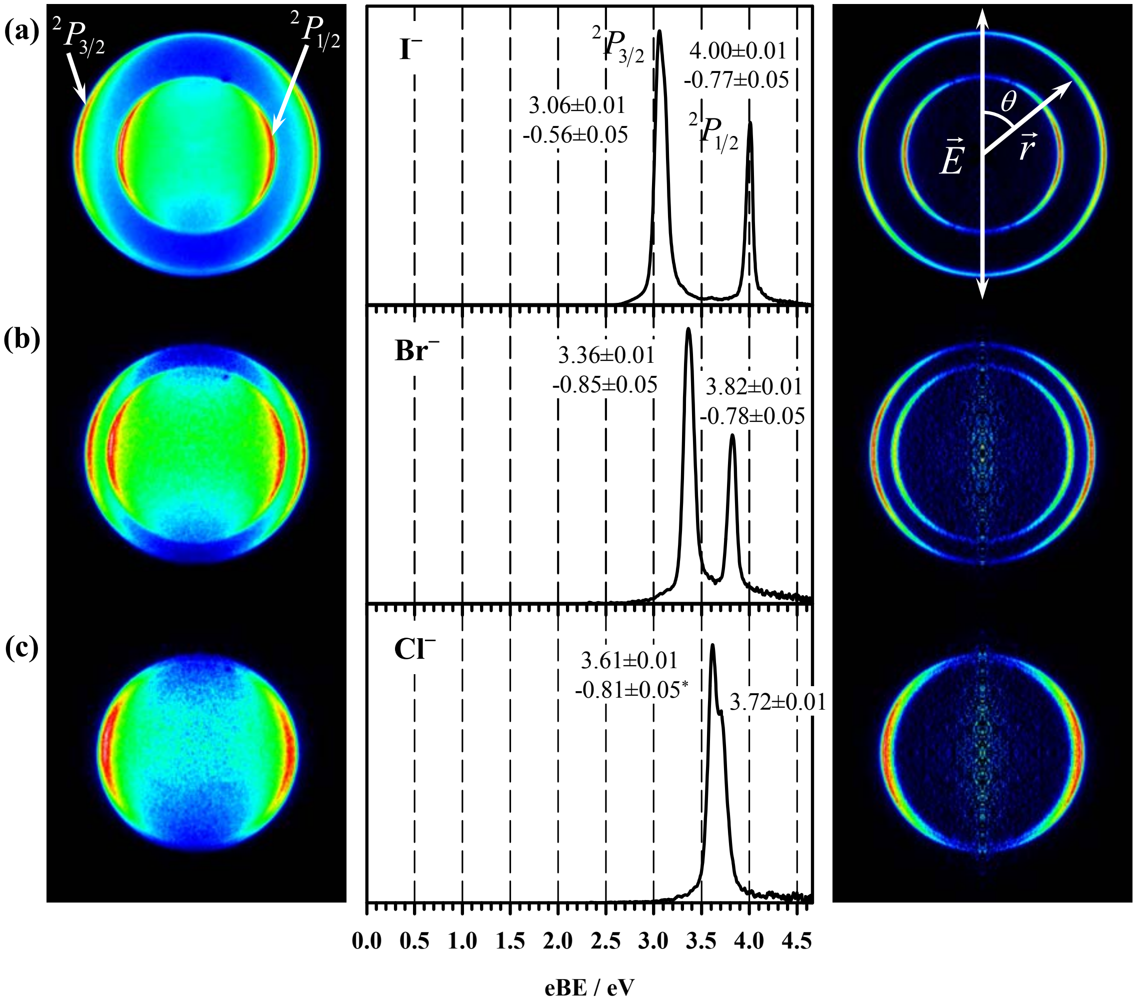

Figure 2.4 Raw (left) and Abel-inverted (right) photoelectron images with the corresponding photoelectron spectra (middle) of the (a) I⁻, (b) Br⁻, and (c) Cl⁻ halogen anions at 266 nm. The laser polarization axis, indicated by a double sided arrow, is vertical in the image plane. For all of the species the outer and inner rings are due to $^2P_{3/2} \leftarrow {}^1S_0$ and $^2P_{1/2} \leftarrow {}^1S_0$ transitions respectively. The vertical detachment energies along with the anisotropy parameters are indicated next to the corresponding spectral features.

[*] The anisotropy parameter is calculated over both $^2P_{3/2}$ and $^2P_{1/2}$ bands because of their significant overlap.

the $^1S_0$ ground state of the anion to the ground $^2P_{3/2}$ (the outer ring) and the excited $^2P_{1/2}$ (the inner ring) spin-orbit states of the neutral. For the direct comparison between the photoelectron spectra of different anions, the spectral intensities are plotted versus the electron binding (eBE) energies calculated by subtracting the electron kinetic energy from the 4.66 eV photon energy. The vertical detachment energies (the eBEs of the spectral peak maxima) and the anisotropy parameters for the observed transitions are indicated next to their photoelectron bands in the spectra. The experimental data clearly show the well-known trend for the Halogens Cl, Br, and I: the electron affinity decreases 3.61 eV,[57-60] 3.36 eV,[57,61] and 3.06 eV [57,62-64] whereas the spin-orbit interaction increases 0.11 eV,[65] 0.46 eV,[65] and 0.94 eV [66] as the atoms get heavier down the group in the Periodic Table.

Both $^2P_{3/2}$ and $^2P_{1/2}$ photodetachment bands from all of the studied halogen anions exhibit angular distributions peaking perpendicular to the laser polarization. It must be emphasized here that from the classical perspectives the photoelectrons should always be emitted in the direction of the oscillating electric field, and therefore the observed perpendicular nature of the angular distributions is purely a quantum mechanical effect. According to the quantum mechanics, the character of the PADs is controlled by the symmetry of the parent anion orbital and the amount of eKE afforded by the photoelectron. The angular momentum conservation law for one-photon, one-electron detachment from atomic anions dictates that $\ell_f = \ell_i \pm 1$, where ℓ_i and ℓ_f are the initial and final orbital angular momentum quantum numbers for the ejected electron. In the case of halogen anions, removing the excess electron from the outer shell p-orbital ($\ell = 1$) results in the *s* ($\ell = 0$) and *d* ($\ell = 2$) outgoing partial photoelectron waves. The interference between these partial waves is the major key for understanding the PADs. The angular distributions can be modeled quantitatively based on the Bethe-Cooper-Zare (BCZ) equation [35,36,67,68]

$$\beta_2 = \frac{\ell(\ell-1)\sigma_{\ell-1}^2 + (\ell+1)(\ell+2)\sigma_{\ell+1}^2 - 6\ell(\ell+1)\sigma_{\ell+1}\sigma_{\ell-1}\cos(\delta_{\ell+1} - \delta_{\ell-1})}{(2\ell+1)\left[\ell\sigma_{\ell-1}^2 + (\ell+1)\sigma_{\ell+1}^2\right]} \tag{2.18}$$

where the δ_ℓ is the phase shift of the ℓth partial wave and $\sigma_{\ell\pm1} = \int_0^\infty R_{nl} r R_{kl\pm1} dr$ is the dipole radial matrix element. The important outcome of Equation 2.18 is that the perpendicular PADs, $\beta_2 < 0$, are only possible due to the partial-wave interference term. The energy dependence of the anisotropy parameter is given by the Wigner threshold law[69]

$$\sigma_\ell \propto eKE^{\ell+\frac{1}{2}} \tag{2.19}$$

predicting that the in the limit of small eKEs, the PAD is determined by the partial wave with the lowest angular momentum. Assuming $\frac{\sigma_{\ell+1}}{\sigma_\ell} = A_{\ell+1} \cdot eKE$, the BCZ equation for the photoelectrons originating from a *p*-shell of atomic anions becomes

$$\beta_2 = \frac{2A_2 eKE(A_2 eKE - 2C)}{1 + 2A_2^2 eKE^2} \tag{2.20}$$

where $A_{\ell+1}$ is a proportionality constant related to the size of negative ion[70] and $C = \cos(\delta_2 - \delta_0)$. Figure 2.5 demonstrates the anisotropy parameter dependence on the

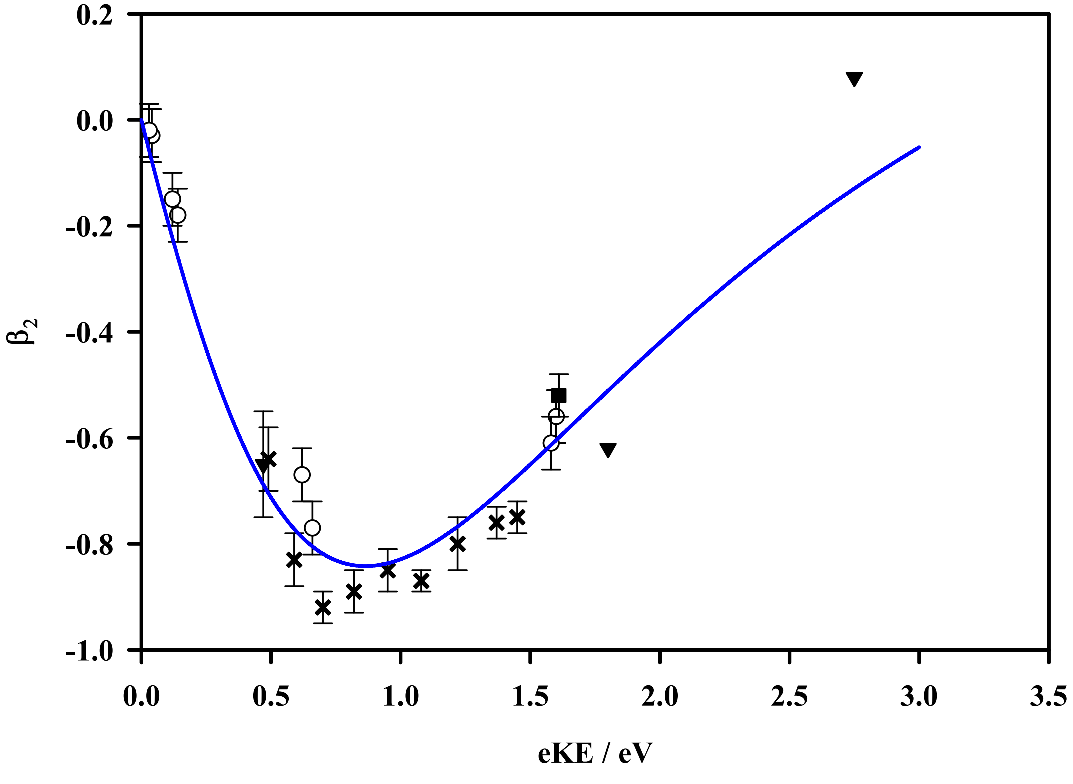

Figure 2.5 Kinetic energy dependence of the anisotropy parameter β_2 for I^-. The open circles represent experimental data obtained in our laboratory. The solid squares, solid triangles, and crosses correspond to the data taken from the work of Neumark,[71] Lineberger,[72] and Mabbs[73] respectively. The solid curve is the Bethe-Cooper-Zare fit (A_2 = 0.55, C = 0.88) to the experimental data.

photoelectron kinetic energy for I^-. At the threshold energies, eKE → 0 eV, the angular distribution is nearly isotropic, $\beta_2 \approx 0$, due to the predominant contribution of the *s*-wave to the photodetachment cross-section. As the kinetic energy increases, the interference between *s* and *d* partial waves drives the anisotropy towards perpendicular PADs ($\beta_2 < 0$). After reaching its minimum at about 0.6 eV the anisotropy trend reverses and β_2 becomes increasingly more positive as the contribution from the *d*-wave dominates at higher eKE. Overall, there is a good agreement between the measured anisotropy parameters for I^- and the BCZ model.

Modeling PADs for the photodetachment from molecular anions is a lot more complex than for atomic anions. For the polyatomic systems the angular momentum is no longer a "good" quantum number and the selection rule $\Delta\ell \pm 1$ does not hold. As a result, the BCZ model in general is not applicable for the molecular anions except in the special cases when the molecular orbital (MO) can be approximated by an atomic orbital (AO) e.g. O_2^-,[74-77] S_2^-,[37] SO^-,[46] NO^-.[44] The accurate evaluation of PADs from the first principles is laborious and requires the calculation of orientation-averaged transition dipole moment matrix elements.[38] Recently, an ab-initio program package[39] has been written for the calculation of total and differential photodetachment cross-sections for negative ions based on the equation-of-motion coupled-cluster theory. The software is currently under development and has been used so far to study the PAD energy dependence for small, di- and triatomic, molecular anions.

Despite the theoretical difficulties, it is possible to learn about the nature of PADs using simpler symmetry-based approaches. One such approach (the *s&p* model)[30,37] is based on the following approximations:

1) The expansion of the outgoing photoelectron wave function is restricted to *s* and *p* partial waves only: $\Psi_f \approx s + p_x + p_y + p_z$.

2) The orientation averaging is accounted for by considering only three "principal" orientations of the anion, with a chosen molecule-fixed axis aligned along the *x*, *y*, and *z* laboratory-frame axes.

3) The allowed characters of emitted partial waves (s, p_x, p_y, p_z) are determined by inspecting the corresponding transition dipole moment matrix element for each of the principal orientations. Owing to the qualitative nature of the model, it is only necessary to identify the non-zero matrix elements. This is easily done using group theory, i.e., requiring that the direct product of the irreducible representations of the parent molecular orbital Ψ_{MO}, the dipole moment operator $\vec{\mu}$, and the outgoing photoelectron wave Ψ_f must contain the totally symmetric irreducible representation Γ_{TS} of the anion point group

$$\Gamma\left(\Psi_f\right)\otimes\Gamma\left(\vec{\mu}\right)\otimes\Gamma\left(\Psi_{MO}\right)\supseteq\Gamma_{TS} \qquad (2.21)$$

The example of the *s&p* analysis for the photoelectron imaging of nitrogen dioxide molecular anion is given below.

The NO_2^- anion has been extensively studied in the past both theoretically[78-82] and experimentally.[83-88] The ground electronic state $X\,^1A_1$ of NO_2^- was found to have a bent equilibrium structure (C_{2v} point group) with $r(\mathrm{NO}) = 1.25 \pm 0.02$ Å and $\angle\mathrm{ONO} = 117.5 \pm 2°$.[85] The 266nm photoelectron spectra, as well as the raw and Abel-inverted photoelectron images, of NO_2^- are shown in Figure 2.6 (a). The experimental data reveal two full photoelectron bands and the beginning of a third band corresponding to the detachment from the ground electronic state of the anion to the X $^2A_1$, A $^2B_2$, and C $^2A_2$ states of the neutral.[86,88] The second excited state B $^2B_1$ of NO_2 is located above C $^2A_2$ at the anion equilibrium geometry and therefore is not accessible with 266nm photon energy.[86] In contrast to the sharp and narrow transition from atomic anions (Figure 2.4), the molecular anion photodetachment bands are typically much broader due to the additional internal degrees of freedom. The A $^2B_2$ band exhibits partially resolved vibrational structure with about 750 cm^{-1} peak spacing due to the ONO bending motion.[86,89] In photoelectron imaging the absolute energy resolution decreases with the electron eKE and therefore the vibrational structure is smeared out for the X $^2A_1$ transition.

Using the C_{2v} group character table and the dipole moment selection rules (Equation 2.21), the photodetachment form a_1 HOMO of NO_2^- is predicted to produce a free-electron wave composed of the p_x ($\vec{E} \parallel \vec{X}_{MF}$), p_y ($\vec{E} \parallel \vec{Y}_{MF}$), s and p_z ($\vec{E} \parallel \vec{Z}_{MF}$) partial waves. The s wave is isotropic and all three p waves are aligned along the laser polarization axis. Thus, the parallel PAD ($\beta_2 > 0$) is anticipated for the X $^2A_1 \leftarrow$X $^1A_1$ transition. For the detachment from b_2 (HOMO-1) and a_2 (HOMO-2) orbitals, the s&p model predicts an isotropic *s* wave (only for the b_2 orbital) and two *p* waves

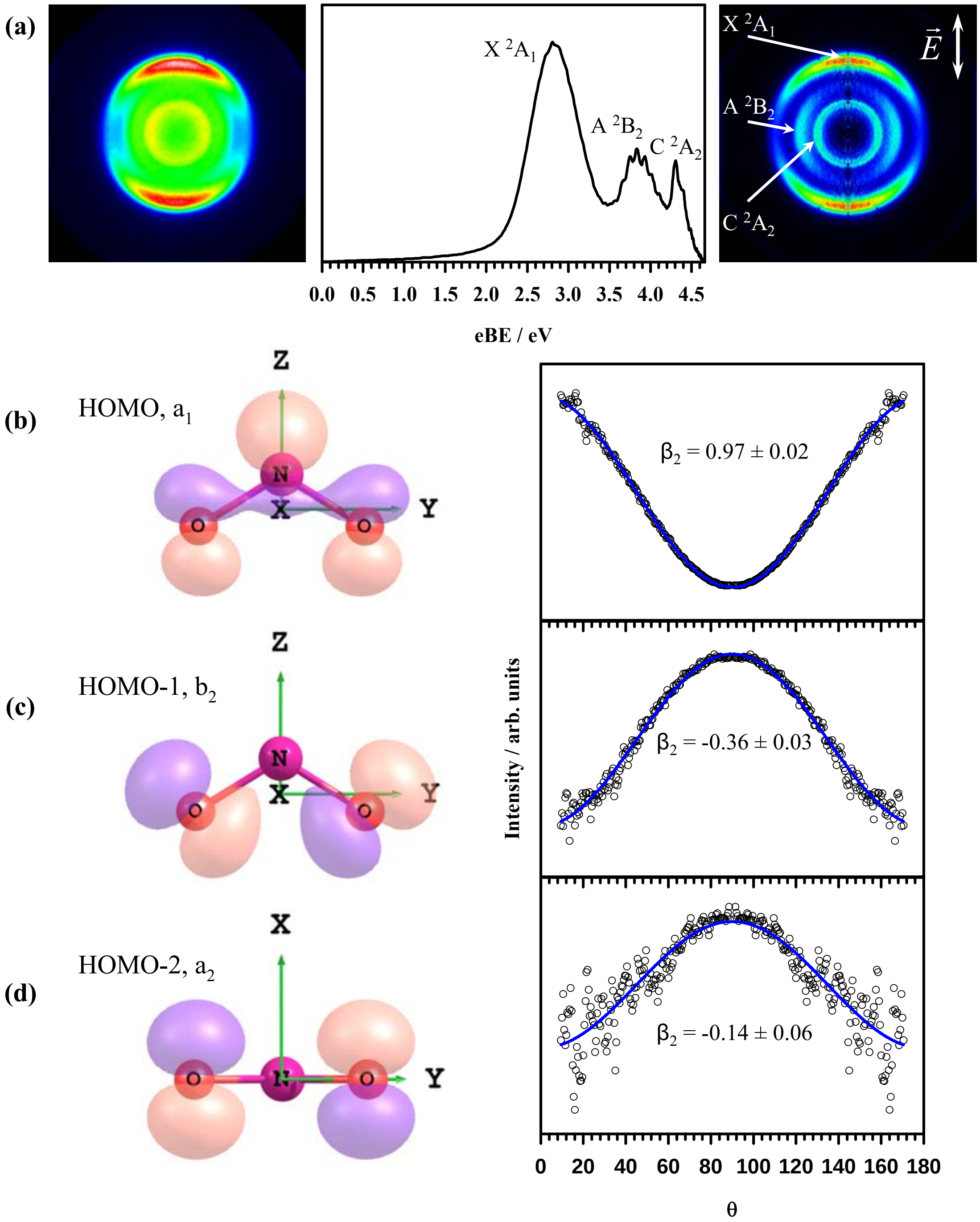

Figure 2.6 Photoelectron imaging of NO_2^- at 266nm. (a) raw image (left), photoelectron spectra (middle) and the Abel-inverted image (right) of the anion. The PADs corresponding to the detachment from a_1, b_2, and a_2 molecular orbitals are shown in the (b), (c), and (d) panels respectively.

perpendicular to the laser polarization direction. A negative value of the β_2 is therefore expected for the A $^2B_2$ and C $^2A_2$ transitions.

The above predictions for the X $^2A_1$ ($\beta_2 > 0$), A $^2B_2$ ($\beta_2 < 0$) and C $^2A_2$ ($\beta_2 < 0$) photodetachment transitions of NO_2^- are in excellent agreement with the experimentally measured anisotropy distributions shown in Figure 2.6 (b)-(d). The qualitative interpretation of anion photoelectron images based on the s&p model will be extensively utilized in the subsequent chapters to determine the symmetries of the observed electronic states.

CHAPTER 3

LOW-LYING ELECTRONIC STATES OF CH_3NO_2 VIA PHOTOELECTRON IMAGING OF NITROMETHANE ANION

3.1 Introduction

Nitromethane, CH_3NO_2, is the simplest nitro-substituted organic compound. It serves not only as a solvent, but synthetic reagent and explosive. The nitromethane molecule has a large dipole moment, 3.46 Debye, [90]which is sufficient for formation of dipole bound anions.[91] This property makes nitromethane attractive for studying gas-phase electron attachment,[92-97] although experimental observation of the dipole bound state has, until recently,[98] remained elusive despite indirect evidence from earlier Rydberg electron transfer experiments.[93] A number of studies have attempted to elucidate the mechanism of electron transfer using free electrons,[99] alkali metal atoms,[92,94-96] or high Rydberg atoms.[93] These studies have shown that nitromethane and nitromethane anion have a number of low-lying electronic states. These states have also been observed by optical absorption and photodissociation,[97,100-102] as well as electron scattering.[92,97,103] However, the assignment of many states has remained ambiguous and discrepancies with theory remain. In this Chapter, we examine and assign several excited states of nitromethane using photoelectron imaging of the nitromethane anion.

Neutral nitromethane has a nearly planar C-NO_2 atomic arrangement. Its lowestunoccupied molecular orbital (LUMO) is a π* orbital localized primarily on the NO_2 group. It has been suggested that the LUMO acts as a gateway to the valence bound anion state.[93,104] Theory has shown that pyramidalization at the N atom lowers the energy of the π*-type orbital allowing electron attachment.[95] Accordingly, experiment shows that nitromethane anion is nonplanar[105] and both theory and experiment are in agreement that the excess electron in $CH_3NO_2^-$ occupies the π* orbital on the nitro group.[94]

While much of the experimental knowledge of nitromethane anion comes from electron transfer experiments, several spectroscopic studies have also been carried out.[93,97,98,105] Early negative-ion photoelectron spectra of the anion showed a broad band at low electron binding energies.[93] The threshold for photodetachment was assigned to the first peak in the photoelectron band at 0.26 ± 0.08 eV. This work was later followed by infrared spectroscopy studies which demonstrated that vibrational excitation of the CH stretches of $CH_3NO_2^-$ resulted in autodetachment.[105,106] More recently, this method has been enhanced by combining infrared excitation with photoelectron imaging detection of the slow electrons from autodetachment.[98] By utilizing high level *ab initio* calculations and a Franck-Condon simulation to fit the experimental spectrum, the adiabatic electron affinity of CH_3NO_2 was reassigned as 0.172 ± 0.006 eV. The high resolution autodetachment spectrum also revealed a weak low energy feature which has been tentatively assigned to detachment of a dipole-bound electron.[98]

Concerning the excited states of nitromethane, electron energy loss measurements reported a low-energy triplet at around 3.8 eV,[103] while an excited singlet state was reported near 4.3 eV.[107,108] Optical absorption spectroscopy shows an intense band centered at 6.25 eV, with a weaker feature at 4.5 eV, both transitions are assigned to excited singlet states.[97] Photodissociation of nitromethane via optical excitation to excited singlet states has been studied for decades, and yet a complete understanding of the dissociation mechanism and the electronic states involved has not been reached.[100-102]

Due to the interesting photochemistry and electron capture dynamics of nitromethane, many theoretical studies on the neutral and radical anion have been carried out.[109-114] Several early theoretical investigations of the excited states of the neutral reported low energy triplet states, with slightly higher energy singlet states. The energies from these modest calculations are qualitative at best, and agreement with the electron transfer studies is mixed.[109-111] Modern *ab initio* methods have been used to study the excited states of nitromethane in relation to its photodissociation.[112-114] In particular, a recent study using the complete active space self-consistent-field procedure with second-order perturbation theory (CASPT2) and the ANO-L basis set identified a number of excited states of nitromethane at various geometries.[112] A summary of some of the previously assigned low-energy electronic states and their relative energies are listed in Table 3.1. The A′ and A″ state labeling in Table 3.1 and throughout this Chapter refers to reflection symmetry with respect to the HCN plane bisecting the ONO bond angle. The italicized state labels in Table 3.1 are intended to follow the usual spectroscopic convention, reflecting the corresponding state ordering at the geometry of neutral nitromethane. However, because of the spreads in the state energies derived from different experiments and theoretical predictions, the state label assignments in Table 3.1 are somewhat uncertain in some cases, particularly so for the $b^3\mathrm{A}''$ and $c^3\mathrm{A}'$ states.

Table 3.1 Energies of excited electronic states of nitromethane relative to the X^1A' ground state.

State[*]	Energy (eV)	Method	Ref
$a\,^3A''$	3.01	Theory[a]	109
	3.13	Theory[b]	110
	3.75	Theory[c]	112
	3.5	MB[d]	107
	3.8	EEL[e]	103
$b\,^3A''$	4.60	Theory[a]	109
	3.78	Theory[c]	112
$c\,^3A'$	3.71	Theory[a]	109
	4.11	Theory[c]	112
$A\,^1A''$	4.56	Theory[a]	109
	3.86	Theory[b]	110
	4.22	Theory[g]	111
	3.97	Theory[c]	112
	4.3	MB[d]	107
	4.3	EEL[e]	108
	4.25	EEL[f]	97
$B\,^1A'$	4.41	Theory[a]	109
	3.41	Theory[b]	110
	4.58	Theory[g]	111
	4.29	Theory[c]	112
	4.5	VUV[f]	97
	4.45	EEL[e]	103
$C\,^1A''$	5.8	Theory[a]	109
	6.43	Theory[b]	110
	6.63	Theory[g]	111
	6.15	Theory[c]	112
	6.25	VUV[f]	97
	6.23	EEL[e]	103
	6.1	EEL[e]	108
	6.23	EEL[e]	97
	6.5	MB[d]	107

[*] The italicized state labels used throughout this work are based on the energetic state ordering expected for the neutral ground-state geometry.
[a] Semiempirical Extended Hückel.
[b] CNDO/s-CI.
[c] CASPT2.
[d] Molecular beam collisions.
[e] Electron energy loss spectroscopy.
[f] Vacuum ultraviolet absorption spectroscopy.
[g] SCF-CI.

These states have been studied only theoretically and we chose the relative CASPT2 energies to determine their energetic order. It should also be emphasized that the state ordering at the anion geometry can be drastically different.

Several observations stemming from the wide range of entries in Table 3.1 are particularly worth noting. First, the excited singlet states have been most extensively studied, and agreement with theory and experiment is reasonable for most assignments. Second, there are few reported experimental observations of excited triplet states. Characterization of these states is important, as they have been proposed to play roles in the photodissociation of nitromethane,[112] but they cannot be detected by direct absorption spectroscopy because of the spin selection rule.

Negative-ion photoelectron spectroscopy has no such limitation. In this study, we use photoelectron imaging to examine $CH_3NO_2^-$ photodetachment at 532, 392, 355, and 266 nm. We find that at least three low lying excited electronic states of nitromethane are accessible with 266 nm photons. The symmetries of the observed excited states of nitromethane are assigned by analyzing the photoelectron angular distributions with the aid of theoretical calculations.

3.2 Experimental Arrangement

The experiment was carried out on a negative ion photoelectron imaging spectrometer described in Chapter 2. Nitromethane vapor in Ar carrier gas was introduced into a high vacuum chamber through a pulsed General Valve (Series 99) nozzle operating at a 50 Hz repetition rate and 30 psi backing pressure. The anions are formed by secondary-electron attachment following collisions with high-energy electrons (1 keV) from an electron gun. The resulting anions are mass-selected using the primary TOF spectrometer. In the velocity-map imaging region, the ion beam is intersected at a right angle with a pulsed linearly polarized laser beam timed to overlap only with the ions of interest. In this work, we use the frequency-doubled (532 nm), tripled (355 nm) or quadrupled (266 nm) output from a pulsed Nd:YAG laser (Spectra Physics, Inc., Lab-50 model with pulse energies 10, 3.5 and 0.07 mJ, respectively). The 392 nm radiation (0.2 mJ, 100 fs pulses) is generated as the second harmonic of an amplified Ti:Sapphire laser system (Spectra Physics, Inc.). The laser radiation is polarized linearly, parallel to the plane of the imaging detector. Photoelectrons are accelerated using an electrostatic lens and focused onto a position-sensitive microchannel plate detector fiber-optically coupled to a phosphor screen. Images are recorded from a phosphor screen using a charge-coupled device (CCD) camera (Roper Scientific Inc.). The reported images represent 10^4–10^5 experimental cycles each. The three-dimensional photoelectron velocity distributions are reconstructed form the images by the inverse Abel transformation using the BASEX program.[54]

3.3 Photoelectron Images and Spectra of Nitromethane Anion

The raw and Abel transformed photoelectron images obtained at 532, 392, 355 and 266 nm, as well as the corresponding photoelectron spectra, are shown in Figure 3.1. The images were recorded at different velocity-mapping potentials and their apparent sizes cannot be compared directly. For quantitative comparison, the spectra are plotted versus electron binding energy (eBE), calculated by subtracting the electron kinetic energy (eKE) from the photon energy.

All photoelectron images in Figure 3.1 show the outer band labeled with the Roman numeral I. The corresponding angular distributions peak in the direction parallel to the laser polarization axis (vertical in the figure plane). In the corresponding spectra, the broad and unstructured band I peaks at eBE = 0.96 eV, which is consistent with the previous determinations of the vertical detachment energy (VDE) of the lowest photodetachment transition in $CH_3NO_2^-$.[93,98]

The 392 nm photoelectron image shows the onset of another feature near the image center, band II, which is also seen at 355 and 266 nm. The 355 nm spectrum reveals partially resolved vibrational structure within band II. This structure is expanded in Figure 3.2, which shows a portion of the 355 nm spectrum corresponding to the spectral range of band II. The partially resolved peaks comprising band II are labeled with 0 – 6, in accordance with the corresponding vibrational quantum numbers, whose assignment is discussed in Section IV.D. We assign the band origin to the first peak rising above the noise level (peak 0), but stress that this assignment is not unambiguous, as is often the case for photodetachment transitions involving a significant geometry change. The assigned origin transition is centered at eBE = 3.07 eV, while the maximum of the overall band II is at 3.36 eV, as determined from the 266 nm spectrum in Figure 3.1. The vibrational structure of band II is washed out at 266 nm due to the decreasing absolute energy resolution afforded by photoelectron imaging at increasing eKEs.

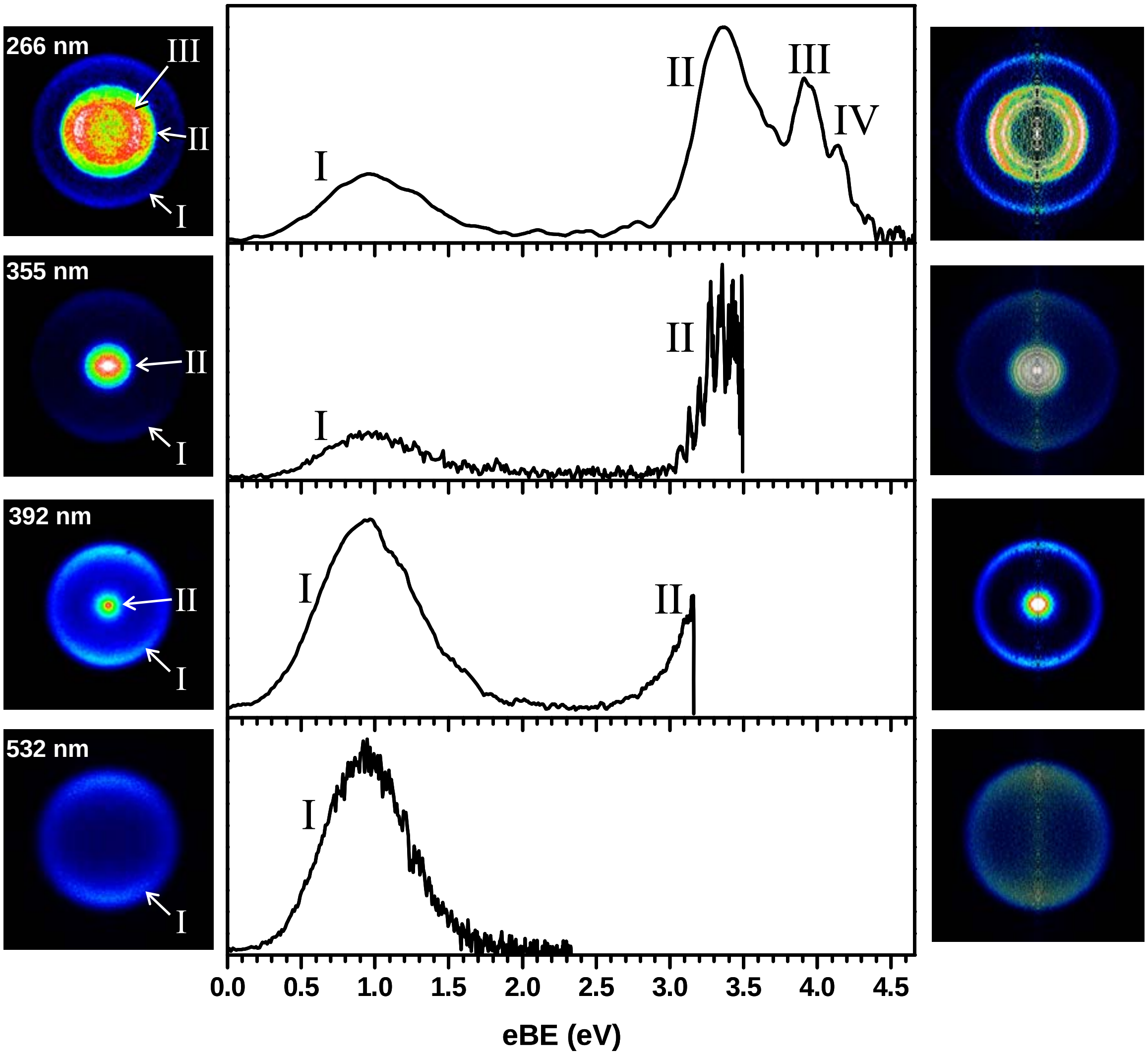

Figure 3.1 Raw (left) and Abel-inverted (right) photoelectron images of nitromethane anion at 266, 355, 392 and 532 nm, shown on varying velocity scales. The laser polarization axis is vertical in the plane of the figure. (Center) Photoelectron spectra obtained from the images.

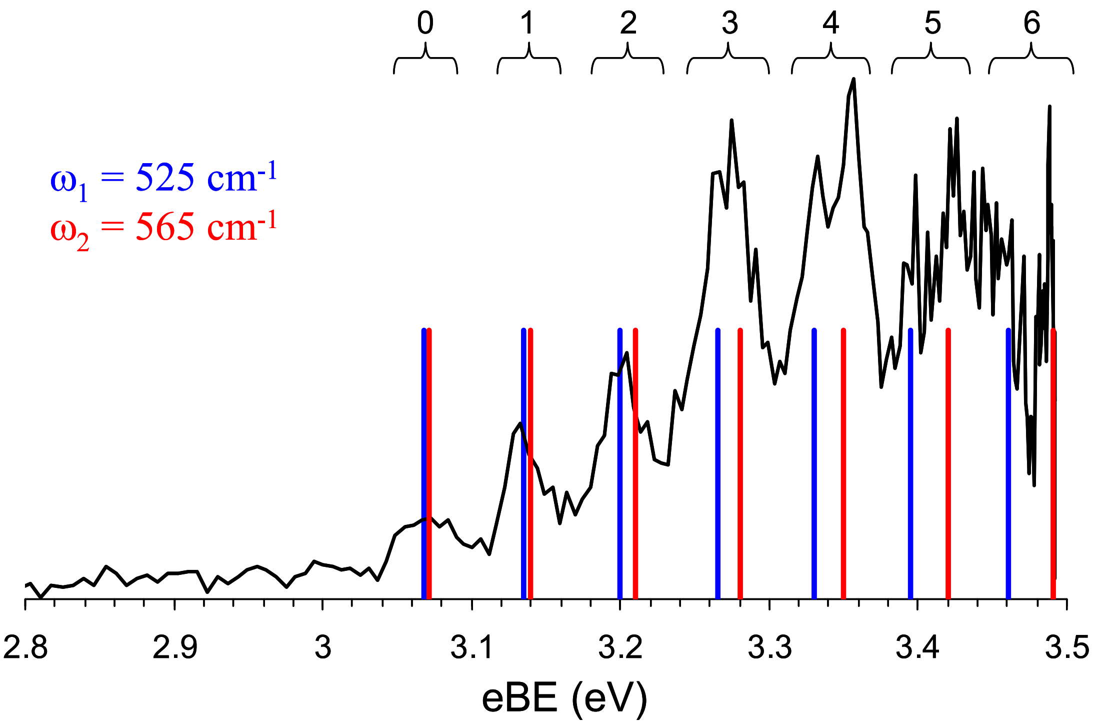

Figure 3.2 Band II in the 355 nm photoelectron spectrum of $CH_3NO_2^-$ from Figure 3.1, showing details of its vibrational structure and individual peak labels (0–6). Superimposed with the experimental spectrum are the stick spectra for two vibrational progressions with the common origin at eBE = 3.07 eV and frequencies ω_1 = 525 cm^{-1} and ω_2 = 565 cm^{-1} (no anharmonicity or combination bands are included).

Table 3.2 Nitromethane photoelectron features, binding energies and anisotropies (β) as measured at different photon energies.

Band[a]	Wavelength (nm)	Transition eBE or VDE (eV)[b]	β [c]	Neutral state assignment
I	532	0.95	0.56	X^1A'
	392	0.97	0.45	
	355	0.95	0.39	
	266	0.96	0.39	
II	355	3.36	-0.16	a^3A''
	266	3.36	-0.34	
II_0	355	3.07	-0.27	v = 0[e]
II_1	355	3.13	-0.28	v = 1
II_2	355	3.20	-0.25	v = 2
II_3	355	3.28	-0.22	v = 3
II_4	355	[d]	-0.19	v = 4
II_5	355	[d]	-0.11	v = 5
III	266	3.91	-0.21	b^3A''
IV	266	4.12	-0.16	$A\,^1A''$

Finally, the 266 nm image and spectrum in Figure 3.1 show the two abovementioned bands, I and II, plus two additional features, III and IV, peaking at eBE = 3.91 and 4.12 eV, respectively. Bands II, III, and IV exhibit angular distributions peaking in the direction perpendicular to the laser polarization axis, in contrast to band I. The photoelectron anisotropy parameters are listed in Table 3.2, along with the electron binding energies determined for the observed transitions at each wavelength. For 355 nm, the angular distributions for individual peaks $II_0 – II_5$ are reported along with the PAD for the entire band II.

3.4 Computational Results

To aid in the analysis of the experimental data, the structural features of the $CH_3NO_2^-$ anion and the CH_3NO_2 neutral molecule in the ground ($X\,^1A'$) and first excited ($a\,^3A''$) electronic states were examined using density functional theory (DFT) at the B3LYP/aug-cc-pVDZ level. All calculations were carried out using the Gaussian 03 program package.[115] For the ground state, the results of these calculations are in general agreement with the higher-level computations by Weber and co-workers.[98] The B3LYP results enable consistent comparison of different electronic states while being less demanding computationally.

The optimized structures with important geometrical parameters are shown in Figure 3.3. In the anion, the plane of the NO_2 group is angled relative to the CN bond, in contrast to the nearly planar C-NO_2 arrangement for the ground-state neutral. The calculated adiabatic electron affinity of CH_3NO_2 (including the zero-point vibrational energy

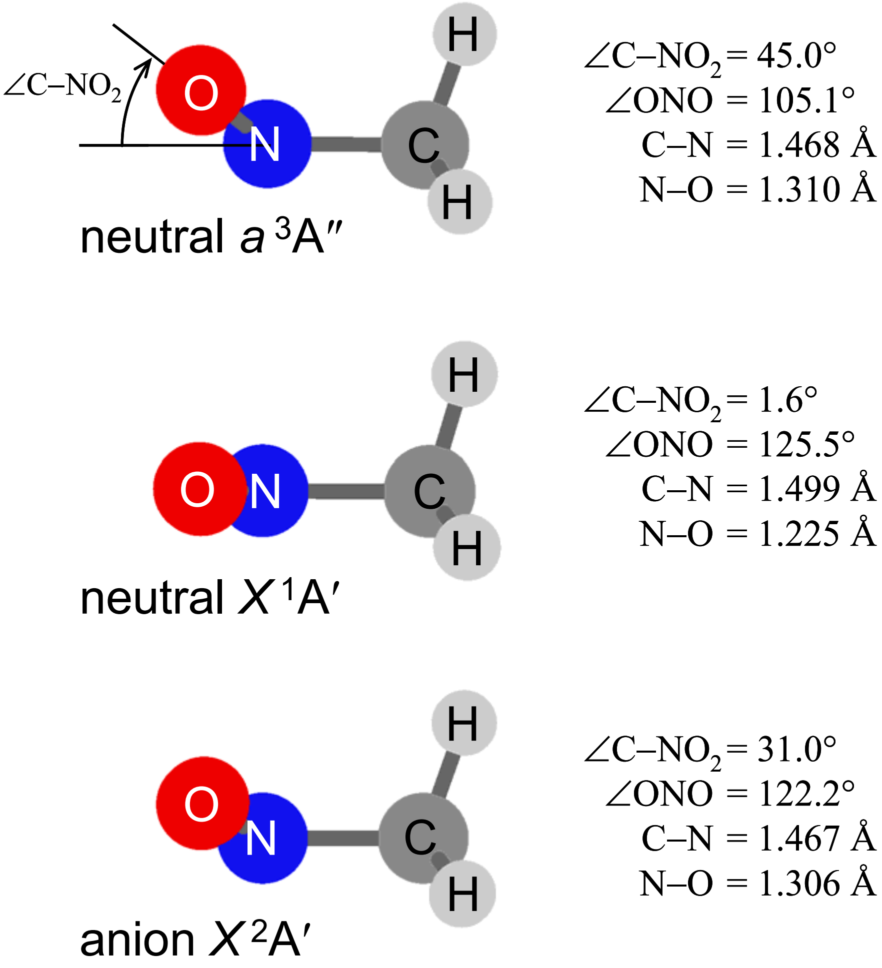

Figure 3.3 Equilibrium geometries of nitromethane anion, $CH_3NO_2^-$ ($^2A'$), the ground state of neutral CH_3NO_2 ($X\,^1A'$), and the lowest-energy excited state of CH_3NO_2 ($a\,^3A''$), optimized at the B3LYP/aug-cc-pVDZ level of theory.

correction) is 0.41 eV, compared to the experimentally determined value of 0.172 ± 0.006 eV.[98] The vertical detachment energy of $CH_3NO_2^-$ is 1.18 eV, compared to the ca. 0.95 eV experimental value determined here and elsewhere.[93] Thus, the B3LYP calculations tend to overestimate, within reasonable limits (< 0.25 eV), both the adiabatic and vertical detachment energies of the anion.

The calculated adiabatic electron binding energy of the lowest-energy triplet ($a\,^3A''$) nitromethane is 2.93 eV, while the anion VDE corresponding to the formation of the $a\,^3A''$ neutral state is 3.24 eV. These values are in good agreement with the experimental observations summarized in Table 3.2: II_0 = 3.07 eV and VDE(II) = 3.36 eV. The optimized geometry of $a\,^3A''$, is qualitatively similar to that of the anion (see Figure 3.3), but two geometric parameters do experience significant changes upon photodetachment. These are in the ONO bond angle and the NO_2 wag angle ($\angle C\text{-}NO_2$), which change by an estimated 17° and 14°, respectively, between the anion and a^3A'' neutral equilibria. Therefore, both the ONO bending and NO_2 wagging vibrational modes should be excited in the $X^2A' \rightarrow a\,^3A''$ photodetachment transition.

In the absence of previous spectroscopic determinations of these mode frequencies for the $a\,^3A''$ state of CH_3NO_2, the B3LYP/aug-cc-pVDZ calculations predict (unscaled) harmonic frequencies of 524 cm^{-1} for the ONO bend and 436 cm^{-1} for the NO_2 wag. Similar calculations with the 6-311++G(3df,3pd) basis set give slightly larger values of 547 and 467 cm^{-1}, respectively. For comparison, the B3LYP/aug-cc-pVDZ calculations for the X^1A' state predict 659 and 609 cm^{-1}, respectively, in very good agreement with experiment: the ONO bending frequency in the ground state of nitromethane has been determined to be 657 cm^{-1},[116] while the corresponding frequency for the NO_2 wagging motion is 603 cm^{-1} (according to Gorse et al.),[116] 613 ± 56 cm^{-1} (Weber and co-workers),[98] or 645 ± 70 cm^{-1} (Compton et al.).[93]

Figure 3.4 shows a qualitative orbital ordering and occupancy diagram for the ground ($X\,^2$A′) electronic state of nitromethane anion derived from the spin-unrestricted DFT calculations. The highest-occupied spin-orbital (α-HOMO) of the anion (11a′α) is of a′ symmetry, while the next three highest-energy spin-orbitals (6a″β, 6a″α, and 5a″β) are all a″. Also indicated in Figure 4 are the ground and first four excited electronic states of neutral nitromethane, resulting from electron removal from the specified anion spin-orbitals, discounting any geometry or electron relaxation. With a Koopmans' theorem[117] approach, Figure 3.4 suggest the following state ordering for neutral nitromethane *at the anion geometry*: $X\,^1$A′, $a\,^3$A″, $b\,^3$A″, $A\,^1$A″, $c\,^3$A′, … This order generally agrees with the summary in Table 3.1, with the exception of the relative placement of the *A* and *c* states. The discrepancy may stem from the geometry difference between the anion and neutral equilibria, as our calculations are for the anion geometry, while Table 3.1 lists state energies relative to the neutral ground state equilibrium.

3.5 Interpretation of the Photoelectron Angular Distributions

Photoelectron angular distributions are related to the symmetry of the parent orbital from which photoelectrons originate.[35-39] While the rigorous theoretical prediction of the photoelectron angular distributions is in general a complicated task,[38,39] a qualitative insight can be derived from a simpler symmetry-based approach (the *s&p* model)[30,37].

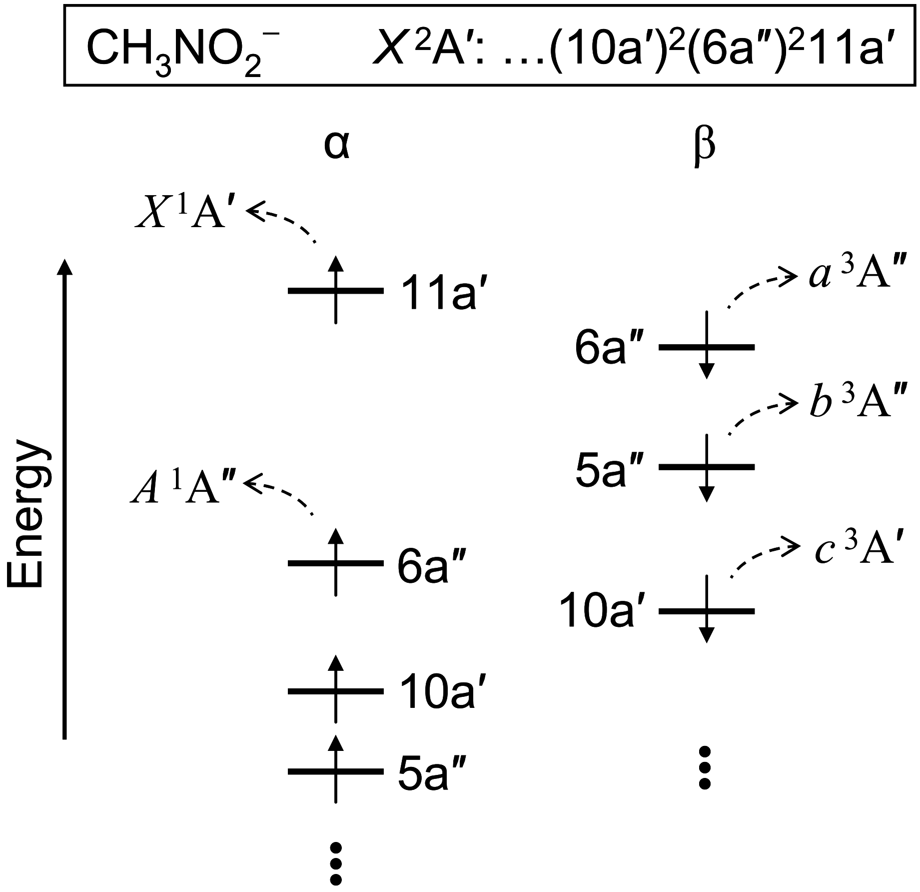

Figure 3.4 Electronic structure of $CH_3NO_2^-$ ($^2A'$) as predicted at the UB3LYP/aug-cc-pVDZ level of theory. The symmetries and energetic ordering of the unrestricted α and β spin-orbitals are shown, along with the electronic states of the neutral resulting from removal of the specified electrons (disregarding any relaxation effects).

An overview of the s&p analysis for the nitrogen dioxide molecular anion (C_{2v} point group) is given at the end of the Chapter 2.

Given the low symmetry of nitromethane anion (C_s point group), the details of the symmetry analysis are particularly straightforward. Predominantly parallel ($\beta > 0$) angular distributions are generally expected in detachment from a′ orbitals, as a partial case of detachment from totally symmetric molecular orbitals[43] (e.g. the detachment from a_1 orbital of NO_2^-). Specifically, if restricted to *s* and *p* waves only, the free-electron wavefunction resulting from detachment from an a′ orbital may consist of *s* waves and two types of *p* waves: one parallel and one perpendicular to the laser polarization direction. Although the exact PAD depends on the matrix-element integrals, such partial-wave combination will tend to yield a predominantly parallel PAD. (All three types of *p*-waves, p_x, p_y, and p_z, are needed for an isotropic angular distribution. Removal of one perpendicular *p*-wave will bias the distribution along the polarization axis.) Similarly, in detachment from an a″ orbital, only the *p* waves perpendicular to the laser polarization direction are allowed, in addition to *s* waves, yielding a predominantly perpendicular ($\beta < 0$) angular distribution.

These predictions, in conjunction with the experimental photoelectron anisotropy parameters in Table 2, aid in assignment of the peaks in the photoelectron spectra. Band I in Figure 1, which exhibits a parallel PAD, is attributed to detachment from an a′ orbital. This assignment is consistent with the predicted symmetry of the anion HOMO (11a′α) (see Figure 4) and hence this band corresponds to the X^1A' state of the neutral. The next three bands in the photoelectron spectra (II–IV) all correspond to $\beta < 0$ and should therefore be assigned to detachment from a″ orbitals. This conclusion agrees with the symmetries of the next three energetically lower $CH_3NO_2^-$ spin-orbitals: 6a″β, 6a″α, and 5a″β (see Figure 4). The next two lower-energy spin-orbitals are of the a′ symmetry and one expects their detachment to yield parallel PADs. Since no additional features are observed in the photoelectron images, we conclude that these channels are not accessible with 266 nm and longer-wavelength photons.

3.6 Electronic States of Neutral Nitromethane at the Anion Geometry

While the assignment of band I to the ground state of nitromethane ($X\,^1$A′) is straightforward based on the previous studies of this system,[93,98] the remaining state assignments are made here for the first time. Assuming the electronic states of the neutral correlate with electron detachment from the corresponding orbitals, we assign band II to the $a\,^3$A″ state, band III to the $b\,^3$A″ state, and band IV to the $A\,^1$A″ state. These assignments are summarized in Table 3.2.

Comparing our assignments to the states in Table 3.1, we find agreement with the predicted state ordering, with the exception of the $c\,^3$A′ state, which is not assigned to any of the features in the present photoelectron images and spectra. Since the $c\,^3$A′ state would result from photodetachment from an a′ orbital, a parallel PAD is expected, but no such features are observed in the images and spectra at large eBEs. This is not surprising, considering that here we access the excited states via vertical transitions at the anion geometry, while the previous studies of nitromethane summarized in Table 3.1 were carried out relative to the neutral ground state. The large geometry difference between the anion X^2A′ and neutral X^1A′ states (see Figure 3.3) could result in a different state ordering and thus explain the absence of the $c\,^3$A′ state in the photoelectron spectra in Figure 3.1. We must, however, cautiously acknowledge that the high-energy features in the 266 nm spectrum in Figure 3.1 are broad and overlapping, so a low intensity feature attributable to the $c\,^3$A′ state might be obscured by the other bands.

3.7 The Singlet-Triplet Splitting in Neutral Nitromethane

The drastic geometry difference between the anion and neutral (see Figure 3.3) results in the extended vibrational progression in the lowest-energy photodetachment transition for $CH_3NO_2^-$.[93,98] (This progression, corresponding to band I in Figure 3.1, is not resolved in the present work.) While the uncertainty in assignment of this band's origin makes the determination of adiabatic electron affinity of CH_3NO_2 difficult, Weber and co-workers recently reported its very precise measurement, EA = 0.172 ± 0.006 eV.[98]

The equilibrium geometry difference between the anion and the lowest-energy triplet state of CH_3NO_2 (the $a\,^3$A″ state) is less pronounced, but the assignment of the corresponding band origin is still not quite straightforward. We assign II_0 (peak 0 in Figure 3.2) as the transition origin, with the corresponding eBE of 3.07 ± 0.01 eV. However, for the singlet-triplet energy splitting calculation, we must account for the possibility that the real 0-0 transition might correspond to the weak, not rising above the noise level, feature at 3.00 eV. Thus, we expand the uncertainty range for the origin transition on the lower-energy side to encompass this ambiguous feature and take the adiabatic electron binding energy of triplet nitromethane to be $3.07\ ^{+0.01}/_{-0.07}$ eV. From this result and the above experimentally determined value of electron affinity of singlet CH_3NO_2, the singlet-triplet splitting in nitromethane is calculated as $2.90\ ^{+0.02}/_{-0.07}$ eV.

3.8 Vibrational Progression in Lowest-Triplet Nitromethane

The 355 nm spectrum in Figure 3.1 shows partially resolved vibrational structure for band II, corresponding to the $X^2\mathrm{A}' \rightarrow a^3\mathrm{A}''$ photodetachment transition. Examining the expanded spectrum of this band in Figure 3.2, we note that at its low-energy onset the observed structure can be described as an evenly spaced progression of peaks (0–3) with an average spacing of ca. 560 cm^{-1}. The higher energy peaks (4-6) appear to broaden and split, suggesting additional underlying structure due to more than one vibrational mode excited in the photodetachment.

As seen in Figure 3.2, the main geometry differences between the anion and the lowest triplet state of CH_3NO_2 are in the ONO bond angle ($\angle$ONO) and the NO_2 wag angle ($\angle$C-NO_2). Vibrations with respect to both of these angles should be excited in photodetachment and considering the magnitudes of the predicted changes (17° and 14°, respectively), one expects both modes to participate to roughly similar extents. This expectation is amplified considering that the predicted frequencies of the ONO bending and NO_2 wagging motions (see Section 3.4), while not degenerate, are both consistent with the observed spacing between the peaks in the photoelectron spectrum. Therefore, accounting for the experimental broadening, the vibrational progressions in both modes will overlap for small numbers of excitation quanta, eventually broadening and splitting the observed peaks as the excitation increases.

To show that the above explanation is consistent with the experiment, Figure 3.2 includes stick spectra for two vibrational progressions with the common origin at eBE = 3.07 eV and frequencies ω_1 = 525 cm^{-1} and ω_2 = 565 cm^{-1} (no anharmonicity or combination bands are included). As the quantum numbers increase, the lines corresponding to the two progressions appear close together initially, but eventually become more separated. (Anharmonicity and combination bands may contribute additional spectral structure). Although the model frequencies ω_1 = 525 cm^{-1} and ω_2 = 565 cm^{-1} differ from the B3LYP predictions of 436 and 524 cm^{-1} (aug-cc-pVDZ basis) or 467 and 547 cm^{-1} [6-311++G(3df,3pd)], the discrepancy is not surprising considering the challenging nature of excited-state calculations. The model spectrum nonetheless captures all principal features of the experimentally observed structure. We therefore conclude that the spectral structure is indeed due to the contributions of at least two vibrational modes excited in the photodetachment, most likely the ONO bending and the NO_2 wagging vibrations.

3.9 Summary

Negative-ion photoelectron imaging at 532, 392, 355, and 266 nm is used to assign several low-lying electronic states of neutral nitromethane, CH_3NO_2, at the geometry corresponding to the anion equilibrium. The photoelectron angular distributions aid in assignment of the symmetries of the observed electronic states. Namely, opposite-sign photoelectron anisotropy parameters are determined for electron detachment from a′ and a″ molecular orbitals. Using a group theoretical approach, aided by the results of DFT calculations, the observed transitions are assigned (in the order of increasing binding energy) to the $X\,^1$A′, $a\,^3$A″, $b\,^3$A″, and $A\,^1$A″ electronic states of neutral nitromethane at the anion geometry. The singlet-triplet ($X\,^1$A′ – $a\,^3$A″) splitting is determined to be 2.90 $^{+0.02}/_{-0.07}$ eV, while the vibrational structure of the band corresponding to the formation of the lowest triplet state is attributed to the ONO bending and NO_2 wagging vibrations excited in the photodetachment.

CHAPTER 4

QUANTUM INTERFERENCE EFFECTS IN PHOTODETACHMENT OF NITROAROMATIC ANIONS

4.1 Introduction

Of special interest to this Chapter is the electronic through-bond coherence of delocalized charge distributions in negative ions. Electronic coherence is a stepping stone for understanding the fundamentals of charge transfer and conductivity in a variety of systems, including light-emitting and solar-energy devices and carbon nanotubes.[118-120] While this topic is of great interest to materials science and electronics industry it is also important in fundamental chemistry. At the heart of molecular orbital theory, orbitals are treated as a coherent superposition of electron wavefunctions localized on different atoms. Therefore, the electronic structure and consequently the chemical properties of the system rely on electronic coherence across the molecule.

In this work we use *meta*- and *para*-dinitrobenzene anions (*m-, p*-DNB$^-$) as model systems to explore the coherence of delocalized electron orbitals in π-conjugated negative ions with high-symmetry structures. Photoelectron imaging spectroscopy is a powerful technique ideally suited to probe the electronic structure of negative ions since it provides the information about both the energies and the symmetries of parent anion orbitals from which an electron has been removed. Photodetachment of an excess electron from a molecular orbital delocalized over two or more equivalent structural moieties of an anion leads to a coherent superposition of emitted electron waves. The phenomenon of dual- (or multi-) center interference in photodetachment is directly related to the quantum interference effect observed in the classic double-slit experiment with electrons.[121] In the case of photodetachment of an isolated molecular anion, the emission centers act as slits and it is impossible to distinguish from which "slit" a photoelectron originates.

Two-center interference in molecular photoinization was theoretically predicted by Cohen and Fano[122] and later observed experimentally for I_2^- anion[43] as well as for the neutral H_2 and N_2 molecules.[123-126] In general, the interference pattern depends periodically on the R/λ ratio, where R is the distance between the emission centers and λ is the de Broglie wavelength of the emitted photoelectron. As a result, quantum interference modulates the photoelectron signal, which is reflected in periodic oscillations of photoelectron angular distributions.

In practice, environmental interactions, perturbations caused by external fields or non adiabatic couplings between the electronic and nuclear degrees of freedom lead to decoherence, i.e. localization of the excess electron on one of otherwise identical centers of the anion. Therefore, interference effects occur only over certain lengths and time-scales for which the symmetry of the parent orbital is conserved. Electron spin resonance studies (ESR) of *m*- and *p*-DNB$^-$ in non aqueous solvents provide an excellent example of the environmental effect on the electronic coherence in these anions. The ESR experiments by Ward[127-129] demonstrate that dinitrobenzene anions generated by alkali metal reduction in ether solvents have its spin mostly localized on one of the nitro groups, while Maki and Geske[130] report two equal nitrogen hyperfine interactions for the anions produced electrolytically in acetonitrile. After much of discussion, it was concluded that charge localization on one of the nitro groups in Ward's experiments was due to formation of complexes of dinitrobenzene anions with alkali cations.

Theoretical calculations of dinitrobenzene anions are very scarce. Recent calculations on *m*-DNB$^-$ anion performed by Nelsen et al.[131] at the UMP2/6-31+G(d) level of theory and the CASSCF study by Mikhailov and coworkers[132] predict planar structure of C_s symmetry for the ground state of the anion. Based on their findings, the authors speculate that the charge localization for *m*-DNB$^-$ should also happen in the gas-phase, independent of the presence of either solvent or counterion.

To test this assumption we carried out gas-phase photoelectron imaging experiments on the *meta*- and *para*-dinitrobenzene anions. The experimental data for both of the studied anions clearly show oscillatory behavior of the anisotropy parameter with respect to the photoelectron kinetic energy due to quantum interference. This indicates that dinitrobenzene anions retain their high symmetry electronic and geometrical structure in the gas phase. In order to further investigate the coherent nature of photoelectron emission of dinitrobenzene anions, we develop a simple semiquantitative approach by treating symmetric anions as two-center molecular interferometers. Accordingly, we approximate the DNB$^-$ HOMOs as a superposition of the corresponding molecular orbitals in nitrobenzene anion (NB$^-$). In this picture, the photodetachment from dinitrobenzene anions is described as the electron emission from two *effective* identical centers, resulting in interference. Using the NB$^-$ photoelectron imaging data in the context of our model, we successfully reproduce the observed interference pattern for *p*-DNB$^-$ anion. The overall good agreement between the theoretical modeling and experimental results supports our conclusions about the high-symmetry electronic structure of the isolated *p*-DNB$^-$ in the gas phase.

In addition, we report the adiabatic electron affinities of 1.61 ± 0.01 eV and 1.97 ± 0.01 eV for *meta*- and *para*- dinitrobenzene molecules respectively. These measurements refine the values obtained previously from the ion / molecule reaction equilibrium and atmospheric pressure photodetachment experiments.

4.2 Experimental

The apparatus used in these experiments is described in Chapter 2. The corresponding nitroaromatic chemical samples seeded in Ar at a stagnation pressure of 25 psig are expanded into a high-vacuum chamber through a pulsed nozzle (General Valve Series 99) running at a repetition rate of either 50 or 70 Hz. The base pressure of 10^{-6} Torr in the source chamber rises up to $4\text{-}9\times10^{-5}$ Torr when the valve is operated. The precursor mixture is prepared by passing carrier gas through a sample holder heated to 40, 100, and 150 ^{0}C for increasing the vapor pressure of nitrobenzene, *meta*-, and *para*-dinitrobenzene respectively. A few millimeters downstream from the nozzle orifice the supersonic jet is crossed with a beam of high energy (~ 1 keV) electrons generated by a homemade electron gun. The negative ions are formed via secondary electron attachment to the neutral molecules.

The resulting anions are pulse-extracted into a Wiley-McLaren time-of-flight mass spectrometer, where the ion beam is accelerated to about 2.5 keV and focussed using an Einzel lens. The ions are detected mass selectively in the detection region with a typical base pressure of $(3–5)\times10^{-9}$ Torr, using a dual-microchannel-plate (MCP) detector (Burle, Inc.) located at the end of the flight tube. Photoelectrons are produced by intersecting mass-selected anions of interest with a linearly polarized laser beam. The second (532 nm), third (355nm) and fourth (266nm) harmonics of the Nd:YAG laser (Spectra Physics Lab 130-50) are used in this experiment. The 390 nm radiation was generated by frequency doubling the fundamental output (780 nm) from a regeneratively amplified Ti:Sapphire laser system (Spectra Physics, Inc.) using a 0.1 mm thick BBO crystal of a femtosecond harmonic generator (Super Optronics, Inc.). When necessary for adequate signal-to-noise the beam is mildly focused by a lens (2 m focal length) positioned 1.3 m before the laser and ion beam crossing. Photoelectrons are velocity-mapped[33] by a static but variable electric field onto a 40 mm MCP detector with P47 phosphor screen (Burle, Inc.) mounted at the end of an internally μ-metal shielded electron flight tube. To minimize experimental background, the potential difference across the two imaging MCPs, normally maintained at 1.0-1.2 kV, is pulsed up to 1.8 kV for only 250ns, in coincidence with the arrival of photoelectrons. A thermoelectrically cooled camera (Roper Scientific, Inc.) records photoelectron pattern illuminating on the phosphor screen and the resulting image, accumulated on CCD chip for about 500-700 experimental cycles, is then transferred to a data acquisition program. Each of the final photoelectron images presented in this Chapter is obtained by combining multiple of such data acquisition frames, thus representing the result of 3-9×10^5 experimental cycles. The energy spectra and angular distributions of the photoelectrons are reconstructed via inverse Abel transform using the BASEX (BAsis Set Expansion) program of Reisler and co-workers.[54]

4.3 Results

In this section we present anion photoelectron imaging data for the nitrobenzene anion as well as for the *meta*- and *para*- isomers of dinitrobenzene anion recorded at 780 (nitrobenzene only), 532, 390, 355, and 266 nm photon energies. The photoelectron images are obtained using the same velocity-mapping voltages and therefore their sizes, reflecting the photoelectron linear momentum values, can be directly compared through the entire dataset. However, the image intensity scales are tuned arbitrary for the best perception of each individual image features and thus do not represent the absolute photodetachment cross-section.

4.3.1 Photoelectron Images of Nitrobenzene Anion

The nitrobenzene anion (NB^-) raw photoelectron images recorded in the 780-266 nm wavelength range are shown in Figure 4.1 along with the corresponding photoelectron spectra. The energy spectra of NB^- contain three main bands, termed A, B and C for the future reference. Bands A and C are present at all studied photon energies (except for the 780 nm spectra where the C is not apparent), while the band B appears only in the 266 nm spectra. The peak A in the spectra is due to a direct photodetachment from the ground X $^2B_1$ state of the anion to the ground X $^1A_1$ state of the neutral nitrobenzene. This band exhibits vibrational structure with a 1370 ± 80 cm^{-1} peak spacing, corresponding to symmetric stretch of the NO_2 group.[133-135] Assuming that the highest eKE vibration peak originates from $v'=0 \leftarrow v''=0$ transition, we determine the adiabatic electron affinity of nitrobenzene to be 1.00 ± 0.01 eV, which matches the value measured previously by Desfrancois and coworkers.[135] CASPT2 calculations for nitrobenzene molecule performed by Swiderek et al.[136] suggest a number of excited electronic states accessible from the X $^1A_1$ state via vertical transitions within 3-8 eV energy range. Accounting for the 1.00 eV AEA of nitrobenzene, the following neutral excited states can be reached in the 266 nm (4.66 eV) photodetachment from X $^2B_1$ state of NB^-: $^3B_2$ (3.31 eV), $^3A_2$ (3.36 eV), $^1A_2$ (3.57 eV), $^3A_1$ (3.62 eV), where the vertical transition energies in parentheses are given with respect to the ground state of the neutral. We therefore identify a broad unstructured feature B in the lower eKE portion of 266 nm photoelectron spectra as a direct photodetachment from the ground state of NB^- to a manifold of the above mentioned excited neutral states. Finally, the inner band C appearing as a compact bright spot in the image center regardless of the photon energy used in the experiment is ascribed to the autodetachment process from a temporary excited state(s) of the NB^- anion.[135,137]

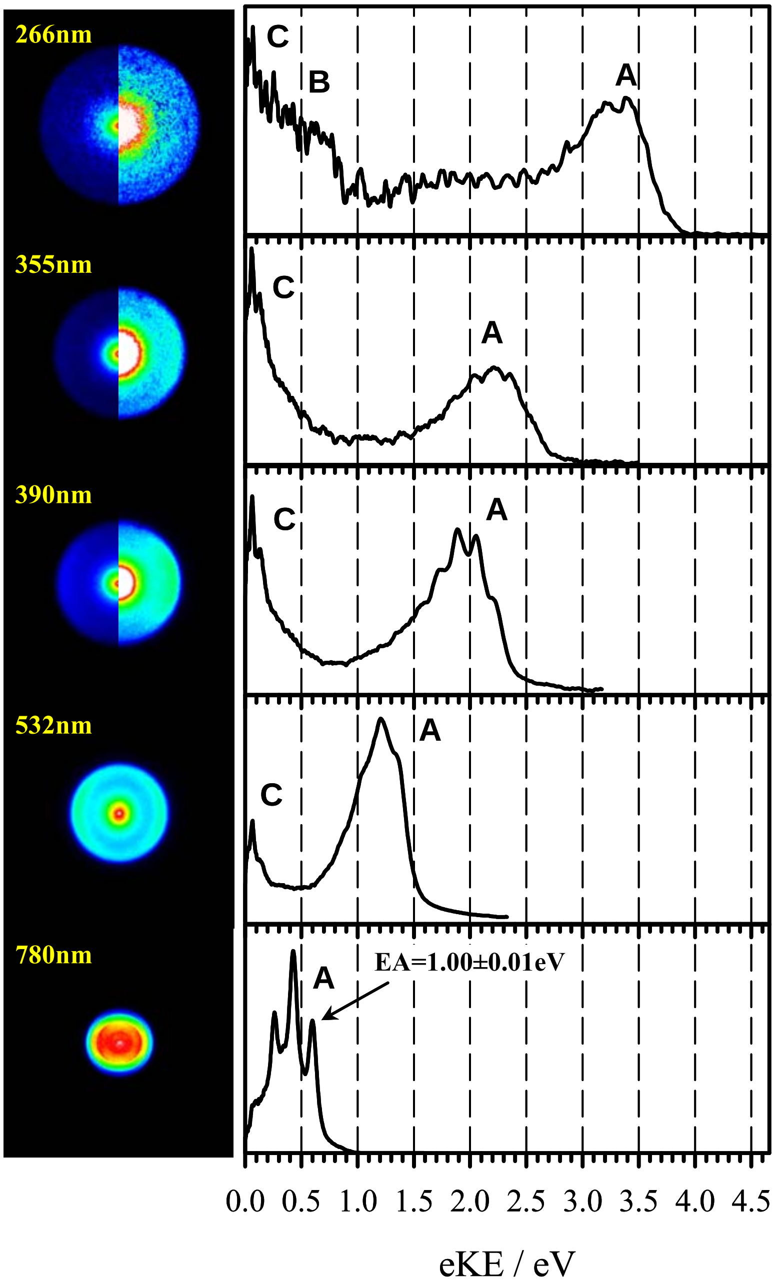

Figure 4.1 Photoelectron images (left) and the corresponding photoelectron spectra (right) of nitrobenzene anion recorded at the selected photon energies. The images for 266, 355 and 390 nm are shown in split scale to highlight higher eKE intensity features. The laser polarization direction is vertical in the image plane.

Table 4.1 Electron kinetic and binding energies along with the anisotropy parameters[d] (β_2) determined from the corresponding spectral features observed in the photodetachment of nitrobenzene anion at different photon energies. See Figure 4.1 and the text for the band assignments.

Wavelength	Peak	eKE, eV	eBE, eV	β_2
780 nm	A_0	0.59	1.00	-0.45±0.03[a]
	A_1	0.43	1.16	-0.30±0.02[a]
	A_2	0.26	1.33	-0.16±0.05[a]
532 nm	A	1.20	1.13	-0.10[b,c]
	C	0.07	2.26	0.02±0.05
390 nm	A	1.89	1.29	-0.41±0.02[b]
	C	0.07	3.11	-0.06±0.10
355 nm	A	2.21	1.28	-0.23±0.06[b]
	C	0.07	3.42	-0.03±0.10
266 nm	A	3.22	1.44	-0.12±0.04[b]
	B	~0.25	~4.41	
	C	0.07	4.59	

[a] The anisotropy parameter is determined for each individual vibrational peak.

[b] The anisotropy parameter is obtained for the entire Frank-Condon region of band A. The vertical detachment energy of the transition is estimated as the expectation value <E> using Equation 4.1.

[c] The anisotropy parameter is derived from the limited number of images collected on the same day.

[d] The uncertainties for anisotropies are given as two standard deviations.

The energetics and anisotropy parameters determined for the NB⁻ spectral features A, B, and C for all studied wavelengths are summarized in Table 4.1. The vertical detachment energies (VDE) are obtained as expectation values of the corresponding photoelectron bands, using

$$\langle E \rangle = \frac{\int_{E_1}^{E_2} I(E) E dE}{\int_{E_1}^{E_2} I(E) dE} \tag{4.1}$$

where E is either electron kinetic or binding energy, $I(E)$ is the photoelectron signal intensity, and the integration is performed over the peak's FWHM interval. We have chosen to determine VDE according to Equation 4.1 for the purpose of consistency through the entire data set for all of the anions, since the energetics for some of the transitions, see for instance feature A in 355 nm spectra of *m*-DNB⁻ (Figure 4.3), cannot be assigned based on the conventional "band maximum intensity" approach. The anisotropy parameters are calculated over the entire Frank-Condon region of photoelectron bands, with the exception of transition A in the 780 nm spectra where vibrational peaks are spaced enough for the individual analysis. For all photon energies the angular distribution of band A is perpendicular with respect to the laser polarization direction, whereas band C has essentially isotropic character, $\beta_2 \approx 0$. The angular distributions of bands B and C at 266 nm are not reported due to their significant overlap.

4.3.2 Photoelectron Images of Meta- and Para-Dinitrobenzene Anions

Photoelectron images and spectra of *para*- and *meta*-dinitrobenzene anions obtained in the 532-266 nm wavelength range are shown in Figures 4.2 and 4.3 respectively. Overall, the photoelectron data for these anions exhibit A, B, and C spectral features similar to those previously observed for the NB^-. The highest eKE features A are assigned correspondingly to $X\,^1A_g \leftarrow X\,^2B_{3u}$ and $X\,^1A_1 \leftarrow X\,^2A_2$ transitions for *p*- and *m*-DNB^-. The apparent vibrational structure in bands A corresponds to a concerted symmetric stretching of the NO_2 groups. The vibrational progression is best resolved for *p*-DNB^- in the 532 nm data and gets smeared out as the photon energy increases due to a limited energy resolution afforded in photoelectron imaging at higher photoelectron kinetic energies.

The position of the first peak, A_0, maximum in the vibrational sequence with the smallest eBE (highest eKE) attributed to (0, 0) transition provides the AEA values of 1.97±0.01eV and 1.61 ± 0.01 eV for *para*- and *meta*- isomers of dinitrobenzene. These results refine previous experimental EA measurements of 2.00 ± 0.10 eV[138] (TDEq), 1.995 ± 0.048 eV[139] (IMRE), <3.100 ± 0.050 eV[137] (PD) for *p*-DNB; and 1.66 ± 0.10 eV[140](IMRE), 1.652 ± 0.048 eV[139] (IMRE), <1.650 ± 0.050 eV eV[137] (PD) for *m*-DNB molecules, where experimental method codes TDEq, IMRE, and PD stand for temperature dependent equilibrium ion-molecule reaction, ion-molecule reaction equilibrium, and photodetachment at atmospheric pressure respectively.

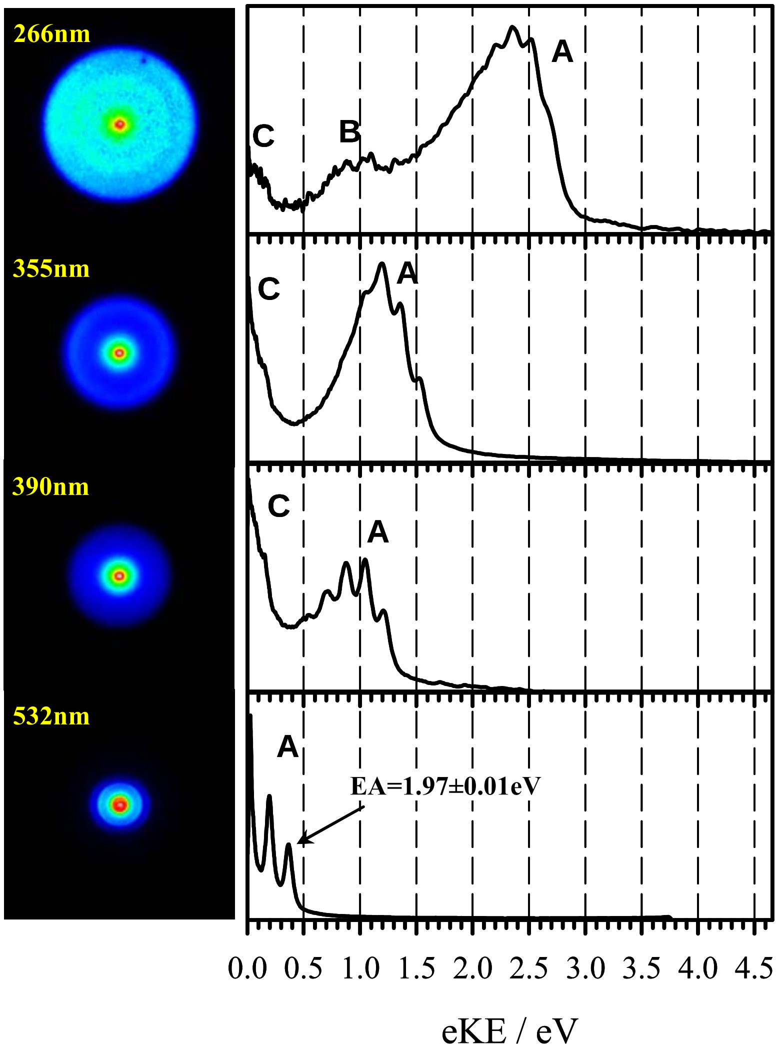

Figure 4.2 Photoelectron images (left) and the corresponding photoelectron spectra (right) of para-dinitrobenzene anion obtained at the selected photon energies. The laser polarization direction is vertical in the image plane.

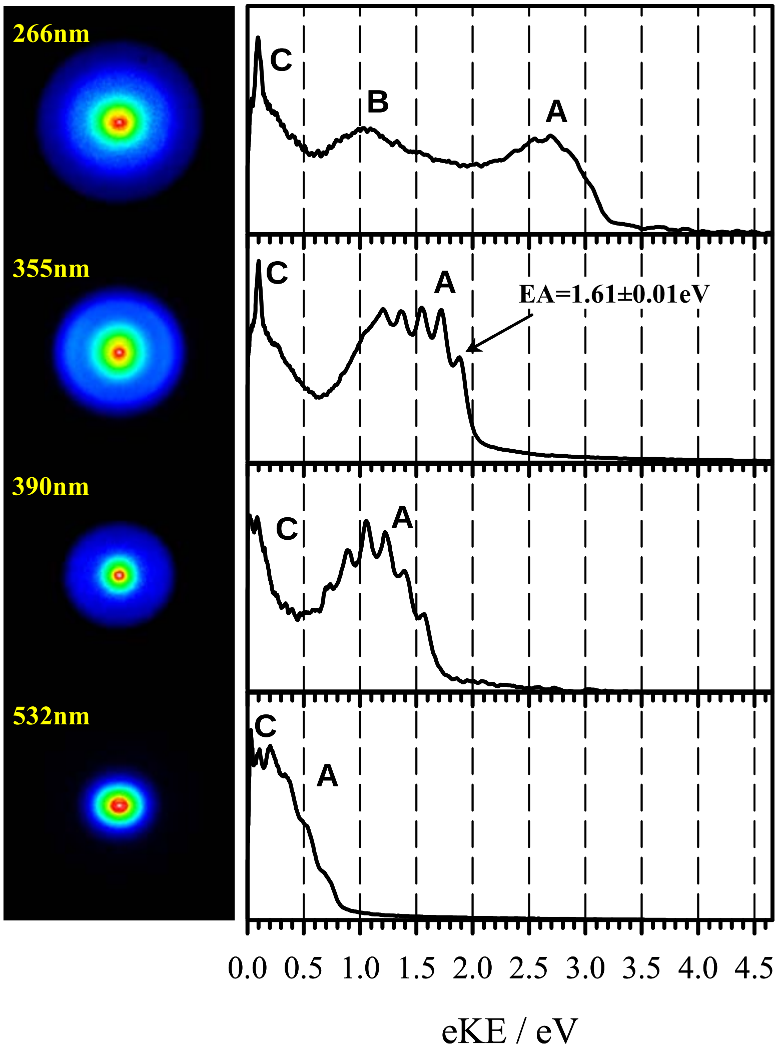

Figure 4.3 Photoelectron images (left) and the corresponding photoelectron spectra (right) of meta-dinitrobenzene anion obtained at the selected photon energies. The laser polarization direction is vertical in the image plane.

Table 4.2 Photoelectron band energies and anisotropy parameters (β_2) determined[c] from *p*-DNB$^-$ photoelectron images recorded at different photon energies. See Figure 4.2 and the text for the spectral band assignments.

Wavelength	Peak	eKE, eV	eBE, eV	β_2
532 nm	A_0	0.36	1.97	-0.57±0.07 [a]
	A_1	0.19	2.14	-0.22±0.03 [a]
	A_2	0.03	2.30	0.02±0.01 [a]
390 nm	A	0.87	2.31	-0.13±0.03 [b]
	C	0.01	3.17	-0.10±0.05
355 nm	A	1.20	2.29	-0.07±0.01 [b]
	C	0.01	3.48	-0.10±0.02
266 nm	A	2.35	2.31	-0.12±0.02 [b]
	B	0.97	3.69	-0.10±0.03 [b]
	C	0.01	4.65	-0.12±0.22

[a] The anisotropy parameter is determined for each individual vibrational peak.

[b] The anisotropy parameter is obtained for the entire Frank-Condon region of band A; vertical detachment energy of the transition is estimated as the expectation value <E> using Equation 4.1.

[c] The uncertainties for anisotropies are given as two standard deviations.

Table 4.3 Photoelectron band energy and anisotropy parameter (β_2) values determined[a] from *m*-DNB$^-$ photoelectron images in Figure 4.3. See text for details of the band assignments.

Wavelength	Peak	eKE, eV	eBE, eV	β_2
532 nm	A_0	0.72	1.61	≤-0.45±0.12
	A_1	0.55	1.78	≤-0.33±0.13
	A_2	0.38	1.95	≤-0.23±0.13
	C	0.10	2.23	-0.14±0.02
390 nm	A	1.06	2.12	-0.20±0.04
	C	0.10	3.08	-0.11±0.07
355 nm	A	1.41	2.08	-0.18±0.01
	C	0.10	3.39	-0.11±0.02
266 nm	A	2.63	2.03	-0.17±0.02
	B	1.05	3.61	-0.09±0.06
	C	0.10	4.56	-0.02±0.14

[a] The band energies of the transitions are estimated as the expectation values <E> using Equation 4.1; anisotropy parameters are calculated for the entire band regions with the uncertainties reported as two standard deviations.

Bands B in 266 nm spectra, shifted towards higher eKE and thus somewhat better resolved than analogous band for NB^{-}, are attributed to the direct photodetachment from the ground states of the anions to uncharacterized excited electronic states of the neutrals. The low eKE features C are similar to that observed in photoelectron signal of nitrobenzene anion and correspond to the autodetachment from metastable anion states.

The electron kinetic and binding energies for the *p*,*m*-DNB^{-} are listed in Tables 4.2 and 4.3 along with the anisotropy parameters for each wavelength. The B and C bands are only slightly perpendicular in character ($\beta_2 \approx -0.10$). In contrast to features C, photoelectron angular distributions for bands A are highly dependent on the electron kinetic energy of the peak. For instance, in 532nm photodetachment of *p*-DNB^{-}, the photoelectron angular distribution (PAD) of peak A_0 ($\beta_2 = -0.56 \pm 0.07$; eKE = 0.36 eV) is strongly perpendicular with respect to the laser polarization axis, while for peaks A_1 ($\beta_2 = -0.22 \pm 0.03$; eKE = 0.19 eV) and A_2 ($\beta_2 = 0.02 \pm 0.01$; eKE = 0.03 eV) the anisotropy parameter quickly approaches zero value (the isotropic distribution), in agreement with the Wigner photodetachment threshold law[69]. As the eKE of photoelectrons increases with higher photon energies, the PAD of the entire band A gets less polarized and reaches its maximum, becomes nearly isotropic ($\beta_2 = -0.07 \pm 0.01$), at 355nm. After this point, the trend reverses back towards more anisotropic PADs, $\beta_2 = -0.12 \pm 0.02$ at the 266nm.

Unfortunately, for *m*-DNB^{-} anion the vibrations in the A band are washed out at the lowest photon energy, 532 nm, because of the strong overlap with the photoelectron signal from the band C. Nonetheless, taking into account that band C anisotropy is quite low and is independent of the photon energy, it is still possible to estimate the upper bound β_2 values of the highest eKE peaks (where the contribution from the C signal is minimal) in the vibrational progression. For the anisotropy analysis, we have assigned positions of the first three vibrational peaks based on the measured electron affinity value of *m*-DNB$^-$ and a typical (0.17 eV) vibrational spacing in band A for the studied nitroaromatic anions. The integration limits were chosen similar to those used in the anisotropy analysis of NB$^-$ and *p*-DNB$^-$ photoelectron data with clearly resolved vibrational peaks. While only approximate, the estimated anisotropies at 532 nm ($\beta_2 \leq -0.45 \pm 0.12$, eKE = 0.72 eV; $\beta_2 \leq -0.33 \pm 0.13$, eKE = 0.55 eV; $\beta_2 \leq -0.23 \pm 0.13$, eKE = 0.38 eV) and the values determined at higher photon energies ($\beta_2 = -0.20 \pm 0.04$, eKE = 1.06 eV; $\beta_2 = -0.18 \pm 0.01$, eKE = 1.41 eV; $\beta_2 = -0.17 \pm 0.02$, eKE = 2.63 eV) show the same variational trend as was previously observed in photodetachment of *p*-DNB$^-$ anion.

4.4 Discussion

To understand the observed anisotropies in photodetachment of the studied nitroaromatic anions, we will use a group theoretical approach which allows establish a simple qualitative relationship between photoelectron angular distributions and the symmetry properties of the corresponding parent anion orbital. The symmetry analysis was described in details in Section 2.8 of this dissertation for the photodetachment of NO_2^- and therefore only a short summary of predicted anisotropy distributions is given below. Figure 4.4 shows the allowed partial-waves in photodetachment from the highest

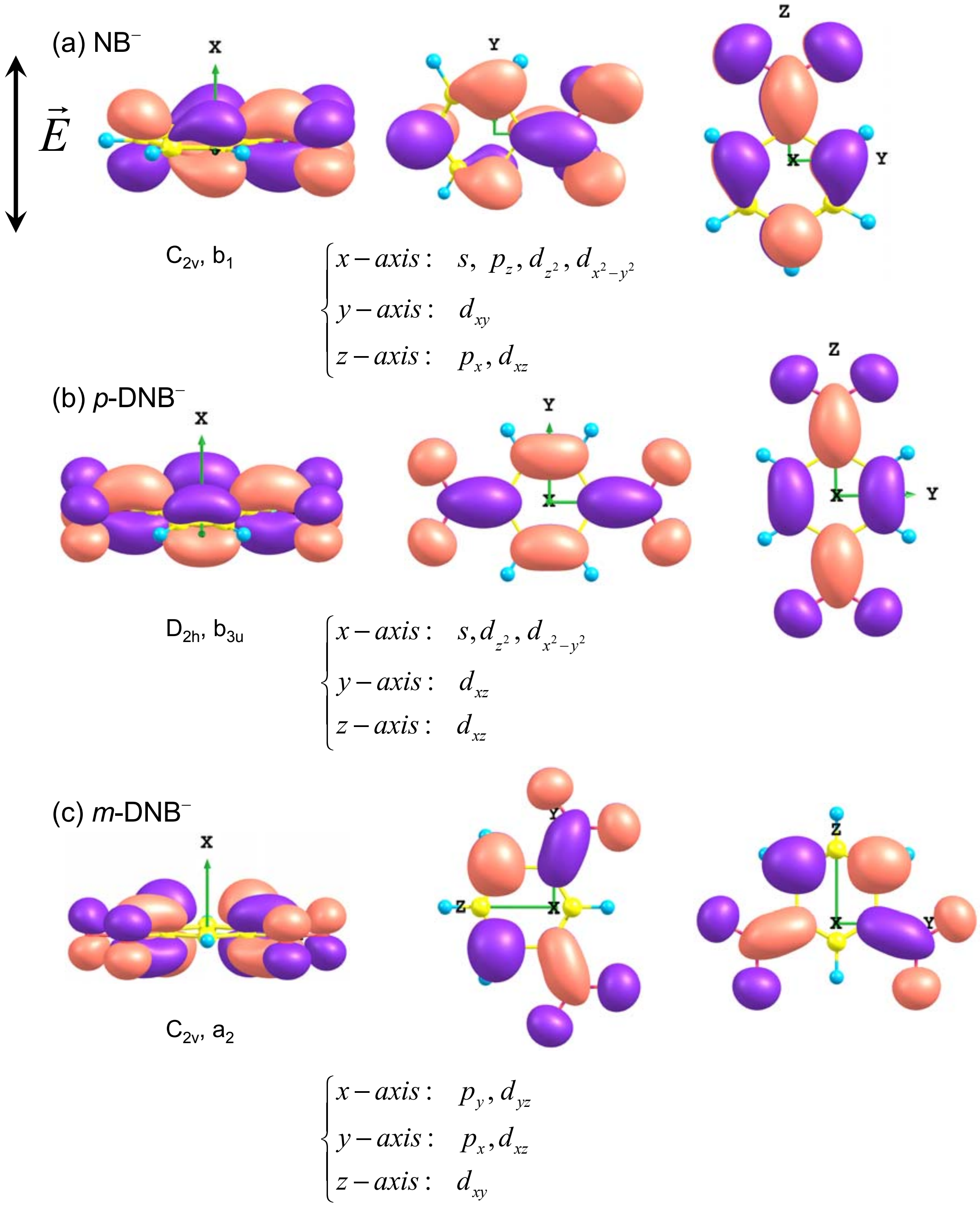

(a) NB^-

C_{2v}, b_1

$$\begin{cases} x-axis: & s,\ p_z, d_{z^2}, d_{x^2-y^2} \\ y-axis: & d_{xy} \\ z-axis: & p_x, d_{xz} \end{cases}$$

(b) *p*-DNB^-

D_{2h}, b_{3u}

$$\begin{cases} x-axis: & s, d_{z^2}, d_{x^2-y^2} \\ y-axis: & d_{xz} \\ z-axis: & d_{xz} \end{cases}$$

(c) *m*-DNB^-

C_{2v}, a_2

$$\begin{cases} x-axis: & p_y, d_{yz} \\ y-axis: & p_x, d_{xz} \\ z-axis: & d_{xy} \end{cases}$$

Figure 4.4 Summary of the allowed partial waves from the group theoretical analysis of (a) NB^-, (b) *p*-DNB^-, (c) *m*-DNB^- HOMOs at three principal orientations (x, y, z) of the anions in the laboratory frame defined by the laser polarization vector $\vec{E}$.

occupied orbitals of (a) NB^-, (b) *p*-DNB^-, and (c) *m*-DNB^- anions. Restricting the expansion of outgoing photoelectron wave to *s* and *p* partial-waves only (s&p model) and considering three "principal" orientations (along x, y, and z laboratory-frame axes) for each molecular anion to account for the orientation averaging, the following anisotropy distributions are expected: (1) $\perp$ for NB^- due to p_z and p_x waves emitted perpendicularly to the laser polarization direction at the x-axis and z-axis alignments respectively, (2) *isotropic* for *p*-DNB^- since only *s* waves are allowed, (3) $\perp$ for *m*-DNB^- because of the perpendicular p_y and p_x waves at the x- and y-axis orientations. While predicted perpendicular PADs for NB^- and *m*-DNB^- anions agree with the experimental observations, the anticipated isotropic distribution ($\beta_2 = 0$) for *p*-DNB^- is clearly in conflict with the measured negative values of anisotropy parameters for this anion. This indicates that s&p approximation has to be extended to the *d* waves for a proper description of photoemission process.

Interestingly, the Bethe-Cooper-Zare (BCZ) model [35,36,67,68] for the *s* and *d* waves emission in the detachment of *p*-shell electrons from atomic anions (Equations 2.18-2.20) provide an excellent fit to the eKE dependent anisotropy dataset for NB^- anion (Figure 4.5), with the exception of one data point (eKE = 1.2 eV, $\beta_2 = -0.10$) for which we have a limited data statistics and therefore exclude it for now from modeling. It should be emphasized that this result is not trivial and in general the BCZ expression is not applicable for the detachment of molecular anions. The overall good agreement between the model and experimental results leads us to the following conclusions:

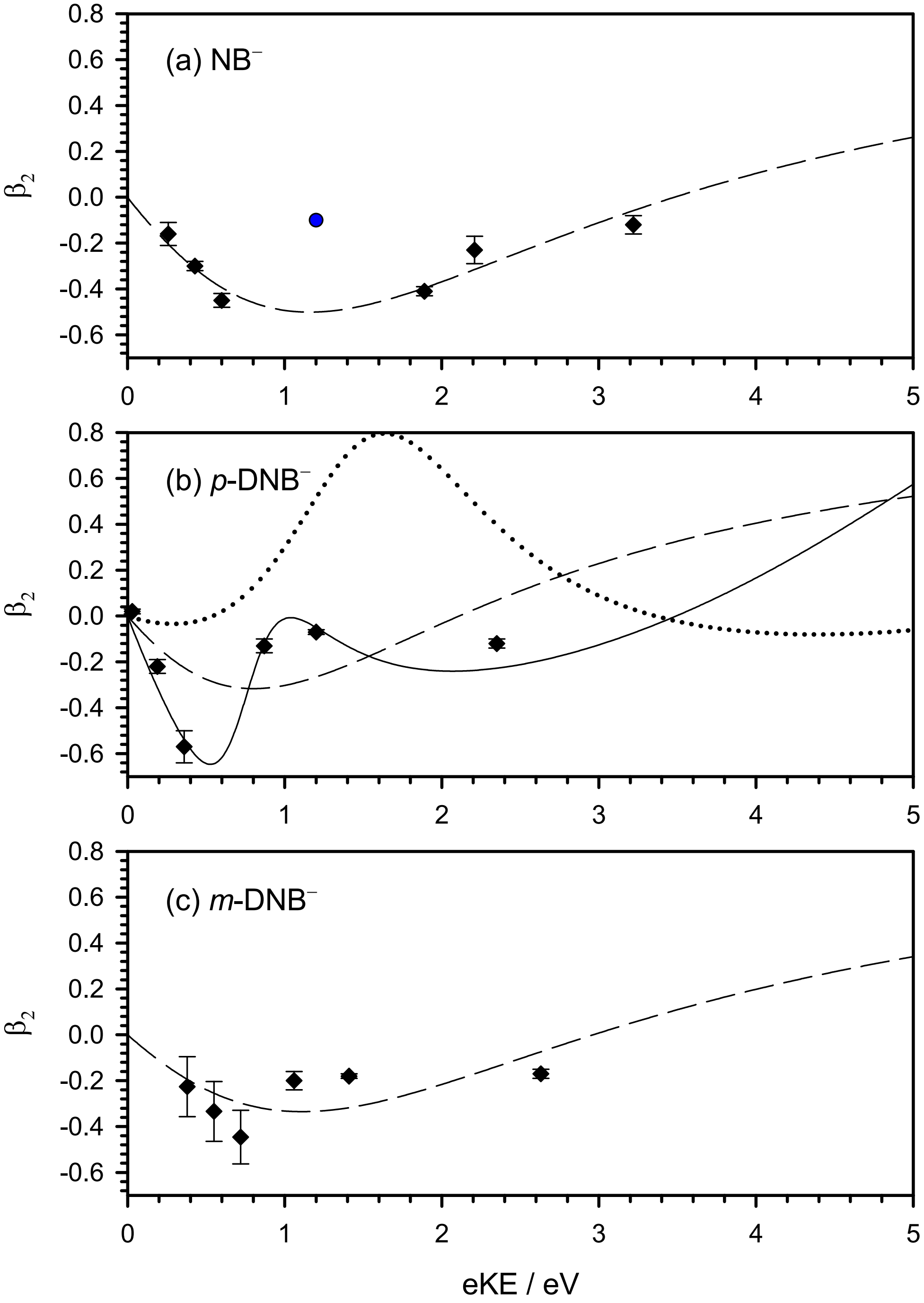

Figure 4.5 The observed anisotropy parameter (β_2) variation in photodetachment of (a) NB$^-$, (b) *p*-DNB$^-$, and (c) *m*-DNB$^-$ anions. The long-dash curve for all of the anions represents the BCZ model fit. In (b), the dotted and solid graphs correspond to the interference modeling with A and δ parameters fixed to those of NB$^-$, and all parameters being adjustable respectively. See text for further details.

(1) the contribution of the *p* waves to the photoelectron signal is not significant, (2) the observed perpendicular angular distributions for NB^- anion is a result of the *s* and *d* partial-wave interference, (3) photodetachment from NB^- can be treated as if originating from a *p* orbital of an atomic like anion, (4) the only principal orientation of NB^- in the laboratory frame capable of providing *s* and *d* waves is along the x-axis (the other allowed d_{xy} and d_{xz} partial waves average out and do not contribute to the photoelectron anisotropy). The application of BCZ model to the *para*- and *meta*- dinitrobenzene anions, the long dashed line in Figures 4.5 (b) and (c), reproduce qualitatively the perpendicular nature of anisotropy distributions ($\beta_2 < 0$), yet do not generate a satisfactory fit to the experimental data. However, considering the high-symmetry electronic structure of the anions and the oscillatory behavior of anisotropy parameters calling for the presence of quantum interfere effect, the poor performance of the model is not surprising since it does not account for the coherent photoelectron emission from multiple centers. The inspection of the parent orbitals shape for *para*- and *meta*- dinitrobenzene anions, suggests that, at least qualitatively, they can be represented as a superposition of two b_1 (HOMO) orbitals of the nitrobenzene anion.

In what follows, we will develop a general two-center interference model, where the emission from each center is approximated as the photodetachment of a *p*-shell atomic anion. A general equation for calculating anisotropy parameter is given by

$$\beta_2 = \frac{2\left(\sigma'(0) - \sigma'\left(\frac{\pi}{2}\right)\right)}{\sigma'(0) + 2\sigma'\left(\frac{\pi}{2}\right)}, \tag{4.1}$$

where σ' is the differential cross-section for detaching an electron from anion in the parallel, $\theta = 0$, and perpendicular, $\theta = \frac{\pi}{2}$, direction with respect to the laser polarization vector. The differential cross-section is obtained from the transition dipole matrix elements by averaging over all molecular orientations of anion in the laboratory frame

$$\sigma'(\theta) = \frac{d\sigma}{d\Omega} = N\int \left| \vec{\varepsilon} \left\langle k \,|\, \vec{r} \,|\, \psi^{MO} \right\rangle \right|^2 d\alpha \cdot d\beta \cdot d\gamma \tag{4.2}$$

In Equation 4.2, $\vec{r}$ is the dipole moment operator, ψ^{MO} and k are correspondingly the parent anion and free-electron wavefunctions, the {α, β, γ} Euler angles specify orientation of the anion in the lab frame defined by the electric field vector $\vec{\varepsilon}$. By expanding the outgoing photoelectron wavefunction in the atomic-like basis set (*s*, *p*, *d*, etc…), the expression for differential cross-section becomes a sum over all possible angular momentum quantum numbers

$$\sigma'(\theta) = N\sum_{l,l'}^{\infty} \sum_{m=-l}^{l} \sum_{m'=-l'}^{l'} C_{k,l,m} C^{*}_{k',l',m'} \Theta_{l,m}(\theta) \Theta^{*}_{l',m'}(\theta), \tag{4.3}$$

The $C_{k,l,m} C^{*}_{k',l',m'}$ product corresponds to the partial differential cross-section of the emitted waves with the corresponding $\Theta_{l,m}(\theta)$ spherical harmonic components independent of the azimuth angle φ. Assuming the $\Delta\ell = \pm 1$, $\Delta m = 0$ selection rules for the photodetachment from an atomic anion, the Equation 4.3 becomes

$$\sigma'(\theta) = N\left(C_{0,0}^2 \Theta_{0,0}^2(\theta) + C_{0,0} C_{2,0} \cos(\delta) \Theta_{0,0}(\theta) \Theta_{2,0}(\theta) + C_{2,0}^2 \Theta_{2,0}^2(\theta) \right), \tag{4.4}$$

where we have chosen to explicitly indicate the phase shift δ between the s and d_{z^2} waves. By substituting $\frac{1}{2\sqrt{\pi}}$ and $\frac{\sqrt{5}}{4\sqrt{\pi}}\left(1-3\cos^2(\theta)\right)$ expressions for the $\Theta_{0,0}(\theta)$ and $\Theta_{2,0}(\theta)$ functions into Equation 4.4, we obtain the following formula for the differential cross-section in the detachment of a p-shell atomic anion

$$\begin{aligned}\sigma'(\theta) = \frac{1}{16\pi}\Big\{4C_{0,0}^2 + C_{2,0}^2\left[5-30\cos^2(\theta)+45\cos^4(\theta)\right]+ \\ +C_{0,0}C_{2,0}\cos(\delta)\left[4\sqrt{5}-12\sqrt{5}\cos^2(\theta)\right]\Big\}\end{aligned}, \tag{4.5}$$

Finally, plugging Equation 4.5 in 4.1 provides us with the expression for anisotropy parameter

$$\beta_2 = \frac{2\left[5/4\,C_{2,0}^2 - \sqrt{5}C_{0,0}C_{2,0}\cos(\delta)\right]}{C_{0,0}^2 + 5/2\,C_{2,0}^2} \tag{4.6}$$

Comparing the derived Equation 4.6 to the BCZ model for the detachment of an atomic anion p orbital

$$\beta_2 = \frac{2\left[\sigma_d^2 - 2\sigma_s\sigma_d\cos(\delta)\right]}{\sigma_s^2 + 2\sigma_d^2} \tag{4.7}$$

we obtain the following relation

$$\begin{cases}\sigma_s = C_{0,0} \\ \sigma_d = \dfrac{\sqrt{5}}{2}C_{2,0}\end{cases} \tag{4.8}$$

The above Equations 4.6 and 4.8 were previously reported by Oana et al.[39] in the context of photodetachment of O$^-$ anion. We have chosen to reproduce their results here, since the intermediate Equation 4.5 for $\sigma'(\theta)$ (omitted in the paper)[39] is necessary for developing the two-center interference model.

We begin our derivation by approximating the outgoing free-electron wave as a linear combination of two plane in-phase-waves emanating from the corresponding photodetachment centers separated by distance R from each other

$$\left|k\right\rangle = \exp(i\vec{k}\cdot(\vec{r}-\vec{r}_0)) + \exp(i\vec{k}\cdot(\vec{r}+\vec{r}_0)) = 2\exp(i\vec{k}\cdot\vec{r})\cos\left(\frac{\pi R}{\lambda}\cos\left(\widehat{k,r_0}\right)\right) \quad (4.9)$$

In Equation 4.9, λ is the de Broglie wavelength of the emitted photoelectron and $\vec{r}_0$ is a vector, $\left|\vec{r}_0\right| = \frac{R}{2}$, pointing in the direction along the line connecting two detachment centers. Using Equations 4.1, 4.2, and 4.9 we get a general form solution for the two-center molecular interferometer aligned perpendicular to the electric field vector

$$\beta_2 = \frac{2\left(\sigma'(0)\int_0^{2\pi}\cos^2\left(\frac{\pi R}{\lambda}\sin(\alpha)\right)\cos^2(\alpha)\,d\alpha - \sigma'\left(\frac{\pi}{2}\right)\int_0^{2\pi}\cos^2\left(\frac{\pi R}{\lambda}\cos(\alpha)\right)\cos^2(\alpha)\,d\alpha\right)}{\sigma'(0)\int_0^{2\pi}\cos^2\left(\frac{\pi R}{\lambda}\sin(\alpha)\right)\cos^2(\alpha)\,d\alpha + 2\sigma'\left(\frac{\pi}{2}\right)\int_0^{2\pi}\cos^2\left(\frac{\pi R}{\lambda}\cos(\alpha)\right)\cos^2(\alpha)\,d\alpha} \quad (4.10)$$

The $\cos^2\left(\frac{\pi R}{\lambda}\sin(\alpha)\right)$ and $\cos^2\left(\frac{\pi R}{\lambda}\cos(\alpha)\right)$ in Equation 4.10 are the interference terms for the parallel and perpendicular ejection of the photoelectron respectively. The orientation averaging is accounted for by integrating the interference terms weighted by the $\cos^2(\alpha)$ function, reflecting the diminishing contribution of each particular molecular alignment to the photoelectron signal as the angle α between the transition dipole moment and the laser polarization increases. By combining Equations 4.5, 4.8 and introducing the explicit energy dependence $\frac{\sigma_d}{\sigma_s} = A \cdot eKE$ from the Wigner threshold law[69], we obtain the expressions for the parallel and perpendicular differential cross-sections

$$\begin{cases} \sigma'(0) = 4 + 16A^2 eKE^2 - 16A\cos(\delta) eKE \\ \sigma'\left(\frac{\pi}{2}\right) = 4 + 4A^2 eKE^2 + 8A\cos(\delta) eKE \end{cases} \tag{4.11}$$

which can be substituted into Equation 4.10 to produce the final formula suitable for modeling the experimental data. We also note here that integrals in the Equation 4.10 are not analytically solvable. However, it does not stop us from fitting data since the integration can be performed numerically for each particular values of eKE while treating R as an adjustable parameter.

The dotted curve in Figure 4.5 (b) represents the output of nonlinear least squares fit (LSF) of our model equation, with the parameters A and δ determined for NB^-, to the measured β_2 values in the photodetachment of *p*-DNB^-. Clearly, our theoretical predictions only qualitatively reproduce the oscillatory trend of experimental data. This result is not unexpected since after all the NB^- and *p*-DNB^- are two different molecular systems. Treating A, δ, and R as the adjustable parameters allows us to quantitatively model, see solid line curve in Figure 4.5 (b), the experimentally observed variation of anisotropy parameter. Moreover, the estimated R value of 7.45 Å is very similar to the 6.82 Å distance (from the B3LYP/aug-cc-pVTZ calculations on *p*-DNB^-) between the mirror oxygen atoms of the opposite nitro groups. This result seems to be plausible since the excess electron charge is mostly localized on the oxygen atoms of two nitro groups, which should ultimately lead to the comparable distance between the effective emission centers.

Modeling of *m*-DNB$^-$ anion is currently in the progress and will be presented in the upcoming publication.

4.5 Summary

Photoelectron imaging was applied to study the electronic through-bond coherence in *meta*- and *para*-dinitrobenzene anions. The experimental data for both of the studied anions exhibit the oscillatory behavior of anisotropy parameter with respect to the photoelectron kinetic energy due to the quantum interference effect, indicating that dinitrobenzene anions retain their high symmetry electronic and geometrical structure in the gas phase. To model a coherent photoelectron emission of dinitrobenzene anions, we developed a simple semiquantitative approach by treating symmetric anions as two-center molecular interferometers. The overall good agreement between the theoretical modeling and experimental results supports our conclusions about the high-symmetry electronic structure of the isolated *para*-dinitrobenzene anion in the gas phase.

CHAPTER 5

SOLVATION INDUCED CLUSTER ANION CORE SWITCHING FROM $NNO_2^-(N_2O)_{n-1}$ TO $O^-(N_2O)_n$

5.1 Introduction

Clusters have long been utilized for studying the microscopic details of intermolecular interactions.[7,141] In particular, the cluster-anion series $X^-\cdot M_n$, where X^- is the core anion and M is the solvent, allow for a molecule-by-molecule evaluation of a solvent's effect on the energy and structure of a charged solute.

The structures and energetics of such systems can be elucidated by photoelectron spectroscopy.[1,141] It is well understood that solvated anions are usually stabilized by ion-neutral interactions. On a pairwise basis, these mostly electrostatically controlled interactions tend to be weaker than the covalent bonds in either the solute or the solvent, but their combined effect for many solvent molecules (and generally accounting for the many-body interactions)[142] can easily exceed a typical covalent bond energy. To the contrary, the corresponding neutral states are usually stabilized to a much lesser degree due to the weaker strength of van der Waals bonding. As a result, solvation tends to increase the vertical detachment energy (VDE) of anionic species. In the absence of chemical rearrangements, the increase is expected to be gradual and monotonic with the number of solvating molecules. Discontinuities in this trend usually signal abrupt changes in the structure of the core anion.

A classic example of such behavior was reported by DeLuca et al.[10] for the $(CO_2)_n^-$, n = 2–13 cluster series, later expanded by Tsukuda et al.[9] for the n = 2–16 range. The photoelectron spectra of the size-selected $(CO_2)_n^-$ cluster anions obtained by these authors display two different photodetachment band series: one corresponding to higher VDEs is observed for the n = 2–6 and n = 14 clusters, and the other, with lower VDEs, is observed in the n = 6-13 range. The VDE discontinuities at n = 6 and 14 cannot be accounted for by ordinary solvation and are attributed to structural changes in the cluster core. Specifically, these changes have been described as a core-switching (at n = 6) from the covalent dimer anion $(O_2CCO_2)^-$, whose structure was originally proposed by Fleischman and Jordan,[11] to the monomer CO_2^- and back (at n = 14).[9,10]

Another study by Tsukuda et al.[12] revealed a similar phenomenon for $(NO)_n^-$. For this cluster series, the VDE was found to increase by nearly 0.8 eV from n = 2 to n = 3, while only moderate consecutive increases (~0.1 eV) were observed in the n = 3–7 range. The VDE trend for n = 3–7 is consistent with stepwise solvation of a charged cluster core, but the abrupt changes occurring between n = 1 and 2 and between n = 2 and 3 once again signal structural changes in the core-anion. In this case, a gradual assembly (or building up) of the core anion is observed as the $(NO)_n^-$ cluster size increases. Specifically, the core anions in these clusters are described as (obviously) NO^- for n = 1, a covalently bound dimer anion for n = 2, and (preferentially) a covalently bound *trimer* anion for n = 3. That is, in the $n \leq 3$ range, the excess electron delocalizes between all available NO moieties. In larger clusters, the size of the anionic core no longer increases with n and the additional NO molecules play the role of neutral solvents.[12]

Multiple isomeric forms of $N_2O_2^-$ have been the subject of an increasing number of studies,[143-149] in part due to the interest in the possible role of their neutral analogues as intermediates in atmospheric processes.[149] Posey and Johnson, using pulsed supersonic expansion of distinct precursor gas mixtures ionized by a fast electron beam, identified three distinct forms of $N_2O_2^-$: (i) the $O_2^-{\cdot}N_2$ ion-molecule complex, observed in the expansion of O_2 seeded in nitrogen; (ii) the C_{2v} symmetry Y-shaped NNO_2^- anion (analogous to CO_3^-), formed in the expansion of pure N_2O; and (iii) an NO dimer anion, *cis*- or *trans*-$ONNO^-$, generated by seeding NO in the Ar carrier gas.[143] In this work, we are primarily concerned with the Y-shaped (NNO_2^-) isomer[143,145,147,149] and changes in its structure under solvation by N_2O.

Cluster formation. Dissociative electron attachment to N_2O is understood to be a preliminary step in the formation of NNO_2^- in electron-impact anion sources[51,150-158]:

$$N_2O(^1\Sigma^+) + e^- \rightarrow N_2O^{-*}(^2\Sigma^+;^2\Pi) \rightarrow O^-(^2P) + N_2 \qquad (5.1)$$

This process yields N_2 and O^- and in the presence of third bodies may be followed by the $O^- + N_2O$ association reaction[143]:

$$O^- + N_2O + N_2O \rightarrow NNO_2^- + N_2O \qquad (5.2)$$

$$O^- + N_2O + N_2O \rightarrow O^-N_2O + N_2O \qquad (5.3)$$

Both reactions 5.2 and 5.3 proceed without a barrier, however the former is more energetically preferred due to formation of a covalent bond, which results in the branching ratio near completely shifted towards 5.2. Such processes in neutral N_2O

clusters have been shown to yield an anionic cluster series, often termed $O^{-}(N_2O)_n$[51,151,154,155,158-160]:

$$(N_2O)_m + e^{-} \rightarrow [N_2O^{-}(N_2O)_{m-1}]^{*} \rightarrow O^{-}(N_2O)_n + (m\text{-}2\text{-}n)N_2O + N_2 \qquad (5.4)$$

In the thermodynamics study on this series for $n = 2–7$, Hiraoka et al. suggested an $NNO_2^{-}(N_2O)_{n-1}$ structural form for these clusters.[159] Based upon the accepted NNO_2^{-} structure for the $n = 1$ member of this cluster series, they also suggested that the first effective solvent shell in $NNO_2^{-}(N_2O)_{n-1}$ is completed at $n = 3$, corresponding to preferential solvation of the two equivalent anionic oxygen sites.

In this Chapter, we discuss the first spectroscopic study of the mass-selected $[O(N_2O)_n]^{-}$, $n = 0–9$ cluster anions by way of photoelectron imaging.[30,47] We identify covalently bound NNO_2^{-} as a core anion in the small ($n = 1–3$) clusters, while in the larger ($n > 3$) clusters O^{-} is determined to be the dominant ionic core. We argue that the strong solvation interactions involving the more localized charge distribution of the atomic anion may provide for preferential stabilization of O^{-} in the larger clusters. These results further demonstrate a solvent's ability to affect chemical structure and highlight the utility of photoelectron imaging for characterizing such phenomena.

5.2 Experimental Details

The photoelectron imaging apparatus used in this study is described in Chapter 2. The $[O(N_2O)_n]^{-}$ clusters are formed by expansion of pure N_2O gas at a stagnation pressure of 2.5 atm through a pulsed supersonic nozzle (General Valve Series 9) operated at a repetition rate of 50 Hz into a high-vacuum chamber with a base pressure of 10^{-6} Torr (rising to $6\text{-}8\times10^{-5}$ Torr when the valve is operated). A focused 1 keV electron beam, propagating counter to the supersonic expansion, is directed straight into the nozzle's throat. This arrangement has been shown by the Johnson group to favor the production of larger clusters,[50] while the use of pure N_2O as a precursor gas should favor the formation of the Y-shaped NNO_2^- isomer.[143] The anions are pulse-extracted into a Wiley-McLaren[52] time-of-flight mass spectrometer. After entering the detection region of the instrument, the ions are detected with mass-resolution using a dual-microchannel-plate (MCP) detector (Burle, Inc.) mounted at the end of the mass-spectrometer's flight tube.

Photoelectrons are produced by intersecting the mass-selected cluster ions of interest with a linearly polarized laser beam. The third and fourth harmonics of the Nd:YAG laser (Spectra Physics Inc., model Lab 130-50) are used as sources of the 355 and 266 nm radiation, respectively. When necessary, in order to enhance signal-to-noise ratio of a photoelectron signal, the laser beam is mildly focused with a lens (2.0 m focal length), positioned 1.3m before the laser and ion beam crossing. Photoelectrons are extracted by a static electric field in the velocity-map[33] imaging assembly through an electron flight tube, internally shielded with μ-metal, and onto a 40 mm MCP detector with a P47 phosphor screen (Burle, Inc.). To minimize backgrounds, the potential difference across the two imaging MCPs, normally maintained at 1.0-1.2 kV, is pulsed up to 1.8 kV for the 250 ns window coinciding with the arrival of photoelectrons. The signal from the phosphor screen is recorded with a CCD camera (CoolSnap, Roper Scientific, Inc.) and typically accumulated for $1\text{-}5\times10^{5}$ experimental cycles. The speed and angular distributions of the photoelectrons are obtained via inverse Abel transform[32] using the BASEX (BAsis Set EXpansion) program.[54]

Supplementary photofragmentation studies are carried out on a separate negative-ion spectrometer,[161] which employs similar ion-generation and mass-selection techniques. The third-harmonic output of the same Nd:YAG laser (355 nm, 15 mJ) is focused to a ~5 mm diameter spot size at the intersection with the ion beam. The resulting photofragments are analyzed using a single-stage reflectron mass-spectrometer and detected with a secondary (off-axis) MCP detector.

5.3 Results

In this section, we present photoelectron imaging and photofragmentation results for the $[O(N_2O)_n]^-$, n = 0–9 cluster anion series. Figure 5.1 shows the 355 nm results (both photoelectron imaging and cluster fragmentation), while Figure 5.2 displays the 266 nm data (photoelectron imaging only).

The raw photoelectron images and the corresponding spectra shown in Figures 5.1 and 5.2 are hereafter referred to as datasets 5.1.n and 5.2.n, respectively, with n = 0–9 referring to the $[O(N_2O)_n]^-$ cluster size. Each photoelectron image shown is the sum of multiple collections, corresponding to a total of $1–5\times10^5$ experimental cycles. All images for a given wavelength are displayed on the same velocity scale. The intensity scales are chosen arbitrarily to highlight the most relevant features of the individual images; therefore, they do not reflect the absolute cross-sections. The $O(^3P, ^1D) \leftarrow O^-(^2P)$

photodetachment transitions[162] in datasets 5.1.0 and 5.2.0 were used for electron kinetic energy (eKE) calibration of the rest of the data. Although the fine structure of the transitions is not resolved in the present case, photoelectron imaging is capable of such resolution, as demonstrated recently by Cavanagh et al.[163]

To elucidate the two-photon character of some of the observed transitions, separate 355 nm photodetachment experiments were carried out with unfocused and slightly focused laser beams, corresponding to average fluences of 1.1×10^6 and 3.7×10^6 W/cm^2, respectively. Figure 5.1 displays the 355 nm results obtained under one or the other set of conditions. In particular, images 5.1.0 and 5.1.4–5.1.9 correspond to the low power density, while images 5.1.1–5.1.3 were recorded with the higher flux. The high-flux images are shown in split scale, highlighting different-intensity features. All 266 nm images (Figure 5.2) were collected with a mildly focused laser beam of 1.0×10^6 W/cm^2 fluence.

Overall, the photoelectron images and the corresponding spectra in Figures 5.1 and 5.2 include two types of features. The first are narrow bands, suggestive of atomic or atomic-like transitions. Others exhibit broader and more complex structures, as typically seen in detachment from molecular anions. These features, as well as energetic and angular considerations, provide the basis for structural characterization of each cluster species. The vertical detachment energies for bands with clearly defined maxima are indicated in Figures 5.1 and 5.2 next to the corresponding spectral features. The second

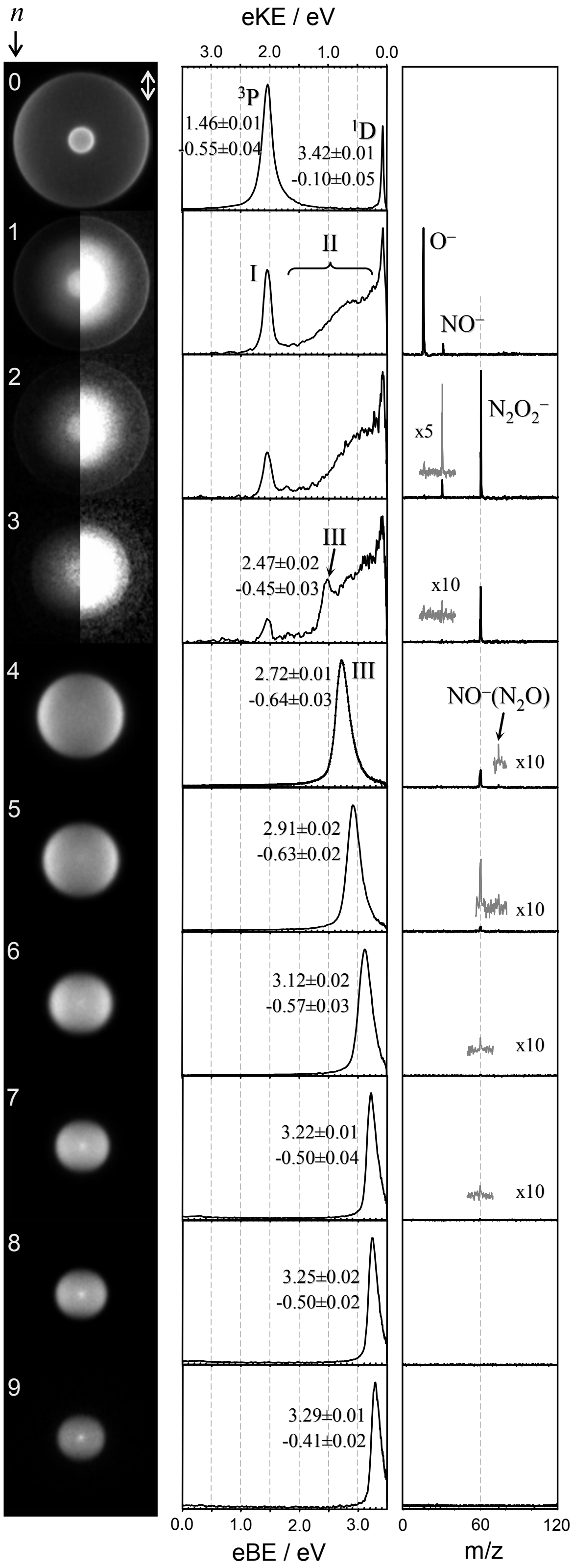
n
eKE / eV
3.0
2.0
1.0
0.0
0
1
2
3
4
5
6
7
8
9
^{3}P
1.46±0.01
-0.55±0.04
^{1}D
3.42±0.01
-0.10±0.05
I
II
III
2.47±0.02
-0.45±0.03
III
2.72±0.01
-0.64±0.03
2.91±0.02
-0.63±0.02
3.12±0.02
-0.57±0.03
3.22±0.01
-0.50±0.04
3.25±0.02
-0.50±0.02
3.29±0.01
-0.41±0.02
O⁻
NO⁻
x5
$N_2O_2^-$
x10
$NO^-(N_2O)$
x10
x10
x10
x10
0.0
1.0
2.0
3.0
eBE / eV
0
60
120
m/z

Figure 5.1 Photoelectron images (left column), the corresponding photoelectron spectra (middle column), and photofragment-ion mass spectra (right column) for the $[O(N_2O)_n]^-$, $n = 0$–9 cluster anion series obtained at 355 nm. The vertical double arrow in the $n = 0$ photoelectron image defines the laser polarization axis for all images. All images are shown on the same velocity scale. The photoelectron spectra are normalized to the corresponding maximum intensities. The vertical detachment energies along with anisotropy parameters for bands with clearly defined maxima are indicated next to the corresponding spectral features. See the text for band assignments and further details. The photofragmentation spectra are normalized relative to the parent ion intensity for each species, so that their decreasing relative intensities reflect the corresponding diminishing photofragmentation cross-sections.

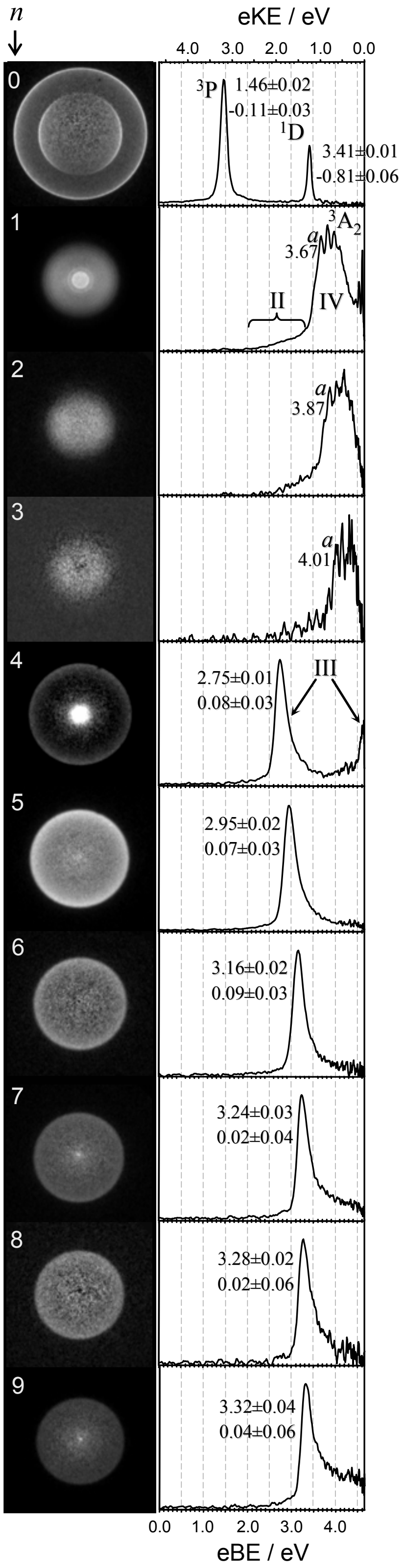

n
eKE / eV
4.0
3.0
2.0
1.0
0.0
0
^{3}P
1.46±0.02
-0.11±0.03
^{1}D
3.41±0.01
-0.81±0.06
1
a
3.67
^{3}A$_2$
II
IV
2
a
3.87
3
a
4.01
4
2.75±0.01
0.08±0.03
III
5
2.95±0.02
0.07±0.03
6
3.16±0.02
0.09±0.03
7
3.24±0.03
0.02±0.04
8
3.28±0.02
0.02±0.06
9
3.32±0.04
0.04±0.06
0.0
1.0
2.0
3.0
4.0
eBE / eV

Figure 5.2 Photoelectron images and the corresponding photoelectron spectra for the $[O(N_2O)_n]^-$, $n = 0–9$ cluster anion series obtained at 266 nm. All images are shown on the same velocity scale. The spectra are normalized to the corresponding maximum intensities. The vertical detachment energies along with anisotropy parameters for bands with clearly defined maxima are indicated next to the corresponding spectral features. See the caption to Figure 5.1 and the text for further details and band assignments.

values, shown just below the VDEs, are the anisotropy parameters (β_2) determined for the corresponding transitions.

5.3.1 The 355 nm Photoelectron Images

The unsolvated O^- photoelectron spectrum at 355 nm (Figure 5.1.0) shows two peaks corresponding to the $O(^3P, ^1D) \leftarrow O^-(^2P)$ transitions with the detachment energies of 1.46 and 3.42 eV, respectively. Similar features (without any measurable solvation-induced shifts) are also present in datasets 5.1.1–5.1.3. The intensities of these signals increase relative to other spectral features upon slight focusing of the laser beam. (Accordingly, in Figure 5.1 we have chosen to display the higher-flux results for n = 1–3, in order to accentuate the O^- features.) This nonlinear behavior indicates that the unshifted O^- transitions in $[O(N_2O)_n]^-$, n = 1–3 result from a two-photon process, ascribed to the photodissociation of the $N_2O_2^-$ cluster core and evaporation of solvent molecules, followed by O^- fragment photodetachment. This nonlinear behavior was not observed for the other transitions in the same spectra.

For brevity, we will refer to these two-photon bands as type I transitions. Similar O^- fragment signatures were seen in the previous studies of NNO_2^- at 532 and 266 nm, [143,147] as well as in the photoelectron spectroscopy studies of the $ONNO^-$ isomer at 355 and <420 nm.[12,143] As discussed in the Introduction, past experiments under similar ion-source conditions have yielded almost exclusively the covalent, Y-shaped (NNO_2^-) isomer of $N_2O_2^-$.[143,147] This isomer is expected to be dominant among the n = 1 species in our experiment. Although the 355 nm photon energy is insufficient for direct detachment of Y-shaped NNO_2^-,[147] the observed type I signals are consistent with its photodissociation, followed by O^- fragment photodetachment. In addition to the type I transitions, dataset 5.1.1 contains a broad band labeled II. This feature is ascribed to direct photodetachment of the $ONNO^-$ isomer,[12,143,148] which is also present in the ion beam.

For $n = 2$ and 3 (Figures 5.1.2 and 5.1.3, respectively), type I (O^- fragment) features are also observed, as well as analogues of band II. While the former do not show any solvation-induced shift, band II moves to progressively higher binding energies as n increases, consistent with solvent stabilization of the $ONNO^-$ anion. These observations suggest similar molecular-anion core structures persisting in the $n = 1$–3 cluster size range. However, Figure 5.1.3 ($n = 3$) contains an additional peak (labeled III) at eBE = 2.47 eV.

The $n = 4$-9 data are similar to $n = 0$ in that the overall structure of the photoelectron spectra is invariant with respect to the laser flux conditions employed in the experiment. The absolute signal levels are significantly larger for $n = 4$–9, compared to $n = 1$–3, and the corresponding photoelectron spectra are strikingly different. Each of the larger species exhibits just one intense and relatively narrow (atomic-like) transition, which peaks at progressively higher binding energies as n increases. The comparison of spectra 5.1.3 and 5.1.4-5.1.9 in Figure 5.1 suggests that the type III transition, observed for $n = 3$, belongs to this progression. For $n = 4$ and 5, type III features are centered at eBE = 2.72 and 2.91 eV, respectively, compared to 2.47 eV for $n = 3$. By interpolation, this spectral series is consistent with $O(^3P) \leftarrow O^-(^2P)$ photodetachment in $O^-(N_2O)_n$, progressively shifted due to solvation with additional N_2O molecules. The angular distributions of the type III transitions for $n \geq 3$ are also qualitatively similar to the corresponding transition in unsolvated O^- ($n = 0$) at the same wavelength, as reflected by the β_2 values included in Figure 5.1.

In summary, the 355 nm photoelectron imaging results suggest a molecular-anion core for the $[O(N_2O)_n]^-$, n = 1-3 clusters and an O^- core for n = 4–9. The exact nature of the covalent core cannot be established based on these data alone, but the results are consistent with both the Y-shaped NNO_2^- and $ONNO^-$ isomers identified by Posey and Johnson.[143] Although we expect the NNO_2^- structure to be dominant under the ion generation conditions employed in the present work, only $ONNO^-$ undergoes direct photodetachment at 355 nm, resulting in band II in the photoelectron spectra shown in Figures 5.1.1–5.1.3.

5.3.2 The 266 nm Photoelectron Images

In the 266 nm data presented in Figure 5.2, a new molecular-type transition (labeled IV) appears for n = 1–3. Band IV shows partially resolved vibrational structure, particularly clear in dataset 5.2.1, which allows us to identify it as a signature of the Y-shaped NNO_2^- anion, arising from detachment to the $^3A_2$ state of the neutral.[147] In order to quantify the solvation-induced shift of band IV, we identify the first (lowest-eBE) vibrational peak (labeled *a*) and use it as a marker (i.e., the detachment energies indicated in Figures 5.2.1-5.2.3 correspond to transition *a*).

The $ONNO^-$ signal (band II, most prominent in dataset 5.2.1) appears as a weak, low-eBE tail of band IV, at a small fraction of the NNO_2^- signal intensity. The two-photon signal from the O^- fragment, seen at 355 nm for $n = 1\text{-}3$, is not observed at 266 nm. Although its absence may be attributed partially to a smaller 266 nm O^- channel dissociation cross-section (compared to 355 nm), we believe that the lower 266 nm laser fluence is primarily responsible for the reduction of the two-photon signal.

We also note that the photoelectron spectrum in Figure 5.2.3 contains no band that can be attributed to the O^- cluster core. This may seem surprising, as the 355 nm results clearly indicate the presence of some $O^-(N_2O)_3$ clusters (feature III in spectrum 5.1.3). However, using band II (arising from the $ONNO^-$ cluster core) as a reference, we do not expect that the signal due to $O^-(N_2O)_3$ in Figure 5.2.3 would rise above the noise level.

The 266 nm spectra for the larger clusters ($n > 3$) are consistent with those obtained at 355 nm, suggesting atomic-anion (O^-) cluster cores. The VDEs indicated for the type III bands in Figures 5.1 and 5.2 differ only within the experimental uncertainty. For $n = 4$, the higher-energy $O(^1D) \leftarrow O^-(^2P)$ photodetachment transition is also observed at a near-zero eKE. This transition is inaccessible for $n > 4$ due to the additional solvent stabilization. While some of the 266 nm images for $n \geq 7$ do show faint central features (eKE ≈ 0), the corresponding contributions to the photoelectron spectra in the low-eKE range are negligibly small.

The anisotropy parameters determined for the $O^-(N_2O)_n$, $n > 3$ clusters at 266 nm (β ranging from 0.02 to 0.08 in Figures 5.2.4–5.2.9) are significantly different from the $\beta = -0.11 \pm 0.03$ value for the corresponding transition in unsolvated O^- (Figure 5.2.0). These variations are thought to reflect resonant photoelectron scattering off the N_2O solvent[44] and will be the subject of an upcoming investigation.

In summary, the 266 nm photoelectron data indicate the same abrupt change in the $[O(N_2O)_n]^-$ cluster-core structure occurring at $n = 4$ as seen in the 355 nm data. The switch from broad molecular transitions in the $n = 1$–3 range to atomic-like bands for $n \geq 4$ suggests a molecular-to-atomic anion ($NNO_2^- \rightarrow O^-$) core switching.

5.3.3 355 nm Photofragmentation

Also reported in Figure 5.1 are the 355 nm photofragment mass-spectra for the mass-selected $[O(N_2O)_n]^-$ cluster anions in the $n = 1$-9 range. These spectra are acquired under the same laser fluence and normalized to the absolute parent ion intensities, and therefore can be used to compare the fragmentation yields for different parent anions. The decrease in the overall fragment-ion intensities with increasing n reflects the gradual closing of the fragmentation channel.

For $n = 1$, the O^- and NO^- photofragments are attributed to the dissociation of NNO_2^- and $ONNO^-$, respectively. The intense O^- signal in the fragment mass-spectrum complements the assignment the O^- band (feature I) in photoelectron spectrum 5.1.1 to the photodetachment of the O^- photofragment of NNO_2^-. The fragmentation results are therefore consistent with a predominance of the NNO_2^- parent-anion structure for $n = 1$.

For $n \geq 2$, the dominant peak in each of the photofragment-ion mass-spectra corresponds to $[O(N_2O)]^-$ ($m/z = 60$). This fragment anion can be formed via at least two different mechanisms: (1) A secondary reaction of the nascent O^- photoproduct of the NNO_2^- cluster core with an N_2O solvent molecule to form a hot $N_2O_2^-$ anion, which may relax by evaporation of any remaining N_2O molecules. (2) Photoexcitation of the NNO_2^- cluster core, which then internally converts to the ground electronic state, leading to cluster predissociation via the loss of solvent molecules. The photofragmentation of NNO_2^- (H_2O) shows that the main photofragment in that case is also $[O(N_2O)]^-$ or $N_2O_2^-$, with a branching ratio of ~96% and the remaining fraction accounting for the smaller contributions from O^- and $O^-(H_2O)$.[164] This result rules out the nascent O^- reaction with the solvent and provides a solid indication that predissociation (following the electronic excitation of the cluster core) is an effective fragmentation mechanism for the NNO_2^- based clusters. This observation echoes with the work of Bowers and co-workers[165,166] for the photodissociation of $CO_3^-(H_2O)$, where they reported a cross section for the CO_3^- product that was 31 times greater than that for the $O^-(H_2O)$ fragment. (The CO_3^- fragmentation channel was also explained by means of vibrational predissociation).[166]

The $N_2O_2^-$ fragment persists through $n = 7$, with no observable contributions from $N_2O_2^-(N_2O)_k$, $k > 0$. Within either of the two above mechanisms of its appearance, the

$N_2O_2^-$ photofragment is a signature of the $N_2O_2^-$ covalent core in the parent cluster. Therefore, the most important aspect of the fragmentation results is the conspicuous drop in the $N_2O_2^-$ yield between $n = 3$ and $n = 4$, which continues with increasing n until its complete disappearance after $n = 7$. This decrease in the $N_2O_2^-$ channel (and, therefore, the overall fragmentation yield) reflects a diminishing fraction of the parent clusters with a covalent $N_2O_2^-$ core over a growing fraction of clusters with an atomic O^- core, which are responsible for the strong photodetachment signals observed for $n \geq 4$. These results complement the photoelectron imaging data in the sense that some degree of coexistence between the atomic and molecular cluster cores is shown to persist over a small range of cluster sizes. More importantly, the two experiments concur in that the main transition from a molecular cluster core to an atomic core occurs between $n = 3$ and $n = 4$.

5.4 Discussion

The present study is the first investigation of the $[O(N_2O)_n]^-$ cluster series in the size range up to $n = 9$ via photoelectron spectroscopy. The experimental results reveal a transition from the molecular (NNO_2^-) to atomic (O^-) cluster core structure occurring between $n = 3$ and 4. Although both core types may coexist, to a degree, through the entire cluster size range studied, an overwhelming predominance of clusters with the molecular core is seen for $n = 1$–3, while the atomic anion based clusters clearly dominate for $n = 4$–9. Accordingly, the $[O(N_2O)_n]^-$ anion population can be described as a combination of the competing distributions of the $NNO_2^-(N_2O)_{n-1}$ and $O^-(N_2O)_n$

clusters. Judging by the signal levels, the $NNO_2^-(N_2O)_{n-1}$ distribution peaks at $n = 1$ and decreases as the cluster size increases, with a very quick falloff after $n = 3$ where the $O^-(N_2O)_n$ series emerges.

The core-switching phenomenon is expected to depend on the relative stabilities of the $O^-(N_2O)_n$ and $NNO_2^-(N_2O)_{n-1}$ cluster anions which is schematically outlined in Figure 5.3. For $n = 1$, covalent bonding in NNO_2^- is energetically favored over the solvation of O^- by N_2O. However, O^- should be solvated more effectively than NNO_2^- due to the more localized charge of the atomic anion. As the number of solvent molecules increases, the difference between the solvent stabilization energies for $O^-(N_2O)_n$ and $NNO_2^-(N_2O)_{n-1}$ may exceed the extra covalent bond energy in NNO_2^-, making the O^--based clusters more favorable energetically. Similar arguments were made previously for the core-switching in $(CO_2)_n^-$.[9,10,167]

The relative stabilities of the $NNO_2^-(N_2O)_{n-1}$ and $O^-(N_2O)_n$ clusters, ΔE_n, can be estimated from the solvent evaporation and bond dissociation energies and expressed approximately as:

$$\Delta E_n = D_0(NNO_2^-) + \Delta_{n-1}\mathrm{VDE}(NNO_2^-) - \Delta_n\mathrm{VDE}(O^-).^{168} \tag{5.5}$$

In Equation 5.5, $D_0(NNO_2^-)$ is the $NNO_2^- \rightarrow O^- + N_2O$ bond dissociation energy, while $\Delta_{n-1}\mathrm{VDE}(NNO_2^-)$ and $\Delta_n\mathrm{VDE}(O^-)$ are the shifts in the NNO_2^- and O^- photoelectron band positions due to the interaction with $(n - 1)$ and n N_2O solvent molecules, respectively.

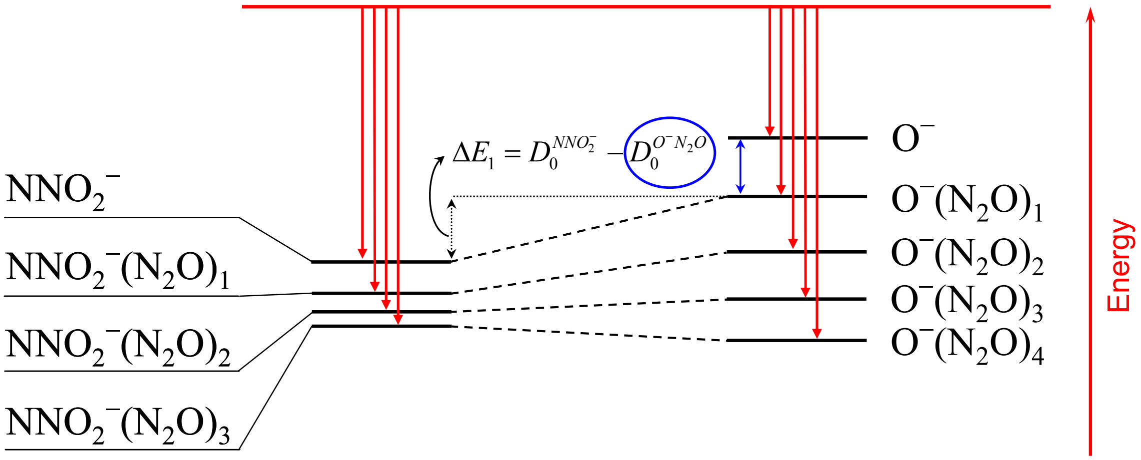

Figure 5.3 Schematic energy diagram of the relative stabilities for $NNO_2^-(N_2O)_{n-1}$ and $O^-(N_2O)_n$ cluster anions illustrating the core-switching mechanism according to thermodynamic model. The relative stabilities, ΔE_n, can be estimated from the experimental values of solvent evaporation and bond dissociation energies using Equation 5.5.

Specifically,

$$\Delta_{n-1}\mathrm{VDE}(\mathrm{NNO_2^-}) = \mathrm{VDE}[\mathrm{NNO_2^-}(\mathrm{N_2O})_{n\text{-}1}] - \mathrm{VDE}[\mathrm{NNO_2^-}] \quad (5.6)$$

$$\Delta_{n}\mathrm{VDE}(\mathrm{O^-}) = \mathrm{VDE}[\mathrm{O^-}(\mathrm{N_2O})_{n}] - \mathrm{VDE}[\mathrm{O^-}]. \quad (5.7)$$

The determination of relative stabilities using Equation 5.5 is based on several approximations. In particular, while assuming that solvent evaporation energy is implicit in the VDE shifts, we neglect the clustering energies on the corresponding neutral surfaces. In determining $\Delta_{n-1}\mathrm{VDE}(\mathrm{NNO_2^-})$, we will use the solvation-induced shift of band IV's peak *a* identified in Figures 5.2.1 – 5.2.3.

Two independent measurements of the $\mathrm{NNO_2^-} \rightarrow \mathrm{O^-} + \mathrm{N_2O}$ dissociation are available in the literature, giving the rather disparate $D_0(\mathrm{NNO_2^-})$ values of 1.40 ± 0.03 eV[148] and 0.57 ± 0.05 eV.[149] In both cases, the dissociation energy is determined from the maximum fragment kinetic energy release in the dissociative photodetachment of $\mathrm{NNO_2^-}$, but via two different pathways: $\mathrm{O(^3P) + N_2O + e^-}$ at 532 nm in Reference [148] and $\mathrm{N(^4S) + NO_2 + e^-}$ at 266 nm in Reference [149]. The latter channel has a better Franck-Condon overlap with the parent $\mathrm{NNO_2^-}$ owing to the bent equilibrium geometry of $\mathrm{NO_2}$. It is therefore expected to yield a less excited $\mathrm{NO_2}$ photofragment (compared to $\mathrm{N_2O}$ in the other channel) and provide a more accurate determination of $D_0(\mathrm{NNO_2^-})$.

Though the VDEs for both the $\mathrm{O^-}$ and $\mathrm{NNO_2^-}$ cluster core types are not available for all cluster sizes studied due to the size-dependent core-preference, we have estimated the "missing" VDE values by interpolating or extrapolating the observed band positions for the series of each core-type. Figure 5.4 displays plots of the cluster-size-dependent

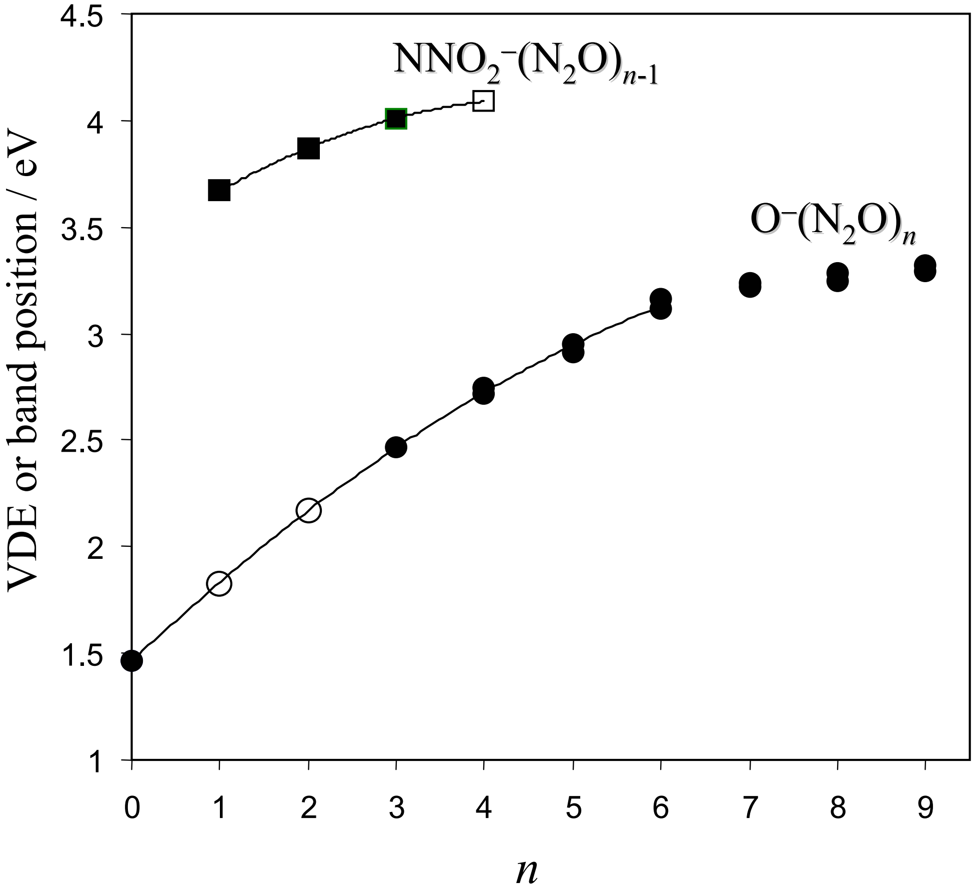

Figure 5.4 The detachment energies of bands III and IV (peak a) for the $O^-(N_2O)_n$ and $NNO_2^-(N_2O)_{n-1}$ cluster anions, respectively. The corresponding bands appear in the photoelectron spectra in Figures 5.1 and 5.2. The solid symbols indicate the direct experimental results, while the open symbols show the interpolated or extrapolated “missing” values.

detachment energies for $O^-(N_2O)_n$ and $NNO_2^-(N_2O)_{n-1}$, determined from bands III and IV (peak *a*), respectively. The solid symbols indicate the direct experimental results, while the open symbols show the interpolated or extrapolated "missing" values. Since the solvent-induced shift in the VDE between $n-1$ and n is approximately equal to the binding energy of the n-th solvent molecule to the cluster, we estimate that the sequential binding energies of the first, second, third, and fourth N_2O's to O^- are 0.37, 0.34, 0.30, and 0.25 eV, respectively. These numbers are strikingly close to the corresponding values of 0.37, 0.34, 0.30, and 0.28 eV for the sequential binding energies of N_2O to OH^- determined previously by Lineberger and co-workers.[169]

From the data summarized in Figure 5.4 and the two aforementioned values of $D_0(NNO_2^-)$, the relative stabilities of the $O^-(N_2O)_n$ and $NNO_2^-(N_2O)_{n-1}$ cluster anions can be calculated using Equation 5.5. The relative stabilities calculated using each literature value of D_0 are listed in Table 5.1. Positive ΔE_n indicate that the corresponding NNO_2^- based clusters are more stable than those with the O^- core. The estimated ΔE_n values based on $D_0 = 1.40$ eV (first column in Table 5.1) suggest that from the thermodynamic standpoint, the $NNO_2^- \rightarrow O^-$ core-switching should not happen at $n = 4$, where our experimental data clearly indicates that the O^- based clusters become the predominant species. However, the relative stabilities calculated using $D_0 = 0.57$ eV (second column in Table 5.1) do show that the core-switching should occur at around $n = 3$, which agrees well with the first appearance of the type III transitions at this cluster size in our experiment.

It is also instructive to compare the experimental estimates of the relative stabilities for the $[O(N_2O)_n]^-$ series with theoretical predictions. To elucidate the relative stabilities of the cluster isomers, *ab initio* calculations were carried out for $O^-(N_2O)_n$ and $NNO_2^-(N_2O)_{n-1}$, $n = 1–4$, using the GAUSSIAN 03 program package.[170] The geometries were optimized at the unrestricted second-order Møller-Plesset perturbation theory (UMP2/aug-cc-pVDZ) level, followed by harmonic frequency calculations at the same theory level to verify that the stationary points found correspond to true potential minima. The computed energies were corrected for zero-point vibrational energies and basis set superposition errors.[171]

The Hartree-Fock (HF) wave functions for all $[O(N_2O)_n]^-$, $n = 1–4$ structures, except for NNO_2^-, possess internal instabilities,[172,173] which can lead to oscillatory behavior during geometry optimization and symmetry breaking in the nuclear framework.[174] In addition, the Møller-Plesset energies based on unstable wavefunctions are also questionable. Therefore, the MP2 results should be viewed as mere estimates to compare with the experimental findings. Figure 5.5 shows the optimized structures for $[O(N_2O)_n]^-$ cluster anions obtained at the MP2/aug-cc-pVDZ level of theory. For $n = 1$, in addition to the NNO_2^- global minimum,[148,175] we find a shallow potential minimum corresponding to a planar $O^-{\cdot}N_2O$ ion-molecule complex, in which the N_2O is bent at 173.4°. The number of structural isomers increases with the cluster size. We found five stable $[O(N_2O)_2]^-$ structures: three with the NNO_2^- cluster core and two with the O^- core. In the calculations for n=3–4 clusters, we did not locate any potential minima corresponding to O^-

Table 5.1 Relative stabilities (ΔE_n/eV) of the $NNO_2^-(N_2O)_{n-1}$ and $O^-(N_2O)_n$ cluster anions. Positive ΔE_n values indicate that the corresponding NNO_2^- based clusters are more stable than those with the O^- core.

n	Experiment[a]	Experiment[b]	MP2[c]	CCSD[d]	CCSD[e]
1	1.03	0.20	0.33	1.01	0.98
2	0.89	0.06	0.24	0.91	–
3	0.73	–0.10	–	–	–
4	0.56	–0.29	≤ 0.07	≤ 0.62	–

[a] Based on the value of $D_0(NNO_2^-) = 1.40 \pm 0.03$ eV by Osborn et al.[148]

[b] Based on the value of $D_0(NNO_2^-) = 0.57 \pm 0.05$ eV by Li et al.[149]

[c] UMP2/aug-cc-pVDZ

[d] CCSD/6-31+G*//MP2/aug-cc-pVDZ

[e] CCSD/aug-cc-pVDZ

based structures. In the case of $O^-(N_2O)_3$, the energies oscillate and the geometry optimization does not converge. For $O^-(N_2O)_4$, we found one stationary point, which is a first-order saddle point corresponding to the structure of D_2 symmetry.

In general, the instability of a HF wavefunction indicates that the independent particle approximation breaks down and there is a broken symmetry solution with lower energy. Thus, a more sophisticated computational model with higher electron correlation and/or multireference approach[176] is necessary for an adequate description of such species. It has been shown that Coupled-Cluster (CC) methods can be successfully applied to treat the instability problem,[177-179] provided that the system can be described by a single configuration wave function. The CC calculations with single and double excitations (at the CCSD/6-31+G*//MP2/aug-cc-pVDZ level) were carried out for some of the cluster structures of interest. Since the geometries and the energies of the clusters can be quite different depending on the particular method and basis set employed in the calculations, for the comparison to CCSD/6-31+G*//MP2/aug-cc-pVDZ results, the geometry optimizations followed by frequency calculations were also performed at the CCSD/aug-cc-pVDZ for $n = 1$ species. No instabilities are detected for the wave functions with the CC calculations.

The relative stabilities ΔE_n, defined as the energy differences between the most stable $O^-(N_2O)_n$ and $NNO_2^-(N_2O)_{n-1}$ structures computed from MP2 and CC results are summarized in the last four columns of Table 5.1. Although both the MP2 and CC calculations find that NNO_2^- is more stable than $O^- \cdot N_2O$, there is a significant discrepancy in the computed relative energies: MP2 estimates that NNO_2^- is more stable

(a)

NNO_2^-, Y-shape C_{2V} $\quad$ $O^-(N_2O)_1$, C_S

(b)

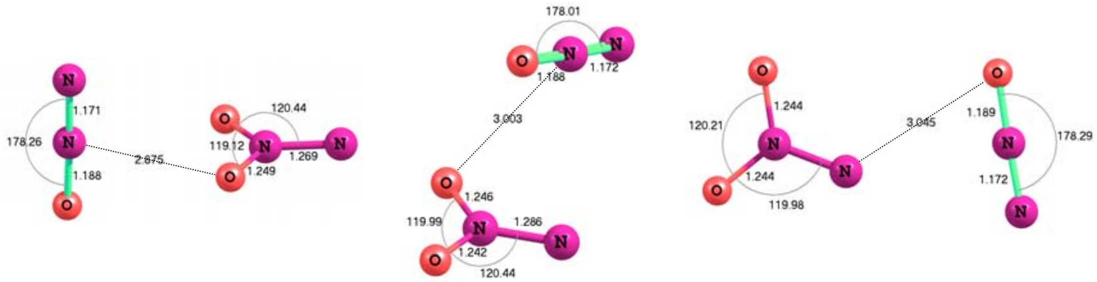

$NNO_2^-(N_2O)_1$, C_S $\quad$ $NNO_2^-(N_2O)_1$, C_1 $\quad$ $NNO_2^-(N_2O)_1$, C_S

$O^-(N_2O)_2$, C_{2h} $\quad$ $O^-(N_2O)_2$, C_2

(c)

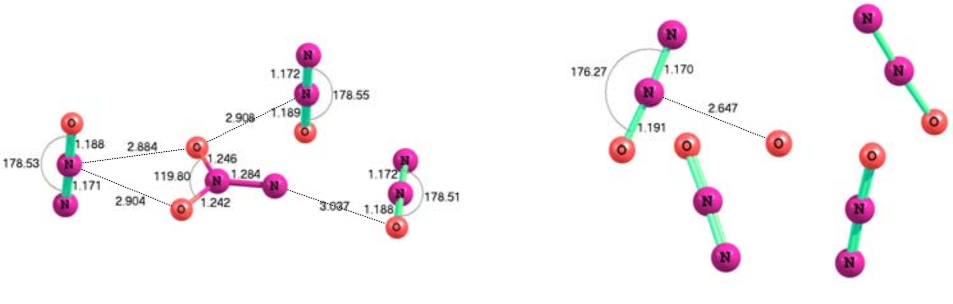

$NNO_2^-(N_2O)_3$, C_1 $\quad$ $O^-(N_2O)_4$, D_2

Figure 5.5 Optimized structures for the $NNO_2^-(N_2O)_{n-1}$ and $O^-(N_2O)_n$, n=1,2, and 4 cluster anions obtained at the MP2/aug-cc-pVDZ level of theory. Structures for the clusters with n=3 are omitted here since geometry optimization did not converge for $O^-(N_2O)_3$. Also, the optimized structure of D_2 symmetry for $O^-(N_2O)_4$ clusters (c) corresponds to a first-order saddle point. See text for further details.

by a mere 0.33 eV, while CC methods yield a difference of about 1 eV. Nonetheless, both the MP2 and CC energies are consistent with the lack of $O^{-}\cdot N_2O$ signatures in the experimental data (Figures 5.1.1 and 5.2.1). The relative stabilities determined by both the MP2 and CC methods indicate that the energy difference between the $O^{-}(N_2O)_n$ and $NNO_2^{-}(N_2O)_{n-1}$ clusters decreases steadily with increasing n, which is consistent with the assumption of O^{-} being solvated more effectively than NNO_2^{-} and is necessary for the core switching to occur. However, both the MP2 and CC methods predict that the NNO_2^{-} based species remain favored energetically even for $n = 4$, where the experiment indicates a nearly complete switch to the O^{-} core type.

Specifically, MP2 predicts the $NNO_2^{-}(N_2O)_3$ to be more stable than $O^{-}(N_2O)_4$ by only 0.07 eV, while the CCSD/6-31+G*//MP2/aug-cc-pVDZ estimates a 0.62 eV difference. We note also that MP2 provides a better quantitative agreement with the estimates of ΔE_n based on $D_0(NNO_2^{-}) = 0.57$ eV,[149] which are in accord with the present experimental observations. The CC calculations closely match the relative stabilities based on the 1.40 eV value of $D_0(NNO_2^{-})$,[148] which are not in agreement with the present experimental results. This outcome is surprising, since one should not expect MP2 performance to be superior to the CC methods, especially given the wave function instability problems discussed above. Therefore, the observed agreement of the MP2 results with the experiment is likely serendipitous.

To conclude, we have obtained two sets of relative stabilities ΔE_n of the $NNO_2^{-}(N_2O)_{n-1}$ vs. $O^{-}(N_2O)_n$ cluster structures, summarized in columns 1 and 2 of Table 5.1. Per Equation 5.5, these estimates are based on our own experimental data and the two available (yet drastically different) measurements of the NNO_2^- bond dissociation energy. One of the ΔE_n series supports and the other contradicts the simple thermodynamic model of the experimentally observed NNO_2^- to O^- core-switching. Although the present experimental results are compelling, the discrepancies between past experimental measurements and theoretical models call for caution in concluding that the suggested thermodynamic mechanism is the only possible explanation for the observed core-switching. Alternatively, it could be possible for the larger clusters ($n \geq 4$) to be formed initially with the O^- core and remain trapped in the corresponding (possibly metastable) state on the timescale of our experiment (tens of microseconds). Such kinetic model would imply the existence of a barrier for the association reaction of O^- with any one of the surrounding N_2O solvent molecules. Certainly, additional experimental data on NNO_2^- bond dissociation energy would help to draw a confident conclusion on the core-switching mechanism. At present, the work of Li and Continetti[149] is believed to provide more accurate determination of $D_0(NNO_2^-)$, supporting the thermodynamic picture of the core-switching reported here.

5.5 Summary

Photoelectron imaging experiments on $[O(N_2O)_n]^-$, n =0–9 at 266 and 355 nm provide clear evidence of a switch from the covalent NNO_2^- cluster core to the atomic O^- core occurring between n = 3 and 4. Although there is some coexistence between the molecular (NNO_2^- and perhaps some $ONNO^-$) and atomic (O^-) core structures, the results suggest an overwhelming predominance of the Y-shaped NNO_2^- cluster core structure for $n = 1–3$ and the atomic O^- core for $n > 3$. The core-switching is explained in terms of a simple thermodynamic model based on the relative stabilities of the $O^-(N_2O)_n$ and $NNO_2^-(N_2O)_{n-1}$ cluster anions. The model argues that despite the greater stability of NNO_2^- relative to the $O^- + N_2O^-$ dissociation limit, an O^- cluster core becomes energetically favored over NNO_2^- for $n > 3$, due to the more effective solvation of the atomic anion. Within this thermodynamic picture, the present results lend indirect support to the past measurement of NNO_2^- bond dissociation energy by Li and Continetti.[149]

CHAPTER 6

TIME-RESOLVED IMAGING OF I_2^- AND IBr^- DIATOMIC MOLECULAR ANIONS

6.1 Introduction

The dynamics of molecular systems on excited potential energy surfaces are most effectively unraveled via direct time-resolved measurements. With the development of new advanced techniques of femtosecond spectroscopy,[180-183] our view of chemical reactions has evolved from the popular emphasis on atomic rearrangements to the explicit accent on the more fundamental dynamics involving transformations of the electronic structure.[28,29] Conceptually, chemical reactions can be viewed in terms of atomic motions on the electronic potential energy landscapes or as the structural and energetic changes involving the molecular orbitals. Both points of view are closely interrelated, yet it is the electrons that control chemical bonding and ultimately determine the reaction's outcome.

In the field of negative-ion spectroscopy, a revolutionary breakthrough in the observation of dynamics from the electronic perspective was accomplished with the Neumark group's introduction of femtosecond photoelectron spectroscopy.[28] The technique, based on a combination of time-resolved pump-probe spectroscopy and anion photoelectron spectroscopy[184] was successfully applied to investigate the intricate details of the photodissociation of I_2^-.[27,185,186] Neumark's original experiments showed that following the excitation with a 780 nm pump pulse, the dissociation is essentially complete within the first 320 fs, yet the interaction between the separating fragments lingers for a further 400 fs.[27,186] These exit-channel dynamics have been attributed to the polarization-induced attraction between the I^- anion and neutral I atom, which corresponds to a shallow well on the long-range part of the $I + I^-$ dissociation potential.

A further advance, which greatly enhanced the capabilities of time-resolved photoelectron spectroscopy, came very recently with the introduction of the photoelectron imaging approach to negative-ion photodetachment. Imaging[31] has proved powerful in many facets of gas-phase dynamics[32,187] and its application to time-resolved studies, as a means of studying electronic-structure evolution in reactions, is particularly rewarding.[188-201] The time-dependent photoelectron angular distributions reflect the transformations of the molecular orbitals, while the time-resolved energy spectra shed light on the details of the reactive potential energy surface and evolution of the molecular structure in real time, along the reaction coordinate.

The I_2^- system was revisited several times,[185,186,201] yet the main experimental focus has remained on the evolution of the energetics, including the effects of interaction between the separating fragments. This emphasis has been largely unaffected even by the introduction of the photoelectron imaging approach,[201] partially due to the complexity of the theory involved in the analysis and interpretation of time-resolved photoelectron angular distributions.[191] Nonetheless, Neumark's group did report time-dependent changes to the photodetachment anisotropy in I_2^- photodissociation.[201] Of particular note is the intriguing transient increase in the β_2 anisotropy parameter occurring around 650 fs, which was hypothesized to reflect the passage through a shallow polarization-induced minimum on the long-range potential.

In this Chapter, we discuss photodissociation dynamics of I_2^- and IBr^- molecular anions studied via time-resolved photoelectron imaging spectroscopy. For clarity, the rest of the Chapter is divided into three main parts.

The first portion of the chapter addresses the bond breaking process from the energetic perspectives. The dynamics along the reaction coordinate in the photodissociation of IBr^- is discussed in a side-by-side comparison with the results of I_2^-, examined under similar experimental conditions. The I_2^- anion, extensively studied in the past, is used as a reference system for interpreting the IBr^- results. The data provide rigorous dynamical tests of the anion electronic potentials. The evolution of the energetics revealed in the time-resolved (780 nm pump, 390 nm probe) I_2^- and IBr^- photoelectron images is compared to the predictions of classical trajectory calculations, with the time-resolved photoelectron spectra modeled assuming a variety of neutral states accessed in the photodetachment. In light of good overall agreement of the experimental data with the theoretical predictions, the results are used to construct an experimental image of the IBr^- dissociation potential as a function of the reaction coordinate.

The second part of the Chapter focuses on evolution of the photoelectron angular distribution during photo-induced dissociation of the anions, with a particular emphasis on the observed dual-center quantum interference effect for the symmetric I_2^-. No energetic changes are observed after about 700 fs, but the evolution of the photoelectron anisotropy persists for up to 2.5 ps, indicating that the electronic wavefunction of the dissociating anion continues to evolve long after the asymptotic energetic limit of the reaction has been effectively reached. The timescale of the anisotropy variation corresponds to a fragment separation of the same order of magnitude as the de Broglie wavelength of the emitted electrons (λ = 35 Å). These findings are interpreted by considering the effect of I_2^- inversion symmetry and viewing the dissociating anion as a dynamic molecular-scale "interferometer", with the electron waves emitted from two separating centers. The predictions of the model are in agreement with the present experiment and shed new light on previously published results.[201]

The reminder of the chapter is devoted to a complimentary time-resolved study on I_2^- using a different (390 nm pump, 390 nm probe) energy scheme. The time-resolved photoelectron data shows that the dissociation on B $1/2_g$ ($^2\Sigma^+$) state of I_2^- proceeds rapidly and the energy spectra becomes essentially that of I^- product within first 400 fs. The external filed mixing of B $1/2_g$ ($^2\Sigma^+$) and a′ $1/2_u$ ($^2\Pi$) states happens on the comparable time scale, which inevitably leads to the loss of interference-induced anisotropy variation from the very beginning of the first oscillation period.

6.2 Experimental

The experiments were carried out on the negative ion photoelectron imaging spectrometer described in Chapter 2. The apparatus employs pulsed negative-ion generation and mass-analysis techniques,[48,49] combined with a velocity-mapped,[202] imaging[31,32] scheme for detection of photoelectrons.

To generate I_2^- and IBr^-, the ambient vapour pressure of IBr seeded in Ar is expanded through a pulsed nozzle (General Valve Series 9 with a Kel-F poppet) operated at a repetition rate of 70 Hz into a high-vacuum chamber with a base pressure of 10^{-6} Torr (rising to 3×10^{-5} Torr when the pulsed valve is operated). The supersonic expansion is crossed with a 1 keV electron beam and the resulting anions are pulse-extracted into a 2 m long Wiley-McLaren time-of-flight mass spectrometer.[203] After the ion beam is accelerated to about 2.5 keV and focussed using an Einzel lens, it enters the detection region with a typical base pressure of 3-5x10^{-9} Torr. The ions are detected mass-selectively using a dual microchannel plate (MCP) detector (Burle, Inc.) at the end of the flight tube.

The mass-selected I_2^- and $I^{79}Br^-$ anions are photolyzed by the 780 nm pump pulses and the evolving electronic structure is probed via photodetachment with delayed 390 nm probe laser pulses. The pump-probe optical line arrangement and data collection for two-colour time-resolved experiments are described in detail in Chapter 2. The regeneratively amplified Ti:Sapphire laser system (Spectra Physics, Inc.) produces 1 mJ, 100 fs pulses at 780 nm. Half of the fundamental output is used as the pump beam, while the other half is channeled through the 100 μm thick BBO crystal of a femtosecond harmonics generator (Super Optronics, Inc.), producing 100 μJ pulses with a bandwidth of 5 nm at 390 nm. The spectral profile of the UV output is monitored using a fiberoptics spectrometer (Ocean Optics, Inc.). The 390 nm probe beam passes through a motorized translation stage (Newport ESP300 Universal Motion Controller) to enable controlled temporal separation of the pump and probe pulses. The pump and probe beam paths are combined before entering the reaction chamber using a dichroic beam splitter. The polarization vectors of the two beams are parallel to each other and to the ion beam axis. Both laser beams are mildly focussed using a 1 m focal length lens positioned approximately 45 cm before the intersection with the ion beam.

The position of zero delay is determined by overlapping the pump and probe pulses in a BBO crystal. By monitoring the third harmonic generation as a function of delay, the cross-correlation before the vacuum chamber entrance window is measured to be about 300 fs (full width at half-maximum). This defines the approximate time-resolution of the experiment. The passage of the beams through the chamber window introduces an additional (dispersion induced) pump-probe delay, which is accounted for by reference to the I_2^- experiments of the Neumark group at the same pump wavelength.[27,186,204]

The photodetached electrons are detected using velocity-map[205] imaging[31] in the direction perpendicular to the ion and laser beams. A 40 mm diameter MCP detector with a P47 phosphor screen (Burle Inc.) is mounted at the end of an internally μ-metal shielded electron flight tube. Images are obtained from the phosphor screen using a CCD camera (Roper Scientific Inc.). To suppress background signals, the potential difference across the two MCPs is only pulsed up to 1.8 kV for a 200 ns wide collection window, timed to coincide with the arrival of the photoelectrons. For the rest of each experimental cycle, the dual-MCP potential difference is maintained at 1.0-1.2 kV, which is not enough to produce a detectable signal.

Extraneous pump or probe photon detachment signals are removed using computer-controlled shutters in the pump and probe beam paths and the data acquisition and correction algorithm described previously in Chapter 2. Each of the images presented in this work represents the result of ~10^5-10^6 experimental cycles.

6.3 Time-Resolved Imaging of the Reaction Coordinate

This section outlines the application of time-resolved photoelectron imaging, supported by theoretical modeling, for "imaging" the reaction coordinate in IBr^- photodissociation, thus providing a rigorous dynamical test of the recently calculated potentials.[206,207] Although modern theory is capable of tackling, to a degree, the more challenging polyatomic systems, diatomic molecules afford the most straightforward tests of structure and dynamics. The present experiments on IBr^- are part of a side-by-side comparative study of the photodissociation dynamics of the I_2^- and IBr^- anions. The former has been studied extensively, both in isolation and in solvated environments.[27,185,186,208-224] Of particular note are the aforementioned experiments by the Neumark group.[27,186,204] The I_2^- anion, therefore, provides an excellent reference system for interpreting the results for IBr^-, for which few theoretical and experimental gas-phase studies are available.[206]

Figure 6.1 displays the relevant electronic potential energy curves for the I_2^- and IBr^- anions, as well as the corresponding neutral molecules. The energy scale for the neutrals in Figures 6.1(a) and (b) is not the same as for the anions in Figures 6.1(c) and (d). Considering the anions first, the ground X and excited A' state potentials of I_2^-,

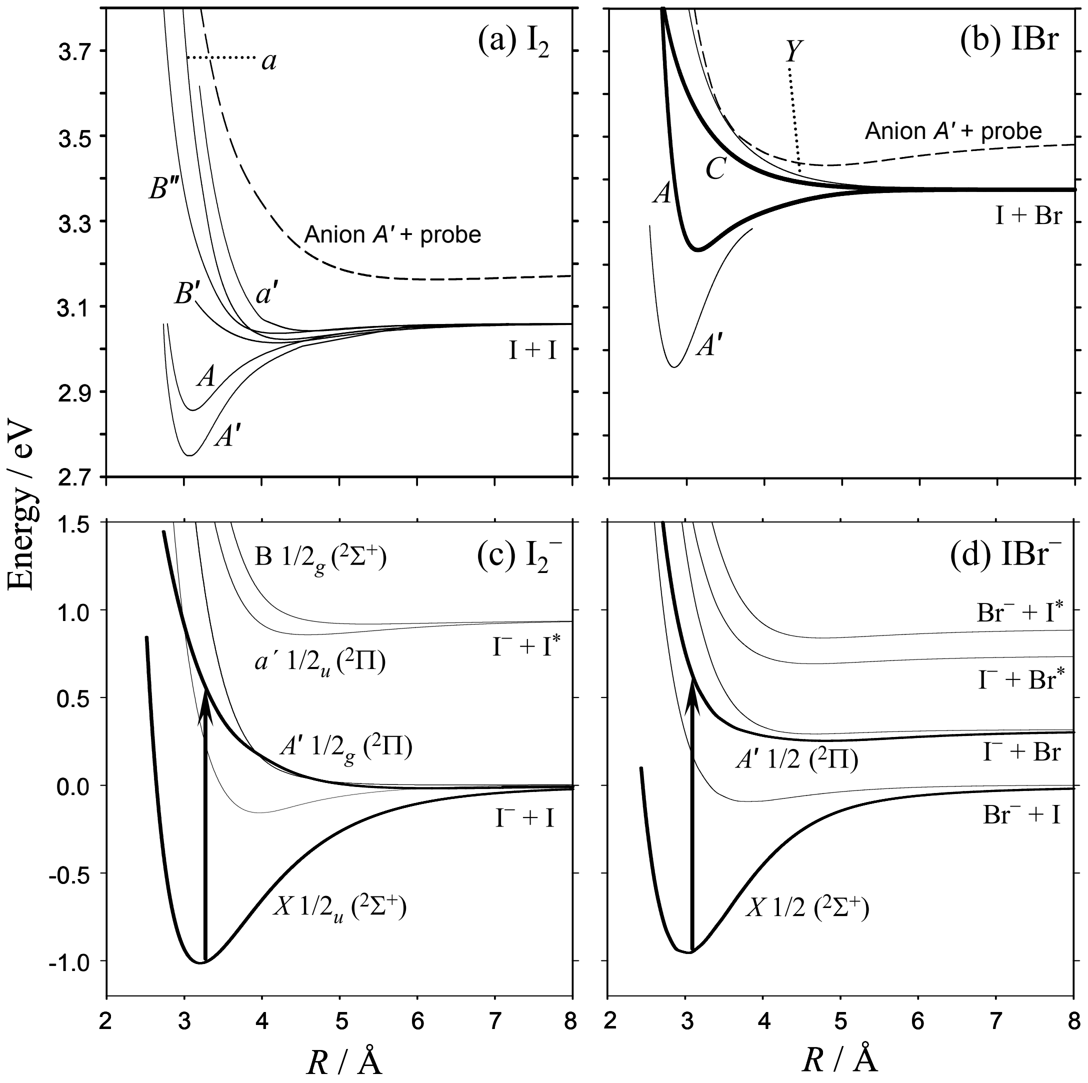

Figure 6.1 Potential energy curves for the relevant electronic states of (a) I_2, (b) IBr and the corresponding anions: (c) I_2^- and (d) IBr^-. The potential curves corresponding to the neutral states of I_2 and IBr are obtained from References [225-232] and [232-234], respectively. The I_2^- potentials are from the scaled calculations in References [235,236], with the exception of the *X* and *A′* states, which are experimentally determined in References [182,183,186,237]. The IBr^- curves are from References [206,207]. The vertical arrows in (c) and (d) represent the pump transition accessing the *A′* states of the respective anions. The dashed curves in (a) and (b) represents the *A′* anion potentials projected on the respective neutral manifolds by the addition of the probe photon energy. Further details are given in the text.

represented by bold lines in Figure 6.1(c), are taken from the experimental work of Zanni et al.,[182,183,186,237] while the other four I_2^- state potentials are from the scaled ab initio calculations of Faeder and Parson.[235,236] The IBr^- potentials in Figure 6.1(d) are the unmodified results of the ab initio calculations by Thompson and Parson[207] for the six lowest states of the anion,[206] with the bold curves again representing the ground *X* and excited *A′* states.

The vertical arrows in Figures 6.1(c) and (d) represent the 780 nm pump photon energy used in the experiments described in this chapter. The corresponding excitations access primarily the respective *A′* states, namely the *A′* 1/2 ($^2\Pi$) state of IBr^- and the *A′* $1/2_g$ ($^2\Pi$) state of I_2^-, where the states are labeled according to Hund's case (c), with the Hund's case (a) notation given in parenthesis. Spin-orbit interaction plays an important role in both anions. At R_e, the ground electronic state equilibrium bond distance, the basic Hund's case (a) character is retained, but spin-orbit mixing of the states becomes increasingly important with increasing internuclear separation.[238]

In I_2^-, the prompt 780 nm dissociation on the *A′* electronic state leads to the lowest-energy product channel, $I^- + I(^2P_{3/2})$, with a 0.6 eV fragment kinetic energy release. The lowest optically bright excited electronic state of IBr^- correlates to the second lowest, $I^- + Br(^2P_{3/2})$ channel. In this case, at 780 nm, the kinetic energy release is 0.2 eV. The dynamics for each case are probed through 390 nm electron detachment with delayed probe laser pulses, accessing the respective manifolds of I_2 and IBr neutral states shown in Figures 6.1(a) and (b). Only the pertinent neutral states accessible by photodetachment from the respective *A′* anion states at the probe photon energy employed here are included in Figures 6.1(a) and (b).

An important distinction between the excited-state interactions in IBr$^-$ and I_2^- is the existence of an attractive well on the *A′* potential in IBr$^-$. To highlight this well, the dashed curve in Figure 6.1(b) represents the IBr$^-$ *A′* state potential offset by 3.18 eV, the probe photon energy, projecting this anion state on the corresponding neutral manifold. In comparison, the analogous *A′* potential well is nearly absent in I_2^-, as indicated by a similar dashed curve in Figure 6.1(a).

Nonetheless, the shallow, 17 meV deep, well on the *A′* potential in I_2^- was observed by Zanni et al.[186] It is attributed to the weak polarization-induced attraction between the separating I$^-$ anion and neutral I atom. In contrast, the more pronounced well on the *A′* potential in IBr$^-$ has never been observed experimentally. Fundamentally, in IBr$^-$ this well is due to charge-switching in the heteronuclear system and can be seen as arising from the different electron affinities of Br and I (3.36 and 3.06 eV, respectively).[239] Hence, as the molecular anion dissociates on the *A′* IBr$^-$ state, the excess electron is shifted from a delocalized molecular orbital into an atomic orbital of the less energetically favorable I$^-$ fragment, causing an attractive interaction between the separating I$^-$ and Br fragments.

The electronic-state potentials for IBr$^-$ were developed only recently[206,207] and to our knowledge have yet to be subjected to dynamical testing. This section describes the first application of femtosecond time-resolved photoelectron imaging to the dissociation of

IBr^-. The experimental approach and simulation methods used in this work are tested on the analogous (but better characterized) I_2^- anion, showing an agreement with previous studies of this system. The time-resolved photoelectron imaging investigation of IBr^- dissociation is then presented and used to generate an experimental portrait of the anion potential for comparison with the ab initio results.

6.3.1 Results

Figure 6.2 shows representative photoelectron images obtained at selected pump-probe delays. The I_2^- and IBr^- images were recorded under similar experimental conditions and are shown alongside each other. The "$t = \infty$" image at the top of the figure was recorded in the one-photon detachment of I^- using only the 390 nm (probe) radiation. The image is shown here for reference, as it represents the asymptotic limit of both the IBr^- and I_2^- dissociation channels yielding iodide anion fragments.

All images in Figure 6.2 were recorded with linearly polarized pump and probe laser beams, the polarization direction being vertical in the plane of the images. The cylindrical symmetry imposed by this polarization geometry enables the complete reconstruction of the photoelectron velocity and angular distributions by means of inverse Abel transformation.[32] The Abel inversion is performed with the Basis Set Expansion (BASEX) program developed by Reisler and co-workers.[240]

The ensuing discussion focuses on the time-dependent photoelectron spectra, shown in Figures 6.3(a) and (b) for the dissociation of I_2^- and IBr^-, respectively. The spectra,

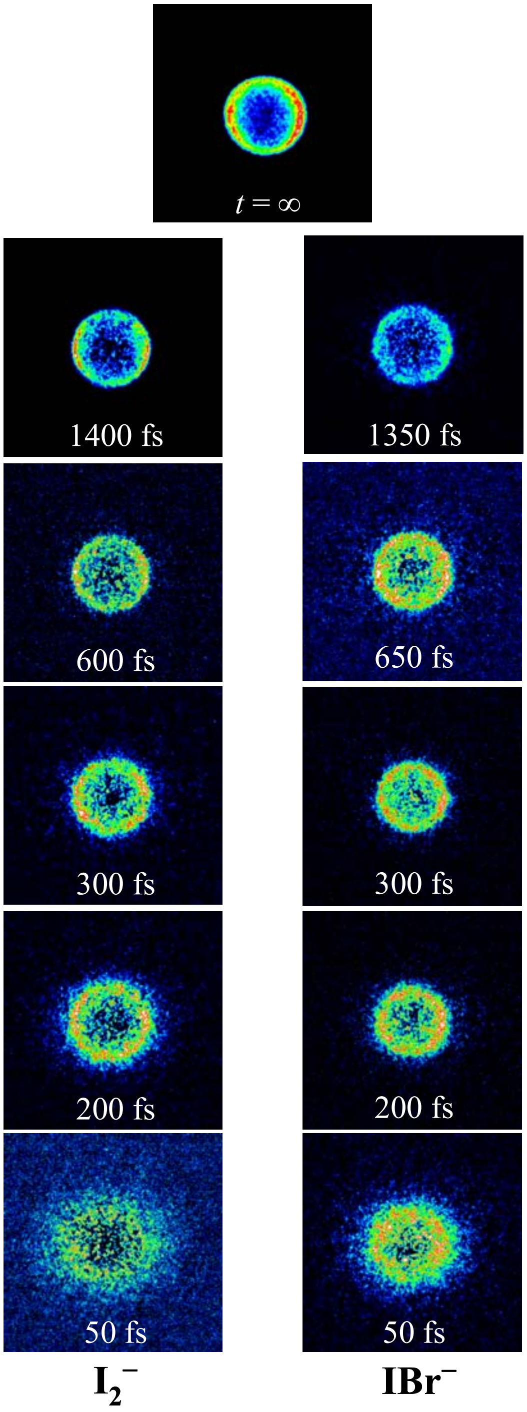

Figure 6.2 Representative time-resolved raw photoelectron images recorded at selected pump-probe delays in the 780 nm pump – 390 nm probe experiments on I_2^- (left) and IBr^- (right). The pump and probe polarization directions are vertical in the plane of the Figure. The images are shown on arbitrary relative intensity scales.

extracted from the images in Figure 6.2 using the BASEX algorithm, quantify the time-dependent changes in the energetics and reflect the evolution of the electronic structure of the dissociating diatomic anions. In both IBr^- and I_2^-, a single evolving band is observed, which asymptotically (at long delays) corresponds to detachment from the final I^- fragment. This conclusion is consistent with the energetics of the band, whose position at long pump-probe delays is in agreement with the electron affinity of atomic iodine (3.06 eV).[239] The asymptotic width of the band reflects the experimental resolution in the relevant energy range, i.e. ~0.05 eV full width at half-maximum.

Examining first the time-dependent I_2^- spectra in Figure 6.3(a), we note a very slight shift in the position of the band toward smaller eKE during the early stages of the dissociation, followed by a reverse shift towards the asymptotic value of eKE = 0.12 eV at longer delays. This transient dip in eKE, first observed by Zanni et al. using 260 nm probe pulses, is attributed to a shallow (0.017 ± 0.010 eV) well on the A' I_2^- potential with a minimum at $R = 6.2$ Å.[186] The well arises from a long-range polarization-induced attraction between the fragments.

Using the I_2^- spectra as a reference for interpreting the IBr^- results, we note that in the latter case the evolving detachment band exhibits a much more pronounced dip in eKE. The distinction between the IBr^- and I_2^- data is best seen with these results presented as the two-dimensional time-energy plots shown in Figure 6.4. Figures 6.4(a) and (b) reflect the evolution of the dissociative wavepackets for I_2^- and IBr^-, respectively, within the relevant eKE range of 0-0.3 eV. The curves plotted over the contour plots in Figure 6.4 represent the classical trajectory simulations described in the following subsection.

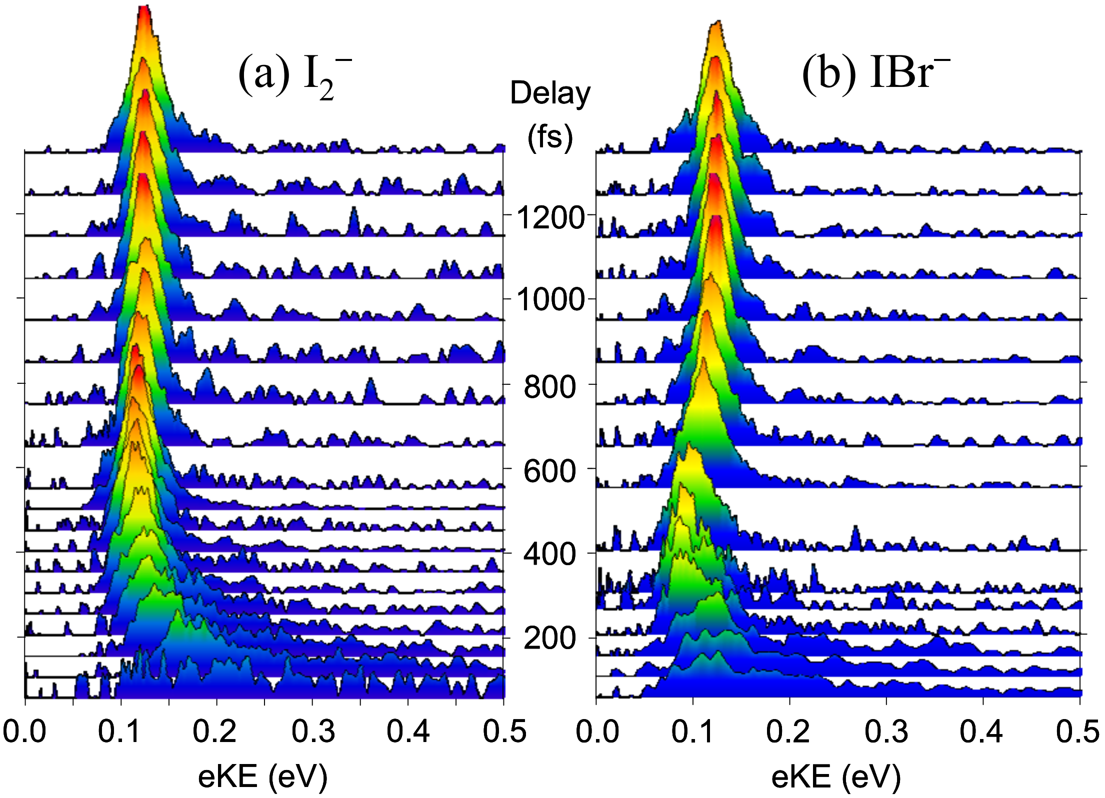

Figure 6.3 Time-resolved photoelectron spectra obtained in the dissociation of (a) I_2^- and (b) IBr^- using a 780 nm pump, while detaching the electrons with 390 nm probe pulses. The spectra are obtained from photoelectron images, a selection of which are shown in Figure 6.2.

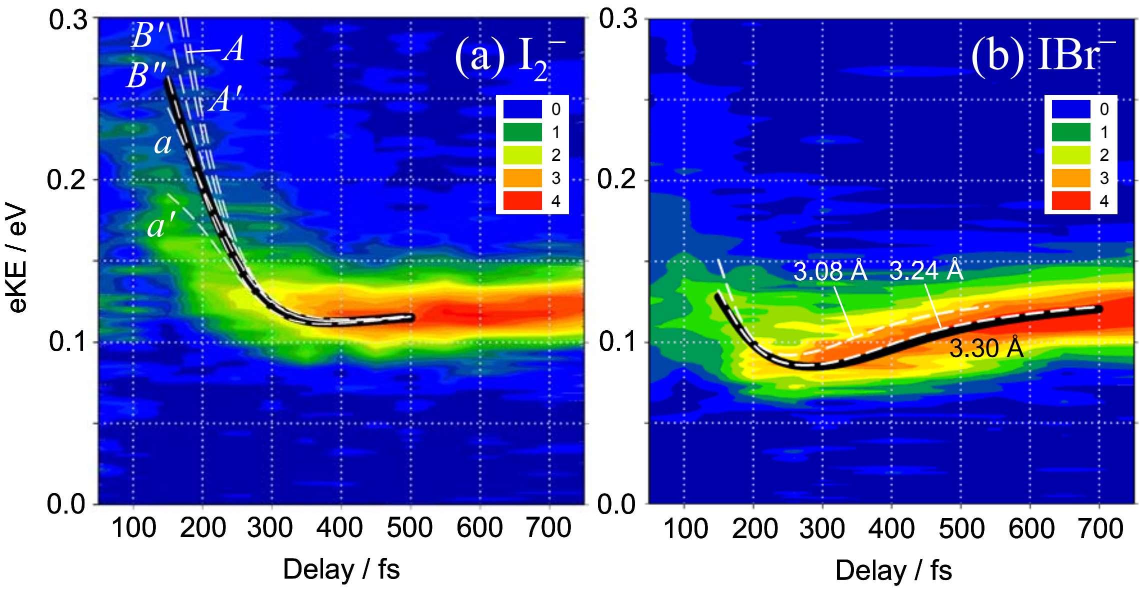

Figure 6.4 Time-energy contour plots of the time-resolved photoelectron spectra shown in Figure 6.3 in the range of 50-550 fs and 0.0-0.3 eV for (a) I_2^- and (b) IBr^-. In (a), the dashed white curves represent trajectory simulations with detachment via the labeled neutral states. The solid black line represents a mean of the individual detachment channels, calculated as described in the text. In (b), the lines represent trajectories corresponding to the different values of R_0 indicated in the figure. The "best fit" (as determined by inspection), corresponding to R_0 = 3.30 Å, is indicated by the solid black line.

6.3.2 Discussion

Both I_2^- and IBr^- dissociations at 780 nm produce the same ionic fragment, the iodide anion. The experiments by Lineberger and co-workers at a similar wavelength indicate the absence of Br^- fragments.[206] It is also important that the probe photons used here do not have sufficient energy to detach an electron from Br^-. Hence, the IBr^- pump-probe experiment is inherently sensitive only to the anion states that correlate to I^- formation.

Knowing the electronic state potentials for IBr^- and I_2^-, it is possible to model the direct dissociation dynamics using a quantum-mechanical[186] or classical approach. The goals of this work are achieved within the classical framework, which confines the quantum-mechanical aspects of the problem to the electronic-state potentials.

The I_2^- and IBr^- dissociation trajectories are obtained by solving Newton's second-law equation

$$\mu \frac{d^2R}{dt^2} = -\frac{dV_{\mathrm{an}}(R)}{dR} \tag{6.1}$$

where R is the internuclear distance, μ is the reduced mass of the diatomic anion and $V_{\mathrm{an}}(R)$ is the potential energy curve for the anion state on which the dissociation takes place. The classical trajectories $R(t)$ obtained by integrating Equation 6.1 reflect the evolution of the expectation value of R for the corresponding quantum wavepackets.

Within the classical framework, the time-resolved photoelectron spectra reflect the evolving difference between the neutral and anion electronic potentials, according to:

$$\mathrm{eKE}(R) = [h\nu + V_{\mathrm{an}}(R)] - V_{\mathrm{nu}}(R) \tag{6.2}$$

where $V_{\mathrm{an}}(R)$ is the anion dissociation potential accessed by the pump laser pulse and $V_{\mathrm{nu}}(R)$ is the electronic potential of the neutral state accessed in the photodetachment by the probe pulse. Therefore, classically, every point on the dissociation trajectory $R(t)$ corresponds to a specific value of the photoelectron kinetic energy.

Since the long-range interactions between neutral fragments are much weaker than the ion-neutral interactions in the dissociating anions, the neutral potential can be seen as essentially flat in the long range. Therefore, at sufficiently long delays, the evolution of the pump-probe spectra in Figures 6.3 and 6.4 reflects the shape of the long-range anion potential on which the dissociation takes place. At shorter internuclear separations, the interactions in the neural systems are important as well and the analysis of the short-delay spectra must include the details of the neutral electronic potential.

In the following subsection, we first describe the application of the model given by Equations 6.1 and 6.2 to the dissociation of I_2^-. This serves to illustrate that the experimental spectra obtained in the present work are in a good agreement with the A' anion potential determined by Zanni et al.[186] Subsequently, the same approach is applied to the dissociation of IBr^-, to test the theoretical A' potential[206] for this system. Considering that this work is the first dynamical test of the calculated IBr^- potential, the experimental results in conjunction with theoretical modeling for this system are used to generate an experiment-based "image" of the dissociation potential.

6.3.3 Modeling I_2^- Dissociation

The I_2^- dissociation trajectory was calculated by substituting the $A'\,1/2_g$ ($^2\Pi$) state potential of I_2^- determined by Zanni et al.[186,237] for $V_{\mathrm{an}}(R)$ in Equation 6.1. The equation of motion was integrated on a time-grid with a constant 1 fs step size. Rather than launching the A' trajectory from the ground electronic state equilibrium bond length (R_e = 3.24 Å),[182,183] R_0 was chosen as a point on the A' anion potential lying above the X state equilibrium by the value of the pump photon energy, $h\nu$ = 1.59 eV. Based on the experimentally determined I_2^- X and A' potentials,[182,183,186,237] this corresponds to R_0 = 3.25 Å, compared to the I_2^- ground-state equilibrium bond length R_e = 3.24 Å.[182,183] Although a minor discrepancy does exist, launching a classical trajectory on the A' potential with R_0 equal to the Franck-Condon bond length requires more energy than is supplied by the pump photon. The initial velocity was assumed to be zero.

Considering the photodetachment (probe) step, there are 10 neutral electronic states of I_2 that correlate asymptotically to the I($^2P_{3/2}$) + I($^2P_{3/2}$) dissociation limit.[241] Of these, seven have been characterized experimentally,[225-230,242-245] while theoretical calculations predict near degeneracy of the other three with one or other of the experimentally measured states.[246,247] In the following, the states are labeled according to the electron configuration from which they arise, in conjunction with the Hund's case (c) notation. The $\ldots(\sigma_g)^m(\pi_u)^p(\pi_g^*)^q(\sigma_u^*)^n$ notation for the electron configuration is abbreviated as *mpqn*,[241] while the Hund's case (c) state labels Ω_i reflect the projection of the total electronic angular momentum quantum number (Ω) and the symmetry designation with respect to inversion ($i = g$ or u). In addition, the Hund's case (a) orbital symmetry designation is given in parenthesis. For example, the lowest excited electronic state of I_2 [see Figure 6.1(a)], arising from the …$(\sigma_g)^2(\pi_u)^4(\pi_g^*)^3(\sigma_u^*)^1$ electron configuration, is the *2431 A′* 2_u ($^3\Pi$) state.

Spin-orbit interaction mixes the electron configurations, making possible the transitions to six of the seven experimentally characterized states of I_2.[236] The exception is the ground *2440 X* 0_g^+ ($^1\Sigma^+$) state, which is not accessible by a one-electron detachment transition from the *2432 A′* $1/2_g$ ($^2\Pi$) state of I_2^- and is therefore not included in Figure 6.1(c). The six solid curves shown in Figure 6.1(c) correspond to the *2431 A′* 2_u ($^3\Pi$),[226,231] *2431 A* 1_u ($^3\Pi$),[229,232] *2431 B′* 0_u^- ($^3\Pi$),[228,231] *2431 B″* 1_u ($^1\Pi$),[225] *2341 a* 1_g ($^3\Pi$),[225,227,231] and *2422 a′* 0_g^+ ($^3\Sigma^-$)[227,230,231] electronic states, all of which are, in principle, accessible in the detachment of the *A′* I_2^- state. The state potentials shown in Figure 6.1(a) are calculated using the experimentally determined parameters, whenever possible. In some cases, extrapolation into the long-range region is necessary, using parameters from the work of Saute and Aubert-Frecon.[231] For reference, Figure 6.1(a) also shows a dashed line corresponding to the bracketed term in Equation 6.2, calculated with the *A′* potential of the anion, allowing for its comparison to the relevant I_2 states.

For each of the six neutral potentials in Figure 6.1(a), the eKE(R) dependence from Equation 6.2 was combined with the I_2^- dissociation trajectory $R(t)$, calculated according to Equation 6.1. In this way, the semi-classical evolution of eKE vs. time is determined. To account for the experimental resolution, the result is convoluted with a 300 fs wide time-broadening function, yielding a projected eKE(t).

The resulting eKE(t) "trajectories", corresponding to the photodetachment to the six neutral states included in Figure 6.1(c), are shown in Figure 6.4(a) as dashed white lines overlaying the experimental contour plot. The original eKE(t) curves were calculated to about 650 fs, corresponding to $R \approx 11$ Å. This approaches the limit of the range where the neutral potentials are known reliably. The corresponding curves in Figure 6.4(a) terminate at a shorter delay on the account of the temporal broadening function convoluted with the original trajectories. The solid black line in Figure 6.4(a) represents a mean eKE from each of the nine possible detachment channels: the six included in the above calculation and the three experimentally uncharacterized neutral states. The mean is calculated assuming equal oscillator strengths for each of the six channels shown in Figure 6.1(c), while weighting the a and a' states by factors of 2 and 3, respectively, to account for the contributions of the experimentally uncharacterized *2341* 2_g ($^3\Pi$), *1441* 0_u^- ($^3\Sigma^+$), and *2332* 3_u ($^3\Delta$) states.[186]

At short pump-probe delays, the mean simulated curve deviates somewhat from the experimental time-energy plot in Figure 6.4(a). There are many factors that may contribute to this discrepancy. First, although the simulations are based, wherever possible, on experimentally determined potentials, at short pump-probe delays many of the neutral states are accessed at the steep inner wall of the potential, above the dissociation limit, necessitating data extrapolation. Second, uncertainties in the experimentally determined potentials may give rise to discrepancies between the simulation and experimental data. For example, R_e for the A' state of I_2^- is reported as 6.2 Å, but with an uncertainty of approximately 10%.[186] Other possibilities include temporal uncertainties in the experimental measurements, the crude nature of the model, particularly the assumption that the oscillator strengths and Franck-Condon factors for all transitions are similar. This assumption is likely to be particularly important in the short-range region, where the neutral states are most divergent. The photon energy most closely matches the detachment via the higher-energy neutral states, which might be expected to increase the Frank-Condon factors to these states with the overall effect of reducing the average eKE.

Given the good agreement between the simulation and the experimental data from 300 fs and on, it is likely that the main sources of disagreement at shorter delays are uncertainties in the repulsive part of the neutral potentials. From the dissociation trajectory $R(t)$, $t = 300$ fs corresponds to $R \approx 6.5$ Å. For $R > 6.5$ Å, the I_2 potentials are relatively invariant with respect to R and any variations in the eKE, therefore, reflect mainly the changes in the anionic A' state potential. The simulation nicely predicts the experimentally observed shift to slightly higher eKE in this region, corresponding to the system moving out of the long-range shallow potential well.

6.3.4 Modeling IBr^- Dissociation

Following the procedure described in the preceding subsection for I_2^-, the IBr^- dissociation trajectories were propagated on a 1 fs time-grid, assuming a zero starting velocity. This being the first test of the newly calculated potentials, the choice of a starting point, R_0, assumes greater importance and is discussed below.

Similar to the I_2^- case, the lowest-energy one-electron detachment from the A' state of IBr^-, arising from the $\ldots(\sigma)^2(\pi)^4(\pi^*)^3(\sigma^*)^2$ electron configuration, leaves the neutral IBr molecule in an excited $\ldots(\sigma)^2(\pi)^4(\pi^*)^3(\sigma^*)^1$, rather than the ground $\ldots(\sigma)^2(\pi)^4(\pi^*)^4(\sigma^*)^0$ configuration. The potential energy curves corresponding to the IBr neutral states are not as extensively characterized as those of I_2. Figure 6.1(d) shows the states that are likely to be relevant in detachment from the anion A' state at the probe photon energy used in the experiment.

The neutral A' state potential employed here is generated by the first-order Rydberg-Klein-Rees procedure using the RKR1 program of Le Roy[232] with the parameters from Radzykewycz et al.[234] The *A*, *C* and *Y* states are calculated using the analytical forms of the potential curves determined by Ashfold and co-workers.[233] In examining our time-resolved IBr^- data, we follow a similar treatment as in the case of I_2^-. However, given the incomplete dataset of the neutral A' state and the "preliminary" nature of the *Y* state potential[233] we limit ourselves to detachment via the *A* and *C* neutral state channels. These two states largely encompass the energy spread available in the final neutral states.

The eKE(t) predicted using Equations 6.1 and 6.2 depends parametrically on R_0. Based on the theoretical results,[206] the A' state of IBr^- is not classically accessible from the ground-state equilibrium geometry at the pump photon energy employed in the experiment. Therefore, we adopt three different approaches to choosing the value of R_0.

The first approach is similar to the one described previously for I_2^-. It is to take the shortest I-Br bond length that energetically, in a classical sense, allows excitation to the A' state of the anion. This corresponds to $R_0 = 3.08$ Å. The trajectory launched from this internuclear distance, calculated according to Equation 6.1, generates, using Equation 6.2 and the convolution with a time-broadening function, one of the white dashed curves shown in Figure 6.4(b). This eKE(*t*) curve corresponds to the averaged contributions of the *A* and *C* neutral channels. Clearly, this trajectory underestimates the time required to reach the bottom of the well on the dissociation potential.

The ground-state bond strength of IBr^- relative to the $\mathrm{I} + \mathrm{Br}^-$ asymptotic limit was recently determined to be $D_0 = 1.10 \pm 0.04$ eV.[206] Examination of the theoretical *X* state potential shows that the calculation underestimates the well depth of the IBr^- ground state [see Figure 6.1(d)].[206] This discrepancy can be corrected by scaling the calculated potential energy curves to reproduce the experimental result value of D_0. Therefore, in our second approach to choosing R_0, we take the point on the A' potential energy curve, which corresponds to the available energy relative to the experimentally determined $\mathrm{I}^- +$ Br dissociation limit. The condition for determining R_0 is hence $V_{A'}(R_0) - V_{A'}(\infty) = h\nu - (D_0 + \Delta\mathrm{EA})$, where $h\nu = 1.59$ eV is the pump photon energy and $\Delta\mathrm{EA} = 0.305$ eV is the difference between the $\mathrm{I}^- + \mathrm{Br}$ and $\mathrm{I} + \mathrm{Br}^-$ asymptotic limits.[239] Assuming the above experimental value of D_0, this calculation yields $V_{A'}(R_0) - V_{A'}(\infty) = 0.185 \pm 0.04$ eV. Comparing this available energy to the calculated IBr^- A' potential energy curve[206,207] yields $R_0 = 3.24 \pm 0.05$ Å. The corresponding eKE(*t*) "trajectory", averaged over the contribution of the *A* and *C* neutral channels, is shown in Figure 6.4(b) as the second dashed line. This trajectory is in better agreement with the experimental time-energy plot than the one for $R_0 = 3.08$ Å.

The third approach to selecting the starting point of the dissociation trajectory takes into account the uncertainty that exists in the relative energetics of the A' and X anion states. Since the calculations underestimate the ground-state dissociation energy, even larger error may be present in the calculated excited-state potential. Within the semi-classical framework, the energetic uncertainty can be accounted for by viewing R_0 as an adjustable rather than predetermined parameter. Hence, the third trajectory in Figure 6.4(b), shown as a solid black line, corresponds to $R_0 = 3.30$ Å, which (by inspection) yields the best agreement of the calculated eKE(t) curve with the experiment.

6.3.5 Test of the IBr^- A′ 1/2 ($^2\Pi$) State Potential: Imaging the Reaction Coordinate

The agreement of the experimental data for I_2^- with the classical-trajectory calculations and the previous work on this system gives confidence in the new time-resolved results on IBr^- dissociation. The comparison of the latter results with the semi-classical predictions based on the recently calculated IBr^- potential energy curves provides the first dynamical test of these calculations. Overall, there is a good agreement of the theoretical predictions with the experimental data. This allows to conclude with confidence that the A' 1/2 ($^2\Pi$) potential of IBr^- calculated by Parson and co-workers[206,207] adequately explains the observed time-resolved dynamics.

The experimental data in Figure 6.4(b) reflect the time-dependent energy envelope of the dissociative wave packet launched by the pump laser pulse on the IBr^- excited-state potential. Every point along the time axis corresponds to a specific expectation value of

R, making it possible to express the data in terms of R, the dissociation coordinate, rather than time. Strictly speaking, the wave packet is characterized by a spread in R values and, therefore, time cannot be unambiguously converted to R. Nonetheless, the calculated classical trajectories $R(t)$ of IBr^- allow for a formal $(t, \mathrm{eKE}) \rightarrow (R, \mathrm{eKE})$ transformation on the experimental dataset. While giving no new quantitative information that could not be obtained from the data in Figure 6.4(b), this procedure provides an important insight into the evolving energy envelope *in the reaction coordinate space*.

According to Equation 6.2, eKE reflects the difference between the anion A' and accessed neutral state potentials, corrected for the probe photon energy. Using an average of the neutral $C\ {}^1\Pi$ and $A\ {}^3\Pi$ potentials as a reference,[233] the eKE coordinate in the experimental dataset, already in the (R, eKE) space, can be transformed into the corresponding potential energy of the A' 1/2 $({}^2\Pi_{1/2})$ anion state, $V_{A'}$. The sequence of the two transforms, using, first, the trajectory $R(t)$, calculated via Equation 6.1 with $R_0 = 3.30$ Å, and, second, the eKE(R) dependence from Equation 6.2 with a mean of the A and C neutral potentials, was performed on the original experimental dataset in Figure 6.4(b) to yield an overall $(t, \mathrm{eKE}) \rightarrow (R, \mathrm{eKE}) \rightarrow (R, V_{A'})$ transformation of the coordinates. The result is shown in Figure 6.5.

This contour plot is, in essence, an experimental image of the dissociation potential as a function of the I–Br internuclear distance. The overall intensity variation with R signifies changes in the experimental signal strength and has no direct bearing on the shape of the potential. The spread in intensity along the energy axis reflects the experimental resolution, superimposed over the energy spread of the dissociative wave

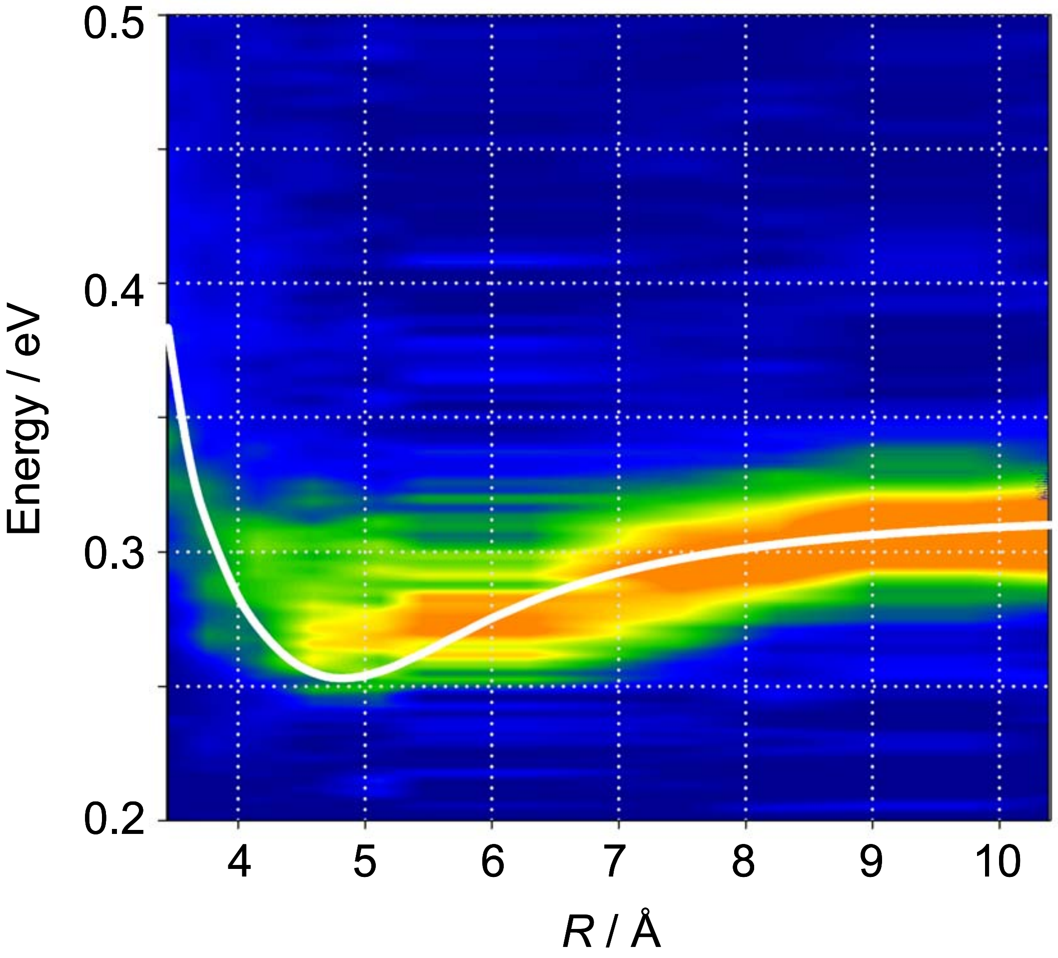

Figure 6.5 An image of the IBr⁻ *A′* potential based on the experimental data and semi-classical model described in the text. The corresponding theoretical potential energy curve[206,207] is shown for comparison as a white line.

packet, as it propagates along the internuclear coordinate. For comparison, the white curve in Figure 5 represents the calculated potential for the IBr^- A' 1/2 ($^2\Pi_{1/2}$) state.[206,207]

The agreement between the theoretical potential energy curve and the experimental image of the potential is remarkably good for $R \geq 6$ Å. The discrepancies observed at shorter bond lengths can be attributed to experimental and theoretical uncertainties. In particular, experimental time broadening leads to partial smearing of the ~60 meV deep well in the image of the potential. To the contrary, no such broadening affects the calculated potential energy curve. In addition, the unavoidable time-energy uncertainty of the time-resolved measurement contributes to the distortion of the potential image. With these uncertainties in mind, the experimental "portrait" of the dissociation potential is in good agreement with theory.[206,207]

6.4 Dynamic Molecular Interferometer: Probe of Inversion Symmetry in I_2^- Photodissociation

This section accentuates the effects of quantum interference on time-resolved photoelectron angular distributions in the photodissociation of I_2^-. The results indicate that the evolution of the electronic wavefunction of the dissociating molecular anion continues long after the asymptotic energetic limit has been effectively reached. Our excitation regime is very similar to that employed by the Neumark group,[27,201] setting the stage for comparable dissociation dynamics. However, in contrast with the previous work, we probe the emergence of the asymptotic I^- fragments much closer energetically to the detachment threshold. The photoelectrons are produced with an asymptotic electron kinetic energy (eKE) of 0.12 eV, compared to 1.6 eV in the Neumark experiments. This corresponds to a significantly larger de Broglie wavelength, which we show to be a critical parameter connecting the photodissociation and electron emission dynamics.

At the heart of our findings is the effect of inversion symmetry on the electronic structure evolution in the exit channel of I_2^- dissociation. Excitation at 780 nm accesses the $A' \, 1/2_g \, (^2\Pi)$ state and yields asymptotic $I(^2P_{3/2})$ + I^- fragments. As long as the electronic wavefunction of the dissociating system retains its inversion symmetry, the electron detachment is subject to interference of two equivalent emission centers, the core iodine atoms, I_A and I_B, which separate at a speed determined by the reaction energetics. Hence, the dissociating I_2^- is a molecular-scale interferometer, with an arm-length R controlled by the time-dependent progress of the reaction. The emitted electron waves are sensitive probes of not only the dissociation dynamics, but also the electron-neutral interactions, such as scattering on the neutral fragments.

In the pump-probe scheme utilized here, the I_2^- "interferometer" samples, over the span of 2-3 ps, an R range from ca. 3 Å to that similar to the 35 Å de Broglie wavelength of the photoelectrons. This sets the stage for intriguing interplay between the fragment separation and electron emission dynamics, characterized by an easily resolvable picosecond timescale.

6.4.1 Results

The 780 nm pump, 390 nm probe photoelectron images were collected in the dissociation of I_2^- at selected delays ranging from zero to ca. 5 ps. Representative images corresponding to 100, 550, 1650, and 2650 fs are shown in Figure 6.6, right. On the left is a time-energy plot showing the evolution of the photodetachment spectrum throughout the dissociation. The plot is generated from the photoelectron spectra extracted from the individual time-resolved photoelectron images.

At $t < 300$ fs, the time-energy plot in Figure 6.6 reveals a narrowing of the photodetachment band, coinciding with the shift of its maximum towards smaller eKE. This is followed by a slight reverse shift to larger eKE at $t = 300$-600 fs. The transient eKE dip is attributed to a shallow, 0.017 ± 0.010 eV, well on the A' I_2^- potential with a minimum at $R = 6.2$ Å, as characterized by Zanni et al.[186] The well arises from a long-range polarization-induced attraction between the $I(^2P_{3/2}) + I^-$ fragments.

The evolution of the photoelectron spectrum effectively stops after 700 fs. The plot in Figure 6.6 extends to 2.85 ps, but the complete data set includes pump-probe delays of up to 5 ps, with no spectral variations observed in the extended range. At $t > 700$ fs, the peak position at eKE = 0.12 eV corresponds to the difference between the probe photon energy, 3.18 eV, and the electron affinity of atomic iodine, 3.06 eV.[239] The asymptotic width of the band, 0.05 eV (full width at half-maximum), reflects the probe bandwidth convoluted with other broadening factors. Overall, the time-resolved spectrum

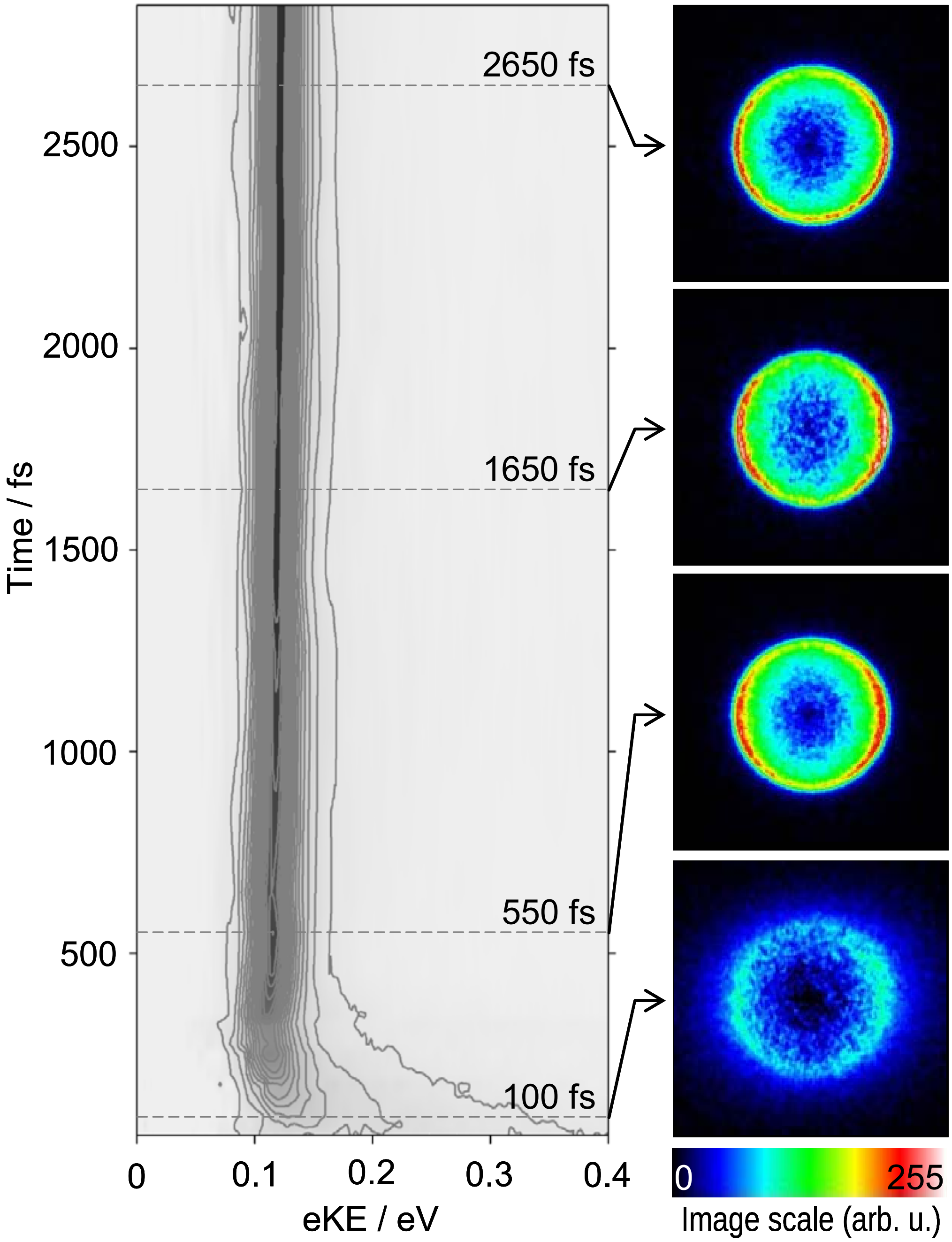

Figure 6.6 Left: the time-resolved photoelectron spectrum obtained in the dissociation of I_2^- using a 780 nm pump and a 390 nm probe. The plot is generated from the photoelectron spectra extracted from the time-resolved photoelectron images. Right: representative raw photoelectron images corresponding to 100, 550, 1650, and 2650 fs (the delays are indicated by dashed lines on the time-energy plot on the left). The pump and probe polarization directions are vertical in the plane of the Figure.

in Figure 6.6 supports the conclusion by Neumark and co-workers that the dissociation is effectively complete after 700 fs.[201]

Although it indeed appears that the electronic identity of the I^- fragment is established early in the dissociation, this conclusion is based on the time-resolved photoelectron spectra only. Photoelectron images contain an additional dimension of information in the angular domain and the analysis reveals that the evolution of the angular distributions continues well beyond 700 fs. For example, it can be discerned by careful inspection of Figure 6.6 that the 1650 fs photoelectron image is slightly more anisotropic than both the 550 and 2650 fs images. The persisting changes in the angular distributions suggest that the evolution of the electronic wavefunction continues after the asymptotic energetic limit has been reached (within the experimental energy resolution). The key to unraveling these dynamics lies in the time-resolved photoelectron angular distributions – *not* the energy spectra.

The quantitative analysis of the angular distributions is summarized in Figure 6.7, which displays the delay-dependence of the anisotropy parameter β_2. The values of β_2 were determined by fitting the experimental time-resolved angular distributions with the equation generally describing two-photon (pump-probe) angular distributions:

$$I(\theta) = b[1 + \beta_2 P_2(\cos\theta) + \beta_4 P_4(\cos\theta)] \qquad (6.3)$$

where $P_2(\cos\theta)$ and $P_4(\cos\theta)$ are the second- and forth-order Legendre polynomials, β_2 and β_4 are the corresponding anisotropy parameters, and b is a normalization constant. The experimental angular distributions were obtained by integrating the Abel-transformed images over the radial range corresponding to the full width (at half-maximum) of the photodetachment band in the energy domain. The β_2 values plotted in Figure 6.7 represent the averages over N (N = 3-10) separate measurements under the same experimental conditions, after testing each set using Dixon's method for datasets with <25 members and rejecting any outliers.[248] The error-bars represent the 95% confidence limits of the experimentally determined mean values. Data points at shorter delays tend to be associated with narrower error-bars, compared to longer delays, because the corresponding measurements typically include larger datasets (larger N). The overall trend in the β_2 values shown in Figure 6.7 is fully repeatable.

The higher-order moment, β_4, is more susceptible to experimental noise, resulting in greater, compared to β_2, errors. Hence, only the β_2 values are plotted in Figure 6.7. It is stressed that the timescales apparent in the time-dependent angular distributions are adequately reflected in $\beta_2(t)$, and therefore reporting only these values is sufficient. We have also carried out the anisotropy analysis by artificially setting β_4 to zero, independent of pump-probe delay. This additional constraint changes (to a small extent) the corresponding β_2 values, yet the overall temporal trends in the data remain unaffected.

After the completion of the dissociation, the photoelectrons originate from the closed-shell I^- fragment. Therefore, the alignment with respect to the pump laser polarization is no longer important in the asymptotic data, i.e., $\beta_4 = 0$, while β_2 at long pump-probe delays can be compared to that in "static" photodetachment of I^- at the same (390 nm) wavelength. The latter, $\beta_2 = -0.17 \pm 0.05$,[249] is indicated in Figure 6.7 by an open circle at $t = \infty$. The corresponding error-bars reflect the 95% confidence interval determined

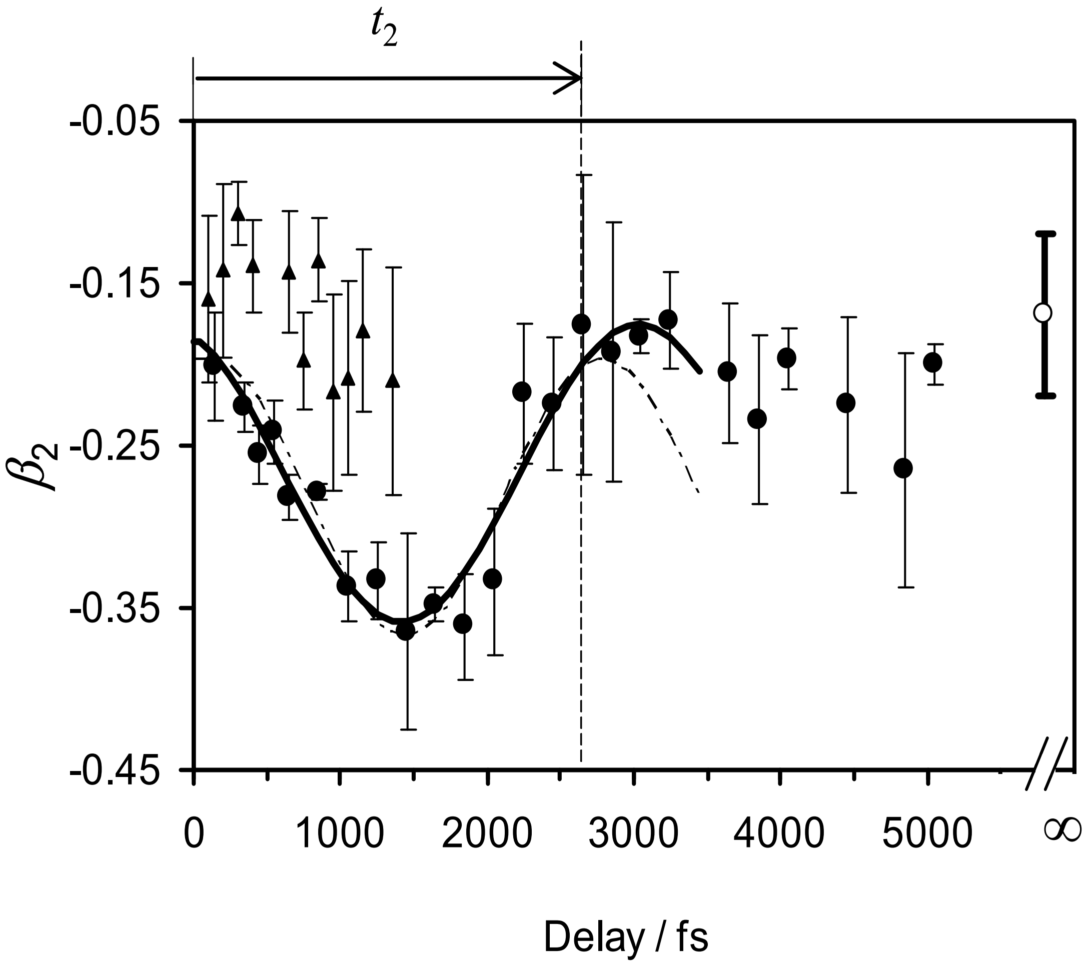

Figure 6.7 Evolution of the β_2 photoelectron anisotropy parameter. Time-resolved I_2^- and IBr^- data are shown as solid circle and triangle symbols respectively with the error-bars determined as described in the text. The open symbol corresponding to "$t = \infty$" reflects the anisotropy value for the isolated I^- photodetachment. The indicated time-interval t_2 corresponds to the 2.5 ps electron localization timescale discussed further in the text. The thick solid curves represents a least-squares fit to the experimental data in the t = 0-3 ps range using Equation 6.4 with a zero phase shift. The fit yields $\lambda = 42.7 \pm 1.1$ Å for the effective de Broglie wavelength of the photoelectrons. The thin dash-dotted curve represents a fit using the same equation with the de Broglie wavelength set to its far-field value of = 35.4 Å, while the phase-shift factor is treated as an adjustable parameter accounting for the near-field electron-fragment interactions. See the text for details.

previously[249] by modeling I^- photodetachment data at different photon energies. This interval includes not only the uncertainty of the 390 nm measurement, but also the cumulative errors attributable to other measurements, as well as theoretical modeling.

6.4.2 Discussion

Given the 1.01 eV bond dissociation energy,[27,185] the excitation of I_2^- at 780 nm results in a 0.58 eV kinetic energy release to the $I(^2P_{3/2}) + I^-$ products, which corresponds to an asymptotic fragment separation speed of 13.3 Å/ps. Figure 6.8 shows the classical dissociation trajectory $R(t)$ calculated for the present case.[250] In the range of $t < 1$ ps, the trajectory was propagated on the A' I_2^- potential characterized by Zanni et al.[186] For $t > 1$ ps, an extrapolation using the above asymptotic speed was used.

Due to the extensive spin-orbit interaction, the A' electronic state of I_2^- is described as an admixture of Hund's case (a) Σ and Π states.[251] Although experimental measurements show that the photofragments from the $A' \leftarrow X$ transition align parallel to the laser polarization axis,[221] the A' state predicted to be predominantly (~90%) Π in character in the Franck-Condon region.[251] The state composition is bond-length (R) dependent, and may therefore affect evolution of the photoelectron angular distributions in time-resolved dissociation. By the time an inter-nuclear separation of 5.3 Å is reached, the Σ-character component of the A' state is predicted to reach ~63%, approaching the asymptotic ($R = \infty$) limit of 67%.[251] In view of these estimates and based on the dissociation trajectory in Figure 6.8, the change in the Σ/Π electronic character in the dissociation process occurs

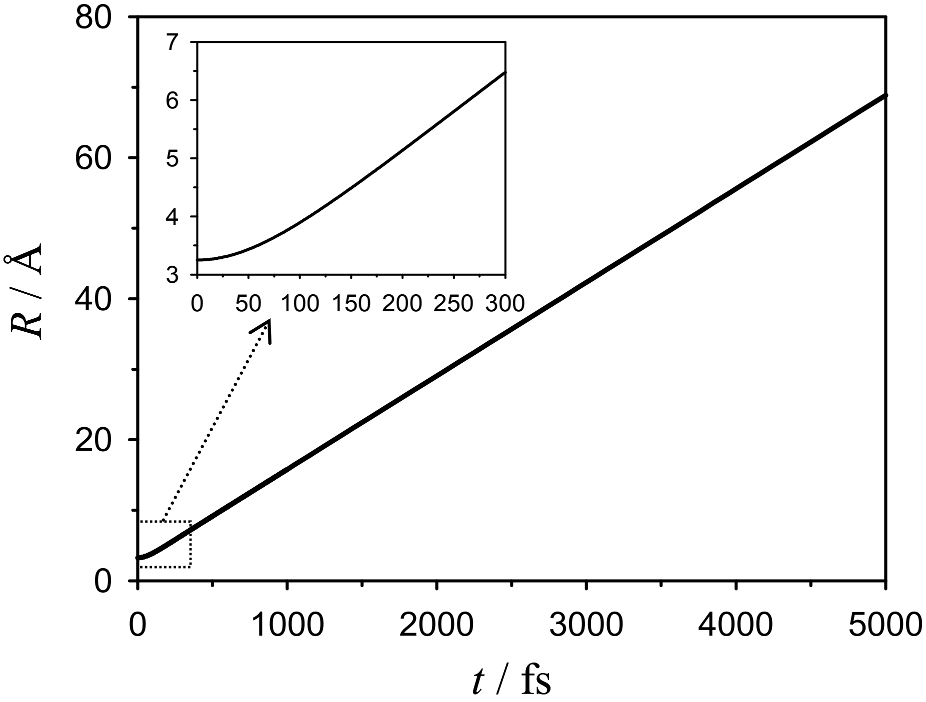

Figure 6.8 The dissociation trajectory of I_2^- on the A' $^2\Pi_{g,1/2}$ excited-state potential accessed using the 780 nm pump. In the 0 to 1 ps range, the trajectory is calculated by solving the classical equation of motion as described in the text. For t > 1 ps, linear extrapolation was used. The inset shows the expanded 0-300 fs range.

on a <200 fs timescale, which is extremely rapid compared to the observed anisotropy variation (see Figure 6.7). Hence, an alternative explanation for the observed effect must be sought. Using the dissociation trajectory (Figure 6.8), the following timescales relevant to our experiment must be considered.

6.4.3 De Broglie Time Scale

Rather than reflecting the change in the R-dependent Σ/Π composition of the excited state, it is apparent by inspection of Figure 6.7 that the anisotropy parameter completes a cycle of evolution within the first 2.5-3 ps. A 2.5 ps delay corresponds to a 36 Å separation between the fragments (see Figure 6.8). This length-scale is a critical clue for understanding the dynamics, as it is remarkably similar to the de Broglie wavelength of the asymptotic (eKE = 0.12 eV) photoelectrons, λ = 35.4 Å. Therefore, the 2.5 ps timescale, hereafter referred to as the de Broglie timescale, denoted t_1, appears to couple the dynamics of the nuclear separation and electron emission.

6.4.4 Electron-Localization Time Scale

On the other hand, as pointed out by Neumark and co-workers,[201] the evolution of the anisotropy parameter should also reflect the change in the electronic wavefunction character from that corresponding to the $A'\,^2\Pi_{g,1/2}$ molecular state to that corresponding to the excess electron localized on one of the atomic fragments. In the present experiment, the time-dependent changes in the anisotropy persist for more than 2 ps. For comparison, having examined 793 nm dissociation of I_2^- with a 264 nm probe, the Neumark group suggested that the localization of the excess electron occurs by 800 fs, when the evolution of the anisotropy in their experiment stops.[201]

The likely mechanism of the localization of the excess electron on one of the fragments relies on the external-field mixing of I_2^- electronic states of *gerade* and *ungerade* symmetry, such as the $A'\ ^2\Pi_{g,1/2}$ and $X\ ^2\Sigma_u^+$ states.[201] In both the Neumark group's and our experiments, the photodissociation and photodetachment occur in the presence of DC fields. Comparing the 40 V/cm field used in this work to the 500 V/cm field in the Neumark experiment,[201] the delocalized nature of the $(I\cdots I)^-$ electronic wavefunction is expected to persist longer in our case. This prediction is indeed seen to be in agreement with the experimental observations.

In examining the effect of the DC field, we have considered measurements with a stronger, 80 V/cm extraction field within the electron imaging lens. The corresponding images are presented in Figure 6.2 alongside the similar measurements on IBr^-, albeit without discussing the angular distributions. Although the 80 V/cm dataset is less-extensive compared to the present work, crude analysis of the 80 V/cm images for I_2^- and IBr^- reveals two qualitative observations relevant here. First, the anisotropy trends in the 80 V/cm I_2^- experiment are similar to the 40 V/cm data reported in this section, with similar characteristic timescales. Second, the photodetachment anisotropy in the IBr^- case does not exhibit a significant variation on the 2.5 ps timescale observed in I_2^-, leveling off at the asymptotic I^- level much earlier in the dissociation process. For example, it can be seen by inspection of the pump-probe images in Figure 6.2 that the 1350 fs I_2^- photoelectron image is more anisotropic than the 1400 fs IBr^- image, with the latter corresponding, essentially, to the asymptotic I^- limit.

A quantitative estimate of the localization timescale can be obtained as follows. For effective state mixing, the two unperturbed potential energy curves must come close enough for the splitting to be comparable to the energy difference between the ($I_A + I_B^-$) and ($I_A^- + I_B$) localized-electron states in the presence of the external field. While the field-induced perturbation is of the order of $H' = eER$, where E is field intensity, a reliable estimate of the R-dependent splitting between two molecular states is quite challenging at large internuclear distances. As an estimate, we take the 0.8 meV splitting between the $A'\ {}^2\Pi_{g,1/2}$ and $X\ {}^2\Sigma_u^+$ states at R = 13 Å, cited by Neumark and co-workers,[201] and further assume that the long-range $(I\cdots I)^-$ potentials scale as R^{-4} (charge – induced-dipole interaction). Then, the g-u energy splitting can be modeled as $\Delta E = C/R^4$, where the coefficient C = 23 eV·Å^4 is chosen to reproduce the above value at R = 13 Å. Requiring $\Delta E \approx H'$, the field-induced transition to a localized-electron state should occur at $R \approx (C/eE)^{1/5}$, which under our experimental conditions (E = 40 V/cm) corresponds to $R \approx$ 35.6 Å. By sheer (unintended) coincidence, this value is very close to the de Broglie wavelength of the asymptotic photoelectrons (λ = 35.4 Å).

The internuclear distance of R = 35.6 Å needed, according to the above estimate, for the electron-localization transition is reached at 2.5 ps, which is hereafter considered as an approximate electron localization timescale, t_2.

6.4.5 The Overall Picture

Hence, two different in nature but similar in magnitude timescales, both coincidentally equal to 2.5 ps, are at play in the experiment: t_1, defined by the photodissociation and photodetachment energetics, and t_2, which depends on the external field.

At early stages of the dissociation, the photodetached electron is emitted from an I_2^- molecular orbital, which can be viewed as a linear combination of atomic orbitals localized on two equivalent centers, separated by time-dependent distance R. As in any interference scenario, the emitted waves are expected to reflect the variation in R/λ, where λ is the de Broglie wavelength. The corresponding timescale, t_1, is the time necessary for the fragments to separate to $R \approx \lambda$, where λ is the de Broglie wavelength of the photoelectrons. Indirect support for this picture is found in the lack of significant long-range time-dependence of β_2 in the case of $IBr^- \rightarrow I^- + Br$ dissociation (Figure 6.7), in which case the electron detachment does not involve two equivalent centers.

For the dissociation to complete in the I_2^- case, the excess electron must localize on one of the fragments, thus breaking the inversion symmetry. *It is not the act of the imaging measurement that collapses the excess-electron wavefunction to a localized atomic orbital.* In any experiment, the wavefunction is collapsed to one of the eigenfunctions of the operator corresponding to the type of measurement involved. In photoelectron imaging, the measurement is the determination of position of an electron impact on the detector and the corresponding eigenfunctions are delta-functions of lab-frame coordinates – not the 5*p* orbitals localized on one of the I atoms. Hence, the photodetachment step does not localize the excess-electron wavefunction. Averaging over many electron impacts on the detector yields the projection of the probability density distribution corresponding to the free-electron wavefunction, ψ_f. The properties of ψ_f are, in turn, determined by the initial (bound) electron state, which can be either localized or delocalized in nature.

The timescale for the electron localization, t_2, is (presumably) defined by external-field mixing of the delocalized (molecular) electronic states. For the present experimental conditions, t_2 is estimated to be ~2.5 ps. This crude estimate agrees with the drop off in β_2 magnitude seen in Figure 6.7. Given the similar values of the two timescales, t_1 and t_2, only the first cycle of the interference-induced anisotropy variation is expected (and seen) in the data. Due to the scaling of t_2 with the extraction field, $t_2 \propto E^{-1/5}$, the experimental grip of this parameter is not very good: for example, a factor of 2 increase in the extraction field would shorten the localization timescale by only 15%. The predicted weak dependence of t_2 on the field may explain why no significant difference is observed between the anisotropy trends in our 40 and 80 V/cm datasets, within the combined uncertainty of both.

At $t > t_2$, the $\mathrm{I}\cdots\mathrm{I}^-$ internuclear distance hardly affects the emitted electron waves, as the parent electron orbital is by now localized on a single center. The corresponding photoelectron images reflect the photodetachment of the isolated I^- fragment and the values of β_2 in Figure 6.7 level off within the confidence limits for I^-.

The following subsection describes, in a semi-quantitative fashion, the two-center interference that defines the detachment dynamics within the first 2.5 ps.

6.4.6 Two-Center Interference Model

The observation of a cycling variation in β_2 on the de Broglie timescale suggests an interference picture for the photodetachment of dissociating I_2^-. A conceptually similar two-center interference view was developed previously for the (static) photodetachment of covalent dimer anions $(CO_2)_2^-$ and $(CS_2)_2^-$.[252] In the present case, the I_2^- $\sigma_u(5p)$ orbital, from which the electron detachment takes place, is described as a linear combination of the 5*p* orbitals of the two dissociating atoms, I_A and I_B: $\sigma_u(5p) = c(5p_A + 5p_B)$, where *c* is a normalization constant. The final-state electron wavefunction is then a linear combination of waves emitted from I_A and I_B.

Considering that the probe wavelength is orders of magnitude greater than the length-scales relevant in the experiment, the photodetachment can be discussed in the electric-dipole approximation. In addition, since at all relevant delays *R* is much smaller than the 390 nm probe wavelength, I_A and I_B emit waves with equal amplitudes, as long as the parent orbital preserves its *ungerade* symmetry. The evolution of the PAD then reflects the change in the relative phases accumulated by the waves from I_A and I_B, as observed in the far field. If we neglect, for the time being, the interaction between the photodetached electron and the neutral fragments, the phase difference is determined, among other factors, by the de Broglie wavelength, λ, and the separation between I_A and I_B, *R*. In the simplest model, not considering the details of the detachment process and orientation averaging, one expects the anisotropy to display periodicity with respect to R/λ, with a period determined by $\Delta(R/\lambda) = 1$.

This model immediately explains, qualitatively, why the anisotropy parameter completes a full cycle within the de Broglie timescale. In order to address the $\beta_2(t)$ behavior semi-quantitatively, we model this evolution with a periodic function:

$$\beta_2(t) = a + b\cos\left(\frac{2\pi R(t)}{\lambda} + \phi\right) \tag{6.4}$$

Equation 6.4 is not intended to represent the exact functional form of $\beta_2(t)$, but merely to model the underlying timescale and periodicity. $R(t)$ is the dissociation trajectory (Figure 6.8), while a and b can be used as adjustable parameters to model the experimental data. Factor ϕ accounts for any phase shift due to the interaction of the emitted electrons with the neutral fragments.

We first neglect the electron-neutral interactions, setting $\phi = 0$. In this case, the position of the first extreme of $\beta_2(t)$ defined by Equation 6.4 is determined by λ. The least-squares fit of $\beta_2(t)$ with $\phi = 0$ to the experimental data in the $t = 0$-3 ps range is shown in Figure 6.7 as a solid curve. The procedure yields $a = -0.267 \pm 0.006$, $b = 0.082 \pm 0.008$ and $\lambda = 42.7 \pm 1.1$ Å. The last value is compared to the 35.4 Å de Broglie wavelength of the 0.12 eV photoelectrons.

With $\phi = 0$, the sum of a and b in Equation 6.4 corresponds to β_2 expected at $R = 0$. While this limit does not occur in the dissociation, it corresponds to a united-atom description of the diatomic anion, whereas the $5p_A$ and $5p_B$ orbitals overlap completely and in phase with each other. Hence, within the model framework, the $R = 0$ limit corresponds to the photodetachment from an atomic p orbital, similar to I^-. It is reassuring that the model value of $\beta_2(R = 0) = a + b = -0.185 \pm 0.010$, as obtained from the above fit, is in excellent agreement with the experimental result for I^- at 390 nm, $\beta_2 = -0.17 \pm 0.05$.[249]

Comparing the model with the experiment, it is necessary to address the discrepancy between the de Broglie wavelength that best reproduces the experimental results, 42.7 Å, and the actual wavelength of 0.12 eV electrons, 35.4 Å. This discrepancy is not trivial, as $\lambda = 42.7$ Å corresponds to eKE = 0.08 eV, falling outside the full width at half-maximum of the observed photodetachment band (see Figure 6.6).

The discrepancy likely stems from the neglect of the interactions between the photodetached electron and the neutral fragments. The 35.4 Å wavelength is calculated in the far field, while the electron-neutral interactions affect the electron wavelength in the near field, contributing to the relative phases of the waves emitted from $\mathrm{I_A}$ and $\mathrm{I_B}$. The effect of these interactions can be accounted for, approximately, by either treating λ in Equation 6.4 as an adjustable parameter corresponding to an effective near-field wavelength or, alternatively, using a non-zero value of ϕ to account to the resulting phase-shift.

The first approach corresponds to the fitting procedure outlined above, yielding $\lambda = 42.7$ Å. The longer effective wavelength of the emitted electrons, compared to the far-field limit, corresponds to a lower kinetic energy of the photoelectrons in the near field, possibly reflecting the effect of the centrifugal barrier in the photodetachment.

The second approach, introducing a non-zero phase factor in Equation 6.4, is in general more accurate, but its inherent disadvantage is that ϕ is expected to depend on R. That is, in the extrapolated $R = 0$ limit we must have $\phi = 0$, corresponding to the united-atom description of I_2^-, while at $R \to \infty$ the phase-shift is expected to reach a non-zero asymptotic value. A simplified version of this approach can be considered by setting λ to its far-field value, 35.4 Å, and treating ϕ as a constant parameter, with the implicit assumption that the change in $\phi(R)$ occurs predominantly at internuclear separations shorter than those relevant to most of the present dataset.

The dashed curve in Figure 6.7 represents a corresponding least-squares fit to the experimental data in the 0-3 ps range, yielding $\phi = -40.9° \pm 6.0°$, $a = -0.283 \pm 0.006$ and $b = 0.086 \pm 0.008$. The negative value of the phase factor is consistent with the alternative description above, i.e., the lengthening of the electron wavelength in the near field. Extrapolating this approach to the united-atom limit, it is necessary to set $\phi = 0$, in which case we get $\beta_2(R = 0) = a + b = -0.197 \pm 0.010$, similar to the above effective-λ approach and once again in excellent agreement with the experimental I^- limit. Overall, the performance of the model with the electron-neutral interactions accounted for with a phase-shift factor is similar to that relying on an effective de Broglie wavelength.

The most important outcome of the admittedly crude model described here is that it correctly describes the *timescale* of the anisotropy variation in the experiment. The model parameters a and b as well as the phase factor ϕ in Equation 6.4 do not affect the timescale. The timescale is controlled by the fragment separation speed [via $R(t)$] and the de Broglie wavelength of the photoelectrons. Both of these parameters are predetermined by the energetics.

Finally, it is instructive to examine the present results in light of the previous findings by Neumark and co-workers, who used a similar 793 nm excitation wavelength, but probed the evolving electronic structure with more energetic 265 nm photons. A decrease in β_2 was observed at delays up to 200 fs, followed by a transient increase peaking at 650 fs.[201] It was hypothesized that this behavior is related to the passage though the shallow polarization-induced potential minimum on the dissociation potential. In view of the present results, an alternative explanation can be put forth. From the 793 nm dissociation energetics, the internuclear distance corresponding to the transient maximum at t = 650 fs is ~11 Å, comparing quite favorably with the 10 Å de Broglie wavelength of the 1.6 eV eKE photoelectrons generated by the probe. Again, the dissociation and electron emission dynamics appear to have a common characteristic parameter, that being the de Broglie wavelength. Hence, the timescale of the anisotropy evolution in the Neumark experiment can also be explained within the model outlined here.

6.5 Photodissociation Dynamics of I_2^- on the B $1/2_g$ $(^2\Sigma^+)$ Excited State

The successful time-resolved photoelectron imaging studies of I_2^- photodissociation dynamics at 780 nm prompted further experimental investigation of this anion. The experiment described in this section is conducted at the same conditions as previous (see Experimental section 6.2 for more details) except the pump photon energy. The 390 nm excitation pulse brings I_2^- to the dissociative B $1/2_g$ ($^2\Sigma^+$) electronic state correlating to the I^- + $I^*(^2P_{1/2})$ product channel (see Figure 6.1). As before, the evolution of the electronic structure is probed through 390 nm electron detachment. The optical line arrangement for the single color experiment has been described in detail in Section 2.7 of Chapter 2 and is omitted here. The cross-correlation between pump and probe pulses was measured to be about 300 fs which defines the temporal resolution in the present experiment.

Figure 6.9 shows the time-resolved spectra along with the representative photoelectron images at selected pump-probe delays for the 390 nm photodissociation experiment on I_2^-. The experimental data indicate a quick, ≤400 fs, evolution of the photoelectron kinetic energy towards the asymptotic maximum value of 0.12 eV. Accounting for our temporal resolution of 300fs, this yields ~100 fs reaction time-scale as an upper bound estimate for reaching the energetic identity of I^- product.

In contrast to the previous studies on I_2^- with 780 nm photoexcitation, photoelectron anisotropy for the current experiment, plotted in Figure 6.10, does not exhibit any clear interference-induced periodic oscillations, at least within the measurement error bars, quickly converging to the β_2 value expected from I^-. A plausible explanation for the lack of clearly resolved quantum interference effect in the observed time-resolved anisotropy trend is that the excess electron gets localized on one of the iodine atoms in the early stage of the dissociation process. As was discussed previously in Section 6.4.4, the proposed mechanism of electron localization involves the destruction of the parent

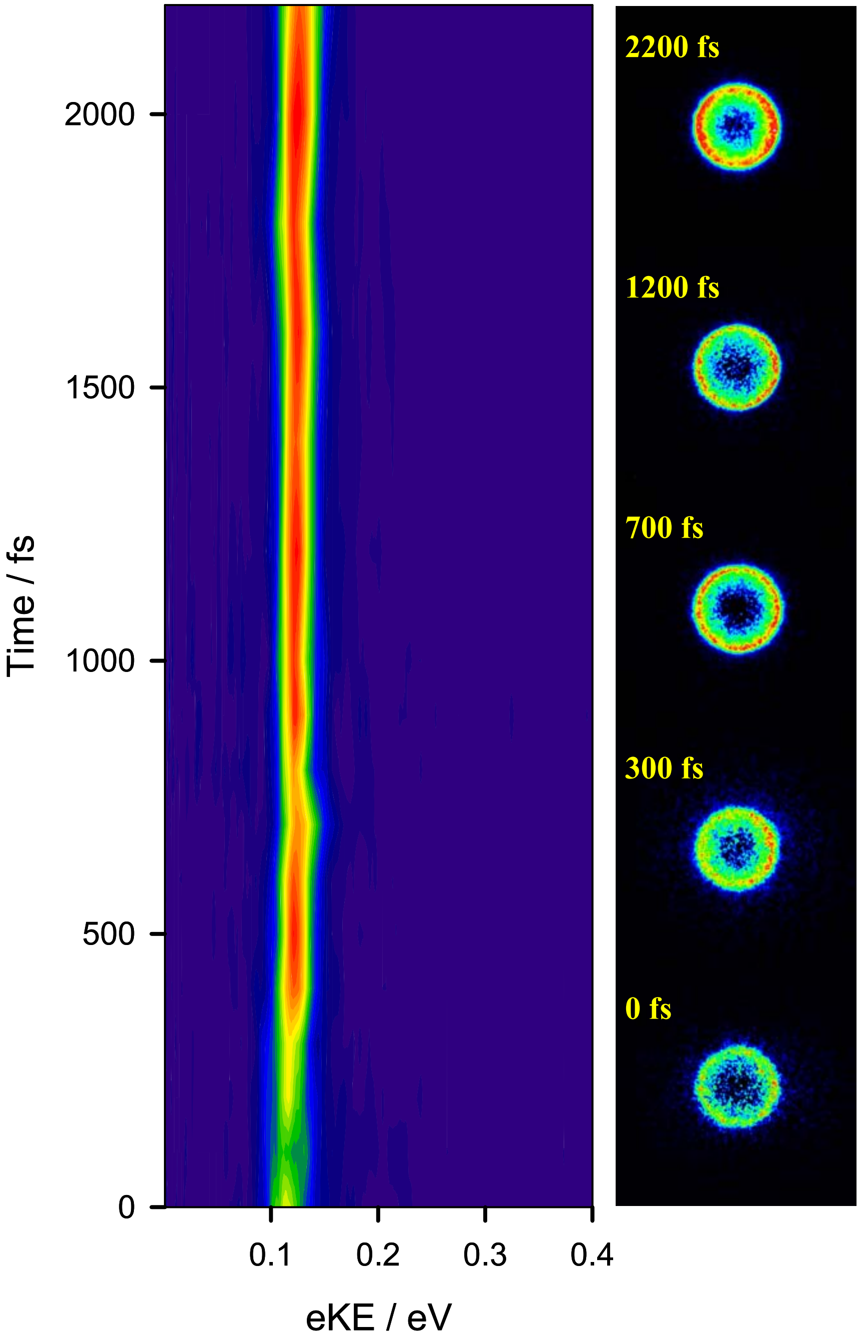

Figure 6.9 Left: the time-resolved photoelectron spectrum obtained in the dissociation of I_2^- using a single color, 390 nm, pump-probe scheme. Right: representative raw photoelectron images corresponding to 0, 300, 700, 1200 and 2200 fs pump-probe time delays. The pump and probe polarization directions are vertical in the plane of the Figure.

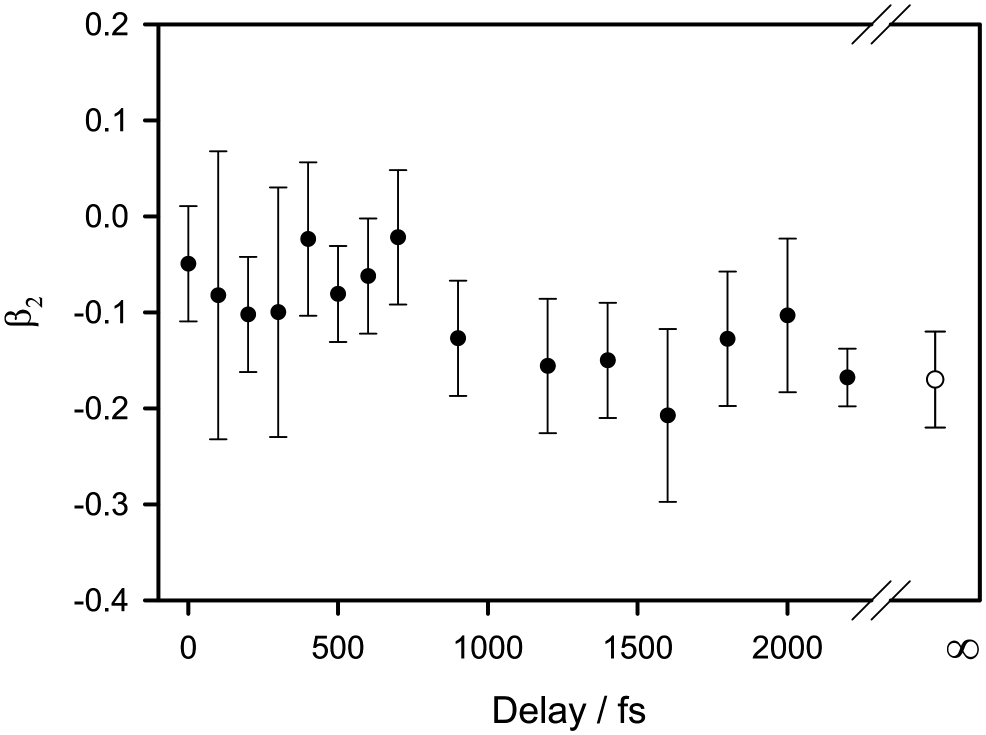

Figure 6.10 Evolution of photoelectron anisotropy parameter β_2 as a function of pump-probe delay in I_2^- photodissociation via $I^- + I^*(^2P_{1/2})$ channel using 390 nm pump and 390 nm probe. In Figure, filled circles indicate time-resolved data while open circle represents t = ∞ value corresponding to the photodetachment from the isolated I^- product.

molecular orbital inversion symmetry due to the external field mixing of electronic states of gerade (*g*) and ungerade (*u*) symmetries. By examining Figure 6.1, we identify a′ $1/2_u$ ($^2\Pi$) potential of the ungerade symmetry, approaching the B $1/2_g$ ($^2\Sigma^+$) surface at larger I-I internuclear distances, as primarily responsible for the change in the wave function character leading to the electron localization.

To estimate the electron localization time-scale we performed theoretical modeling of I_2^- dissociation dynamics on the B $1/2_g$ ($^2\Sigma^+$) electronic state using the same approach as described in Section 6.3.3. The results of classical trajectory calculations are shown in Figure 6.11. Considering the electron localization time-scale it is important to note that (i) dissociation of I_2^- on the B state (Figure 6.11) proceeds faster than on the A′ state (Figure 6.8); and (ii) B and a′ potentials are significantly less separated in energy than the ground and A′ surfaces. Therefore, it is anticipated that the *g-u* state mixing in the current experiment should occur at significantly smaller pump-probe delays than determined ~2.5 ps time interval in the previously studied case for the I^- + I($^2P_{3/2}$) channel. This qualitative conclusion supports our original hypothesis about the absence of quantum interference effect in the measured PADs. For the quantitative evaluation of the electron localization time we follow the procedure outlined in Section 6.4.4. Specifically, we are looking for the internuclear R distance at which the splitting between the B and a′ states is on the order of the field-induced perturbation $H'(R) = eER$, where E is field intensity (40 V/cm in current experiment) between velocity map imaging lens in our instrument. To do so, we fit the R-dependent splitting $\Delta E(R)$ between two molecular states with a

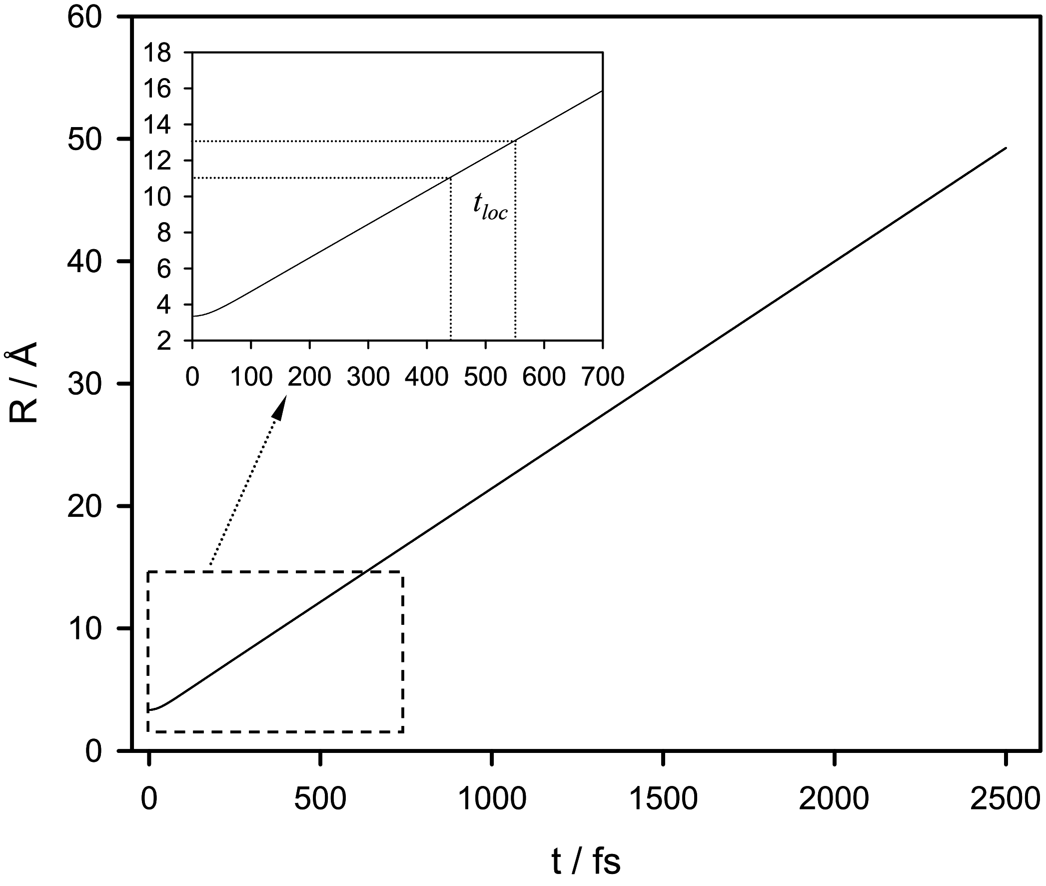

Figure 6.11 The dissociation trajectory of I_2^- on the B $1/2_g$ ($^2\Sigma^+$) excited state potential[207] accessed with 390 nm pump photon. The trajectory is calculated by integrating Equation 6.1 on a time-grid with a constant 1 fs step size. The inset shows the expanded 0-700 fs range pertinent to the electron localization time-scale t_{loc}.

forth degree polynomial of the form $A/r^2 + B/r^3 + C/r^4$ and then require $\Delta E(R) = H'(R)$. Finding numerically roots of the obtained fifth order equation provides us with the following R values of 11, 13, 118 Å, and two complex numbers. From the above results we have to consider only 11 and 13 Å, while 118 Å is unreasonably large and the last two complex internuclear distances do not bear any physical meaning. Using the dissociation trajectory in Figure 6.11 and computed R values, we estimate that the electron localization should happen within first 450-550 fs. Finally, it is necessary to correct the above prediction for the experimental pump-probe temporal resolution, which defines the upper limit of 150-250 fs for the electron localization time scale.

In conclusion, the theoretical modeling of I_2^- photodissociation dynamics on B $1/2_g$ ($^2\Sigma^+$) excited state calls for a fast, within a few hundred femtoseconds, evolution of photoelectron angular distribution to the asymptotic limit of I^- product due to the early localization of the parent molecular orbital on a single atomic center by the external electrostatic field. Our experimental findings, in particular the absence of interference induced anisotropy oscillations, support the model predictions.

6.6 Summary

Time-resolved anion photoelectron imaging was applied to study the photodissociation dynamics of I_2^- and IBr^- anions along the reaction coordinate. The results for IBr^- are discussed in comparison with photodissociation of I_2^- on the analogous electronic state, investigated under similar experimental conditions. Previous studies on the I_2^- anion[27,186,204] were used as a reference for interpreting the IBr^- results.

The evolution of the energetics revealed in the time-resolved (780 nm pump, 390 nm probe) I_2^- and IBr^- photoelectron images was compared to the results of classical trajectory calculations on the respective A' excited-state anion potentials. The time-resolved photoelectron spectra were modeled assuming that a variety of neutral states were accessed in the probe-induced photodetachment. The experimental spectra for I_2^- obtained in the present work are in good agreement with the A' anion potential previously determined by Zanni et al. based on the measurements at a different (260 nm) probe wavelength.[186] The experimental data and theoretical modeling of the IBr^- dissociation provide the first rigorous dynamical test of the recently calculated A' potential[206] for this system. In light of the good overall agreement of the experimental data with the theoretical predictions, the results are used to construct a snapshot of the IBr^- dissociation potential.

Time-resolved photoelectron imaging of I_2^- excited to the A' $1/2_g$ $(^2\Pi)$ electronic state, reveals the effect of quantum interference in time-resolved photoelectron angular distributions. In contrast to the previous studies,[27,186,204] the emerging fragments are probed in a low electron kinetic energy regime (eKE = 0.12 eV), giving a better handle on the evolving photoelectron anisotropy and the inherent timescales.

While no change in the energetics is discerned after 700 fs, the photoelectron anisotropy exhibits what appears to be the first cycle of a variation persisting for up to 2.5 ps. Hence, the anion electronic wavefunction continues to evolve long after the energetic limit of the dissociation has been reached (within the energy resolution of the experiment). The observed timescale of the anisotropy variation corresponds to the internuclear separation of the same order of magnitude as the de Broglie wavelength of the emitted electrons (λ = 35.4 Å). Therefore, this wavelength is a critical parameter connecting the photodissociation and electron emission dynamics.

We interpret these findings by considering the effect of I_2^- inversion symmetry on the electronic structure evolution in the dissociation. The dissociating anion is viewed, effectively, as a two-center dynamic "interferometer", which samples, over the span of the dissociation process, a wide internuclear separation range. Two different in nature but similar in magnitude timescales are argued to play a role: (1) the de Broglie timescale, defined as the de Broglie wavelength of the emitted electrons divided by fragment separation speed; and (2) the electron localization timescale, describing the breaking of the inversion symmetry of the parent electronic wavefunction. The predictions of the model concerning these timescales are in good agreement with the experiment.

Time-resolved photoelectron imaging of I_2^- with 390 nm excitation shows a rapid photodissociation dynamics on the B $1/2_g$ ($^2\Sigma^+$) excited state surface. Both the photodetachment energetics and angular distributions reach their asymptotic values of I^- product on a time scale of 400-500 fs. The theoretical modeling of I_2^- dissociation suggests early, ≤550 fs, localization of the excess electron on one of the iodine atomic centers, which explains the absence of interference-induced oscillation pattern in the time-resolved anisotropy parameter (β_2) values.

CHAPTER 7

TIME-RESOLVED PHOTOELECTRON IMAGING OF THE I^- CHANNEL IN PHOTODISSOCIATION OF MIXED TRIHALIDE ANIONS

7.1 Introduction

Trihalide anions are small molecular systems with a very rich and complex photochemistry. Among all trihalide anions I_3^- has been studied most extensively. Zanni et al.[253,254] investigated photodissociation dynamics of I_3^- at 390 nm in the gas phase using femtosecond time-resolved photoelectron spectroscopy. In this experiment, the authors detect the formation of I^- and I_2^- anionic photofragments with approximately 1:1 branching ratio. Time-dependent periodical oscillations in photoelectron signal, with the subsequent revivals at 45 and 90.5 ps, were attributed to a coherent vibrational motion of I_2^- product. The observed oscillations correspond to an average vibrational excitation of 70% of I_2^- bond dissociation energy (D_0). The subsequent gas-phase photodissociation experiments on I_3^- by Nagata[255,256] and Neumark[257,258] show that the I^- photoproduct is generated via both $I^- + I_2$ and $I^- + 2I$ channels. The experimental results and theoretical calculations[256] indicate that the two-body dissociation mechanism is exclusively available through a non-adiabatic transition from an excited state of I_3^- correlating to the three-body channel.

Compared to I_3^-, the mixed trihalide anions were studied to a much lesser degree. The first photodissociation experiment on mixed trihalide anions in the gas phase was done by Sanov et al.[259] The photodissociation dynamics of $BrICl^-$ and IBr_2^- anions was examined by monitoring the time-dependent 400 nm pump – 800 nm probe yield of I^- fragment. The photodissociation of the trihalide anions near 400 nm primarily leads to diatomic anion products. Two product channels, IBr^- and ICl^-, with the branching ratio ~ 4:1 were observed in the photodissociation of $BrICl^-$ and only IBr^- fragments are detected for IBr_2^- anion. The observed diatomic fragment anions are formed in highly excited vibrational states ($\sim 0.9 \cdot D_0$ for IBr^- product). Analogous to I_2^- product in I_3^- experiment,[253,254] the coherent vibrational motion of IBr^- (in the photodissociation of both $BrICl^-$ and IBr_2^- anions) was also observed as time-dependent oscillation of I^- signal in the photofragment mass spectrum. No revivals of the IBr^- wave-packet were detected in the trihalide anion experiment. Taking into account the higher degree of vibrational excitation of IBr^- ($\sim 0.9 \cdot D_0$) compared to that of I_2^- ($\sim 0.7 \cdot D_0$), the authors suggest that IBr^- wave-packet revivals are smeared out by a higher-order anharmonicity near dissociation threshold. The simulations of the wave-packet dynamics on IBr^- ground state potential energy surface support this assumption.[259]

The successful studies on $BrICl^-$ and IBr_2^- anions have been furthered by our group. Mabbs and coworkers[41] investigated the evolution of I^- channel in I_2Br^- photodissociation using time-resolved photoelectron imaging spectroscopy. The 388 nm pump – 388 nm probe photoelectron data show that the localization of the excess electron wave function on the atomic anion fragment happens on about 300 fs time-scale. However, the evolution of I^- photoelectron band towards its asymptotic limit of the isolated product persists up to 1 ps due to the interaction between the atomic anion with the neutral counter fragment(s).

In this Chapter we present time-resolved photoelectron imaging study of I_2Cl^- and $BrICl^-$ trihalide anions with several dissociation pathways. The photodissociation dynamics of the anions is explored by monitoring the evolution of I^- fragment. The time-resolved photoelectron images reflect the transformation of the electronic wavefunctions from the excited I_2Cl^- and $BrICl^-$ molecular anions to the atomic-anion fragment (I^-). The experimental data reveal fast (within first 100 fs) generation of I^- product in the dissociation of I_2Cl^-, while the I^- signal from $BrICl^-$ anion appears at much longer pump-probe delays (~ 700 fs). We tentatively assign the difference in the reaction time-scales to the distinct dissociation pathways available for the anions to form I^- product. Specifically, coupled-cluster calculations suggest that the three-body dissociation channel $I^- + I + Cl$ is directly accessible for the I_2Cl^- which results in the rapid production of I^-. This route is not energetically reachable for the $BrICl^-$ and therefore the generation of I^- is only possible through the $I^- + BrCl$ channel. The two-body reaction pathway for this anion involves a nuclear rearrangement as the initial step before dissociation can proceed. The additional time required for the structural transformation of $BrICl^-$ results in the delayed appearance of the I^- feature in the time-resolved spectra. It should be emphasized here that the above hypotheses are based on the preliminary experimental results and more data collection is necessary to draw definite conclusions.

7.2 Experimental

The experimental arrangement used in this work is essentially of that previously described in Chapter 2 for both “static” and time-resolved studies. Thus only the details relevant to the present experiments are discussed here.

The I_2Cl^- and $BrICl^-$ anions are formed by crossing a supersonic expansion of ICl and IBr seeded in Ar with a beam of high energy electrons. The precursor mixture is prepared by passing Ar carrier gas at a stagnation pressure of 20 psig through a Teflon sample holder containing equal amounts of IBr and ICl crystals at room temperature. The resulting mixture is expanded through a pulsed nozzle (General Valve Series 9) operated at a repetition rate of 70 Hz into a high-vacuum chamber with a base pressure of 3×10^{-7} Torr (rising to $\sim4\times10^{-5}$ Torr when the valve is operated). Negative ions formed by crossing a supersonic jet with a 1 keV electron beam are pulse-extracted into a Wiley-McLaren time-of-flight mass spectrometer, where the ion beam is accelerated to ~ 2.5 keV and focussed using an Einzel lens. The ions are detected mass selectively using a dual-microchannel-plate (MCP) detector (Burle, Inc.) at the end of the flight tube. Photoelectrons produced by intersecting mass-selected anions of interest with a linearly polarized laser beam are then extracted in the direction perpendicular to the plane of anion and laser beams using the velocity mapping electrostatic lenses.[33,34] After travelling through an internally μ–metal shielded "field-free" flight tube, the photoelectron cloud is projected onto position sensitive imaging detector (Burle, Inc.). The experimental background is suppressed by maintaining a low (1.0-1.2 kV) potential difference across the two imaging MCPs for all the time but in the presence of photoelectron signal, when the potential is pulsed up to 1.8 kV for about 200ns in coincidence with the arrival of photoelectrons. An illuminating pattern on the phosphor screen produced by photoelectrons is recorded by a CCD camera (Roper Scientific, Inc.) and then transferred to data acquisition software. The temporarily resolved pump-probe images are obtained by removing the incidental pump-only or probe-only photoelectron signals from the original pump+probe images using computer-controlled shutters in the laser beam paths and the data acquisition and correction algorithm described previously in Chapter 2. Each of the final photoelectron images reported in this work corresponds to a collection of ~10^6 experimental cycles.

The photoelectron spectra and angular distributions are extracted simultaneously from the central slice through the reconstructed sphere along the laser polarization axis using the BASEX (BAsis Set Expansion) program of Reisler and co-workers.[54]

The time-resolved experiments are conducted using 390 nm femtosecond pulses in a "single-color" regime (see Section 2.7 for detailed description of the optical arrangement). Both pump and probe beams are generated by frequency doubling the output from a regeneratively amplified Ti:sapphire laser system (Spectra Physics Inc.), producing fundamental output centered around 780nm, 1 mJ/pulse with a temporal pulse width of ~90 fs measured by a single-shot autocorrelator (Positive Light SSA). The fundamental radiation is frequency doubled in BBO crystal of a femtosecond harmonics generator (Super Optronics Inc.), delivering 270 μJ pulses at 390 nm.

The frequency doubled light is separated into two beams, pump and probe, using a 50% beam splitter. One of the beams travels through a fixed optical path length, while the other is directed through a motorized translation stage (Newport ESP300 Universal Motion Controller) to enable controlled temporal separation of the pump and probe pulses. Finally, the beams are recombined before entering the detection chamber using a second 50% beam splitter. The zero pump-probe delay is found by varying one of the beams optical path until a pattern of interference fringes shows up indicating that two coherent beams are overlapped both in time and in space. The pump-probe cross-correlation width is measured to be about 250 fs, which defines the approximate time resolution for these experiments.

7.3 Results and Discussion

Figure 7.1 shows the summary of computed energetics for iodine contained mixed trihalide anions. The electronic structures and dissociation energies for two- and three-body channels of the IXY^- trihalide anions (X, Y = Cl, Br, I) are calculated using coupled-cluster method with single and double excitations (CCSD). All calculations are performed with GAUSSIAN 03 program package.[170] The all-electron standard aug-cc-pVDZ basis set is used for chlorine and the aug-cc-pVDZ-PP basis sets with relativistic

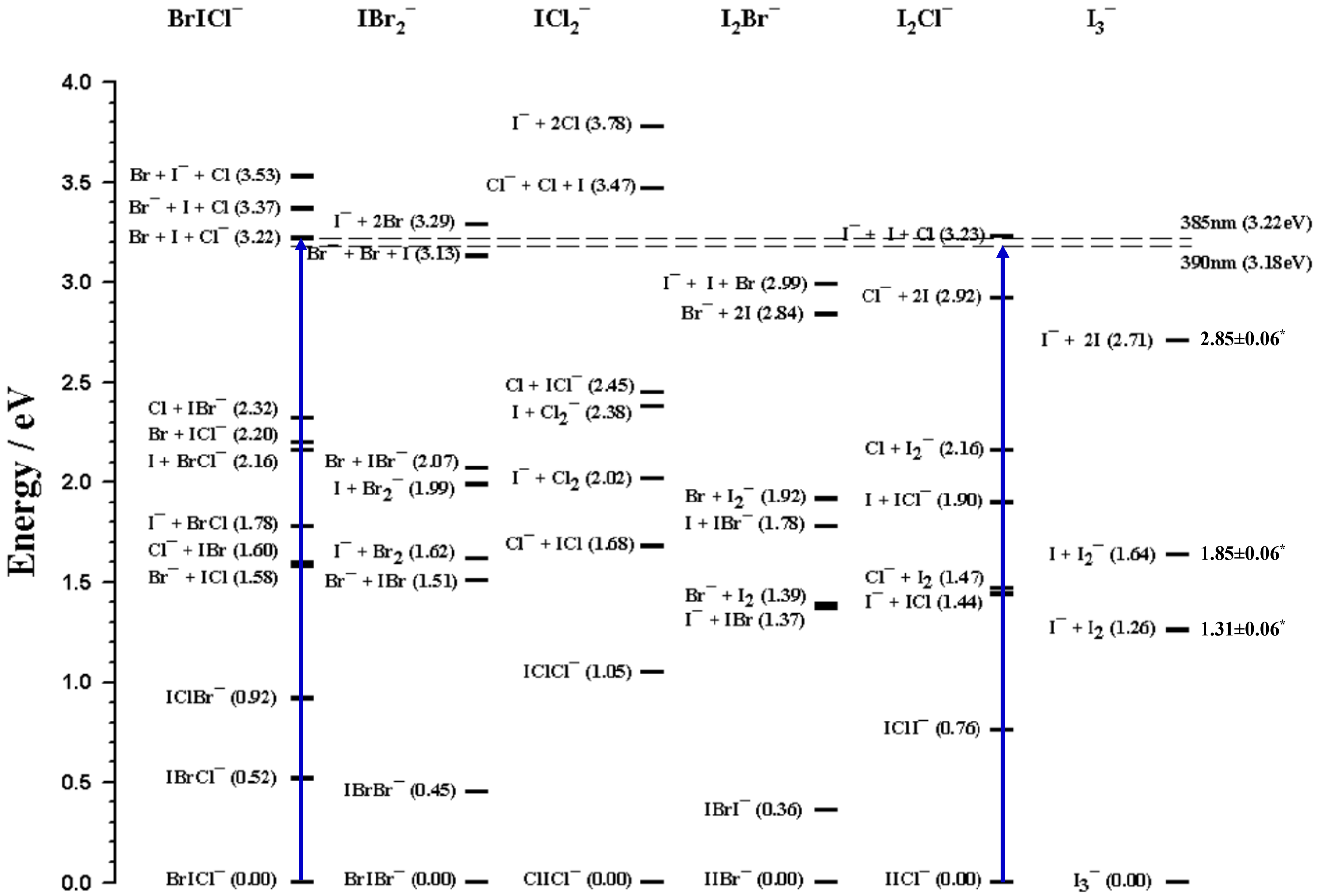

Figure 7.1 Energy diagram of photodissociation product channels for the iodine containing trihalide anions. The energy values in parenthesis are calculated relative to the most stable isomer for each particular trihalide anion using CCSD method. The blue arrows correspond to the excitation photon energy used in the present experiments. * The experimental values[255-258,263,264] for I_3^- dissociation energetics are given without parenthesis for comparison with the computational results.

pseudopotentials[260] obtained from the EMSL Basis Set Library[261,262] are used for iodine and bromine atoms. The vibration frequencies are calculated at the same level of theory to confirm that the optimized structures correspond to the true potential minima. All calculated trihalide anions possess linear geometry in their ground states. The final energies of molecular species are corrected for zero-point vibrational energies.

To our best knowledge, there are no experimental measurements on the energetics of trihalide anions, except for I_3^-.[255-258,263,264] In order to test the validity of obtained theoretical results, the dissociation energies for I_3^- are computed at the same level of theory for comparison with experiment. The calculated values for $I^-(^1S)$+ $I_2(X\,^1\Sigma_g^+)$, $I(^2P_{3/2})$ + $I_2^-(X\,^1\Sigma_u^+)$, and $2I(^2P_{3/2})$ + $I^-(^1S)$ dissociation channels are 1.26, 1.64, and 2.71 eV, respectively. These values are in good agreement with the corresponding 1.31±0.06, 1.85±0.06, and 2.85±0.06 experimental energies.

There are several possible structural isomers of the mixed trihalide anions: two for I_2X^- (IIX^-, IXI^-) and IX_2^- (IXX^-, XIX^-), X = Cl, Br; and three ($BrICl^-$, $IBrCl^-$, and $IClBr^-$) for the $BrICl^-$. For all studied trihalide anions, the calculations predict that the most stable isomer is the one with the iodine atom in the middle e.g. $BrICl^-$, $IICl^-$, $BrIBr^-$, etc… The energy difference between the most stable and second stable isomers ranges from 0.36 eV (I_2Br^-) up to 1.05 eV (ICl_2^-). These results are in accord with the previous theoretical findings by Sanov et al.[259] as well as with the simple chemical intuition suggesting that the most stable isomer should contain the most electropositive atom (i.e. I) in the middle, thus minimizing the coulomb repulsion between two terminal

(Cl and/or Br) atoms with partial negative charges. In principle, the structural isomers can significantly complicate interpretation of experimental results. Luckily, these isomers are not expected to be present in any significant quantities in our experiment because of the large difference in the formation energy relative to those with the most stable structures. In addition, none of the higher energy isomers was observed for the IBr_2^- and $BrICl^-$ anions generated at similar experimental conditions.[259]

Figure 7.2 shows one-photon photoelectron images of isolated species corresponding to the anionic fragments (I^-, ICl^-, IBr^-, and I_2^-) which are energetically accessible (see Figure 7.1) upon excitation of I_2Cl^- and $BrICl^-$ anions at 390/385 nm. In Figure 7.2, we do not report photoelectron data for the Cl^- [EA(Cl) = 3.61 eV[59]] and Br^- [EA(Br) = 3.36 eV[61]] products. These anions are not expected to produce any photoelectron signal since their detachment energies are larger than the photon energy (3.18/3.22 eV) available in the current experiments.

The raw photoelectron images and energy spectra obtained at selected pump-probe delays in the dissociation of I_2Cl^- and $BrICl^-$ are presented in Figures 7.3 and 7.4 respectively. Both time-resolved experiments were conducted in a single color regime, using the same photon energy for pump and probe, yet with slightly different wavelengths for I_2Cl^- (390nm) and $BrICl^-$ (385nm). Increasing photon energy in the case of $BrICl^-$ helps to enhance the time-resolved signal due to larger photodetachment and photo-fragmentation cross-sections for I^- product. The photoelectron spectra for short (up to 300fs) time delays exhibit broad band transition (type M) corresponding to the detachment from a molecular orbital, while at longer pump-probe delays the spectra

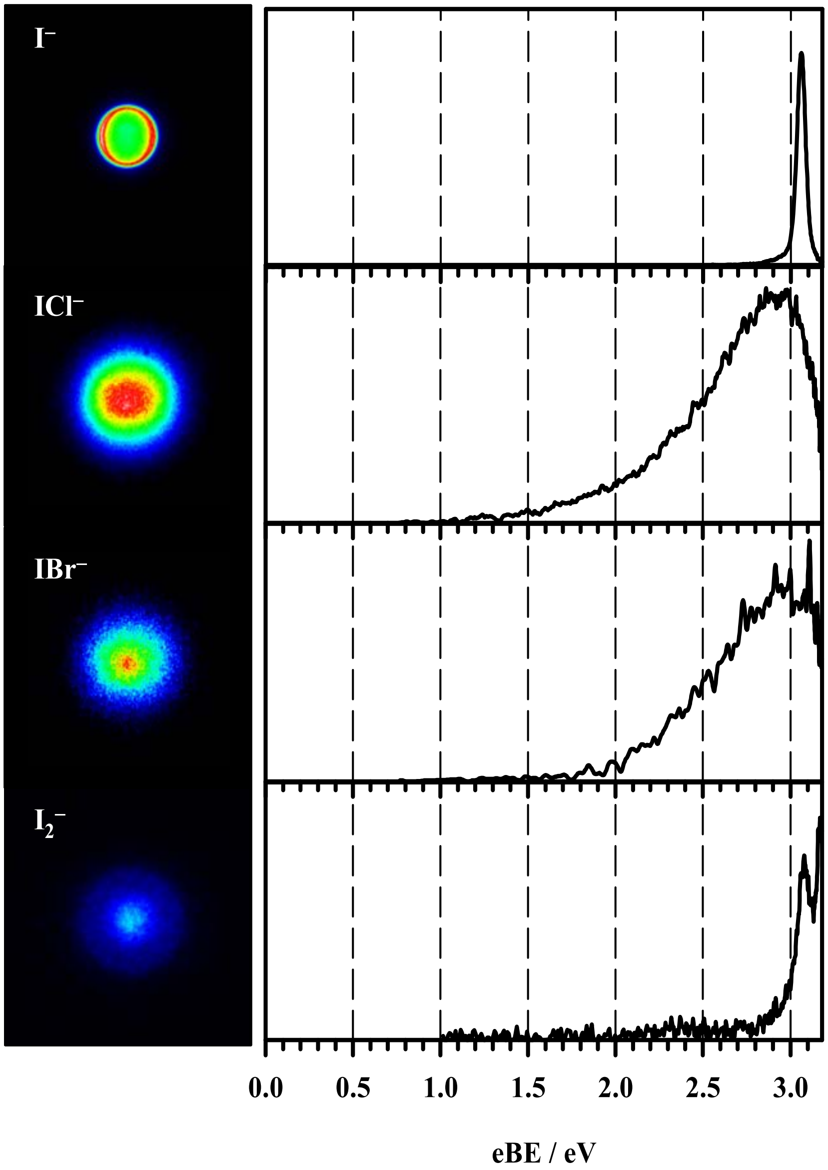

Figure 7.2 Raw photoelectron images (left) and corresponding photoelectron spectra (right) of ionic photofragments forming in the photodissociation of I_2Cl^- (I_2^-, ICl^-, I^-) and $BrICl^-$ (IBr^-, ICl^-, I^-). The photoelectron data for Br^- (EA = 3.36 eV[61]) and Cl^- (AEA = 3.61 eV[59]) products are omitted here since 390/385 nm (3.18/3.22 eV) photon energies employed in the present experiments are not sufficient to detach an electron from these anions.

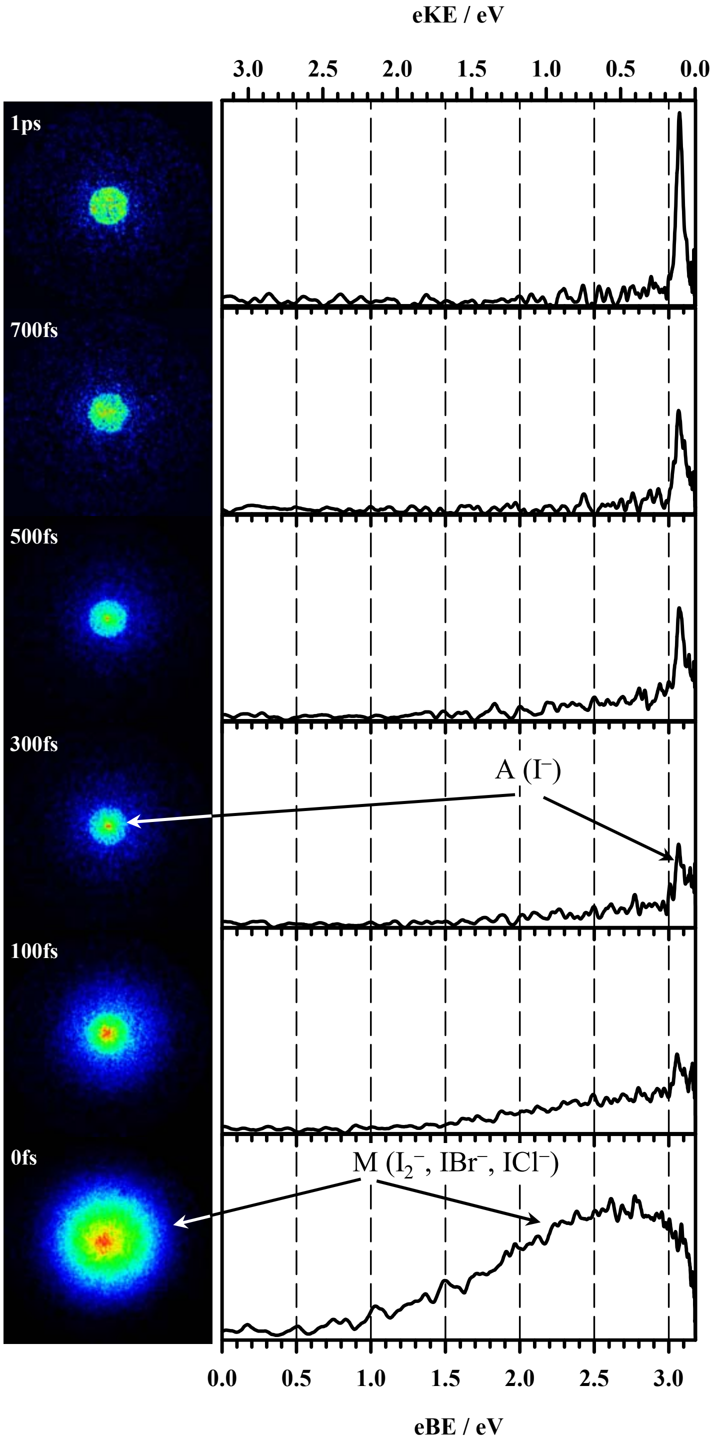

Figure 7.3 Time-resolved raw photoelectron images (left) and corresponding photoelectron spectra (right) obtained in dissociation of I_2Cl^- using 390 nm pump and 390 nm probe. The laser polarization is vertical in the image plane.

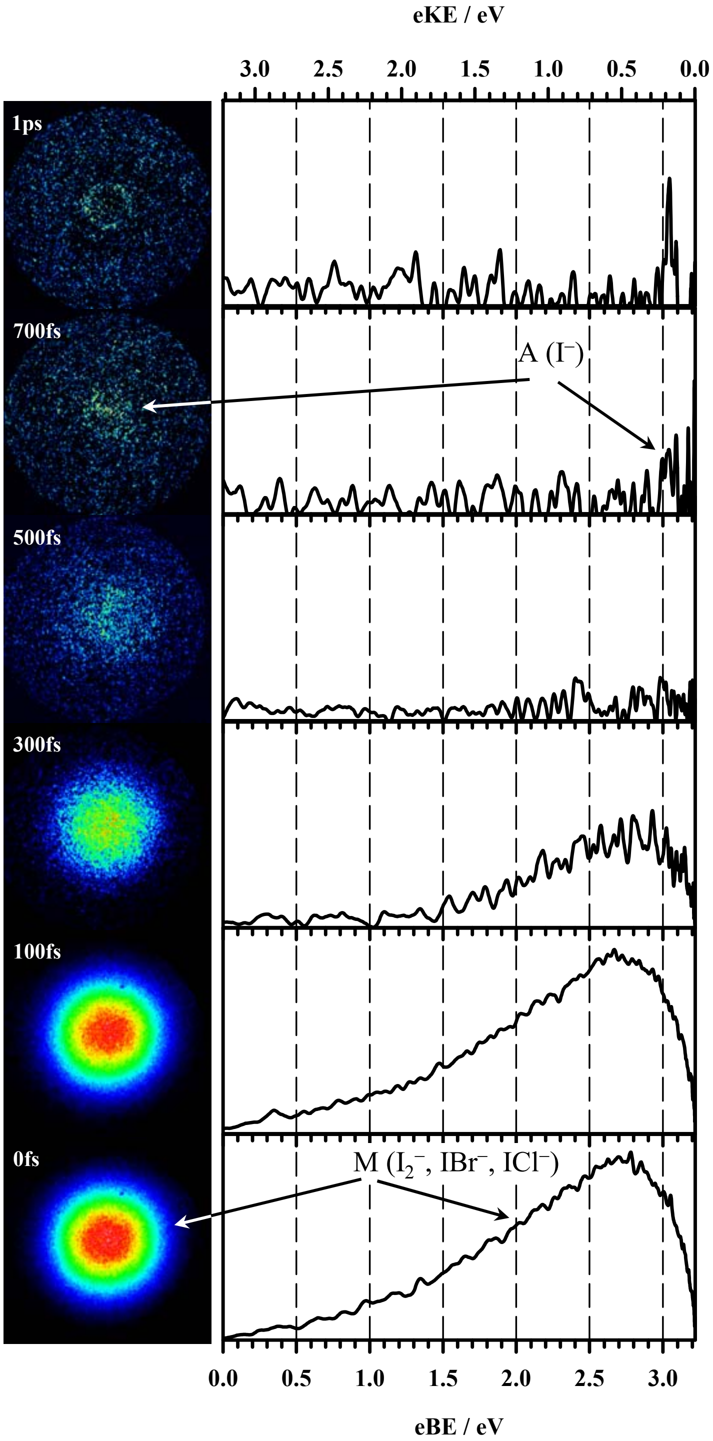

Figure 7.4 Time-resolved raw photoelectron images (left) and corresponding photoelectron spectra (right) obtained in dissociation of $BrICl^-$ using 385 nm pump and 385 nm probe. The laser polarization is vertical in the image plane.

evolve into single sharp atomic-like peak (type A) energetically matching to the $^1S_0 \leftarrow {}^2P_{3/2}$ transition from I^- (EA = 3.059 eV[64]).

There are two possible origins of type M transitions. It could arise due to either detachment from diatomic anion products or coherent two-photon absorption by the parent anions. A two-photon-detachment process in the presence of both pump and probe laser beams should produce photoelectron signal four times as much as that resulting from one of the beams. Subtracting twice the amount of pump-only and probe-only photoelectron signals from the pump+probe image at 0 fs time delay leaves a fare amount of signal intensity in the latter. This suggests that at least the major part of the two photon signal comes from the detachment of diatomic anion photoproducts. The observed structureless broad bands (M) span the entire spectral region of possible molecular-anion fragments (see Figure 7.2), preventing us from determining the contribution of each individual product channel. However, based on the previously measured[259] 4:1 branching ration for IBr^- and ICl^- channels in 392 nm photodissociation of $BrICl^-$, we expect that in our experiment on this trihalide anion the major portion of the photoelectron signal also comes from IBr^- fragment. The bright feature M fades out on a time-scale of ~500 fs due to a quick dephasing of the initially localized vibrational wave-packets. We do not observe any revivals of these bands at longer delays (up to 100 ps). This behavior is expected and was previously observed by Sanov et al.[259] for vibrationally hot diatomic fragments in the photodissociation study on $BrICl^-$ and IBr_2^- anions with similar excitation photon energies.

Although time-resolved photoelectron spectra for both I_2Cl^- and $BrICl^-$ anions show similar evolution trend from molecular to atomic like features, the time-scales for the appearance of the type A signal are quite different. In case of I_2Cl^-, the signal from I^- fragment shows up within first 100 fs and energetically is already at the asymptotic limit of the isolated atomic anion. In contrast to rapid production of I^- from I_2Cl^-, the appearance of this channel in the photodissociation of $BrICl^-$ is delayed until much longer time (~ 700 fs), pointing to a different reaction pathway. In addition, the observed I^- signal is also much weaker then that from I_2Cl^-, and according to the previous study[259] on photodissociation dynamics of $BrICl^-$ anion is hardly expected to be observed with 385 nm pump photon energy.

By inspecting the energy diagram in Figure 7.1 and accounting for a typical ±0.2 eV energy uncertainty in the CCSD calculations, we note that the formation of I^- from I_2Cl^- may occur either through concerted three-body

$$I_2Cl^- \rightarrow I^- + I + Cl \tag{7.1}$$

or two-body

$$I_2Cl^- \rightarrow I^- + ICl \tag{7.2}$$

dissociation processes. The analogous three-body channel for $BrICl^-$ anion is not accessible at 385 nm and the two-body dissociation leading to the I^- product must involve the nuclear rearrangement

$$[Br\text{-}I\text{-}Cl]^- \rightarrow [IBrCl]^- \text{ or } [BrClI]^- \rightarrow I^- + BrCl \tag{7.3}$$

The synchronous three-body dissociation is a direct process resulting in fast generation of I^-, while the structural transformation of $BrICl^-$ necessary for the two-body formation of I^- takes time. This explains the difference in the time-scales for the appearance of I^- feature in the time-resolved photoelectron spectra of the studied trihalide anions.

As was mentioned earlier in the introduction section of this Chapter, the experiments performed by Nagata[255,256] and Neumark[253,254,257,258] reveal competition between $I^- + 2I$ and $I^- + I_2$ photoinduced reactions, where the two-body channel requires a non-adiabatic transition from an excited state of I_3^- correlating to the three-body channel. Assuming similar photochemical dynamics for I_2Cl^- and $BrICl^-$, the absorption of 390/385 nm light initiates photodissociation of these anions on the potential energy surfaces leading to the simultaneous cleavage of both bonds. Specifically, the following triatomic channels are expected to be accessible at the photon energies used in our experiments: $Cl^- + 2I$ and $I^- + I + Cl$ for I_2Cl^-; $Br + I + Cl^-$ and perhaps $Br^- + I + Cl$ for $BrICl^-$. At the same time, the $Br + I^- + Cl$ channel is not reachable with 385 nm radiation based on our CCSD results. Nonetheless, at some point during dissociation of the trihalide anions the population from the three-body-channel excited state(s) is diabatically transferred to the states with the two-body dissociation asymptotes. Therefore, we anticipate that both $I^- + ICl$ and $I^- + BrCl$ channels are open due to the non-adiabatic nature of the I_2Cl^- and $BrICl^-$ photodissociation dynamics. The above mechanism is also indirectly supported by our experimental observation of the increase of I^- signal with larger (385 nm compared to 390 nm) photon energy in the time-resolved photoelectron experiment on $BrICl^-$.

According to the energy diagram (Figure 7.1) the 390 nm excitation is energetically barely sufficient to initiate three-body dissociation process. Hence, event a small increase in the photon energy should result in a better photofragmentation cross-section and consequently a better I^- signal through a non-adiabatic transition to the I^- + BrCl product channel. On the other hand, if the two-body channel were directly accessible then such a small change in the excitation energy would hardly affect the product yield of I^-, especially taking into account that 390 nm (3.18 eV) energy is about 1.8 times as much as that necessary to reach this dissociation pathway. Moreover, the direct access of the two-body channel would lead to a prompt formation of I^- contrary to the delayed appearance of this product in our time-resolved spectra for $BrICl^-$ anion.

7.4 Summary

The photodissociation dynamics of I_2Cl^- and $BrICl^-$ anions has been studied by monitoring the evolution of I^- channel using time-resolved photoelectron imaging spectroscopy. The pump-probe photoelectron images and energy spectra clearly demonstrate the transformation of electronic structure from the excited molecular anions to the atomic-anion fragment. The preliminary experimental data reveal fast (within first 100 fs) dissociation of I_2Cl^-, while the I^- signal from $BrICl^-$ anion shows up at much longer pump-probe delays (~ 700 fs). Based on the experimental data available for the photodissociation of I_3^- [255,256,258] and our theoretical results, we tentatively ascribe this intriguing difference in the reaction time-scales to the distinct dissociation pathways the anions have to undergo for the formation of I^- product. In particular, the three-body dissociation channel $I^- + I + Cl$ is directly accessible for the I_2Cl^- which results in the rapid production of I^-. To the contrary, this route is not energetically available for the $BrICl^-$ and thus the generation of I^- is only possible through the $I^- + BrCl$ channel. The two-body reaction pathway for this anion requires a nuclear rearrangement as the initial step before dissociation can proceed, which results in the delayed appearance of the I^- feature in the time-resolved spectra.

CHAPTER 8

FUTURE DIRECTIONS

This Chapter describes future possible experiments and is intended to motivate a forthcoming research based on the proposed ideas. The Chapter is divided into two major parts corresponding to the type of proposed measurements i.e. static or time-resolved. The term "static" is used here in the context of one-photon (non-time-resolved) photoelectron imaging and by no means should be treated as "static effect" since photodetachment of negative ions is a *dynamic process* regardless of the number of photons involved.

8.1 Static Photoelectron Imaging of Dinitroaromatic Anions

Static photoelectron imaging study on meta- and para-dinitrobenzene anions was presented in Chapter 4. For a comprehensive understanding of electronic coherence in dinitrobenzene anions, it is necessary to complete photoelectron imaging of the third "missing" isomer, ortho-dinitrobenzene anion (*o*-DNB$^-$). Unlike the other isomers, the geometrical structure of *o*-DNB$^-$ is predicted to be non-planar due to the steric repulsion of the NO_2 groups. Nevertheless, the through-bond electronic coherence is expected to be preserved at some extent in this anion since both nitro groups are not entirely perpendicular to the plane of the benzene ring. Accordingly, the magnitude of anisotropy parameter oscillation (due to quantum interference effect) observed in photoelectron imaging of *o*-DNB$^-$ at several wavelengths (in 780 – 266 nm range) will serve as a sensitive probe of the degree of electron delocalization left in the anion.

The other possible photoelectron imaging experiments to further explore the electronic coherence in molecular anions may be conducted on the larger (polycyclic) pi-conjugated systems containing two NO_2 or CN groups. Most of such anions are difficult to bring to the gas phase because of their large molecular weight. This problem can be solved by generating anions in non-aqueous solvents (e.g. dimethylformamide, acetonitrile, 1,2-dimethoxyethane, etc…) via alkali metal reduction of the corresponding neutral molecules and then injecting the obtained anions into the high-vacuum chamber using electrospray ionization (ESI) technique.

8.2 Time-Resolved Experiments

8.2.1 Trihalide Anions

A preliminary 390 nm pump – 390 nm probe photoelectron imaging study on I_2Cl^- and $BrICl^-$ anions has been described in Chapter 7 of this dissertation. Apart from finishing data collection for a journal publication, these anions are excellent targets for 390 nm pump – 266 nm probe time-resolve experiments. Although the proposed experiments are expected to be challenging due to the lower intensity of the 266 nm radiation, the resultant time-resolved photoelectron signal might be even better than in the single color experiment because of the larger photodetachment cross-section of halide atomic anions at 266 nm. In addition, the 266 nm light allows explore the rich photochemistry of the trihalide anions at a full degree by probing the evolution of Br^- and Cl^- channels. The photofragment yield of these atomic anions formed via direct three-body dissociation pathways should be much larger than for I^- product generated indirectly through a non-adiabatic transition to the two body channel (see Chapter 7 for more details). This implies even larger photodetachment signals from Br^- and Cl^- compared to I^- fragment.

Despite the number of gas phase photodissociation experiments[253-258] of I_3^-, no photoelectron imaging study has been done on this system. The most resent work on I_3^- by Nagata et al.[256] suggests that three-body dissociation ($I_3^- \rightarrow I^- + 2I$) near 400 nm occurs preferentially as a "charge asymmetric" process with the excess electron shared between two terminal iodine atoms. It was demonstrated in Chapter 6 for I_2^- dissociation that the photodetachment of two identical centers leads to a quantum interference effect manifesting itself in periodical oscillations of photoelectron anisotropy distribution as the I-I internuclear distance increases in time. Therefore, the same phenomena is anticipated to be observed in proposed 390 nm pump – 390 nm probe photoelectron imaging experiment on I_3^-, provided of course that the extra electron is indeed delocalized between terminal atoms.

Finally, to the best author's knowledge, there are no photodissociation experiments performed on polyatomic halide anions (n>3). The photochemistry of these species is expected to be even more interesting (due to the larger number of available reaction pathways) than for trihalide anions. This makes polyatomic halide anions an appealing target for the time-resolved photoelectron imaging investigation.

8.2.2 Para-Dinitrobenzene Anion

The static photoelectron imaging of dinitrobenzene anions (see Chapter 4) has already yielded fruitful results demonstrating the quantum interference effect in photodetachment of molecular negative ions with high-symmetry structure. However, it turned out that para-dinitrobenzene anion (*p*-DNB$^-$) is also an excellent candidate for the time-resolved photoelectron imaging experiments. The matrix-isolation absorption study[137,265] indicate that *p*-DNB$^-$ exhibits two intense absorption bands centered around 800 and 400 nm respectively. Both of these transitions are conveniently accessed with the fundamental (~ 800 nm) and second harmonic (~ 400 nm) output of our Ti:sapphire femtosecond laser system. Considering the energy scheme for the time-resolved experiment, the 800 nm pump – 400 nm probe is the best choice to begin with. The 800 nm pulse definitely brings the system in an excited anionic state since the pump photon energy (1.55 eV) is less than adiabatic electron affinity of *p*-DNB$^-$ (1.97 ± 0.01 eV). The rough estimates based on B3LYP/aug-cc-pVTZ calculations predict the following energetics for the possible C-N bond dissociation channels

$$(\mathrm{X}\ ^2\mathrm{B}_{3u})\ [\mathrm{O_2N\text{-}Ph\text{-}NO_2}]^- \rightarrow (\mathrm{X}\ ^2\mathrm{A}_1)\ \mathrm{O_2N\text{-}Ph}\bullet + (\mathrm{X}\ ^1\mathrm{A}_1)\ \mathrm{NO_2}^-,\ D_0 = 2.90\ \mathrm{eV} \quad (8.1)$$

$$(\mathrm{X}\ ^2\mathrm{B}_{3u})\ [\mathrm{O_2N\text{-}Ph\text{-}NO_2}]^- \rightarrow (\mathrm{X}\ ^1\mathrm{A}_1)\ \mathrm{O_2N\text{-}Ph}^- + (\mathrm{X}\ ^2\mathrm{A}_1)\ \mathrm{NO_2},\ D_0 = 3.23\ \mathrm{eV} \quad (8.2)$$

It should be emphasized that dft calculations usually overestimate bond dissociation energies (sometimes as much as 0.5 eV). Comparing the calculation results with 3.09 eV[239] for $C_6H_5NO_2 \rightarrow C_6H_5 + NO_2$ points out that this is the case for our estimates since the C-N bond strength for *p*-DNB$^-$ should be less than that in the neutral nitrobenzene molecule. Nonetheless, even assuming ≤1 eV error, the calculation results suggest that no NO_2 fragmentation should occur in the proposed experiment using 800 nm pump photons and therefore the time-resolved photoelectron signal will reflect the evolution of the excited state anionic wave-packet. The single color 400 nm pump – 400 nm probe experiment on *p*-DNB$^-$ might also work if there is an accessible bound anionic state in the vicinity of the excitation pulse energy. This way, it can be possible to observe the evolution of O_2N-Ph$^-$ and NO_2^- channels in the photodissociation of para-dinitrobenzene anion.

Another interesting direction is to monitor the charge-transfer processes in the [D-B-A]$^-$ delocalized anionic systems, where B is the conductor bridge (a pi-conjugated molecule) between the donor (D) and acceptor (A) groups. For a time-resolved experiment a pump photon must be in resonance with a charge-transfer transition which makes the excess electron to hop from donor to acceptor moiety. As was describe previously in Section 8.1 these bulky anions can be delivered to the gas-phase using electrospray ionization source.

APPENDIX A

CoolImage DATA ACQUISITION SOFTWARE

This Appendix describes the data acquisition software CoolImage developed by the author of this dissertation during his Ph.D. career in Sanov group. The material in the Appendix is conveniently organized into two main parts devoted to the user interface and the code structure of the program respectively.

The original motivation for this project was our interest in the event counting algorithm allowing collect photoelectron images with improved resolution and signal-to-noise ratio. As the time was going by, the initially little piece of code matured into a full-featured data acquisition program highly tuned for the data collection and manipulation for both static and time-resolved photoelectron imaging experiments. Accordingly, although the program can be used as general purpose image recording software, it is expected to be particularly useful in the field of photoelectron or photofragment-ion imaging.

In its current implementation, CoolImage works with two types of CCD cameras: CoolSnap$_{HQ}$ (Photometrics division of Roper Scientific, Inc.) and DALSA Pantera 1M30 (DALSA Corporation). The access to the cameras is provided through the system call of the corresponding manufacture's library functions contained in pvcam32.dll (CoolSnap$_{HQ}$) and xclibwnt.dll (DALSA 1M30). Also, the default.fmt file generated by XCAP program (EPIX, Inc.) is necessary for the proper initialization of DALSA 1M30 camera. So far, CoolImage program is compiled as a 32-bit application and has been extensively tested only under Windows XP (up to service pack 3). Although no major problems are expected with the newer versions of Microsoft operation systems such as Vista or Windows 7, it will be highly desirable to recompile the program for a 64-bit architecture to achieve a better performance.

Concerning the CoolImage GUI, some of the program interface is crafted analogous in the look and feel to that of the WinView software (Roper Scientific, Inc.), which was purchased by our group from Photometrics together with CoolSnap$_{HQ}$ CCD camera. It should be emphasized here, that CoolImage program is written from scratch and DOES NOT contain any fragment of the code pertinent to the WinView. A similar to the WinView part of CoolImage GUI was designed in such way intentionally for the user convenience. In addition, the functionality of many "alike" interface options in CoolImage has been significantly extended or reduced depending on our specific needs. Therefore, a user should carefully read CoolImage GUI manual (A-1 section of this Appendix) as even akin interface features may behave quite differently from their original implementation in the WinView.

CoolImage program is available without charge for an academic institution or non-profit research organization and can be obtained by contacting Professor Andrei Sanov (Sanov@email.arizona.edu). The software is provided "As Is" without any expressed or implied warranty. Neither Sanov Group nor The University of Arizona bear responsibility for any damages the program may cause to your computer or CCD camera, yet every possible effort was made to produce CoolImage as a “bug-free” high performance software.

A-1 Graphical User Interface (GUI)

A-1.1 CoolImage Desktop

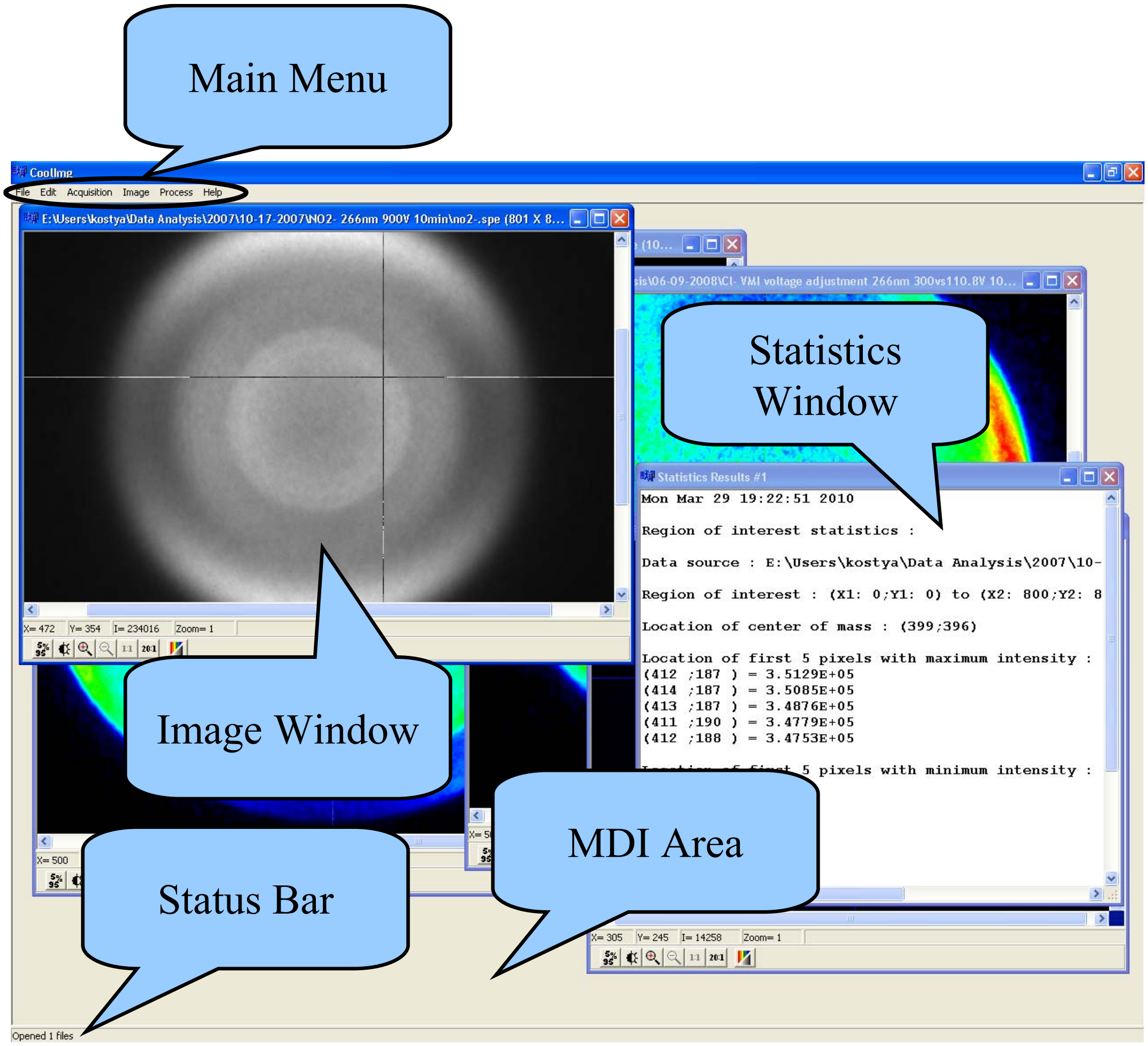

```
Mon Mar 29 19:22:51 2010

Region of interest statistics :

Data source : E:\Users\kostya\Data Analysis\2007\10-

Region of interest : (X1: 0;Y1: 0) to (X2: 800;Y2: 8

Location of center of mass : (399;396)

Location of first 5 pixels with maximum intensity :
(412 ;187 ) = 3.5129E+05
(414 ;187 ) = 3.5085E+05
(413 ;187 ) = 3.4876E+05
(411 ;190 ) = 3.4779E+05
(412 ;188 ) = 3.4753E+05

Location of first 5 pixels with minimum intensity :
```

CoolImage Desktop may contain the following GUI elements: Main Menu, Image Window(s), Statistic Window(s), MDI (Multiple Document Interface) Area, and Status Bar. The Main Menu, MDI Area and Status Bar items are always present, while the Image and Statistics windows are only opened/generated upon a user request. The detailed information on various GUI components can be found in the corresponding subsections of this Appendix.

A-1.2 Main Menu

The Main Menu provides a user with access to a variety of commands and options available in CoolImage program. Presently, Main Menu consists of the following submenu categories: File, Edit, Acquisition, Image, Process, and Help. The composition of Main Menu is context-sensitive, i.e. certain submenus and commands are only accessible depending on the selected type of document (Image Window, Statistics Window, or None), availability of hardware resources (camera, COM ports, Optical Shutters), and current stage of data acquisition process.

A-1.3 MDI Area

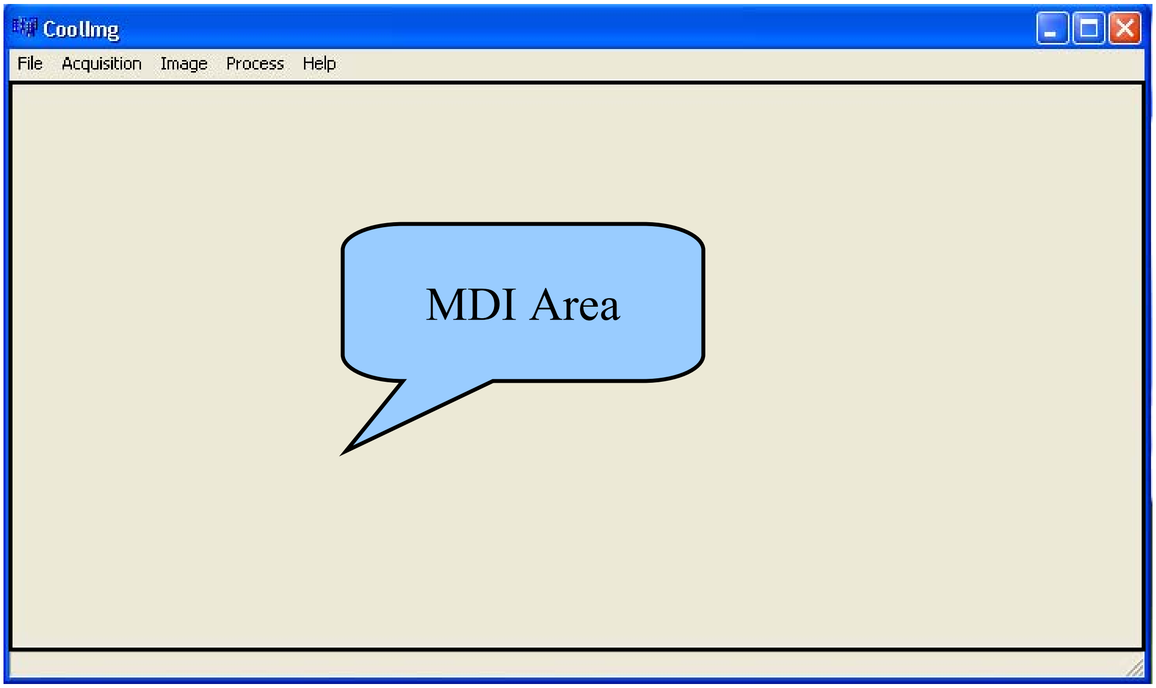

Multiple Document Interface (MDI) Area is the grey rectangular area between the Main Menu and Status Bar. As it name stands, this GUI component is essentially a container capable of holding different types of documents. Presently, CoolImage works with two types of data forms (documents) – the Image and Statistics Windows.

A-1.4 Image Window

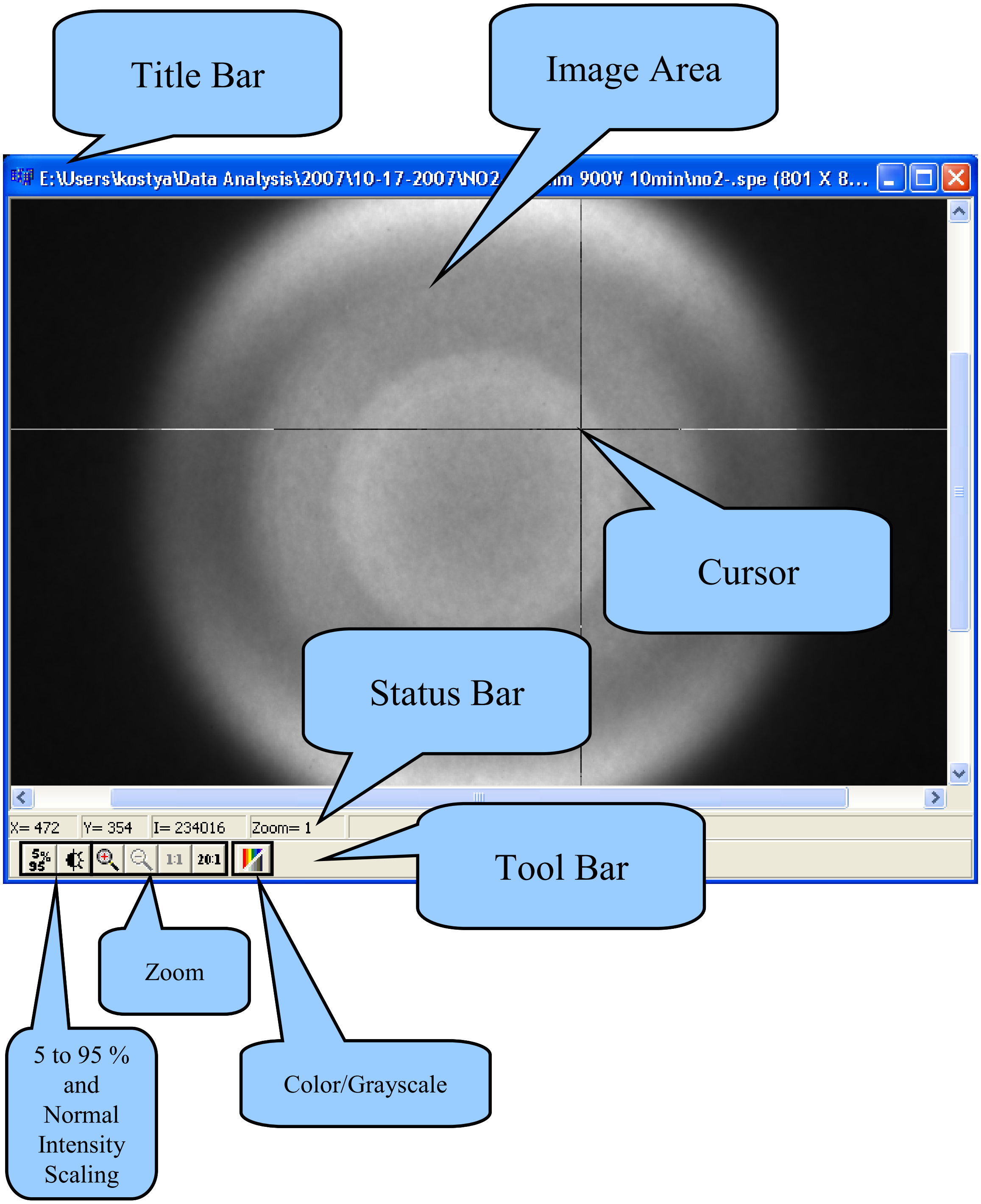

X= 472 Y= 354 I= 234016 Zoom= 1

The Image Window is composed of the Title Bar, Image Area, Cursor, Status Bar, and Tool Bar interface elements. The Title Bar contains a name and dimensions (number of pixels in the x and y direction shown in parentheses) of an image. If the image was saved previously then its name is that of the file including the full directory path and the drive letter. Otherwise, the image is named "Untitled #N", where N is a sequence number.

The Image Area represents a color map of the array of accumulated intensities transferred from a camera CCD chip. The Image coordinate system is arranged in the conventional way, with the upper left pixel (X=0;Y=0) set as the Image Origin. Accordingly, the X (horizontal) and Y (vertical) coordinates are ranging from 0 to the $N_x - 1$ and $N_y - 1$ respectively, where N_x and N_y are the image dimensions.

The Cursor is represented by two lines (horizontal and vertical) displayed in the inverse mode for a better perception. The intersection of the Cursor lines corresponds to a position of the current pixel in the image. The current pixel coordinates (X and Y) as well as the zoom level are shown in the Status Bar. A user can navigate Cursor to the desired pixel either by using the arrow keys on a keyboard or by pointing with a mouse cursor and then pressing the right mouse button.

The Tool Bar accommodates the buttons of the following functional categories: intensity scaling (5 to 95 % or normal), image zoom (zoom in, zoom out, 1:1 scaling, 1:20 scaling), color scheme (either 256 colors or grayscale).

A-1.5 Statistics Window

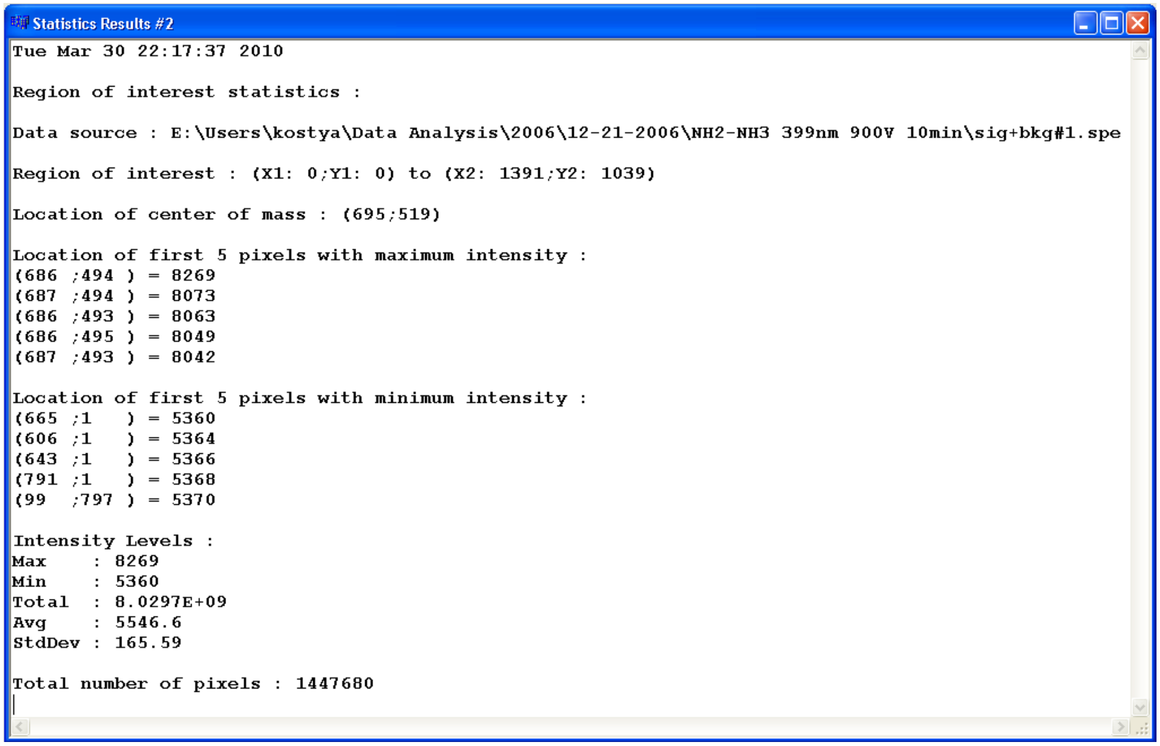

```
Tue Mar 30 22:17:37 2010

Region of interest statistics :

Data source : E:\Users\kostya\Data Analysis\2006\12-21-2006\NH2-NH3 399nm 900V 10min\sig+bkg#1.spe

Region of interest : (X1: 0;Y1: 0) to (X2: 1391;Y2: 1039)

Location of center of mass : (695;519)

Location of first 5 pixels with maximum intensity :
(686 ;494 ) = 8269
(687 ;494 ) = 8073
(686 ;493 ) = 8063
(686 ;495 ) = 8049
(687 ;493 ) = 8042

Location of first 5 pixels with minimum intensity :
(665 ;1   ) = 5360
(606 ;1   ) = 5364
(643 ;1   ) = 5366
(791 ;1   ) = 5368
(99  ;797 ) = 5370

Intensity Levels :
Max    : 8269
Min    : 5360
Total  : 8.0297E+09
Avg    : 5546.6
StdDev : 165.59

Total number of pixels : 1447680
```

An Image Statistics Window is generated by the Image Statistics Dialog upon a user request. The output provides the following basic information about either the whole image or its selected area: name of the data source (typically a file name of the image), coordinates of the region of interest area, location of the center of mass, location of the first five pixels with the maximum and minimum intensities, image intensity statistics (minimum, maximum, total, average intensities, and the standard deviation value), as well as the total number of pixels in the region of interest. If necessary the statistics results can be saved in ASCII format for bookkeeping.

A-1.6 Status Bar

The Status Bar provides a user with information about the status of the most resent operation performed in CoolImage, e.g. operation on files 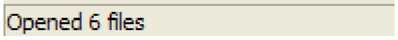 Opened 6 files , data acquisition progress 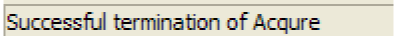 Successful termination of Acqure , etc …

A-1.7 File Menu

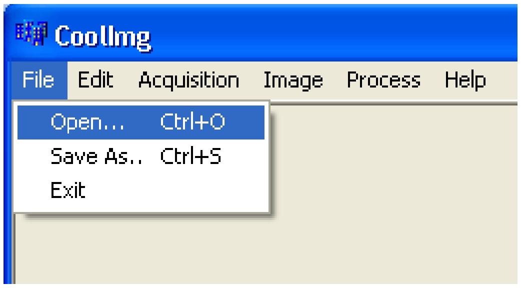

The File Menu contains the following commands: Open (calls standard Windows Open File Dialog), Save (calls standard Windows Save File Dialog), Exit (exits CoolImage program). Presently, CoolImage can open and save images in two formats: an ASCII file organized in a matrix form (then the image dimensions are N_x = number of columns, N_y = number of raws) and a WinView binary .spe file for a backward compatibility.

A-1.8 Edit Menu

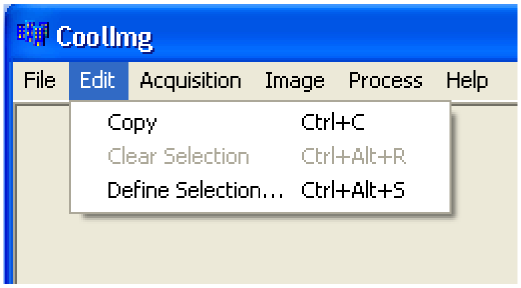

The Edit Menu provides access to the following commands: Copy (copies the current bitmap of the image, i.e. just an image picture itself and not the internal array of original image intensities), Clear Selection (clears Region of Interest selection in current image), Define Selection (calls Region Selection Dialog to define Region of Interest selection). The Copy command is useful for inserting the picture of Image to a Power Point presentation or general purpose graphics editor software.

A-1.8.1 Region Selection Dialog

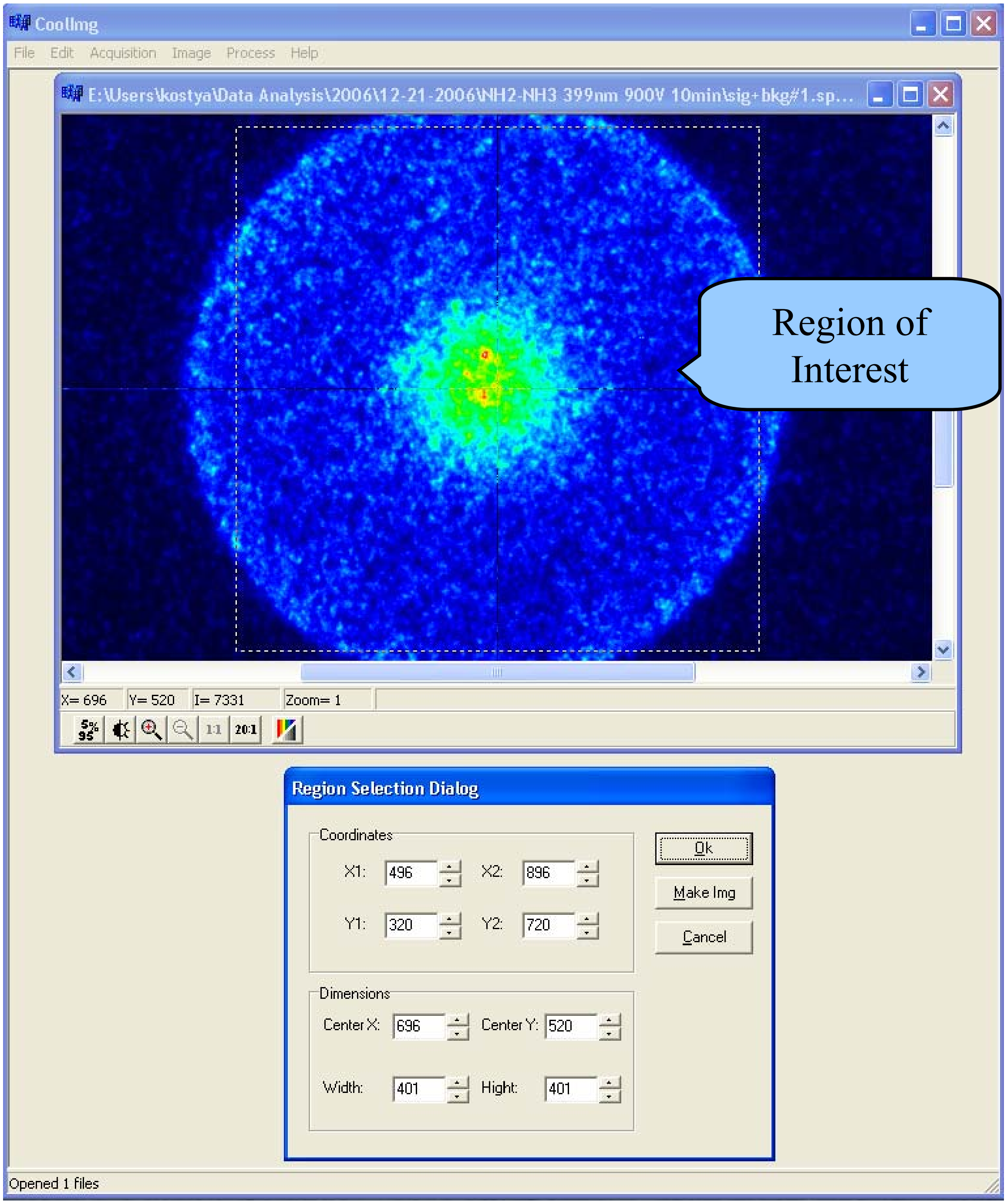

E:\Users\kostya\Data Analysis\2006\12-21-2006\NH2-NH3 399nm 900V 10min\sig+bkg#1.sp...

X= 696 Y= 520 I= 7331 Zoom= 1

X1: 496
X2: 896
Y1: 320
Y2: 720

Center X: 696
Center Y: 520
Width: 401
Hight: 401

Opened 1 files

The Region Selection Dialog provides a convenient way of defining the Region of Interest (ROI) area, i.e. a rectangular part of the Image on which a user want to perform an operation. A ROI border is highlighted by a short dashed line drawn in the inverse mode for a better perception. The selection can be defined by specifying the coordinates of the upper left and bottom right corners of ROI or by assigning the center of ROI and its dimensions, the width and height. While both approaches are equivalent, it is more convenient to think about photoelectron transitions in terms of the latter. The "Make Img" button allows create a new image from selected ROI. This option is very handy for trimming an image for further data analysis.

In addition, there is another quick way of specifying ROI without even calling Region Selection Dialog. The selection is achieved by pointing a mouse cursor to an upper left corner of desired ROI and then visually drawing selection with the left mouse button pressed down. The final size of ROI depends on a mouse cursor position upon release of the mouse left button.

A-1.9 Acquisition Menu

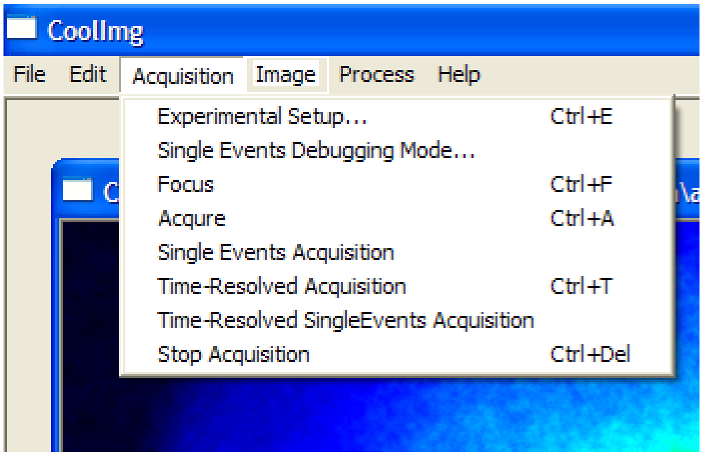

The Acquisition Menu offers the following set of options controlling camera and experimental settings, as well as the manner the data collection is preformed: Experimental Setup (calls Experimental Setup Dialog), Single Events Debugging Mode (calls Single Events Debugging Dialog), Focus (starts acquisition without accumulating data, i.e. each subsequent readout from camera overrides the previous stored in the data array), Acquire (performs data collection in a normal regime), Single Events Acquisition (same as Acquire with the addition of Event Counting algorithm), Time-Resolved Acquisition (performs time-resolved data collection by manipulating optical shutters), Time-Resolved Single Events Acquisition (same as Time-Resolved Acquisition with the addition of Event Counting), Stop Acquisition (terminates any of the above data-acquisition processes).

A-1.9.1 Experimental Setup Dialog

The Experimental Setup Dialog provides numerous options for controlling the hardware (camera and shutters) and data-acquisition process. Some of the options are camera specific, and thus their availability depends on particular hardware used in the experiment.

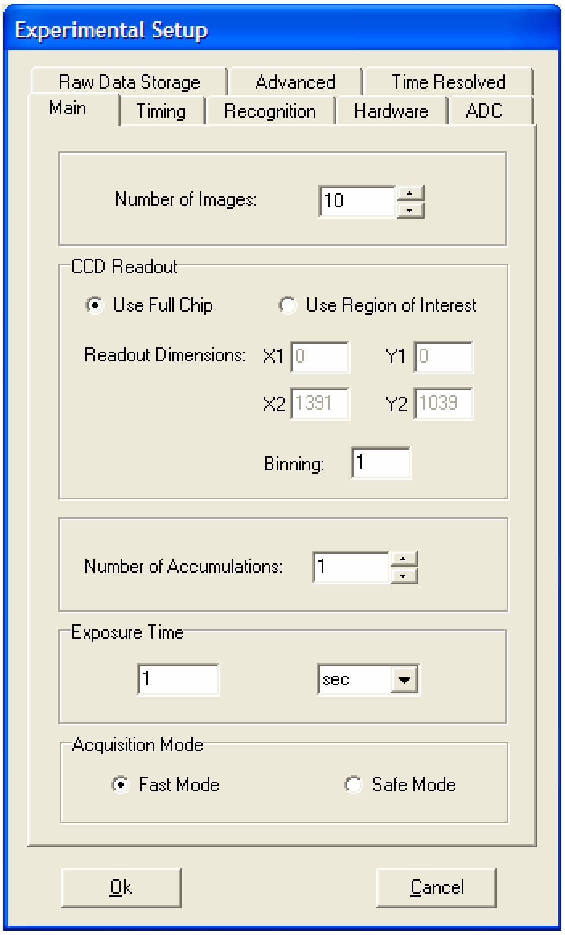

Number of Images: 10

CCD Readout

● Use Full Chip ○ Use Region of Interest

Readout Dimensions: X1 0 Y1 0

X2 1391 Y2 1039

Binning: 1

Number of Accumulations: 1

Exposure Time

1 sec

Acquisition Mode

● Fast Mode ○ Safe Mode

The Main Tab allows specify the readout Region of Interest from CCD chip, Binning (combination of several pixels to a super pixel), Exposure time, Acquisition Mode, and Number of Images and Accumulations to collect. The Exposure time corresponds to a period of time between readouts for which a camera accumulates signal on a CCD chip. An image can contain several accumulations, where each accumulation is performed for the specified Exposure amount of time. The picture of Image on a computer screen is only updated when the collection of current image is completed. The total acquisition amount of time for an Image = Number of images × Number of accumulations × Exposure time. For instance, if a user requested 10 images and 5 accumulations with 1 second Exposure time then the final Image collection time is 50 seconds during which the Image picture was updated 10 times.

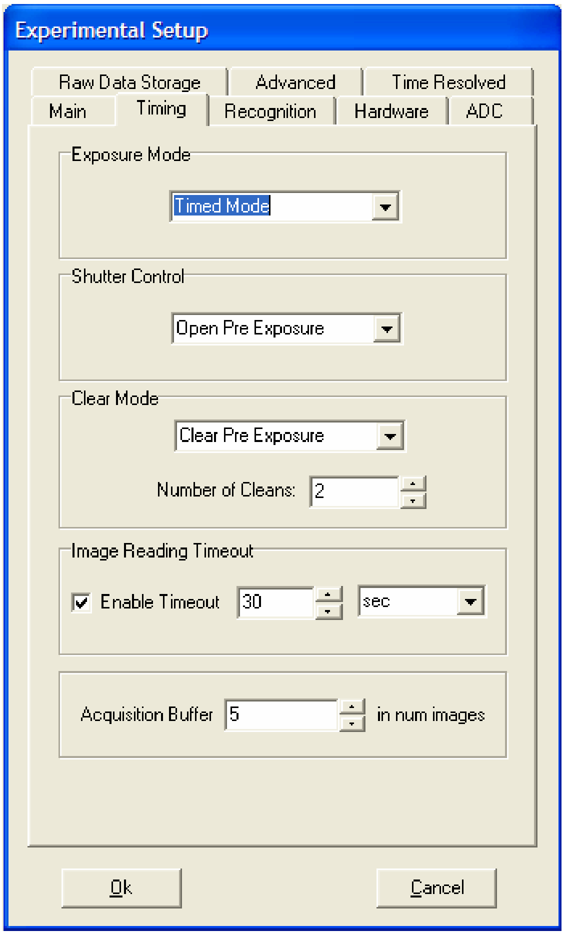

Exposure Mode: Timed Mode

Shutter Control: Open Pre Exposure

Clear Mode: Clear Pre Exposure

Number of Cleans: 2

Image Reading Timeout: ☑ Enable Timeout 30 sec

Acquisition Buffer 5 in num images

All options in the Timing Tab, but Image Reading Timeout (the maximum amount of time CoolImage will wait for a camera to provide next available CCD readout; if no readout is available within specified period of time the acquisition process is aborted), are specific to CoolSnap$_{HQ}$ camera, and therefore an interested reader is referred to the original camera manual (can be downloaded from www.photomet.com) for their complete description.

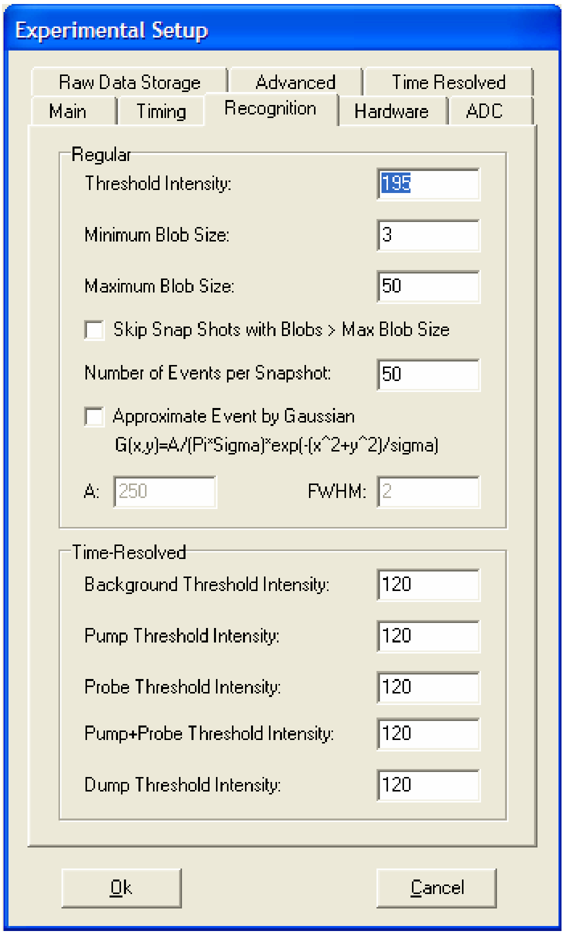

Regular

Threshold Intensity: 195

Minimum Blob Size: 3

Maximum Blob Size: 50

☐ Skip Snap Shots with Blobs > Max Blob Size

Number of Events per Snapshot: 50

☐ Approximate Event by Gaussian
G(x,y)=A/(Pi*Sigma)*exp(-(x^2+y^2)/sigma)

A: 250 FWHM: 2

Time-Resolved

Background Threshold Intensity: 120

Pump Threshold Intensity: 120

Probe Threshold Intensity: 120

Pump+Probe Threshold Intensity: 120

Dump Threshold Intensity: 120

The Recognition Tab allows adjust variety of parameters used in the Event Counting algorithm. The Threshold parameters define the minimum intensity a pixel must have to be considered as a signal. Furthermore, only events containing number of pixels within [Min .. Max] Blob Size range are treated as real and are added to the Image. Finally, the center of mass of an event can be approximated by a Gaussian function which is requested by turning on "Approximate Event by Gaussian" option.

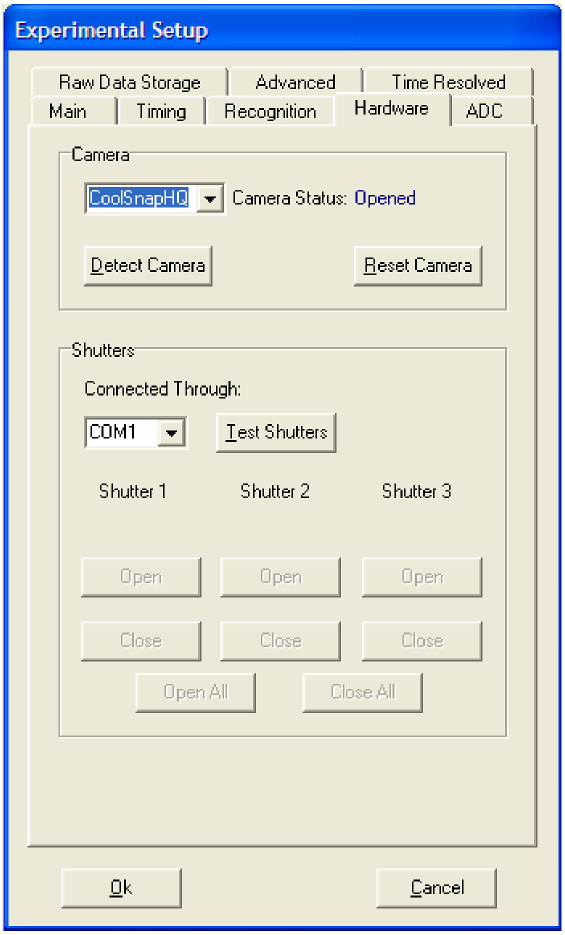
Camera: CoolSnapHQ
Camera Status: Opened
Connected Through: COM1

The Hardware Tab provides access to the camera and shutters (connected through the designated COM port) hardware resources.

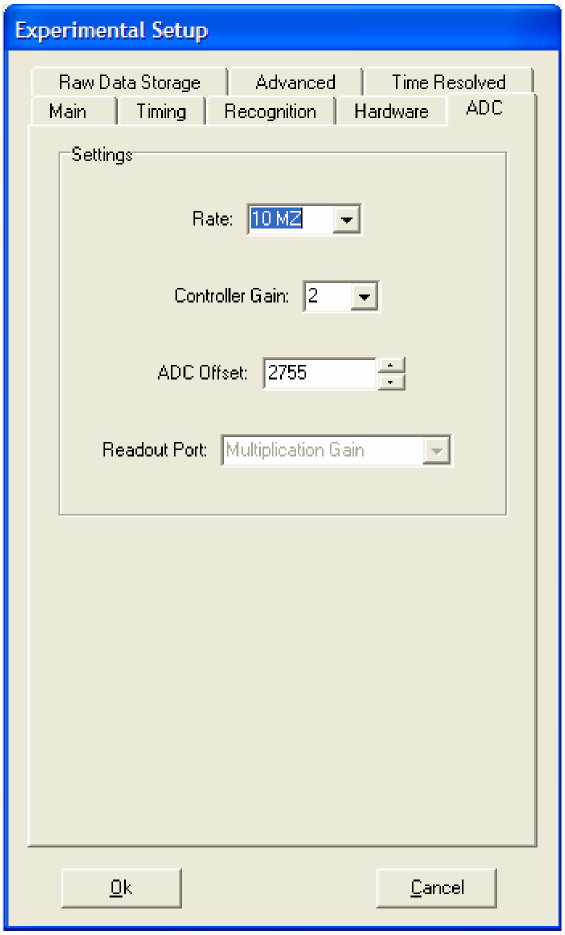

Rate: 10 MZ

Controller Gain: 2

ADC Offset: 2755

Readout Port: Multiplication Gain

The options in the ADC Tab specific to CoolSnap$_{HQ}$ camera allow to setup data transfer rate and ADC (Analog to Digital Conversion) Offset parameter.

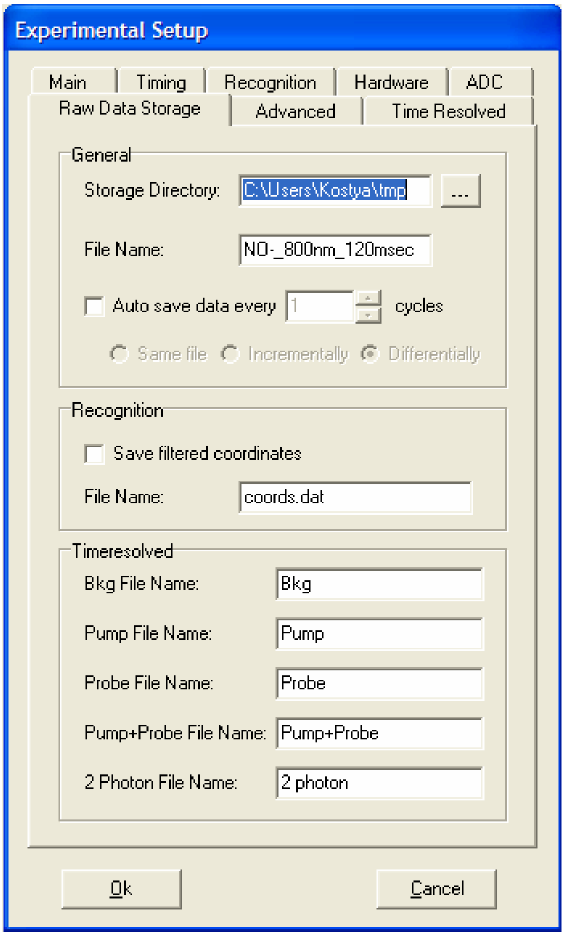

General

Storage Directory: C:\Users\Kostya\tmp

File Name: NO-_800nm_120msec

☐ Auto save data every 1 cycles

○ Same file ○ Incrementally ● Differentially

Recognition

☐ Save filtered coordinates

File Name: coords.dat

Timeresolved

Bkg File Name: Bkg

Pump File Name: Pump

Probe File Name: Probe

Pump+Probe File Name: Pump+Probe

2 Photon File Name: 2 photon

The Raw Data Storage Tab provides access to autosave options. Basically, the acquired image will be saved (incrementally, differentially, or to the same file) during data-acquisition process after each specified number of cycles. In the case of Event Counting data-acquisition, only coordinates with intensity above Threshold will be saved. The binary file (.dat) with the thresholded pixels can be used for further offline Event Recognition (see Section A-1.11.1).

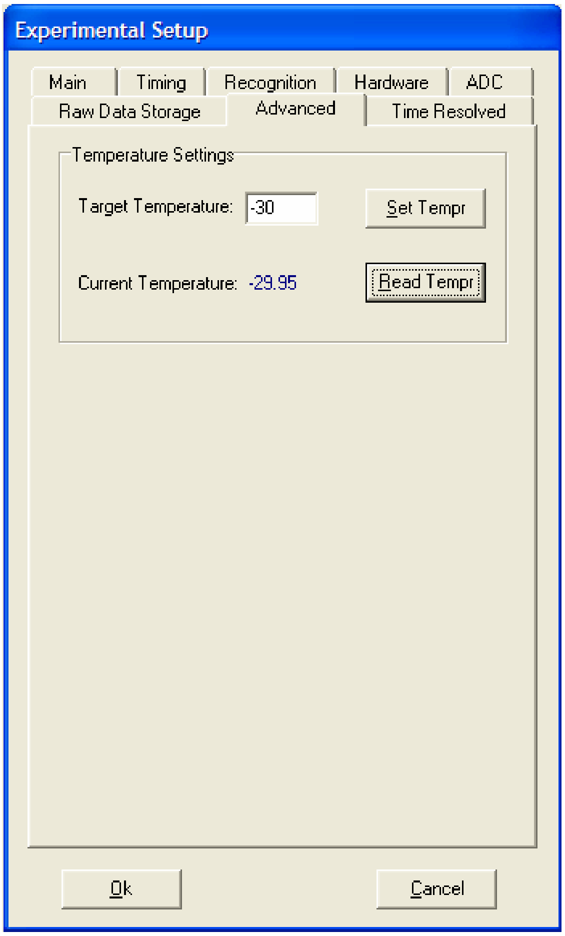

Target Temperature: -30

Current Temperature: -29.95

The Advanced Tab allow to set or check the temperature of CoolSnap$_{HQ}$ camera CCD chip.

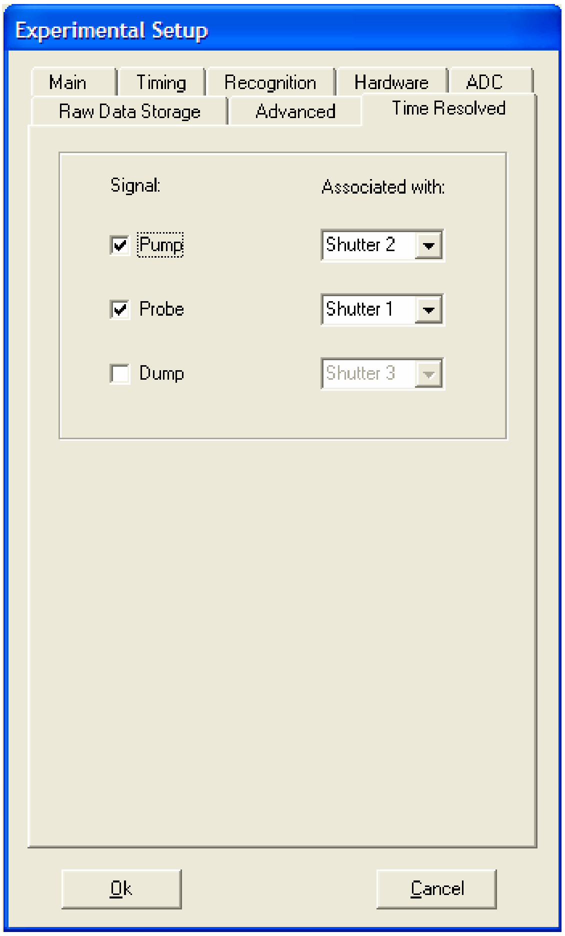

Signal:

Associated with:

☑ Pump Shutter 2

☑ Probe Shutter 1

☐ Dump Shutter 3

The Time-Resolved Tab allows associate shutters with particular type (pump, probe, and dump) of the laser beam.

A-1.9.2 Single Events Debugging Dialog

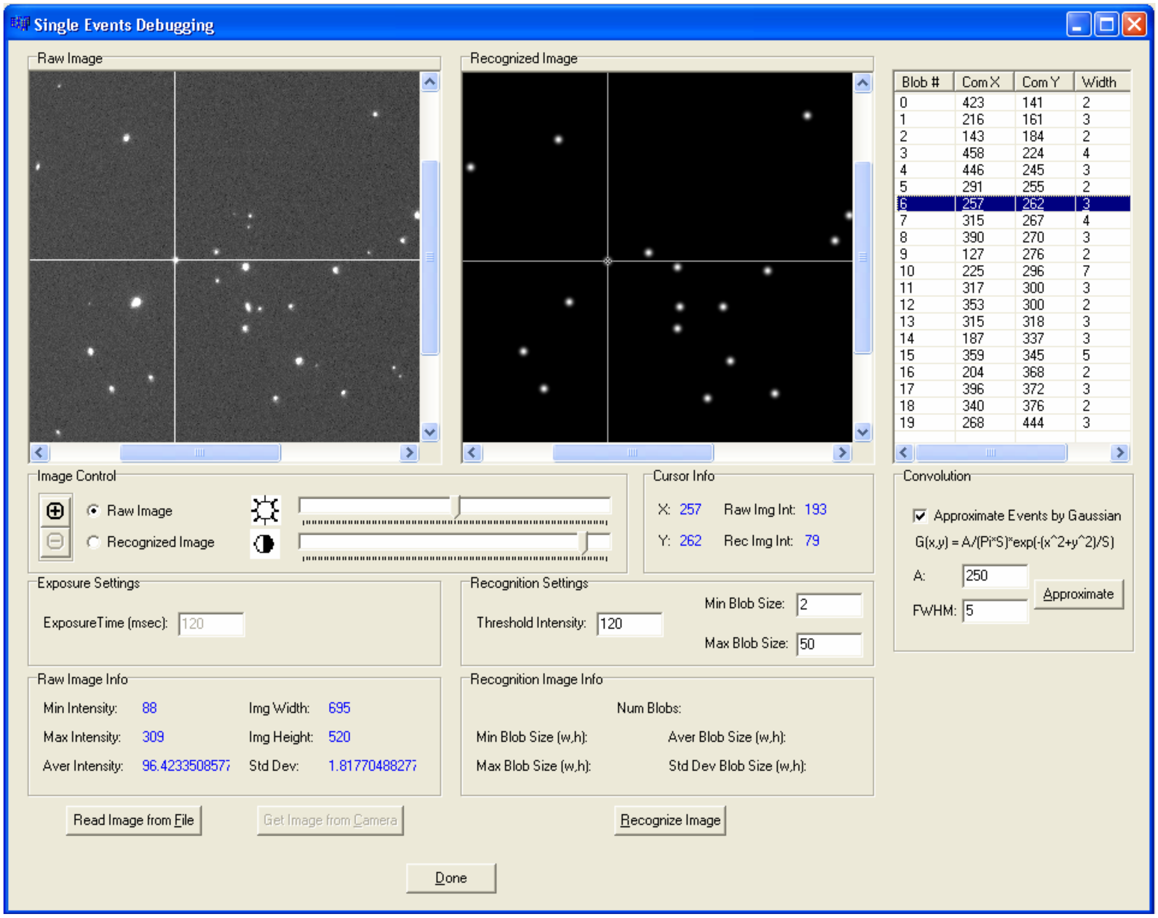

Blob #	Com X	Com Y	Width
0	423	141	2
1	216	161	3
2	143	184	2
3	458	224	4
4	446	245	3
5	291	255	2
6	257	262	3
7	315	267	4
8	390	270	3
9	127	276	2
10	225	296	7
11	317	300	3
12	353	300	2
13	315	318	3
14	187	337	3
15	359	345	5
16	204	368	2
17	396	372	3
18	340	376	2
19	268	444	3

● Raw Image
○ Recognized Image

X: 257 Raw Img Int: 193
Y: 262 Rec Img Int: 79

☑ Approximate Events by Gaussian
G(x,y) = A/(Pi*S)*exp(-(x^2+y^2)/S)
A: 250
FWHM: 5

ExposureTime (msec): 120

Threshold Intensity: 120
Min Blob Size: 2
Max Blob Size: 50

Min Intensity: 88 Img Width: 695
Max Intensity: 309 Img Height: 520
Aver Intensity: 96.4233508577 Std Dev: 1.81770488277

Num Blobs:
Min Blob Size (w,h): Aver Blob Size (w,h):
Max Blob Size (w,h): Std Dev Blob Size (w,h):

The Single Events Debugging Dialog provides an interactive preview of the results of Event Counting procedure. It is a convenient way of determining Threshold, Min and Max Blob Size parameters before running “Single Events Acquisition” data collection.

A-1.10 Image Menu

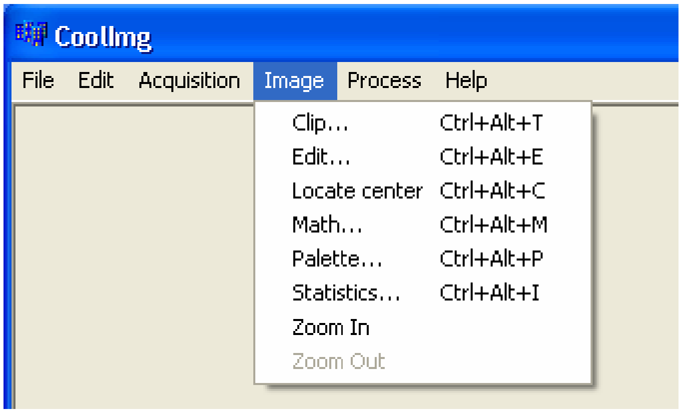

The Image Menu provides the following commands: Clip (calls Clip Image Dialog), Edit (calls Edit Image Dialog), Locate center (finds an image center using Bordas criteria[266]), Math (calls Image Math Dialog), Palette (calls Image Palette Dialog), Statistics (calls Image Statistics Dialog), Zoom In, Zoom Out.

A-1.10.1 Clip Image Dialog

The Clip Image Dialog allows clip image intensities which are either below or above specified values. For example, if Clip Low = 0 is requested then all pixels with intensities < 0 will be zeroed.

A-1.10.2 Edit Image Dialog

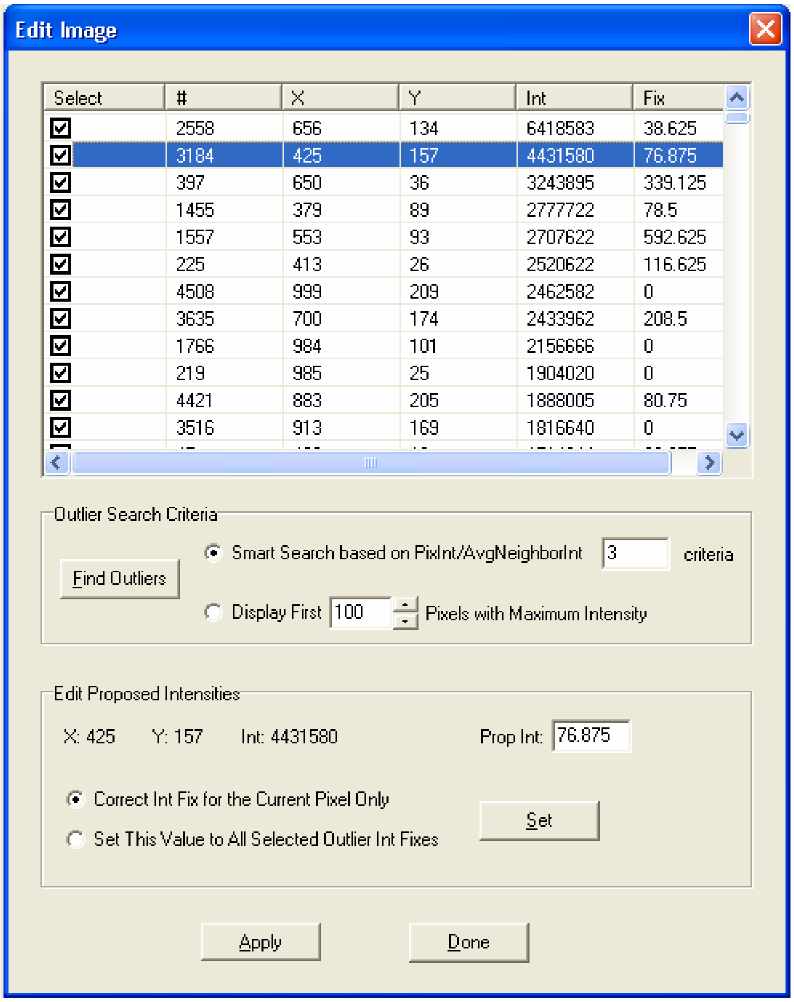

Select	#	X	Y	Int	Fix
☑	2558	656	134	6418583	38.625
☑	3184	425	157	4431580	76.875
☑	397	650	36	3243895	339.125
☑	1455	379	89	2777722	78.5
☑	1557	553	93	2707622	592.625
☑	225	413	26	2520622	116.625
☑	4508	999	209	2462582	0
☑	3635	700	174	2433962	208.5
☑	1766	984	101	2156666	0
☑	219	985	25	1904020	0
☑	4421	883	205	1888005	80.75
☑	3516	913	169	1816640	0

Outlier Search Criteria

● Smart Search based on PixInt/AvgNeighborInt 3 criteria

○ Display First 100 Pixels with Maximum Intensity

Edit Proposed Intensities

X: 425 Y: 157 Int: 4431580 Prop Int: 76.875

● Correct Int Fix for the Current Pixel Only

○ Set This Value to All Selected Outlier Int Fixes

The Edit Image Dialog allows remove spurious high intensity pixels from an image. This feature is particularly useful for images acquired with inexpensive cameras, which do not have thermoelectrical cooling of a CCD chip. An example of such image acquired with our DALSA 1M30 camera is given below.

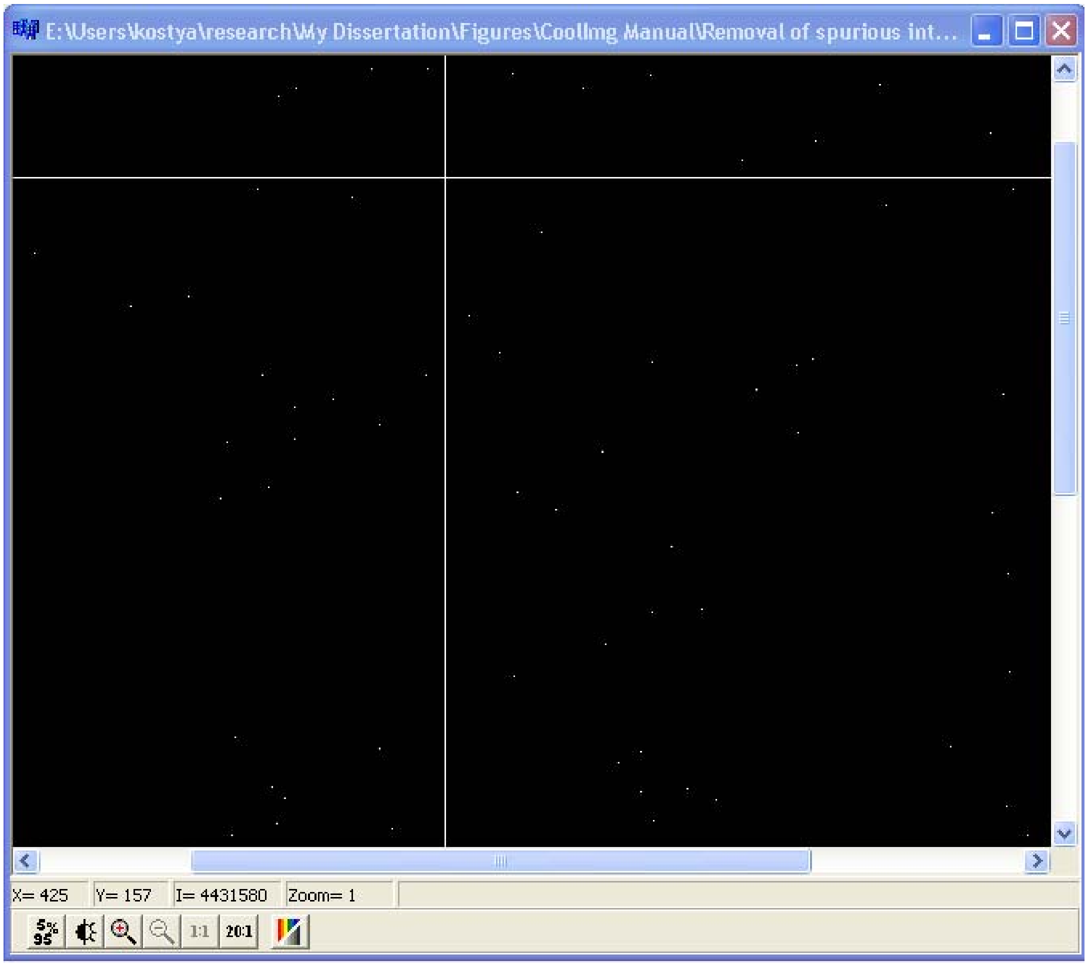

E:\Users\kostya\research\My Dissertation\Figures\CoolImg Manual\Removal of spurious int...

X= 425 Y= 157 I= 4431580 Zoom= 1

The Edit Image Dialog provides two options to search for the outlier intensities. The first choice is just to inspect a number of pixels with the highest intensities. The second approach is based on a smart search algorithm. Typically, an intensity of a spurious pixel is very different from those of the adjacent pixels. Therefore, it is possible to efficiently locate all pixels with unnaturally high intensities by comparing intensity of the current pixel to the average intensity of its neighbor pixels.

A-1.10.3 Image Math Dialog

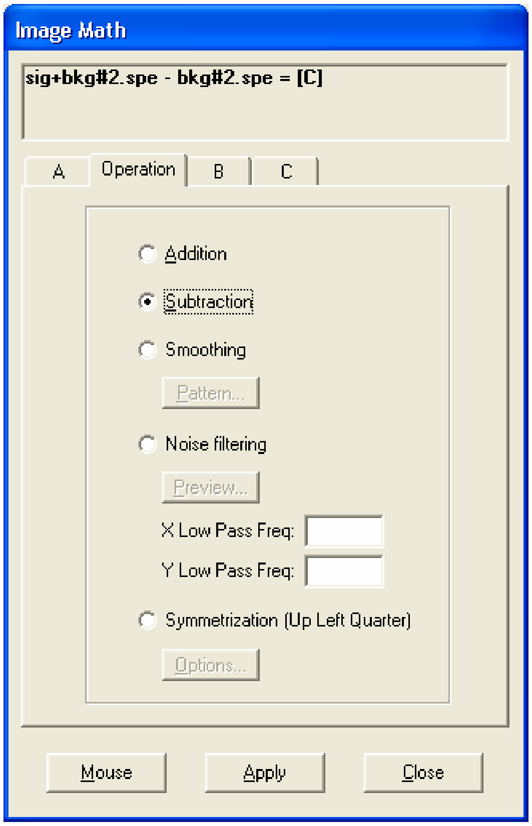

Image Math

sig+bkg#2.spe - bkg#2.spe = [C]

○ Addition
● Subtraction
○ Smoothing
○ Noise filtering
X Low Pass Freq:
Y Low Pass Freq:
○ Symmetrization (Up Left Quarter)

The Image Math Dialog offers a convenient way of performing the following operations on images:

1) Binary operations of type A *op* B = C, where *op* is addition or subtraction of two images or an image and a number.

2) Unary operations of type *op*(A), where *op* is Smoothing, Noise filtering, and Symmetrization. In order to use Smoothing option, it is necessary to define moving average matrix pattern

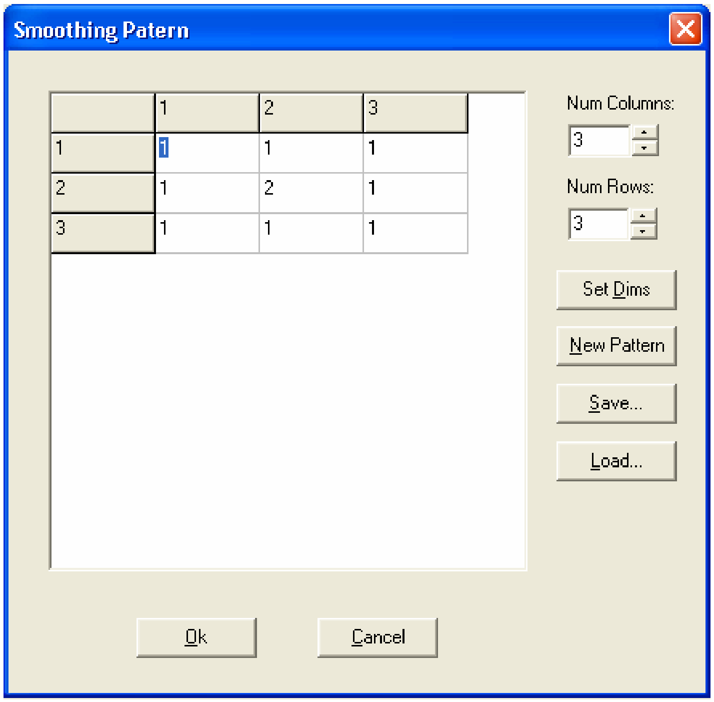

	1	2	3
1	1	1	1
2	1	2	1
3	1	1	1

Num Columns: 3

Num Rows: 3

which can be saved for future use.

The embedded Noise Filtering Dialog provides an alternative way of removing noise from an image. Mathematically speaking, the Low Pass Frequency filtering and Moving averaging are essentially the same thing since according to the Convolution Theorem $f \otimes g = F^{-1}\left(F\left(f\right)\cdot F\left(g\right)\right)$, where f and g are the signal and filter functions, F and F^{-1} stand for Fourier and inverse Fourier transform. Nonetheless, we have chosen to implement both of the approaches for the user convenience. An example of application of low pass frequency filter to experimental data using Noise Filtering Dialog is given below

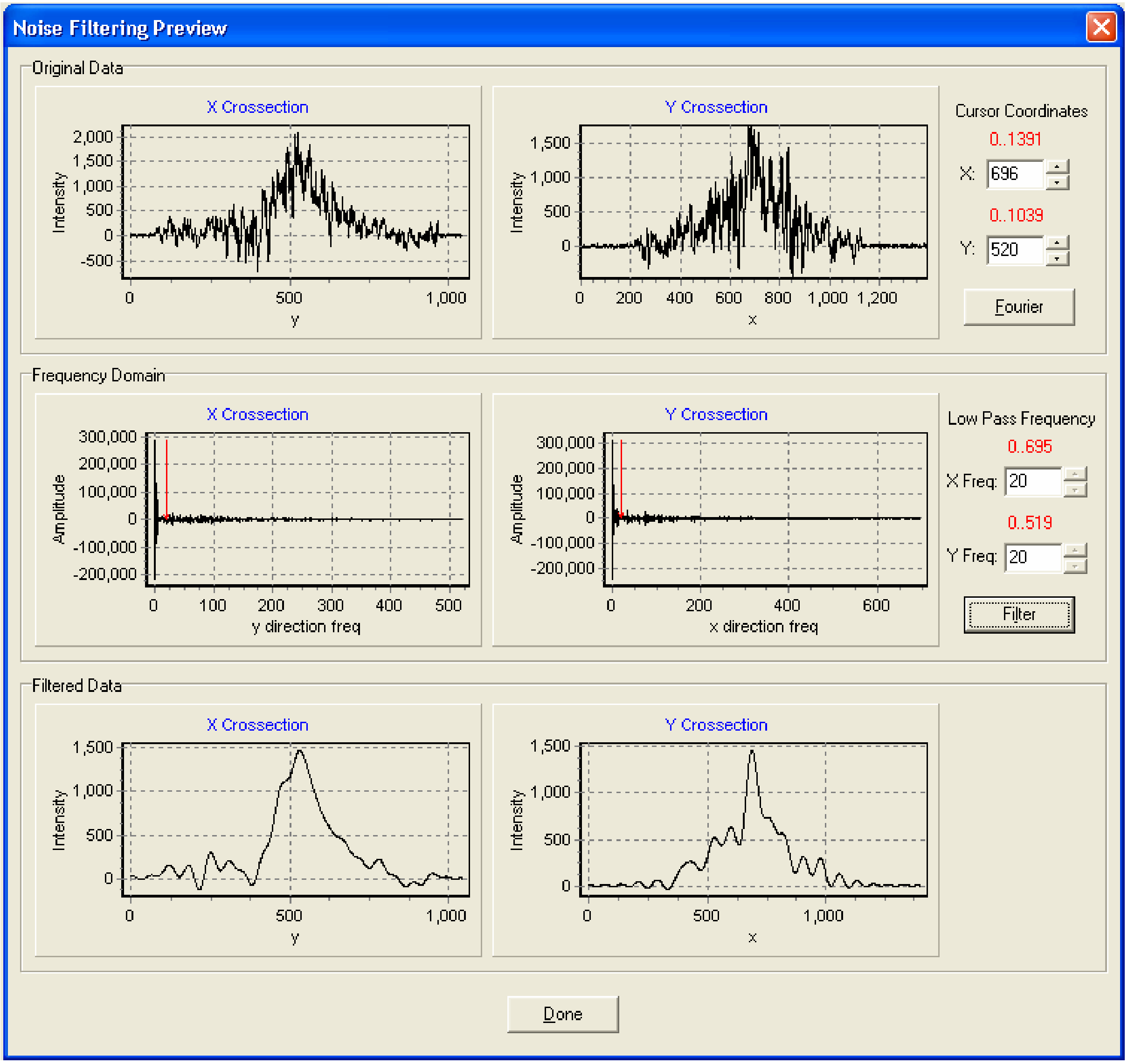

Cursor Coordinates

0..1391

X: 696

0..1039

Y: 520

Low Pass Frequency

0..695

X Freq: 20

0..519

Y Freq: 20

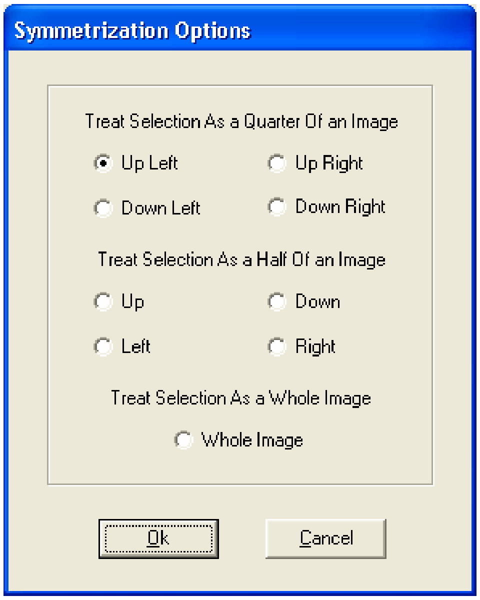

Symmetrization Options

Treat Selection As a Quarter Of an Image

● Up Left ○ Up Right

○ Down Left ○ Down Right

Treat Selection As a Half Of an Image

○ Up ○ Down

○ Left ○ Right

Treat Selection As a Whole Image

○ Whole Image

Finally, the Symmetrization operation can be performed on a quarter, a half, and a whole image by selecting the corresponding option in the Symmetrization Options Dialog.

A-1.10.4 Image Palette Dialog

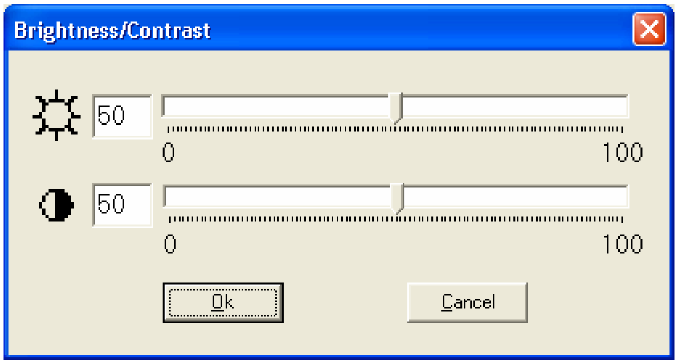

Brightness/Contrast

☼ 50

◐ 50

The Image Palette Dialog allows adjust the brightness and contrast of an image.

A-1.10.5 Image Statistics Dialog

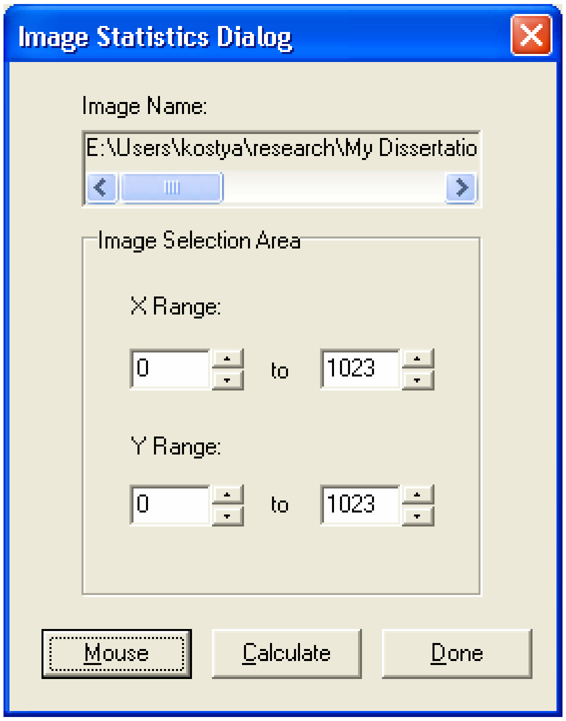

Image Name: E:\Users\kostya\research\My Dissertatio

X Range: 0 to 1023

Y Range: 0 to 1023

The Image Statistics Dialog generates a simple statistics report for the selected ROI or the entire image. See Statistics Window Section for the detailed description of the statistics output.

A-1.11 Process Menu

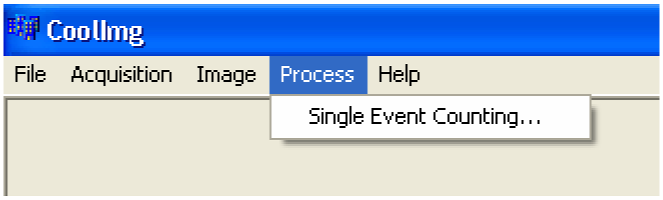

Presently, the Process Menu contains only one command – Single Event Counting, which calls Single Event Counting Dialog.

A-1.11.1 Single Event Counting Dialog

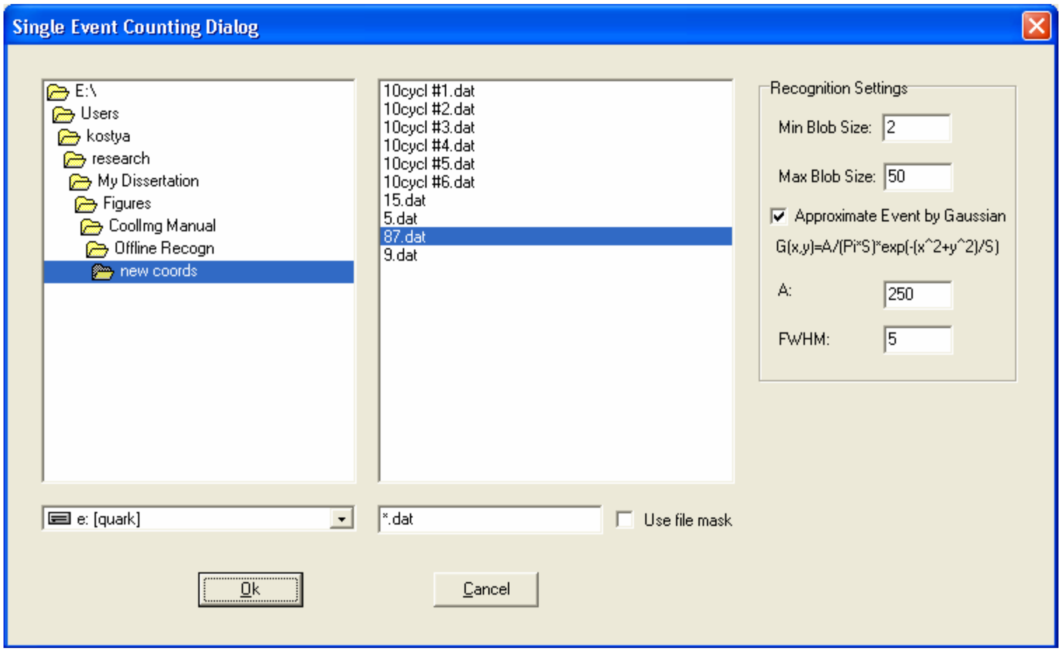

E:\
Users
kostya
research
My Dissertation
Figures
CoolImg Manual
Offline Recogn
new coords

10cycl #1.dat
10cycl #2.dat
10cycl #3.dat
10cycl #4.dat
10cycl #5.dat
10cycl #6.dat
15.dat
5.dat
87.dat
9.dat

e: [quark]

*.dat

☐ Use file mask

Min Blob Size: 2

Max Blob Size: 50

☑ Approximate Event by Gaussian

G(x,y)=A/(Pi*S)*exp(-(x^2+y^2)/S)

A: 250

FWHM: 5

The Single Event Counting Dialog allows user to perform Event Counting procedure in the offline regime using previously autosaved binary file (.dat), which contains coordinates and intensities of thresholded pixels from data acquisition. An example of post-processing for the photoelectron signal of I^- at 390 nm is given below

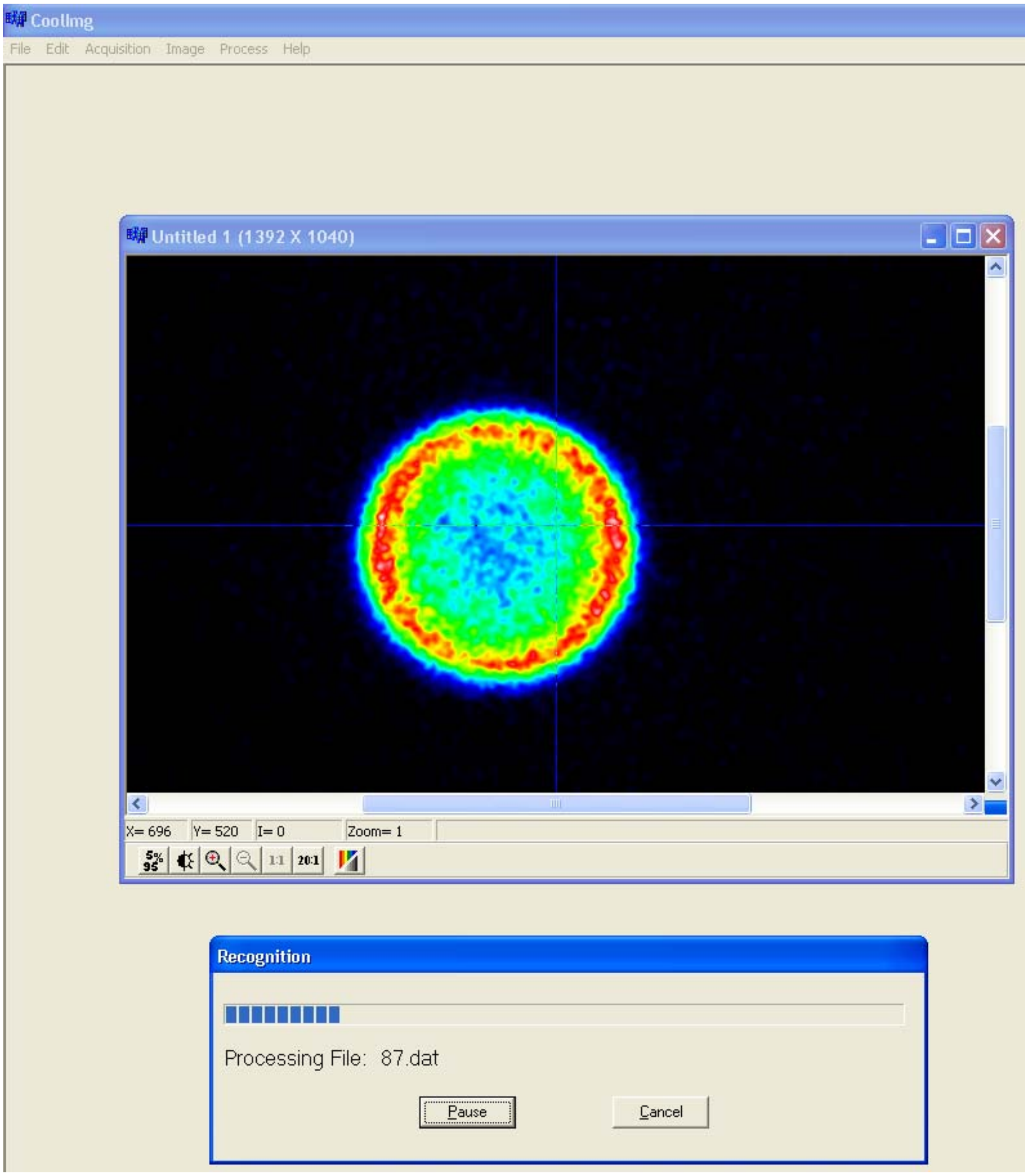

X= 696 Y= 520 I= 0 Zoom= 1

Processing File: 87.dat

A-1.12 Help Menu

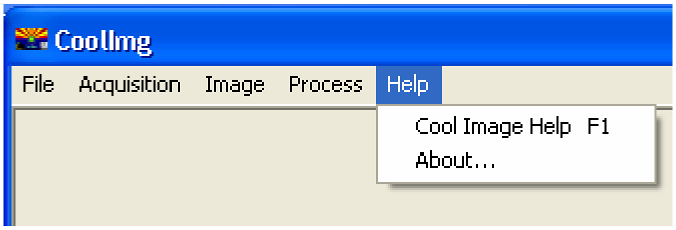

The Help Menu has two commands which provide assistance with Cool Image software: Cool Image Help (a context sensitive help), About (provides a brief information about Cool Image).

Cool Image
Version 1.2

Brewed by Kostyantyn Pichugin
Andrei Sanov's Research Group
Department of Chemistry
The University of Arizona
Contact: sanov@email.arizona.edu

A-2 CoolImage Internals: The Code Structure

The Cool Image program is written in C++ language using Borland C++ Builder IDE (version 6). Currently, Cool Image consists of 37 program units. Each unit may contain several files, e.g. a header file (.h), a C++ code file (.cpp), a graphical components file (.dfm), etc … Due to excessive amount, thousands and thousands, lines of code only general description of the software structural components and their functionality is given below.

Unit Name	Unit Files (<Unit Name>.extension)	Description
AcquisitionExperSetupForm	.h, .cpp, .dfm, .ddp	Implements Experimental Setup Dialog and corresponding class methods to check entered experimental settings for consistency.
acquisitionthread	.h, .cpp	Contains implementation of different types of data-acquisition threads: Focus, Acquire, Time-Resolved, etc…
blob	.h, .cpp	Contains all classes and definitions pertinent to Single Event Counting.
camera	.h, .cpp	Defines fundamental abstract TCamera class and its specific implementation for the CoolSnap$_{HQ}$ and DALSA DALSA 1M30 cameras.
CameraManager	.h, .cpp	Contains TCameraManager singleton class responsible for camera auto-detection and generation of appropriate camera type class instance.

CameraNotFoundForm	h, .cpp, .dfm	Implements Camera not found Dialog which shows at the program startup if no camera was detected. It also allows user to permanently disable camera auto-detection when the program starts.
CDFolder	.h, .cpp, .dfm, .ddp	Provides a helper GUI class for displaying Change Folder Dialog.
ClipImage_Form	h, .cpp, .dfm	Implements Clip Image Dialog class.
clock	.h, .cpp	A simple timer class used to check for camera response timeout during data-acquisition.
coolimg	.bpr, .cpp, .dsk, .exe, .ico, .res, .tds	Main program. Loads, initializes all software components and shows the main CoolImage window.
CoolImgSettings	.h, .cpp	Contains TCoolImgAppSettings class for reading and storing various program settings in CoolImg.ini file.
dyn2darr	.h, .cpp	Defines template class TDynamicArr providing memory management and variety of mathematical operations on two-dimensional arrays of different data types (int, double, etc …).
EditImage_Form	.h, .cpp, .dfm, .ddp	Implements Edit Image Dialog

ExperimentalSetUp	.h, .cpp	Contains TExperimentalSetup class for reading and storing various experimental settings in CoolImg.ini file.
fft_lib	.h, .cpp	Implements 2D Fast Fourier Transform algorithm for noise filtering
gaussconv	.h, .cpp	Contains a small helper class to approximate Events by 3D Gaussian functions.
HelpAboutForm	.h, .cpp, .dfm, .ddp	Implements Help About Dialog
imagecontrol	.h, .cpp	Contains TImageControl template class for managing Image Windows of different data types.
imagefilter	.h, .cpp	Contains TImageFilter class for raw image thresholding.
imagemathdialog	.h, .cpp, .dfm, .ddp	Implements Image Math Dialog.
imagemathprogressinfoform	.h, .cpp, .dfm, .ddp	A simple form showing progress of different mathematical operations requested through the Image Math Dialog.
ImageStatisticsForm	.h, .cpp, .dfm, .ddp	Implements Image Statistics Dialog

Img_Form	.h, .cpp, .dfm, .ddp	Implements Image Form including Action Manager and Image Menu merging with Main Menu when an Image Window is selected.
Info_Form	.h, .cpp, .dfm, .ddp	A form containing ASCII text area. Presently is used to display Image Statistics output.
LocateImageCenterProgressInfoForm	.h, .cpp, .dfm	A simple form showing progress of the Locate Image Center command.
mainform	.h, .cpp, .dfm, .ddp	Defines Cool Image main form including the Main Menu, Action Manager, Open and Save File dialogs, as well as the corresponding subroutines for creating Image Window, calling various Dialogs, lunching acquisition thread, reading and writing data files.
NoiseFilteringPreview_Form	.h, .cpp, .dfm, .ddp	A form allowing preview the results of low pass frequency filtering of experimental data.
paletteform	.h, .cpp, .dfm, .ddp	Defines Image Palette Dialog for adjusting brightness and contrast of an image.
process_singleeventcountingdialog	.h, .cpp, .dfm, .ddp	Defines Single Event Counting Dialog, which allows user to perform Event Counting procedure in the offline regime

recognitionprogressfrom	.h, .cpp, .dfm, .ddp	A simple form showing progress of Process Single Envent Counting command.
recognitionthread	.h, .cpp	A thread running Single Envent Counting procedure requested by Single Event Counting Dialog.
regionselectordialog	.h, .cpp, .dfm, .ddp	Defines Region Selector Dialog, which provides a user with convenient means of choosing ROI within an image.
selectregion	.h, .cpp	A rectangular TShape object visualizing ROI.
SingleEventsDebuggingForm	.h, .cpp, .dfm, .ddp	Defines Single Events Debugging Dialog for previewing the results of Single Events Counting procedure.
smothingpaterndialog	.h, .cpp, .dfm, .ddp	A helper form used in Image Math dialog for entering moving average matrix template.
SymmetrizationOptionsForm	.h, .cpp, .dfm, .ddp	A helper form used in Image Math dialog for selecting an image symmetrization option.
vmmd3	.h, .cpp	Implements the low level access to the VMMD3 (Uniblitz, Inc.) controller allowing operate optical shutters.

REFERENCES

(1) Wenthold, P. G.; Lineberger, W. C. *Accounts of Chemical Research* **1999**, *32*, 597.

(2) King, B. T.; Michl, J. *Journal of the American Chemical Society* **2000**, *122*, 10255.

(3) Broadus, K. M.; Kass, S. R. *Journal of the American Chemical Society* **2001**, *123*, 4189.

(4) Barry Halliwell; Gutteridge, J. *Free Radicals in Biology and Medicine*, 4 ed.; Oxford University Press, USA, 2007.

(5) Maier, J. P. *Journal of Physical Chemistry A* **1998**, *102*, 3462.

(6) Fleming, G. R.; Wolynes, P. G. *Physics Today* **1990**, *43*, 36.

(7) Castleman, A. W.; Bowen, K. H. *Journal Of Physical Chemistry* **1996**, *100*, 12911.

(8) Crompton, T. R. *Determination of Anions: A Guide for the Analytical Chemist*, 1 ed.; Springer, 1996.

(9) Tsukuda, T.; Johnson, M. A.; Nagata, T. *Chemical Physics Letters* **1997**, *268*, 429.

(10) DeLuca, M. J.; Niu, B.; Johnson, M. A. *Journal of Chemical Physics* **1988**, *88*, 5857.

(11) Fleischman, S. H.; Jordan, K. D. *Journal of Physical Chemistry* **1987**, *91*, 1300.

(12) Tsukuda, T.; Saeki, M.; Zhu, L.; Nagata, T. *Chemical Physics Letters* **1998**, *295*, 416.

(13) Puckett, L. J.; Lineberg.Wc. *Bulletin of the American Physical Society* **1969**, *14*, 261.

(14) Lineberg.Wc; Woodward, B. W. *Physical Review Letters* **1970**, *25*, 424.

(15) Lineberg.Wc; Woodward, B. W.; Branscom.Lm. *Bulletin of the American Physical Society* **1970**, *15*, 430.

(16) Puckett, L. J.; Lineberg.Wc. *Physical Review A* **1970**, *1*, 1635.

(17) Lineberg.Wc. *Bulletin of the American Physical Society* **1971**, *16*, 1348.

(18) Hotop, H.; Patterso.Ta; Lineberg.Wc. *Bulletin of the American Physical Society* **1972**, *17*, 150.

(19) Lineberg.Wc; Patterso.Ta. *Chemical Physics Letters* **1972**, *13*, 40.

(20) Patterso.Ta; Hotop, H.; Lineberg.Wc. *Bulletin of the American Physical Society* **1972**, *17*, 1128.

(21) Brauman, J. I.; Smyth, K. C. *Journal of the American Chemical Society* **1969**, *91*, 7778.

(22) Smyth, K. C.; McIver, R. T.; Brauman, J. I.; Wallace, R. W. *Journal of Chemical Physics* **1971**, *54*, 2758.

(23) Smyth, D. C.; Brauman, J. I. *Journal of Chemical Physics* **1972**, *56*, 4620.

(24) Smyth, K. C.; Brauman, J. I. *Journal of Chemical Physics* **1972**, *56*, 1132.

(25) Johnson, M. A.; Alexander, M. L.; Lineberger, W. C. *Chemical Physics Letters* **1984**, *112*, 285.

(26) Posey, L. A.; DeLuca, M. J.; Johnson, M. A. *Chemical Physics Letters* **1986**, *131*, 170.

(27) Greenblatt, B. J.; Zanni, M. T.; Neumark, D. M. *Chemical Physics Letters* **1996**, *258*, 523.

(28) Neumark, D. M. *Annual Review of Physical Chemistry* **2001**, *52*, 255.

(29) Stolow, A.; Bragg, A. E.; Neumark, D. M. *Chemical Reviews* **2004**, *104*, 1719.

(30) Sanov, A.; Mabbs, R. *International Reviews in Physical Chemistry* **2008**, *27*, 53.

(31) Chandler, D. W.; Houston, P. L. *Journal of Chemical Physics* **1987**, *87*, 1445.

(32) Heck, A. J. R.; Chandler, D. W. *Annual Review Of Physical Chemistry* **1995**, *46*, 335.

(33) Eppink, A.; Parker, D. H. *Review of Scientific Instruments* **1997**, *68*, 3477.

(34) Parker, D. H.; Eppink, A. T. J. B. *Journal Of Chemical Physics* **1997**, *107*, 2357.

(35) Cooper, J.; Zare, R. N. *J. Chem. Phys.* **1968**, *48*, 942.

(36) Cooper, J.; Zare, R. N. Photoelectron angular distributions. In *Atomic collision processes*; Geltman, S., Mahanthappa, K. T., Brittin, W. E., Eds.; Gordon and Breach, Science Publishers: New York, London, Paris, 1968; Vol. XI-C; pp 317.

(37) Surber, E.; Mabbs, R.; Sanov, A. *J. Phys. Chem. A* **2003**, *107*, 8215.

(38) Oana, C. M.; Krylov, A. I. *Journal of Chemical Physics* **2007**, *127*, 234106.

(39) Oana, C. M.; Krylov, A. I. *Journal of Chemical Physics* **2009**, *131*, 124114.

(40) Goebbert, D. J.; Pichugin, K.; Sanov, A. *Journal of Chemical Physics* **2009**, *131*, 164308.

(41) Mabbs, R.; Pichugin, K.; Surber, E.; Sanov, A. *Journal of Chemical Physics* **2004**, *121*, 265.

(42) Mabbs, R.; Pichugin, K.; Sanov, A. *Journal of Chemical Physics* **2005**, *122*, 174305.

(43) Mabbs, R.; Pichugin, K.; Sanov, A. *Journal of Chemical Physics* **2005**, *123*, 054329.

(44) Velarde, L.; Habteyes, T.; Grumbling, E. R.; Pichugin, K.; Sanov, A. *Journal of Chemical Physics* **2007**, *127*, 084302.

(45) Reid, K. L. *Annual Review of Physical Chemistry* **2003**, *54*, 397.

(46) Surber, E. Photoelectron imaging of molecular and cluster anions. Ph.D., University of Arizona, 2005.

(47) Mabbs, R.; Surber, E.; Sanov, A. *Analyst* **2003**, *128*, 765.

(48) Johnson, M. A.; Lineberger, W. C. Pulsed Methods for Cluster Ion Spectroscopy. In *Techniques for the Study of Ion Molecule Reactions*; Farrar, J. M., Saunders, W. H., Eds.; Wiley: New York, 1988; pp 591.

(49) Nadal, M. E.; Kleiber, P. D.; Lineberger, W. C. *Journal Of Chemical Physics* **1996**, *105*, 504.

(50) Robertson, W. H.; Kelley, J. A.; Johnson, M. A. *Review of Scientific Instruments* **2000**, *71*, 4431.

(51) Klots, C. E.; Compton, R. N. *Journal of Chemical Physics* **1978**, *69*, 1636.

(52) Wiley, W. C.; McLaren, I. H. *Review of Scientific Instruments* **1955**, *26*, 1150.

(53) Nadal, M. E. The study of the photodissociation and recombination dynamics of mass-selected cluster ions: Solvent effects on the structure and dynamics of the ionic chromophore. Ph.D. Thesis, University of Colorado, 1996.

(54) Dribinski, V.; Ossadtchi, A.; Mandelshtam, V. A.; Reisler, H. *Review of Scientific Instruments* **2002**, *73*, 2634.

(55) Yang, C. N. *Physical Review* **1948**, *74*, 764.

(56) Blatt, J. M.; Biedenharn, L. C. *Reviews of Modern Physics* **1952**, *24*, 258.

(57) Berry, R. S.; Reimann, C. W. *Journal of Chemical Physics* **1963**, *38*, 1540.

(58) Trainham, R.; Fletcher, G. D.; Larson, D. J. *Journal of Physics B-Atomic Molecular and Optical Physics* **1987**, *20*, L777.

(59) Berzinsh, U.; Gustafsson, M.; Hanstorp, D.; Klinkmuller, A.; Ljungblad, U.; Martenssonpendrill, A. M. *Physical Review A* **1995**, *51*, 231.

(60) Martin, J. D. D.; Hepburn, J. W. *Journal of Chemical Physics* **1998**, *109*, 8139.

(61) Blondel, C.; Cacciani, P.; Delsart, C.; Trainham, R. *Physical Review A* **1989**, *40*, 3698.

(62) Neiger, M. *Zeitschrift Fur Naturforschung Section a-a Journal of Physical Sciences* **1975**, *A 30*, 474.

(63) Webster, C. R.; Mcdermid, I. S.; Rettner, C. T. *Journal of Chemical Physics* **1983**, *78*, 646.

(64) Hanstorp, D.; Gustafsson, M. *Journal of Physics B-Atomic Molecular and Optical Physics* **1992**, *25*, 1773.

(65) *Ralchenko, Yu., Kramida, A.E., Reader, J., and NIST ASD Team (2008). NIST Atomic Spectra Database (version 3.1.5), [Online]. Available:*

http://physics.nist.gov/asd3 [2009, December 27]. National Institute of Standards and Technology, Gaithersburg, MD. .

(66) Moore, C. E. *Atomic Energy Levels*; National Bureau of Standards, U.S. Government: Washington D.C., 1958.

(67) Bethe, H. A. *Handbuch der Physik* **1933**, *24*, 483.

(68) Cooper, J.; Zare, R. N. *J. Chem. Phys.* **1968**, *49*, 4252.

(69) Wigner, E. P. *Physical Review* **1948**, *73*, 1002.

(70) Hanstorp, D.; Bengtsson, C.; Larson, D. J. *Physical Review A* **1989**, *40*, 670.

(71) Davis, A. V.; Wester, R.; Bragg, A. E.; Neumark, D. M. *Journal of Chemical Physics* **2003**, *118*, 999.

(72) Gilles, M. K.; Ervin, K. M.; Ho, J.; Lineberger, W. C. *Journal Of Physical Chemistry* **1992**, *96*, 1130.

(73) Matthew Van, D.; Jie, W.; Foster, M.; Richard, M. *The Journal of Chemical Physics* **2009**, *131*, 204306.

(74) Celotta, R. J.; Bennett, R. A.; Levine, J.; Hall, J. L.; Siegel, M. W. *Physical Review a* **1972**, *6*, 631.

(75) Burch, D. S.; Smith, S. J.; Branscomb, L. M. *Physical Review* **1958**, *112*, 171.

(76) Sherwood, C. R.; Garner, M. C.; Hanold, K. A.; Strong, K. M.; Continetti, R. E. *Journal Of Chemical Physics* **1995**, *102*, 6949.

(77) Lin, P.; Lucchese, R. R. *Journal of Chemical Physics* **2001**, *114*, 9350.

(78) Bonaccor.R; Petrongo.C; Scrocco, E.; Tomasi, J. *Theoretica Chimica Acta* **1969**, *15*, 332.

(79) Andersen, E.; Simons, J. *Journal of Chemical Physics* **1977**, *66*, 2427.

(80) Kirk, A. P.; Rudolph, C. M.; Edwin, L. S., III; Woods, R. C. *The Journal of Chemical Physics* **1991**, *94*, 414.

(81) Mahapatra, S.; Koppel, H.; Cederbaum, L. S. *Journal of Chemical Physics* **1999**, *110*, 5691.

(82) Liang, J.; Pei, K.; Li, H. *Chemical Physics Letters* **2004**, *388*, 212.

(83) Herbst, E.; Patterson, T. A.; Lineberger, W. C. *The Journal of Chemical Physics* **1974**, *61*, 1300.

(84) Woo, S. B.; Helmy, E. M.; Mauk, P. H.; Paszek, A. P. *Physical Review A* **1981**, *24*, 1380.

(85) Ervin, K. M.; Ho, J.; Lineberger, W. C. *Journal of Physical Chemistry* **1988**, *92*, 5405.

(86) Weaver, A.; Metz, R. B.; Bradforth, S. E.; Neumark, D. M. *Journal of Chemical Physics* **1989**, *90*, 2070.

(87) Daniel, F.; Warren, E. T.; Marilyn, E. J. *The Journal of Chemical Physics* **1993**, *99*, 7393.

(88) Luong, A. K.; Clements, T. G.; Continetti, R. E. *International Journal of Mass Spectrometry* **2002**, *220*, 253.

(89) Gillispie, G. D.; Khan, A. U.; Wahl, A. C.; Hosteny, R. P.; Krauss, M. *Journal of Chemical Physics* **1975**, *63*, 3425.

(90) R. D. J. Nelson; D. R. J. Lide; Maryott, A. A. *Natl. Stand. Ref. Data Ser. (U.S., Natl. Bur. Stand.) 10* **1967**.

(91) Desfrancois, C.; Abdoul-Carime, H.; Schermann, J. P. *International Journal Of Modern Physics B* **1996**, *10*, 1339.

(92) Lobo, R. F. M.; Moutinho, A. M. C.; Lacmann, K.; Los, J. *Journal of Chemical Physics* **1991**, *95*, 166.

(93) Compton, R. N.; Carman, H. S.; Desfrancois, C.; Abdoulcarmine, H.; Schermann, J. P.; Hendricks, J. H.; Lyapustina, S. A.; Bowen, K. H. *Journal Of Chemical Physics* **1996**, *105*, 3472.

(94) Brooks, P. R.; Harland, P. W.; Redden, C. E. *Journal of the American Chemical Society* **2006**, *128*, 4773.

(95) Brooks, P. R.; Harland, P. W.; Redden, C. E. *Journal of Physical Chemistry A* **2006**, *110*, 4697.

(96) Brooks, P. R.; Harland, P. W.; Harris, S. A.; Kennair, T.; Redden, C.; Tate, J. F. *Journal of the American Chemical Society* **2007**, *129*, 15572.

(97) Walker, I. C.; Fluendy, M. A. D. *International Journal of Mass Spectrometry* **2001**, *205*, 171.

(98) Adams, C. L.; Schneider, H.; Ervin, K. M.; Weber, J. M. *Journal of Chemical Physics* **2009**, *130*, 074307.

(99) Alizadeh, E.; Ferreira da Silva, F.; Zappa, F.; Mauracher, A.; Probst, M.; Denfil, S.; A, B.; Maerk, T. D.; Limao-Viera, P.; Scheier, P. *International Journal of Mass Spectrometry and Ion Processes* **2008**, *271*, 15.

(100) Butler, L. J.; Krajnovich, D.; Lee, Y. T.; Ondrey, G.; Bersohn, R. *Journal of Chemical Physics* **1983**, *79*, 1708.

(101) Kwok, H. S.; He, G. Z.; Sparks, R. K.; Lee, Y. T. *International Journal of Chemical Kinetics* **1981**, *13*, 1125.

(102) Guo, Y. Q.; Bhattacharya, A.; Bernstein, E. R. *Journal of Physical Chemistry A* **2009**, *113*, 85.

(103) Flicker, W. M.; Mosher, O. A.; Kupperman, A. *J. Chem. Phys.* **1980**, *72*, 2788.

(104) Sommerfeld, T. *Physical Chemistry Chemical Physics* **2002**, *4*, 2511.

(105) Weber, J. M.; Robertson, W. H.; Johnson, M. A. *Journal of Chemical Physics* **2001**, *115*, 10718.

(106) Schneider, H.; Vogelhuber, K. M.; Schinle, F.; Stanton, J. F.; Weber, J. M. *Journal of Physical Chemistry A* **2008**, *112*, 7498.

(107) Fluendy, M. A. D.; Lunt, S. *Molecular Physics: An International Journal at the Interface Between Chemistry and Physics* **1983**, *49*, 1007

(108) McAllister, T. *The Journal of Chemical Physics* **1972**, *57*, 3353.

(109) McEwen, K. L. *Journal of Chemical Physics* **1960**, *32*, 1801.

(110) Harris, L. E. *Journal of Chemical Physics* **1973**, *58*, 5615.

(111) Mijoule, C.; Odiot, S.; Fliszar, S.; Schnur, J. M. *Theochem-Journal of Molecular Structure* **1987**, *34*, 311.

(112) Arenas, J. F.; Otero, J. C.; Pelaez, D.; Soto, J. *Journal of Chemical Physics* **2005**, *122*.

(113) Arenas, J. F.; Otero, J. C.; Pelaez, D.; Soto, J.; Serrano-Andres, L. *Journal of Chemical Physics* **2004**, *121*, 4127.

(114) Arenas, J. F.; Otero, J. C.; Pelaez, D.; Soto, J. *Journal of Chemical Physics* **2003**, *119*, 7814.

(115) Frisch, M. J.; Trucks, G. W.; Schlegel, H. B.; Scuseria, G. E.; Robb, M. A.; Cheeseman, J. R.; Montgomery, J. J. A.; Vreven, T.; Kudin, K. N.; Burant, J. C.; Millam, J. M.; Iyengar, S. S.; Tomasi, J.; Barone, V.; Mennucci, B.; Cossi, M.; Scalmani, G.; Rega, N.; Petersson, G. A.; Nakatsuji, H.; Hada, M.; Ehara, M.; Toyota, K.; Fukuda, R.; Hasegawa, J.; Ishida, M.; Nakajima, T.; Honda, Y.; Kitao, O.; Nakai, H.; Klene, M.; Li, X.; Knox, J. E.; Hratchian, H. P.; Cross, J. B.; Bakken, V.; Adamo, C.; Jaramillo, J.; Gomperts, R.; Stratmann, R. E.; Yazyev, O.; Austin, A. J.; Cammi, R.; Pomelli, C.; Ochterski, J. W.; Ayala, P. Y.; Morokuma, K.; Voth, G. A.; Salvador, P.; Dannenberg, J. J.; Zakrzewski, V. G.; Dapprich, S.; Daniels, A. D.; Strain, M. C.; Farkas, O.; Malick, D. K.; Rabuck, A. D.; Raghavachari, K.; Foresman, J. B.; Ortiz, J. V.; Cui, Q.; Baboul, A. G.; Clifford, S.; Cioslowski, J.; Stefanov, B. B.; Liu, G.; Liashenko, A.; Piskorz, P.; Komaromi, I.; Martin, R. L.; Fox, D. J.; Keith, T.; Al-Laham, M. A.; Peng, C. Y.; Nanayakkara, A.; Challacombe, M.; Gill, P. M. W.; Johnson, B.; Chen, W.; Wong, M. W.; Gonzalez, C.; and Pople, J. A. Gaussian 03, Revision C.02; Gaussian, Inc.: Wallingford CT, 2004.

(116) Gorse, D.; Cavagnat, D.; Pesquer, M.; Lapouge, C. *Journal of Physical Chemistry* **1993**, *97*, 4262.

(117) Koopmans, T. *Physica* **1934**, *1*, 104.

(118) Scholes, G. D.; Rumbles, G. *Nature Materials* **2006**, *5*, 683.

(119) Kilina, S.; Tretiak, S. *Advanced Functional Materials* **2007**, *17*, 3405.

(120) Emberly, E.; Kirczenow, G. *Nanotechnology* **1999**, *10*, 285.

(121) Joensson, C. *Zeitschrift Fur Physik* **1961**, *161*, 454.

(122) Cohen, H. D.; Fano, U. *Physical Review* **1966**, *150*, 30.

(123) Akoury, D.; Kreidi, K.; Jahnke, T.; Weber, T.; Staudte, A.; Schoffler, M.; Neumann, N.; Titze, J.; Schmidt, L. P. H.; Czasch, A.; Jagutzki, O.; Fraga, R. A. C.; Grisenti, R. E.; Muino, R. D.; Cherepkov, N. A.; Semenov, S. K.; Ranitovic, P.; Cocke, C. L.; Osipov, T.; Adaniya, H.; Thompson, J. C.; Prior, M. H.; Belkacem, A.; Landers, A. L.; Schmidt-Bocking, H.; Dorner, R. *Science* **2007**, *318*, 949.

(124) Weber, T.; Kreidi, K.; Akoury, D.; Jahnke, T.; Schoffler, M.; Schmidt, L. P.; Jagutzki, O.; Foucar, L.; Havermeier, T.; Neumann, N.; Schmidt-Bocking, H.; Dorner,

R.; Osipov, T.; Belkacem, A.; Prior, M.; Landers, A.; Ranitovic, P.; Cocke, C. L. *Journal of Electron Spectroscopy and Related Phenomena* **2007**, *156*, XX.

(125) Rolles, D.; Braune, M.; Cvejanovic, S.; Geßner, O.; Hentges, R.; Korica, S.; Langer, B.; Lischke, T.; Prümper, G.; Reinköster, A.; Viefhaus, J.; Zimmermann, B.; McKoy, V.; Becker, U. *Radiation Physics and Chemistry* **2006**, *75*, 1514.

(126) Zimmermann, B.; Rolles, D.; Langer, B.; Hentges, R.; Braune, M.; Cvejanovic, S.; Gessner, O.; Heiser, F.; Korica, S.; Lischke, T.; Reinkoster, A.; Viefhaus, J.; Doerner, R.; Mckoy, V.; Becker, U. *Nature Physics* **2008**, *4*, 649.

(127) Raymond, L. W. *The Journal of Chemical Physics* **1960**, *32*, 410.

(128) Ward, R. L. *Journal of the American Chemical Society* **1961**, *83*, 1296.

(129) Ward, R. L. *Journal of Chemical Physics* **1962**, *36*, 1405.

(130) August, H. M.; David, H. G. *The Journal of Chemical Physics* **1960**, *33*, 825.

(131) Nelsen, S. F.; Weaver, M. N.; Konradsson, A. E.; Telo, J. P.; Clark, T. *Journal of the American Chemical Society* **2004**, *126*, 15431.

(132) Mikhailov, M. N.; Mendkovich, A. S.; Kuzminsky, M. B.; Rusakov, A. I. *Journal of Molecular Structure: THEOCHEM* **2007**, *847*, 103.

(133) Green, J. H. S.; Harrison, D. J. *Spectrochimica Acta Part a-Molecular Spectroscopy* **1970**, *A 26*, 1925.

(134) Baronetskii, A. O.; Kuzyants, G. M. *Bulletin of the Academy of Sciences of the Ussr Division of Chemical Science* **1980**, *29*, 1267.

(135) Desfrancois, C.; Periquet, V.; Lyapustina, S. A.; Lippa, T. P.; Robinson, D. W.; Bowen, K. H.; Nonaka, H.; Compton, R. N. *Journal of Chemical Physics* **1999**, *111*, 4569.

(136) Krohl, O.; Malsch, K.; Swiderek, P. *Physical Chemistry Chemical Physics* **2000**, *2*, 947.

(137) Mock, R. S.; Grimsrud, E. P. *Journal of the American Chemical Society* **1989**, *111*, 2861.

(138) Chowdhury, S.; Grimsrud, E. P.; Heinis, T.; Kebarle, P. *Journal of the American Chemical Society* **1986**, *108*, 3630.

(139) Fukuda, E. K.; Mciver, R. T. *Journal of the American Chemical Society* **1985**, *107*, 2291.

(140) Chowdhury, S.; Heinis, T.; Grimsrud, E. P.; Kebarle, P. *The Journal of Physical Chemistry* **1986**, *90*, 2747.

(141) Sanov, A.; Lineberger, W. C. *Physical Chemistry Chemical Physics* **2004**, *6*, 2018.

(142) Yourshaw, I.; Zhao, Y. X.; Neumark, D. M. *Journal Of Chemical Physics* **1996**, *105*, 351.

(143) Posey, L. A.; Johnson, M. A. *Journal of Chemical Physics* **1988**, *88*, 5383.

(144) Hacaloglu, J.; Suzer, S.; Andrews, L. *Journal of Physical Chemistry* **1990**, *94*, 1759.

(145) Jacox, M. E. *Journal of Chemical Physics* **1990**, *93*, 7622.

(146) Jacox, M. E.; Thompson, W. E. *Journal of Chemical Physics* **1990**, *93*, 7609.

(147) Arnold, D. W.; Neumark, D. M. *Journal Of Chemical Physics* **1995**, *102*, 7035.

(148) Osborn, D. L.; Leahy, D. J.; Cyr, D. R.; Neumark, D. M. *Journal Of Chemical Physics* **1996**, *104*, 5026.

(149) Li, R. J.; Continetti, R. E. *Journal of Physical Chemistry A* **2002**, *106*, 1183.

(150) Warman, J. M.; Bakale, G.; Fessende.Rw. *Journal of Chemical Physics* **1972**, *57*, 2702.

(151) Knapp, M.; Echt, O.; Kreisle, D.; Mark, T. D.; Recknagel, E. *Chemical Physics Letters* **1986**, *126*, 225.

(152) Sojka, Z.; Che, M. *Journal of Physical Chemistry* **1996**, *100*, 14776.

(153) Bass, A. D.; Lezius, M.; Ayotte, P.; Parenteau, L.; Cloutier, P.; Sanche, L. *Journal of Physics B-Atomic Molecular and Optical Physics* **1997**, *30*, 3527.

(154) Weber, J. M.; Leber, E.; Ruf, M. W.; Hotop, H. *Physical Review Letters* **1999**, *82*, 516.

(155) Leber, E.; Barsotti, S.; Bommels, J.; Weber, J. M.; Fabrikant, I. I.; Ruf, M. W.; Hotop, H. *Chemical Physics Letters* **2000**, *325*, 345.

(156) Kryachko, E. S.; Vinckier, C.; Nguyen, M. T. *Journal of Chemical Physics* **2001**, *114*, 7911.

(157) Suter, H. U.; Greber, T. *Journal of Physical Chemistry B* **2004**, *108*, 14511.

(158) Hanel, G.; Fiegele, T.; Stamatovic, A.; Mark, T. D. *International Journal of Mass Spectrometry* **2001**, *205*, 65.

(159) Hiraoka, K.; Fujimaki, S.; Aruga, K.; Yamabe, S. *Journal of Physical Chemistry* **1994**, *98*, 8295.

(160) Yamamoto, S.; Mitsuke, K.; Misaizu, F.; Kondow, T.; Kuchitsu, K. *Journal of Physical Chemistry* **1990**, *94*, 8250.

(161) Velarde, L.; Habteyes, T.; Sanov, A. *Journal of Chemical Physics* **2006**, *125*, 114303.

(162) Neumark, D. M.; Lykke, K. R.; Andersen, T.; Lineberger, W. C. *Physical Review A* **1985**, *32*, 1890.

(163) Cavanagh, S. J.; Gibson, S. T.; Gale, M. N.; Dedman, C. J.; Roberts, E. H.; Lewis, B. R. *Physical Review A* **2007**, *76*, 052708.

(164) Velarde, L. Ph. D. dissertation. Ph.D., University of Arizona, 2008.

(165) Snodgrass, J. T.; Kim, H. S.; Bowers, M. T. *Journal of Chemical Physics* **1988**, *88*, 3072.

(166) Roehl, C. M.; Snodgrass, J. T.; Deakyne, C. A.; Bowers, M. T. *Journal of Chemical Physics* **1991**, *94*, 6546.

(167) Shin, J. W.; Hammer, N. I.; Johnson, M. A.; Schneider, H.; Gloss, A.; Weber, J. M. *Journal of Physical Chemistry A* **2005**, *109*, 3146.

(168) Roszak, S.; Leszczynski, J. *Computational Chemistry (Singapore, Singapore)* **2001**, *6*, 179.

(169) Kim, J. B.; Wenthold, P. G.; Lineberger, W. C. *Journal of Chemical Physics* **1998**, *108*, 830.

(170) Frisch, M. J.; Trucks, G. W.; Schlegel, H. B.; Scuseria, G. E.; Robb, M. A.; Cheeseman, J. R.; Montgomery, J. J. A.; Vreven, T.; Kudin, K. N.; Burant, J. C.;

Millam, J. M.; Iyengar, S. S.; Tomasi, J.; Barone, V.; Mennucci, B.; Cossi, M.; Scalmani, G.; Rega, N.; Petersson, G. A.; Nakatsuji, H.; Hada, M.; Ehara, M.; Toyota, K.; Fukuda, R.; Hasegawa, J.; Ishida, M.; Nakajima, T.; Honda, Y.; Kitao, O.; Nakai, H.; Klene, M.; Li, X.; Knox, J. E.; Hratchian, H. P.; Cross, J. B.; Bakken, V.; Adamo, C.; Jaramillo, J.; Gomperts, R.; Stratmann, R. E.; Yazyev, O.; Austin, A. J.; Cammi, R.; Pomelli, C.; Ochterski, J. W.; Ayala, P. Y.; Morokuma, K.; Voth, G. A.; Salvador, P.; Dannenberg, J. J.; Zakrzewski, V. G.; Dapprich, S.; Daniels, A. D.; Strain, M. C.; Farkas, O.; Malick, D. K.; Rabuck, A. D.; Raghavachari, K.; Foresman, J. B.; Ortiz, J. V.; Cui, Q.; Baboul, A. G.; Clifford, S.; Cioslowski, J.; Stefanov, B. B.; Liu, G.; Liashenko, A.; Piskorz, P.; Komaromi, I.; Martin, R. L.; Fox, D. J.; Keith, T.; Al-Laham, M. A.; Peng, C. Y.; Nanayakkara, A.; Challacombe, M.; Gill, P. M. W.; Johnson, B.; Chen, W.; Wong, M. W.; Gonzalez, C.; Pople, J. A. Gaussian 03; Rev. B.01 ed.; Gaussian, Inc.: Wallingford CT, 2004.

(171) Boys, S. F.; Bernardi, F. *Molecular Physics* **1970**, *19*, 553.

(172) Seeger, R.; Pople, J. A. *Journal of Chemical Physics* **1977**, *66*, 3045.

(173) Fukutome, H. *International Journal of Quantum Chemistry* **1981**, *20*, 955.

(174) Paldus, J.; Veillard, A. *Molecular Physics* **1978**, *35*, 445.

(175) Snis, A.; Panas, I. *Chemical Physics* **1997**, *221*, 1.

(176) Gordon, M. S.; Schmidt, M. W.; Chaban, G. M.; Glaesemann, K. R.; Stevens, W. J.; Gonzalez, C. *Journal of Chemical Physics* **1999**, *110*, 4199.

(177) Hiberty, P. D. The Breathing Orbital Valence Bond Method. In *Modern Electronic Structure Theory and Applications in Organic Chemistry* Ernest, R. D., Ed.; World Scientific Publishing Company, 1997; pp 320.

(178) Szalay, P. G.; Vazquez, J.; Simmons, C.; Stanton, J. F. *Journal of Chemical Physics* **2004**, *121*, 7624.

(179) Pasinszki, T. *Physical Chemistry Chemical Physics* **2008**, *10*, 1411.

(180) Zewail, A. H. *Journal Of Physical Chemistry* **1996**, *100*, 12701.

(181) Zewail, A. H. *Journal of Physical Chemistry A* **2000**, *104*, 5660.

(182) Zanni, M. T.; Davis, A. V.; Frischkorn, C.; Elhanine, M.; Neumark, D. M. *Journal of Chemical Physics* **2000**, *112*, 8847.

(183) Zanni, M. T.; Davis, A. V.; Frischkorn, C.; Elhanine, M.; Neumark, D. M. *Journal of Chemical Physics* **2000**, *113*, 8854.

(184) Ervin, K. M.; Lineberger, W. C. Photoelectron Spectroscopy of Negative Ions. In *Advances in Gas Phase Ion Chemistry*; Adams, N. G., Babcock, L. M., Eds.; JAI Press: Greenwich, 1992; Vol. 1; pp 121.

(185) Zanni, M. T.; Taylor, T. R.; Greenblatt, B. J.; Soep, B.; Neumark, D. M. *Journal of Chemical Physics* **1997**, *107*, 7613.

(186) Zanni, M. T.; Batista, V. S.; Greenblatt, B. J.; Miller, W. H.; Neumark, D. M. *Journal of Chemical Physics* **1999**, *110*, 3748.

(187) Houston, P. L. *Accounts Of Chemical Research* **1995**, *28*, 453.

(188) Seideman, T. *Journal of Chemical Physics* **1997**, *107*, 7859.

(189) Seideman, T. *Journal of Chemical Physics* **2000**, *113*, 1677.

(190) Seideman, T. *Physical Review a* **2001**, *64*, 042504.

(191) Seideman, T. *Annual Review of Physical Chemistry* **2002**, *53*, 41.

(192) Blanchet, V.; Lochbrunner, S.; Schmitt, M.; Shaffer, J. P.; Larsen, J. J.; Zgierski, M. Z.; Seideman, T.; Stolow, A. *Faraday Discussions* **2000**, *115*, 33.

(193) Blanchet, V.; Zgierski, M. Z.; Stolow, A. *Journal of Chemical Physics* **2001**, *114*, 1194.

(194) Schmitt, M.; Lochbrunner, S.; Shaffer, J. P.; Larsen, J. J.; Zgierski, M. Z.; Stolow, A. *Journal of Chemical Physics* **2001**, *114*, 1206.

(195) Lochbrunner, S.; Larsen, J. J.; Shaffer, J. P.; Schmitt, M.; Schultz, T.; Underwood, J. G.; Stolow, A. *Journal of Electron Spectroscopy and Related Phenomena* **2000**, *112*, 183.

(196) Lochbrunner, S.; Schultz, T.; Schmitt, M.; Shaffer, J. P.; Zgierski, M. Z.; Stolow, A. *Journal of Chemical Physics* **2001**, *114*, 2519.

(197) Suzuki, T.; Wang, L.; Kohguchi, H. *Journal of Chemical Physics* **1999**, *111*, 4859.

(198) Wang, L.; Kohguchi, H.; Suzuki, T. *Faraday Discussions* **1999**, *113*, 37.

(199) Davies, J. A.; LeClaire, J. E.; Continetti, R. E.; Hayden, C. C. *Journal of Chemical Physics* **1999**, *111*, 1.

(200) Bragg, A. E.; Wester, R.; Davis, A. V.; Kammrath, A.; Neumark, D. M. *Chemical Physics Letters* **2003**, *376*, 767.

(201) Davis, A. V.; Wester, R.; Bragg, A. E.; Neumark, D. M. *Journal of Chemical Physics* **2003**, *118*, 999.

(202) Eppink, A. T. J. B.; Parker, D. H. *Review Of Scientific Instruments* **1997**, *68*, 3477.

(203) Wiley, W. C.; McLaren, I. H. *Rev. Sci. Instr.* **1955**, *26*, 1150.

(204) Greenblatt, B. J.; Zanni, M. T.; Neumark, D. M. *Science* **1997**, *276*, 1675.

(205) Eppink, A. T. J. B.; Parker, D. H. *Rev. Sci. Instr.* **1997**, *68*, 3477.

(206) Sanford, T.; Han, S.-Y.; Thompson, M. A.; Parson, R.; Lineberger, W. C. *The Journal of Chemical Physics* **2005**, *122*, 054307.

(207) Thompson, M. A.; Parson, R., I2- and IBr- potentials (personal communication).

(208) Alfano, J. C.; Kimura, Y.; Walhout, P. K.; Barbara, P. F. *Chemical Physics* **1993**, *175*, 147.

(209) Kliner, D. A. V.; Alfano, J. C.; Barbara, P. F. *Journal of Chemical Physics* **1993**, *98*, 5375.

(210) Walhout, P. K.; Alfano, J. C.; Thakur, K. A. M.; Barbara, P. F. *Journal of Physical Chemistry* **1995**, *99*, 7568.

(211) Banin, U.; Ruhman, S. *Journal Of Chemical Physics* **1993**, *98*, 4391.

(212) Gershgoren, E.; Banin, U.; Ruhman, S. *Journal of Physical Chemistry a* **1998**, *102*, 9.

(213) Yasumatsu, H.; Koizumi, S.; Terasaki, A.; Kondow, T. *Journal of Chemical Physics* **1996**, *105*, 9509.

(214) Yasumatsu, H.; Terasaki, A.; Kondow, T. *Journal of Chemical Physics* **1997**, *106*, 3806.

(215) Amar, F. G.; Perera, L. *Zeitschrift Physik D* **1991**, *20*, 173.

(216) Gertner, B. J.; Ando, K.; Bianco, R.; Hynes, J. T. *Chemical Physics* **1994**, *183*, 309.

(217) Bianco, R.; Hynes, J. T. *Journal of Chemical Physics* **1995**, *102*, 7864.

(218) Bianco, R.; Hynes, J. T. *Journal of Chemical Physics* **1995**, *102*, 7885.

(219) Benjamin, I.; Barbara, P. F.; Gertner, B. J.; Hynes, J. T. *Journal of Physical Chemistry* **1995**, *99*, 7557.

(220) Ray, D.; Levinger, N. E.; Papanikolas, J. M.; Lineberger, W. C. *Journal of Chemical Physics* **1989**, *91*, 6533.

(221) Papanikolas, J. M.; Vorsa, V.; Nadal, M. E.; Campagnola, P. J.; Buchenau, H. K.; Lineberger, W. C. *Journal of Chemical Physics* **1993**, *99*, 8733.

(222) Nandi, S.; Sanov, A.; Delaney, N.; Faeder, J.; Parson, R.; Lineberger, W. C. *Journal of Physical Chemistry a* **1998**, *102*, 8827.

(223) Sanov, A.; Nandi, S.; Lineberger, W. C. *Journal of Chemical Physics* **1998**, *108*, 5155.

(224) Sanov, A.; Sanford, T.; Nandi, S.; Lineberger, W. C. *Journal of Chemical Physics* **1999**, *111*, 664.

(225) Tellinghuisen, J. *Journal of Chemical Physics* **1985**, *82*, 4012.

(226) Zheng, X. N.; Fei, S. L.; Heaven, M. C.; Tellinghuisen, J. *Journal of Chemical Physics* **1992**, *96*, 4877.

(227) Churassy, S.; Martin, F.; Bacis, R.; Vergès, J.; Field, R. W. *Journal of Chemical Physics* **1981**, *75*, 4863.

(228) Viswanathan, K. S.; Tellinghuisen, J. *Journal of Molecular Spectroscopy* **1983**, *101*, 285.

(229) Appadoo, D. R. T.; Le Roy, R. J.; Bernath, P. F.; Gerstenkorn, S.; Luc, P.; Vergès, J.; Sinzelle, J.; Chevillard, J.; D'Aignaux, Y. *Journal of Chemical Physics* **1996**, *104*, 903.

(230) Lawley, K. P.; MacDonald, M. A.; Donovan, R. J.; Kvaran, A. *Chemical Physics Letters* **1982**, *92*, 322.

(231) Saute, M.; Aubert-Frécon, M. *Journal of Chemical Physics* **1982**, *77*, 5639.

(232) Le Roy, R. J. "A computer program implementing the first-order RKR method for determining diatomic molecule potential energy curves," University of Waterloo, 2004.

(233) Wrede, E.; Laubach, S.; Schulenburg, S.; Brown, A.; Wouters, E. R.; Orr-Ewing, A. J.; Ashfold, M. N. R. *Journal of Chemical Physics* **2001**, *114*, 2629.

(234) Radzykewycz, D. T.; Littlejohn, C. D.; Carter, M. B.; Clevenger, J. O.; Purvis, J. H.; Tellinghuisen, J. *Journal of Molecular Spectroscopy* **1994**, *166*, 287.

(235) Faeder, J.; Delaney, N.; Maslen, P. E.; Parson, R. *Chemical Physics Letters* **1997**, *270*, 196.

(236) Faeder, J.; Parson, R. *Journal Of Chemical Physics* **1998**, *108*, 3909.

(237) Zanni, M. T., Private Communication.

(238) Maslen, P. E.; Faeder, J.; Parson, R. *Chemical Physics Letters* **1996**, *263*, 63.

(239) *CRC Handbook of Chemistry and Physics*, 84 ed.; CRC Press: Boca Raton, Florida, 2004.

(240) Dribinski, V.; Ossadtchi, A.; Mandelshtam, V. A.; Reisler, H. *Rev. Sci. Instr.* **2002**, *73*, 2634.

(241) Mulliken, R. S. *Journal of Chemical Physics* **1971**, *55*, 288.

(242) Tromp, J. W.; Le Roy, R. J. *Journal of Molecular Spectroscopy* **1985**, *109*, 352.

(243) Tellinghuisen, J. *Journal of Chemical Physics* **1973**, *58*, 2821.

(244) Tellinghuisen, J. *Journal of Chemical Physics* **2003**, *118*, 3532.

(245) Martin, F.; Bacis, R.; Churassy, S.; Vergès, J. *Journal of Molecular Spectroscopy* **1986**, *116*, 71.

(246) Teichteil, C.; Pelissier, M. *Chemical Physics* **1994**, *180*, 1.

(247) de Jong, W. A.; Visscher, L.; Nieuwpoort, W. C. *Journal of Chemical Physics* **1997**, *107*, 9046.

(248) Snedecor, G. W.; Cochran, W. G. Statistical Methods; 7th ed.; Iowa State University Press: Ames, Iowa, 1980; pp 507.

(249) Mabbs, R.; Surber, E.; Sanov, A. *The Journal of Chemical Physics* **2005**, *122*, 054308.

(250) Mabbs, R.; Pichugin, K.; Sanov, A. *Journal of Chemical Physics* **in press**.

(251) Maslen, P. E.; Faeder, J.; Parson, R. *Chemical Physics Letters* **1996**, *263*, 63.

(252) Mabbs, R.; Surber, E.; Sanov, A. *Chemical Physics Letters* **2003**, *381*, 479.

(253) Zanni, M. T.; Greenblatt, B. J.; Davis, A. V.; Neumark, D. M. *Proc. SPIE* **1998**, *3271*, 196.

(254) Zanni, M. T.; Greenblatt, B. J.; Davis, A. V.; Neumark, D. M. *Journal of Chemical Physics* **1999**, *111*, 2991.

(255) Zhu, L.; Takahashi, K.; Saeki, M.; Tsukuda, T.; Nagata, T. *Chemical Physics Letters* **2001**, *350*, 233.

(256) Nakanishi, R.; Saitou, N.; Ohno, T.; Kowashi, S.; Yabushita, S.; Nagata, T. *Journal of Chemical Physics* **2007**, *126*.

(257) Choi, H.; Bise, R. T.; Hoops, A. A.; Neumark, D. M. *Journal of Chemical Physics* **2000**, *113*, 2255.

(258) Hoops, A. A.; Gascooke, J. R.; Faulhaber, A. E.; Kautzman, K. E.; Neumark, D. M. *Journal of Chemical Physics* **2004**, *120*, 7901.

(259) Sanov, A.; Sanford, T.; Butler, L. J.; Vala, J.; Kosloff, R.; Lineberger, W. C. *Journal of Physical Chemistry a* **1999**, *103*, 10244.

(260) Kirk, A. P.; Detlev, F.; Erich, G.; Hermann, S.; Michael, D. *The Journal of Chemical Physics* **2003**, *119*, 11113.

(261) Feller, D. *Journal of Computational Chemistry* **1996**, *17*, 1571.

(262) Schuchardt, K. L.; Didier, B. T.; Elsethagen, T.; Sun, L. S.; Gurumoorthi, V.; Chase, J.; Li, J.; Windus, T. L. *Journal of Chemical Information and Modeling* **2007**, *47*, 1045.

(263) Do, K.; Klein, T. P.; Pommerening, C. A.; Sunderlin, L. S. *Journal of the American Society For Mass Spectrometry* **1997**, *8*, 688.

(264) Taylor, T. R.; Asmis, K. R.; Zanni, M. T.; Neumark, D. M. *Journal of Chemical Physics* **1999**, *110*, 7607.

(265) Shida, T.; Iwata, S. *The Journal of Physical Chemistry* **1971**, *75*, 2591.

(266) Bordas, C.; Paulig, F.; Helm, H.; Huestis, D. L. *Review of Scientific Instruments* **1996**, *67*, 2257.